Development and Testing of a High Speed Hydraulic Manipulator with Single Time Scale Visual Servoing

by

© Migara Haripriya Liyanage

A thesis submitted to the School of Graduate Studies for the partial fulfillment of the requirements for the degree of Doctor of Philosophy

Faculty of Engineering and Applied Science
Memorial University of Newfoundland
St. John's, Newfoundland, Canada

May 2014

Abstract

Automation of production processes has enabled to meet the dramatic demand for manufactured products that has grown out of the increase in world population. In existing industries greater production requirements and improvement in product quality call for faster industrial robots. This study details the design and development of a high-speed visual servoing system for industrial applications. The proposed visual servoing system consists of a high speed robotic manipulator, a high-speed camera system and an embedded controller.

The proposed robotic manipulator has the configuration of a Selective Compliant Assembly Robotic Arm (SCARA). It uses two custom-designed double vane rotary hydraulic actuators for driving the links of the robot. The SCARA system was mathematically modeled and simulated. Based on the simulation results, the hydraulic actuators were sized for optimal performance. A prototype actuator was subsequently designed, manufactured and experimentally evaluated. The test results show that the proposed actuator is capable of reaching torques of up to 460 Nm in 30 ms with a payload of 12 kg. This is not possible with electric motors of similar size. Then the proposed SCARA was designed and fabricated using the proposed actuators. The end effector of this manipulator was capable of reaching velocities of up to 2.7 ms^{-1} with a payload of 5.3 kg. Comparable performance is not feasible with contemporary

SCARA type robots.

The proposed robot was designed for handling payloads up to 15 kg with speeds of up to 2 ms^{-1}. This often results in flexing of the links and twisting of the support column, adding external disturbances to the system. A high-speed camera system was designed and built to obtain the position of the end effector as feedback for the controller. It uses a two dimensional Position Sensitive Detector as the image sensor. An electronic circuit was designed and built for signal conditioning and data acquisition from the Position Sensitive Detector. It was then calibrated to account for non-linearities on the image sensor. The camera was constructed using this Position Sensitive Detector circuit, a lens and an infra red filter.It was then calibrated to estimate the extrinsic and intrinsic parameters. This camera was capable of carrying out measurements at frequencies of up to 1350 Hz. The measurements made by this camera produced an average absolute accuracy of 0.31 mm and 0.37 mm in x and y directions, respectively.

A Field Programmable Gate Array was used in this study as the platform for developing an embedded controller for the robot. Using contemporary Field Programmable Gate Array technology, a powerful virtual processor can be synthesized and integrated with custom hardware to create a dedicated controller that out performs some of the conventional microcontroller and microprocessor based designs. The Field Programmable Gate Array based controller takes advantage of both hardware features and virtual processor technology. The input, output interfaces for this controller were implemented using hardware. Complex functions that are difficult to be implemented in hardware were implemented using a virtual soft processor. Four different types of controllers were implemented and tested. These include hardware proportional-derivative, software proportional-derivative, single time scale visual servoing and set

point modification type controllers. The proposed implementation carried out single time scale visual servoing at frequencies of up to 330 Hz.

Acknowledgements

During my stay at MUN I have learned a lot about engineering through working in this project. I was very fortunate to involve in a project which consists of mechanical design, electronic circuit design, fabrication, programming and testing. It is a rare opportunity that a PhD candidate gets to work on a real life project which involve work in almost all the labs in Engineering. It was a privilege to work with Dr. Nicholas Krouglicof. I pay my profound gratitude to him for being my supervisor. His wisdom and knowledge in engineering has honed me to be a hands on engineer. I would also like to thank Dr. Raymond Gosine, Dr. Andrew Vardy and Prof. Andrew Fisher for being in my supervisory committee.

I take this opportunity to thank the Memorial University of Newfoundland, Natural Science and Engineering Research Council of Canada (NSERC), Atlantic Canada Opportunities Agency (ACOA), Research and Development Corporation Newfoundland and Labrador (RDC), The Boeing Company and Baader-Canopolar Inc, St Johns for providing the funds to carry out this research.

I am grateful to Dr. Louis L. Whitcomb of Department of Mechanical Engineering, The Johns Hopkins University, Baltimore, MD, USA for agreeing to serve as my external examiner. I would also like to thank Dr. Ralf Bachmayer and Dr. Geoff

Rideout for serving as my internal examiners. I thank them for taking their valuable time to review my thesis. Their comments and suggestions have helped me to improve the quality of my thesis.

I would like to thank Dr. Geoff Rideout for his valuable guidance that he gave me for the section on bond graph modeling. I would also like to thank Dr. Amy Hsiao for proof reading my thesis.

The support from the technical staff was indispensable in carrying out this research. In this regard, my special thanks to Mr. Ken Brown of the Technical Services Division of MUN for fabricating this robotic arm. I would like to thank Mr. Matthew Curtis for all his help with the hydraulic system in the Structures Lab. I would also take this opportunity to thank Messrs. Tom Pike, Brian Pretty, Steve Steel, Don Taylor and Ms. Caroline Koenig who always supported me when I needed help.

My thanks to fellow graduate students Messrs. Taufiqur Rahman, Dions Hicks, Michael Morgan, Dennis Fifield and Oscar De Silva. Their support during experiments, valuable suggestions and help in trouble shooting was extremely useful. The support that I have received from the work term students was an immense help in conducting this research. I would like to thank Messrs. Nikhil Pansare and Mathew Roberts for their help.

My gratitude to Mr. Eranda Harinath and Mr. Chitral Angammana for helping me to find this amazing opportunity at MUN. I also take this chance to thank Dr. George Mann. My special gratitude Ms. Hari Priyai Sekaran for being a source of motivation throughout my study.

Last but not least I take this opportunity to thank my parents Mrs. Amai Liyanage and Mr. Dharmasena Liyanage and my relatives for all the support and encouragement throughout my career. I humbly pay my profound gratitude to them.

Finally, I would like to dedicate my thesis to my mother Mrs. Amai Liyanage and my father Mr. Dharmasena Liyanage.

Table of Contents

List of Tables

List of Figures

Chapter 1

Introduction

In recent years there has been an increase in the use of robots for industrial purposes despite the downward economic trends in many industrialized nations. The operational stock of multipurpose industrial robots have increased up to 1.1 million units in 2011, which is almost an 8.9% increase from the previous year. The trend is expected to continue up to 2015 [5]. There are several driving factors towards this upward trend: (1) demand for higher production targets due to the increase in world population, (2) requirements to meet quality standards due to intense competition, (3) the need to replace human operators in tasks that involve monotonous industrial production lines or hard physical work and (4) the performance of tasks where repeatability is not feasible with human beings. These robots have performed a wide variety of tasks including material handling, welding, assembly operations and material dispensing operations such as painting and food processing[6].

The main industries that use robots are the automotive industry, electronics, rubber and plastics, food and beverage [6]. Out of the total number of robots used, 36% of the industrial robots in 2011 are found in the automotive industry. This is because

of the requirement to automate production facilities involving heavy duty tasks that makes it challenging for human beings to perform. However, in recent years the requirement for large production volumes has been the motivating factor behind the automation of these facilities. One industry that has seen increased demand over the years is the food industry. Large production rates make it difficult to meet quality standards. The food industry comprises only 2.6% of the total industrial robots used in 2011 [6]. This is because there has been much less emphasis on automation of food processing facilities.

Increase in production requirements have resulted in larger material volumes on production lines. In addition, the speeds of these industrial lines have also increased. Increase in production requirements have resulted in faster production lines handling larger material volumes. Therefore, robots that are capable of performing various operations on these production lines at high speeds, handling large masses, are essential. An industrial manipulator which is capable of following a predetermined trajectory at high speeds would be particularly useful for these application areas; however, the accuracy of the operation should not be compromised for the sake of speed.

Most industrial robots use electric power for operation unless they handle large masses [7]. Electric motors are used whenever the applications require speed. However, other alternatives to electric power should to be considered for the development of novel high-speed systems which can deliver large torques. One such option is hydraulic power. It has been used for a very long time in the operation of various industrial systems [8], [9], [10]. Hydraulic actuators are preferred over electric motors whenever large masses are handled. This is because hydraulic systems can handle a large amount of power [8]. However, little work has been done over the years to exploit the

power density in hydraulic systems for producing high speeds. This may be because hydraulic systems are considered to be very complex. High pressure lines may result in leaks and may cause contamination [8]. However, with the advancement of various modern technologies hydraulic systems could be designed in a such way that these systems are leak-proof with a high degree of reliability. Any system developed for an industrial production facility needs to be robust, reliable and capable of operating over extended periods. It should also have fewer moving parts so that it results in less maintenance in order to avoid downtime. Modern hydraulic systems have the capacity to meet these requirements.

Development of a robust controller is an important part of the robot design. In recent years there have been developments in the sub-micron process technology [11]. There have also been advancements in field programmable gate array (FPGA) technology. FPGAs have gained acceptance over Application-Specific Integrated Circuit (ASIC) for industrial control applications [12], [11]. This is largely because FPGAs could be reconfigured on site by the designer to suit a variety of design requirements. The FPGAs provide feasibility to implement functions in hardware which result in much faster processing times. The fact that virtual processors could be implemented in FPGAs gives the designers a chance to use both the advantages of hardware and software based implementation [13]. Parallelism is another advantage of FPGAs which could be used in some of the applications [14]. Therefore, FPGA-based embedded system technology could provide attractive solutions in implementing controllers in the field of robotics.

1.1 Motivation

In recent years, the demand for production requirements has increased rapidly. One such industry which has increased demand over the years is the food industry. For example, a typical large-scale poultry plant could process up to 250,000 birds per day at a rate of 180 birds per minute [15]. Higher production rates result in production lines transporting large volumes at high speeds. A conveyor belt of such poultry processing plant could transport up to 100 poultry pieces per minute at a speed of 0.4 m/s. This makes it difficult to conduct manual operations on these lines. Production lines which transport large numbers make manual inspection difficult and costly. It also makes it difficult to meet the required quality standards. The boneless products produced by a typical plant traditionally employ manual inspection. This results in a significant proportion of the parts (almost 25%) containing bone fragments or cartilage.

Conveyor belts involve planar operations. Hence, SCARA type manipulators are preferred. Currently, these are widely used to perform tasks such as defect removal, pick-and-place, circuit board and mechanical assembly operations. Current SCARA type manipulators usually use electric motors as actuators [16], [7]. A contemporary Adept® Cobra s800 SCARA robot is shown in Fig. 1.1 [2]. This robot has a rated payload of 2 kg and and it is suitable for operation under speeds of 0.9 ms^{-1}.

Conventional high-speed robots cannot handle large payloads while the robots used for handling large pay loads are not capable of reaching high speeds. Some of the operations in industrial facilities require handling of large payloads of up to 15 kg at speeds that is greater than 1 ms^{-}1. Typically, large motors have to be used whenever large speeds are required. This limits the performance of these robots due to motor inertia. Whenever large loads or torques are handled, hydraulic power is used. How-

Figure 1.1: Contemporary Adept® Cobra s800 SCARA manipulator [2]

ever, currently there is no manipulator which has the capability of handling payloads up to 15 kg at speeds of up to 2 $ms^{-}1$ [2]. Therefore, the development of efficient actuators that can meet these goals is required.

Some robotic operations are often associated with fast starts, stops and speed reversals. When a robotic arm moves a large payload at high accelerations, it produces significant inertial forces. These forces can be large enough to produce significant deflections in the mounted structure. In addition, during a high-speed operation, flexing of the links may also occur. This amplifies the deflection of the end effector (EE) from the desired position. Accurate tracking during high speed operations of a manipulator is important for performing some of the industrial operations. Therefore,

there is a need to develop more effective control algorithms which could address the EE displacement.

Practical implementation of controllers in hardware is an important part of control system design. FPGAs define a new generation of controllers. In recent years, FPGA technology has greatly improved due to the enhancement of sub-micron process technology [11]. It provides a single chip architecture which could lead to more integrated solutions. The logic level implementation of functions results in faster execution times. It also allows the implementation of designs with dedicated parallel architectures, further reducing the execution time of algorithms [12]. FPGAs could provide a potential for modern control system applications.

1.1.1 Proposed Visual Servoing System

The main emphasis of this work is to develop a high-speed SCARA type robotic manipulator with visual servoing. This manipulator is expected to perform operations on industrial production lines such as conveyor belts. The EE of this manipulator is capable of covering a two dimensional (2-D) workspace profile. This study has only considered the development of a 2-D positioning system of the manipulator.

Conventional SCARA type industrial robots use electric motors. However, hydraulic actuators are capable of producing high power-to-weight ratios and power-to -volume ratios that are much larger than comparable electric motors. The torque-to-inertia ratio is also large, so that it is able to reach very high accelerations [8]. Hydraulic actuators are preferred over the electric counterparts when higher speeds are required with fast starts, stops and speed reversals [7], [8]. Therefore, the links of this manipulator will be driven using hydraulic actuators. Double vane rotary type actuators are

used in order to cancel out the unbalanced shaft forces that could be excessive during high accelerations. High response electro-hydraulic servo valves are used to control the hydraulic flow in and out of the actuators. The SCARA manipulator consists of two links and an EE. The actuators are directly coupled to the links. An EE is expected to be mounted at the end of the second link.

The actuators of this manipulator are instrumented with encoders. These provide the relative angular position of the links. In order to control the arm an absolute measurement is required as feedback. This is obtained using a high-speed camera with a 2-D position sensitive detector (PSD) as the image sensor. It tracks an infra red (IR) marker which is mounted on to the EE of the robot.

The motion controller is implemented in hardware using a microcontroller and an FPGA. Microcontrollers provide a contemporary solution to digital control system implementation. The FPGA provided an integrated single-chip embedded system, which was used to implement complex control algorithms. The high-speed imaging system was used to carry out position based visual servoing (PBVS). This algorithm used link angles and EE position as feedback. A schematic diagram of the proposed system is shown in Fig. 1.2.

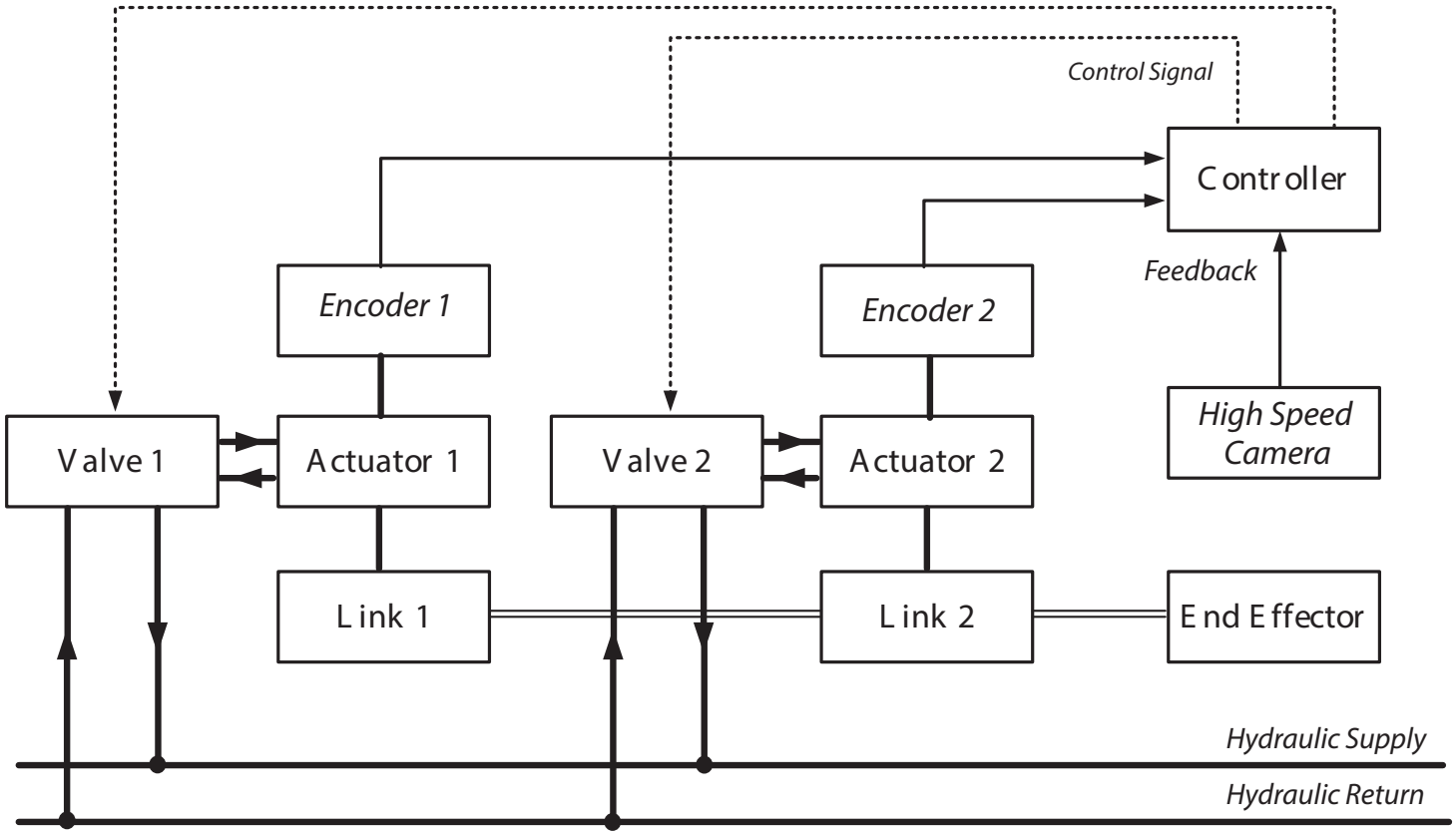

Figure 1.2: The schematic diagram of the proposed system

1.1.2 Major Contributions From the Thesis

The major contributions from this study are as follows.

Modeling and analysis of a high speed SCARA type manipulator with hydraulic actuators on a compliant support using bond graph theory: Bond graph theory was used for modeling the proposed system. Bond graphs were developed for sub-components of the system which included electro-hydraulic servo valve, hydraulic actuators, SCARA arm and the compliant support. The dynamic performance of the manipulator at high speeds for various displacements and trajectories was analyzed using the work profile of these bond graphs. The deflection of the compliant support column was used to analyze the effects of torsional vibration on the EE.

Development and testing of a high speed SCARA type robotic manipulator with hydraulic actuators: A custom-designed hydraulic actuator was developed and fabricated for high speed robotic applications. Experimental tests were carried out to evaluate the performance of this actuator. A high-speed SCARA type manipulator was fabricated using the actuators. These were used to drive the links of the arm. Tests were carried out to evaluate the dynamic performance of the arm.

Development of an Embedded system for controlling the manipulator using an FPGA: A compact single chip solution is implemented for the controls of the robot. An embedded system was designed and developed using an FPGA for controlling the arm. Both hardware and a virtual processor were used for implementing the required function for the control operation. The interfacing comprised feedback from the encoders and the high-speed camera and control signals to a digital to analog converter (DAC). Interfacing functions for quadrature decoders of encoders, Serial

Peripheral Interface Input (SPI/in) of the high speed camera and the Serial Peripheral Interface Output (SPI/out) of servo valve driver were implemented in the hardware. The Propositional Derivative (PD) type controller was implemented in both hardware and in the virtual processor. Functions for estimating the EE position from the camera signals were implemented in the virtual processor.

Development and Testing of a High Speed Camera for position measurement: A camera for high speed position measurement applications was developed. This camera used a 2-D PSD as the image sensor for high speed sensing. An electronic circuit was developed for signal conditioning and data acquisition from the PSD. Then the camera was fabricated using a housing, this sensor circuit, an IR filter and the connections. A calibration methodology for an infra-red camera was derived in order to carry out position measurements with a high accuracy. Under this the image sensor and camera were calibrated to estimate the intrinsic parameters. Next an on-site calibration was carried out to estimate the extrinsic parameters. This camera was tested next to evaluate the accuracy of the results.

Development of a Set Point Modification Based control strategy to address the effect of vibration on the End Effector position: The vibration of the support column results in considerable deflection of the EE. A feed forward control strategy using the feedback from the encoders and the camera was proposed. The proposed algorithm is based on a modification of the predetermined set points of the joint angles to follow a specific trajectory. This algorithm was implemented in an FPGA and tested for performance.

Development of a single time scale visual servoing control strategy: In

contemporary visual servoing systems the vision loop operate at a much slower speed. This study proposed a technique to develop a high speed, single time scale visual servoing system. It integrates a 2-D PSD-based optical position sensing system as the exteroceptive sensor and high resolution joint encoders as proprioceptive sensors. The control algorithm was implemented in an FPGA based hardware platform.

1.1.3 Organization of the Thesis

The rest of the thesis is organized as follows.

Chapter 2 covers the development of mathematical model for a high SCARA type robotic manipulator with hydraulic actuators.

Chapter 3 presents details the design of the proposed robotic manipulator. It includes the design details of the custom-built hydraulic actuator and the robotic arm. This chapter also carries out a finite element analysis of the components designed.

In Chapter 4, the proposed visual servoing system is modeled using a bond graph based methodology. It also includes a simulation of the system for the proposed single time scale visual servoing based control strategy and set point modification based control strategy.

Chapter 5 provides the details of the design and fabrication of the high-speed camera system. It includes design of the signal conditioning circuit and the data acquisition system. It also provides the calibration details of this camera.

The details of the FPGA based embedded system development are outlined in Chap-

ter 6. It also provides the details of development of the input output interface. A virtual processor is developed to perform complex functions. This chapter also covers hardware and software based implementation of various controllers.

Chapter 7 presents the experimental results. These include the testing of the actuators and the robotic arm. Test results are also presented for testing of the proposed controllers.

Chapter 8 presents the conclusions and final remarks. Possible avenues for future work are also discussed in this chapter.

Chapter 2

Modeling and Simulation of the High Speed SCARA Manipulator with Rotary Hydraulic Actuators

2.1 Introduction

SCARA type manipulators are widely used to perform tasks such as defect removal, pick-and-place, brushing, peg-in-hole, circuit board and mechanical assembly operations. Often these tasks require both high-speed maneuvering of the end-effector and accurate tracking. Some of the operations require handling of large payloads of up to 15 kg at high speeds. Conventional high-speed robots cannot handle large payloads, while the robots generally used for handling large payloads are usually not capable of reaching high speeds [2], [17], [18]. In addition, vibration could be an issue due to inertia effects. The application of servo hydraulics can potentially result in a manipulator which is capable of reaching high speeds with relatively large payloads.

Typically, large electric motors are used whenever large speeds or torques are required. The performance of these robots, however, is limited due to motor inertia [19]. Parallel kinematic mechanisms with stationary actuators are often used to produce high speeds. These mechanisms are very accurate and have a high stiffness [20]. Some parallel mechanisms are capable of reaching accelerations of up to 785 ms^{-2} which is almost 80 times the gravitational acceleration [21]; however, they cannot be used with a large payload and have a limited operating envelope. In order to overcome the problem of inertia, drive system components, including the actuator and power transmission components are isolated from the moving parts by being connected via belt drives. However, this introduces backlash and friction into the system. Based on this principle, some studies proposed alternatives such as the wire-driven FALCON (FAst Load CONveyance) robot [22]. The three-degree of freedom (DOF) M.I.T. direct-drive manipulator was proposed in a study by Youcef-Toumi and Kuo [23]. It performs tracking at speeds of 3 m/s with accelerations of up to 3.8 times the gravitational accelerations and accuracies of between 0.05 - 0.1 mm. However, there is no study that has considered using the power available in hydraulics to combine high-speed manipulation with large payloads.

Hydraulic power has been used for decades. The applications for electro-hydraulic servo systems are diverse. These include manufacturing systems, materials test machines, active suspension systems, mining machinery, fatigue testing, flight simulation, paper machines, ships and electromagnetic marine engineering, injection molding machines, robotics, and steel and aluminum mill equipment [24]. Electro-hydraulic servo systems are frequently used in construction, industry, and heavy load motion control and mobile equipment applications. This is due to the fact that they provide the advantage of a high power-to-weight ratio, stiffness and short response time of hydraulic

drives in performing their tasks [10]. Although there is a wide range of actuation technologies, none of them currently rivals the overall performance (power density, bandwidth, stress, stroke) of conventional hydraulic actuation [25]. Hydraulic systems are also commonly used in aircraft, due to their reliability, high power-to-weight ratio and accuracy which make them an ideal choice for actuation of flight surfaces [24].

Hydraulic systems have many advantages. Compared to electric motors, hydraulic actuators are capable of producing power-to-weight ratios up to 5 times and power-to volume ratios up to 10 to 20 times [8]. Furthermore, they have an excellent rate of dimension compared to their delivered torque. Hence, they can be used in environments where large loads have to be handled or available space is scarce. Their high torque-to-inertia ratio results in high acceleration capability. These systems also have a long record of reliability as they may be operated under continuous, intermittent, reversing and stalled conditions. Hydraulic systems have a higher stiffness compared to other drive devices. Therefore, the drop in speed is negligible when large loads are applied [8].

This makes hydraulic servo actuators suitable for direct drive applications, especially when they are provided with hydrostatic bearings, so that Coulomb friction is eliminated [26]. Hydraulic systems have the additional advantages of mechanical simplicity (few moving parts), physical strength and speed. They use hydraulic servo valves and analog resolver units for control and feedback [27]. Thermal limitations associated with electric motors do not apply to hydraulic actuators since the hydraulic fluid cools and lubricates the system. The design of hydraulic actuators is relatively simple as they comprise only valves and pumps. They have a high rate of response with fast

starts, stops and speed reversals [8], [7].

Motion control systems that require either very high force or wide bandwidth are often addressed more efficiently with electro-hydraulic rather than electromagnetic means. In general, applications with bandwidths of greater than about 20 Hz or control power greater than about 15 kW, may be regarded as suitable for servo-hydraulic techniques [24].

In spite of these advantages, servo-hydraulic systems have several inherent disadvantages. Hydraulic power is not readily available like electric power. Generating the high pressure hydraulic fluid is also complex. Motors, pumps, accumulators and hydraulic lines are required to implement such systems. This leads to a very low energy efficiency [28],[29]. Hydraulic systems impose an upper temperature limit. There is a fire and explosion hazard if these systems are used near a source of ignition. However, high-temperature-resistant fluids have been developed to lower the risk of ignition. Contamination due to hydraulics is another major drawback. Owing to the high pressures involved in hydraulic lines, leaks are imminent. Especially, in environments which handle food, it may be important for the system to be free from any contamination. Therefore, the system has to be robust enough in design if these are used in food processing environments. Hydraulic systems involve high precision devices such as valves etc. Manufacturing of such high precision devices is an expensive process [8].

This chapter outlines the development of a novel SCARA type robotic manipulator for high-speed applications. An actuator suitable for such a manipulator should be of light weight, compact in size and capable of reaching high speeds. Two custom-made direct drive double vane rotary actuators are used to drive the revolute joints in

this study. These actuators are designed for high pressure (3000 psi) to produce the required speed and torque. They are light weight, compact in size and have very low rotor inertia. The proposed arm is robust and suitable for operation in demanding environments such as those found in the food processing industry or electronic assembly lines where they are often used. The EE position of this arm can be accurately controlled with a considerable degree of repeatability. Although leakage is an issue, it could be overcome by using a leak-proof, redundant seal design or by using fluids such as water or glycerin depending on the industry.

An important stage in designing such a manipulator is the development of a mathematical model for the robot. The proposed system was modeled using Matlab®-Simulink. A dynamic analysis of the performance of the robot was then carried out. This was used to establish some of the design parameters of the proposed actuator. A suitable actuator design was then proposed. Based on the actuator design and the desired operating envelope, a configuration for the SCARA arm was proposed. Once the system was developed, initial tests were carried out to evaluate the performance of this manipulator. The test results were used to validate the proposed model of the system.

2.2 Related Literature

The main source of literature regarding hydraulic systems is by Merritt [8]. Manring [30] provides an extension of Merritt [8] with illustrative case studies on some of the industrial applications. Jelali and Kroll [31] described the modeling, identification and control aspects of hydraulic systems. It also provides a comprehensive list of past studies with specific approaches to some of the problems.

There are large number of studies on servo-hydraulics. Many studies in the past have considered servo-hydraulic actuators ([9], [32], [33], [34], [35], [36], [37] and [27]). However, most of these studies focus on issues with respect to the control problem of hydraulics ([10], [38], [39], [40], [41], [42] and [9]). Only a few studies ([26], [43], [39] and [33]) have considered servo-hydraulic actuators on industrial robots. However, a study which considers hydraulics for controlling a high speed robotic arm has never been reported.

The mathematical models that govern the hydraulic systems are quite standard. The development of proper models for hydraulic servo actuators is helpful in many ways [37]. Several studies have presented the mathematical models of hydraulic actuators [9], [32], [33], [44], [34], [45], [36], [37]. An analysis of a linear actuator system has been presented in [31],[29], [9]. Heintze et al. [26], and Bilodeau [46] analyzed rotary hydraulic actuators.

There is a lack of studies on servo-hydraulics considering actual industry related problems. Most studies on servo-hydraulics have considered issues related to linear actuators [47], [48] and [49]. Among these, only a few studies have used servo-hydraulic actuators to drive manipulators. Bu and Yao [33] considered linear actuators for driving revolute joints. Linear actuators on revolute joints may limit displacement and performance. There are a limited number of studies on rotary actuators Heintze [26], Bilodeau [46] and [50]. These studies have considered modeling and control of single vane rotary actuators. There has also been a study considering the development of a 6-DOF manipulator with hydraulic actuators using water [51]. However, it was developed for large payload handling and does not consider high-speed operation. None

of these studies has either proposed a double vane rotary hydraulic actuator suitable for continuous high speed manipulator applications or detailed the design of such a high performance actuator.

2.3 Development of the Proposed System

Conventional commercially available SCARA manipulators use brushless DC motors to drive the links. Such manipulators require large DC motors to deliver large torques or speeds. Such motors introduce additional inertia to the system. To handle the problem of inertia, these revolute joints can be coupled with gears or belt drives. This could reduce the performance by introducing delays, slips and friction. Consequently, the SCARA designs with electric motors have limited capabilities in terms of handling large payloads at very high speeds.

The SCARA type robotic arm proposed in this study is expected to operate in a planar x-y work profile without the EE. It consists of two links. Two custom-made direct drive double vane rotary actuators are used to drive the revolute joints. Double vane rotary hydraulic actuators are selected to cancel out any excessive unbalanced forces on the shaft. These actuators are equipped with high response electro-hydraulic servo valves to control the flow of hydraulic fluid in and out of the actuators. The hydraulic fluid to the servo valves is supplied by a high pressure source operating at a pressure of 20.7 MPa (3000 psi). An interface comprising a microcontroller was developed for controlling the arm. A schematic diagram of the proposed SCARA arm is shown in Fig. 2.1. This study does not consider the prismatic joint at the end of the second link which is application dependent.

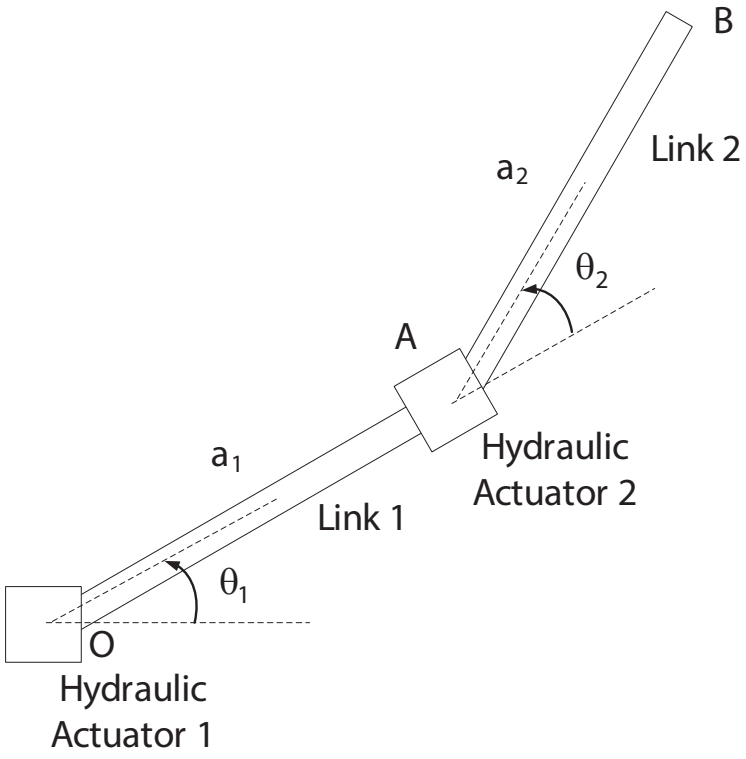

Figure 2.1: A schematic diagram of the proposed SCARA manipulator

2.4 Problem Formulation and Dynamic Model

The proposed system is modeled by considering different subsystems. These subsystems comprise electro-hydraulic servo valves, rotary hydraulic actuators, the SCARA arm and the controller. This section outlines the development of mathematical models for each subsystem.

2.4.1 Model for the Servovalve

Electro-hydraulic servo valves are used for regulating the flow in and out of the actuators. A high response MOOG© G761 series servo valve is considered for this application. An illustration of the valve is given in Fig. 2.2. It consists of a spool which

has lands machined into it moving in a cylindrical sleeve. The lands are aligned with apertures cut into the sleeve in such a way that movement of the spool progressively changes the exposed aperture size and alters differential oil flow between two control ports [24]. When there is a displacement in the spool, it connects the pressure port of the hydraulic supply to one of the two actuator chambers and the reservoir to the other chamber. The spool in the valve is controlled by a flapper-nozzle first stage. A schematic diagram of the cross-section of the specific valve is shown in Fig. 2.3.

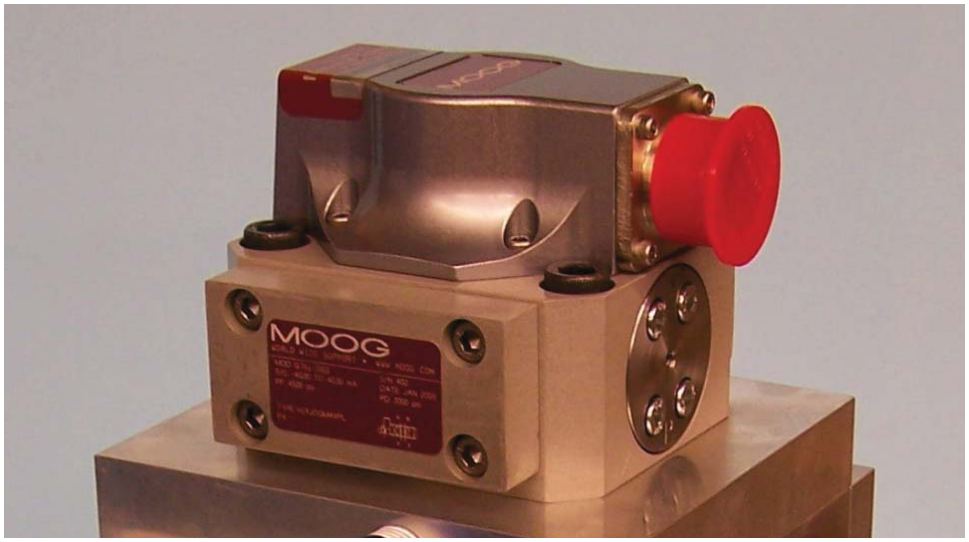

Figure 2.2: The Moog© G761 valve[3]

The valve provides a four-pin electrical box connector for the electrical connections. A schematic diagram of the electrical connections along with the coils is shown in Fig. 2.4. These coils are connected serially as shown in the figure by connecting terminals B and C. The total resistance of the coil will be $R = R_1 + R_2$ and the inductance of the coil will be $L = L_1 + L_2$.

The displacement of the flapper is generated by an electro-magnetic force result-

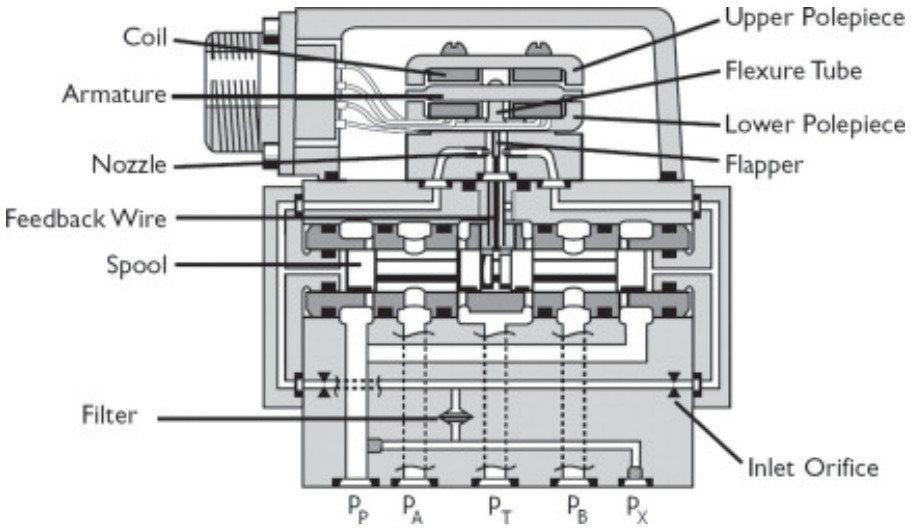

Figure 2.3: A schematic diagram of cross-section of the servovalve [3], [4]

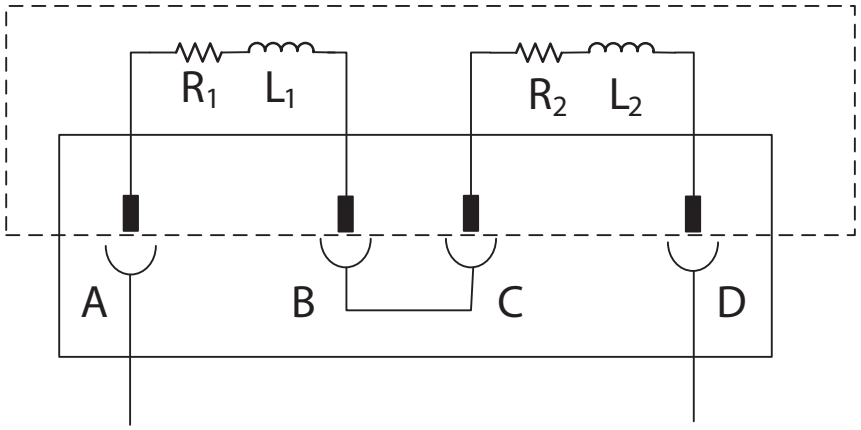

Figure 2.4: A schematic diagram of the servovalve coils

ing from the current flow through two magnetic coils. These magnetic coils could be considered as two series connected resistors and inductors. Using basic circuit theory:

$$I(s) = \frac{1}{Ls + R} U(s) \tag{2.1}$$

Where $I(s)$ is the induced current, L is the coil inductance, R is the coil resistance and $U(s)$ is the voltage command signal applied to the coils.

The relationship between the spool displacement X_v and the induced current in the coil $I(s)$ is assumed to be a first order transfer function. This is given by:

$$X_v(s) = \frac{1}{T_v s + 1} I(s) \tag{2.2}$$

T_v is the first order time constant representing the spool dynamics.

2.4.2 Model for the SCARA Manipulator

Fig. 2.1 shows a SCARA with notations. The links 1 and 2 are denoted by a_1 and a_2. The joint angles are denoted by θ_1 and θ_2. Joint angles shown here are relative joint angles since the encoders provide relative angles. The forward kinematics of the EE is estimated using simple geometric relations. Hence:

$$p_x = a_1 cos\theta_1 + a_2 cos(\theta_1 + \theta_2) \tag{2.3}$$

$$p_y = a_1 sin\theta_1 + a_2 sin(\theta_1 + \theta_2) \tag{2.4}$$

The inverse kinematics of the robotic arm can also be obtained using basic geometric relations. Hence:

$$C = cos\theta_2 = \frac{p_x^2 + p_y^2 - a_1^2 - a_2^2}{2a_1 a_2} \tag{2.5}$$

$$D = \pm\sqrt{1 - cos^2\theta_2} \tag{2.6}$$

$$\theta_2 = atan2(D, C) \tag{2.7}$$

$$\theta_1 = atan2(p_y, p_x) - atan2(a_2 sin\theta_2, a_1 + a_2 cos\theta_2) \tag{2.8}$$

The generalized equation for torque of a serial manipulator is given by [7]:

$$\mathbf{T} = M(q)\ddot{\mathbf{q}} + \mathbf{V}(q, \dot{q}) + \mathbf{G}(q) \tag{2.9}$$

Where $\mathbf{T}$ denotes the torque in each link. Joint variables, including the rotational angle (θ) of each joint is given by $\mathbf{q}$. $M(q)$ is the manipulator inertia matrix. $\mathbf{V}(q, \dot{q})$ is the Coriolis matrix and $\mathbf{G}(q)$ is the vector of gravitational forces.

By considering the Lagrangian dynamics of a SCARA arm we can derive the following equations for the torques in link 1 (T_1) and link 2 (T_2) [52]:

$$\begin{aligned} T_1 = [(\frac{m_1}{3} + m_2 + m_3)a_1^2 + (\frac{m_2}{3} + m_3)a_2^2 + (m_2 + 2m_3) \\ a_1 a_2 cos\theta_2]\ddot{\theta_1} + [(\frac{m_2}{3} + m_3)a_2^2 + (\frac{m_2}{2} + m_3) \\ a_1 a_2 cos\theta_2]\ddot{\theta_2} - (m_2 + 2m_3)a_1 a_2 sin\theta_2(\dot{\theta_1}\dot{\theta_2} + \frac{\dot{\theta_2^2}}{2}) \end{aligned} \tag{2.10}$$

$$\begin{aligned} T_2 = [(\frac{m_2}{3} + m_3)a_2^2 + (\frac{m_2}{2} + m_3)a_1 a_2 cos\theta_2]\ddot{\theta_1} + \\ (\frac{m_2}{3} + m_3)a_2^2\ddot{\theta_2} + \frac{1}{2}(m_2 + 2m_3)a_1 a_2 sin\theta_2 \dot{\theta_1}^2 \end{aligned} \tag{2.11}$$

Where, the masses of rotary actuators are considered to be m_1, m_2 and the mass of the EE is considered to be m_3. The mass of the links of the robotic manipulator is considered to be negligible.

2.4.3 Model for the Rotary Actuator

The hydraulic system consists of a double vane type rotary actuator, an electro-hydraulic two-land-four-way servo valve, a hydraulic power unit and other basic components used for a hydraulic supply. The high response servo valve (Moog© G761 series) acts as a regulating device for the oil flow. The hydraulic actuator consists of two compartments separated by a movable part or vane which produces rotary motion based on the direction of oil flow. A schematic diagram of a cross-section of the double vane actuator is shown in Fig. 2.5. It shows the chambers 1 and 2.

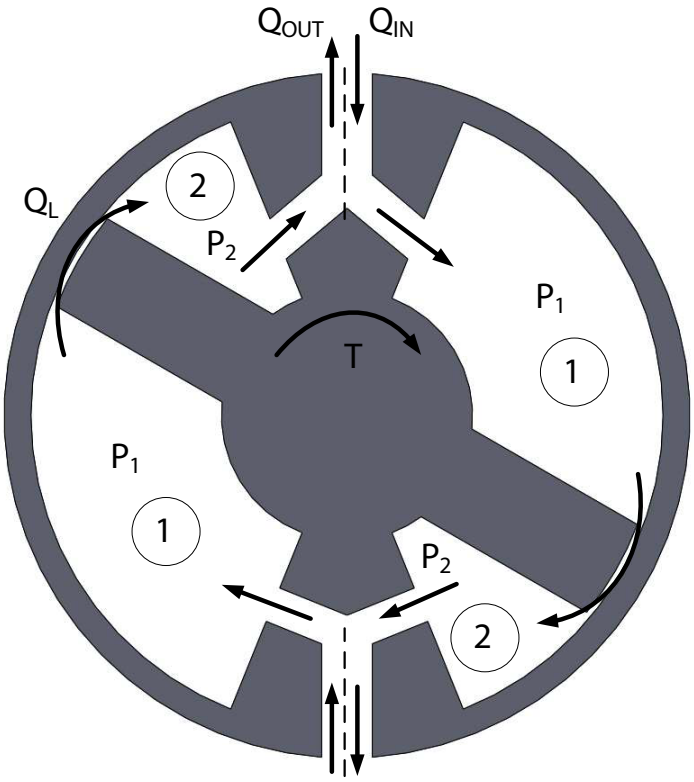

Figure 2.5: A cross section of the double vane rotary actuator

The basic mathematical relationships for hydraulic servo systems have been given in Merrit [8]. The dynamics of rotary hydraulic actuators coupled to a servo valve is described by a number of theoretical relations as given in [26], [46] and [50].

The Fig. 2.5 illustrates the rotation of the shaft in a clockwise direction. The pressure in Chamber 1 should be higher than that of the pressure in Chamber 2. This is accomplished by displacing the spool valve so that it connects the oil supply to the Chamber 1. It results in an oil flow from the supply into the Chamber 1 and oil flowing out from the Chamber 2 to the tank. This flow is turbulent and the relation between the flow and effort variables (flow rate and pressure) is given by the square-root law [46]. Considering that the flow through the spool valve is similar to the flow through an orifice, these relationships are given by [8]:

$$Q_1 = c_d A_v \sqrt{\frac{2}{\rho}(P_s - P_1)} \tag{2.12}$$

$$Q_2 = c_d A_v \sqrt{\frac{2}{\rho}(P_2 - P_T)} \tag{2.13}$$

Where Q_1 is the flow rate into the chambers, Q_2 is the flow rate from the chambers, c_d is the orifice flow coefficient, A_v is the area of valve opening, ρ is the density of fluid, P_s is the supply pressure, P_T is the tank pressure, P_1 is the pressure in chamber 1 and P_2 is the pressure in chamber 2.

In order to move the vane counter-clockwise, the spool valve moves in the opposite direction with flow into the right chamber. Thus:

$$Q_1 = c_d A_v \sqrt{\frac{2}{\rho}(P_1 - P_T)} \tag{2.14}$$

$$Q_2 = c_d A_v \sqrt{\frac{2}{\rho}(P_s - P_2)} \tag{2.15}$$

Cross-port leakage occurs when there is a high differential pressure across the two chambers of the actuator. This is given by:

$$Q_L = c_d A_L \sqrt{\frac{2}{\rho}(P_1 - P_2)} \tag{2.16}$$

Where Q_L is the oil leakage rate and A_L is the area of oil leakage.

The area of the spool valve opening is a function of the spool displacement. Thus,

$$A_v = K_v x_v \tag{2.17}$$

Where A_v is the area of the valve opening, K_v is the circumference of the cylindrical spool and x_v is spool displacement.

Furthermore, when the system is subjected to high supply pressures the total system including the actuator and conduits expand. Using the principles of continuity and fluid compressibility, pressure can be related to flow rate as follows [8]:

$$P_1 = \frac{\beta}{V_1} \int (Q_1 - D_M \dot{\theta} - Q_L)\, dt \tag{2.18}$$

$$P_2 = \frac{\beta}{V_2} \int (Q_L + D_M \dot{\theta} - Q_2)\, dt \tag{2.19}$$

Where P_1 and P_2 denote pressure in chambers 1 and 2, V_1 and V_2 denote the initial volume in chambers 1 and 2, β denotes the effective bulk modulus of the system, D_M

denotes the actuator displacement coefficient given in displaced fluid volume per unit of angular displacement and $\dot{\theta}$ denotes angular velocity of the revolute joints.

The torque available to rotate the arm is the torque resulting from the pressure difference across the vane less the torque required to overcome viscous friction of the fluid and Coulomb friction and/or stiction torque of the actuator shaft. Therefore, by considering torque balance:

$$T_A = D_M(P_1 - P_2) - \sigma\dot{\theta} - c_t(\theta - \theta_f) + T_c \tag{2.20}$$

Where, T_A is the net actuator torque, σ is the viscous friction coefficient of oil, c_t is the torsional stiffness of the connecting shaft between the actuator and robotic link, θ_f is the final position of the actuator and T_c is the coulomb friction torque.

2.4.4 Controller Development

Uncertainties such as external disturbances, leakages and uncompensated friction will contribute to highly nonlinear dynamics of hydraulic systems ([8], [33]). There have been several approaches used in controlling hydraulic systems in past studies. Some of these use linear control theory ([53], [54] and [9]). As an alternative approach, nonlinear adaptive force control was considered in Alleyne [55]. Heinrichs [56] states that the force/torque control of hydraulic actuators is a difficult task. In hydraulic applications where static and dynamic friction is present, Tafazoli [39] proved that acceleration-assisted tracking control would be more appropriate. Multi-variable control of the hydraulic joints work master robot has been considered in [43].

However, the current study considered simple PD-based independent joint controllers.

For a given joint angle, the PD joint control law gives:

$$u = K_p T_d \frac{de}{dt} + K_p e \tag{2.21}$$

Where u is the servo valve current, K_p is the proportional gain, and T_d and T_i are the derivative and reset times, respectively.

In developing the proposed mathematical model it was assumed that there was a controlled clearance fit between the vanes and actuator housing. Therefore, the effects of friction and viscous forces on the vane could be neglected. It was assumed that the temperature changes in the hydraulic fluid would not have an effect on the actuator leakage. It was also considered that the arm is securely held and there would be no effects of external disturbances such as vibration of the support column during the operation.

A basic schematic diagram which shows different subsystems of the system is shown in Fig. 2.6. Matlab®-Simulink toolbox was used to model the system and obtain results. It has the capability of solving models of nonlinear systems numerically. The Runge-Kutta method for solving differential equations of order four with a fixed step size of 1 ms was used as the solver. A servo valve pressure of 20.7 MPa (3000 psi) was considered for simulation purposes. For simulation purposes it was assumed that each actuator is 3 kg in weight.

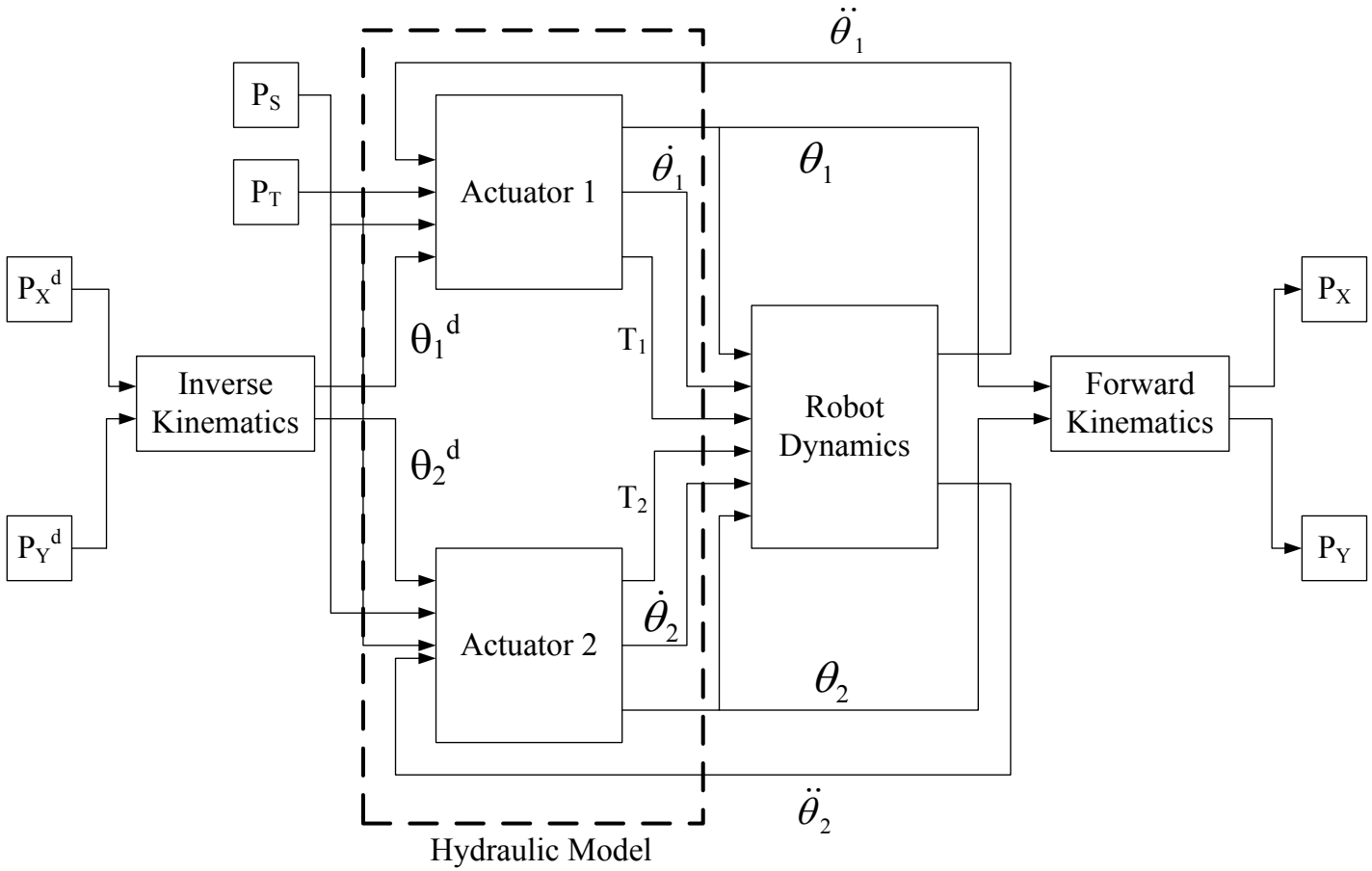

Figure 2.6: Schematic drawing with components of the simulated system

2.5 Simulation Results

Contemporary methods such as the Ziegler–Nichols method [57] are not suitable for a manipulator which carries a heavy payload. This is because, when the system attains its marginal stability the excessive vibration could potentially damage the actuator and the manipulator components. Therefore, a trial-and-error method was used for tuning the P,D parameters of the controller. In control theory, step response provides the details of time behavior of a given dynamic system [58]. Applications of this manipulator would include pick and place and defect removal. This requires high speed positioning of the EE on a 2-D plane. This operation could be replicated using a step response of the system.

The proposed manipulator was tested for various step input values over the operating envelope of the EE. These provided a satisfactory dynamic performance of the arm. The system performance is discussed in this section for two different cases. One is a case with a single step input and the other being several step inputs. The performance of the robot was also analyzed considering different masses as the EE payload.

2.5.1 End Effector Response to a Single Step Input

In the first case the system performance parameters are given for an EE step input from (0.9 m, 0 m) to (0.2 m, 0.6 m) with a 10 kg EE payload. Fig. 2.7 shows the variation of x-, y- position of the EE in the workspace. With the controller parameters, the system error decreases rapidly and settles to a steady state in 0.23 s.

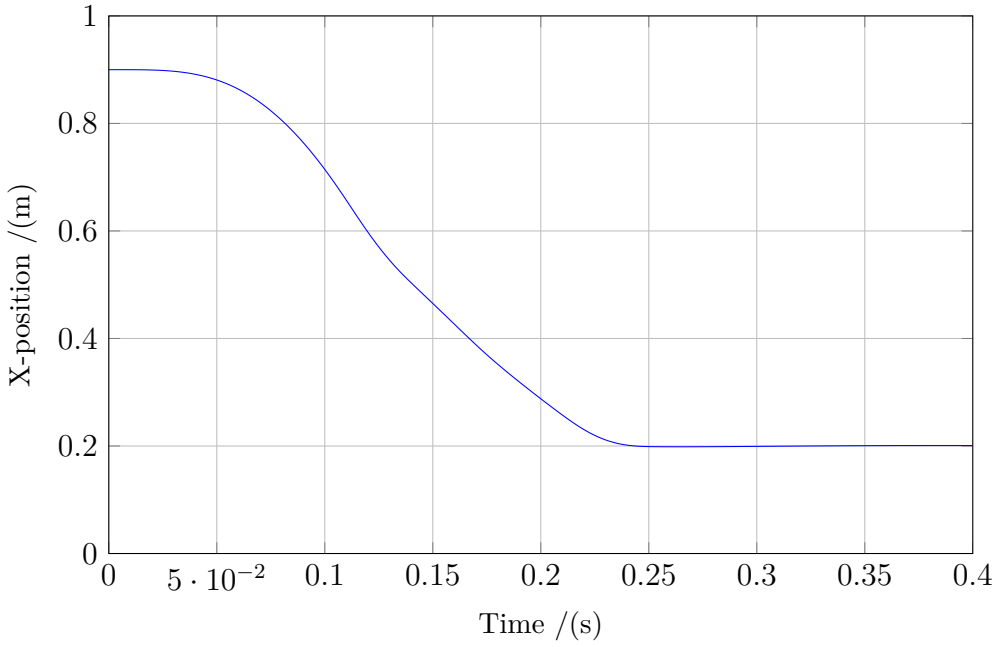

(a) EE x-position

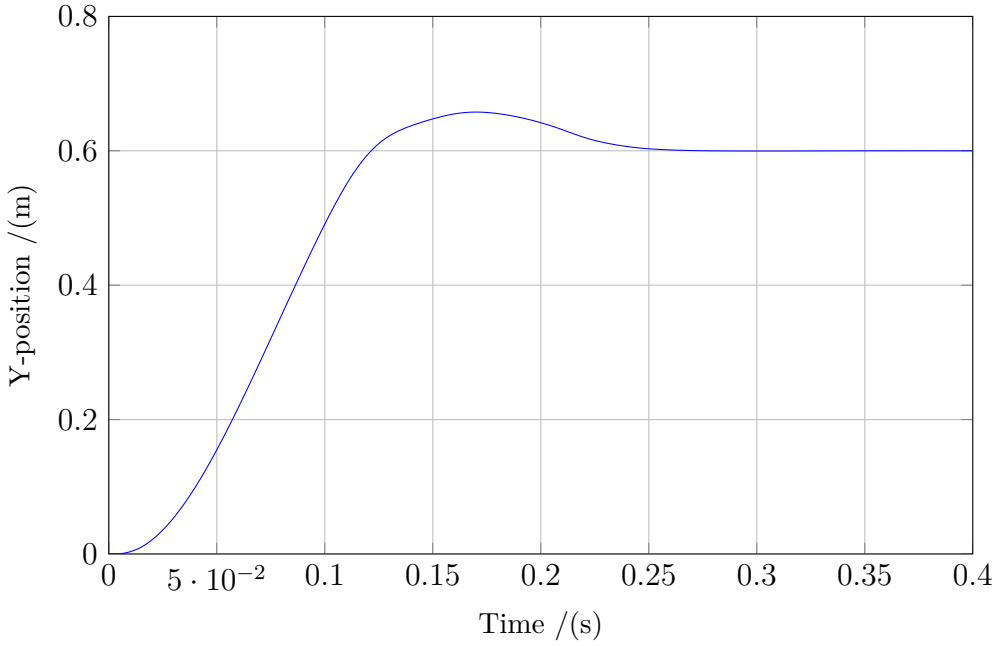

(b) EE y-position

Figure 2.7: Variation of $xy-$ position of the EE over time

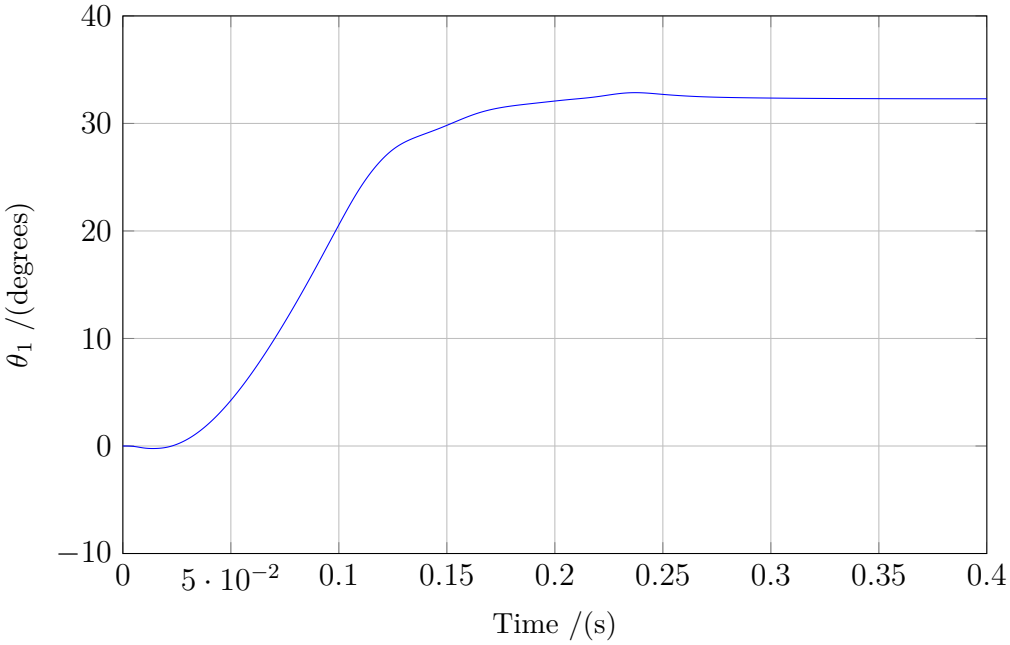

(a) Joint angle of actuator 1

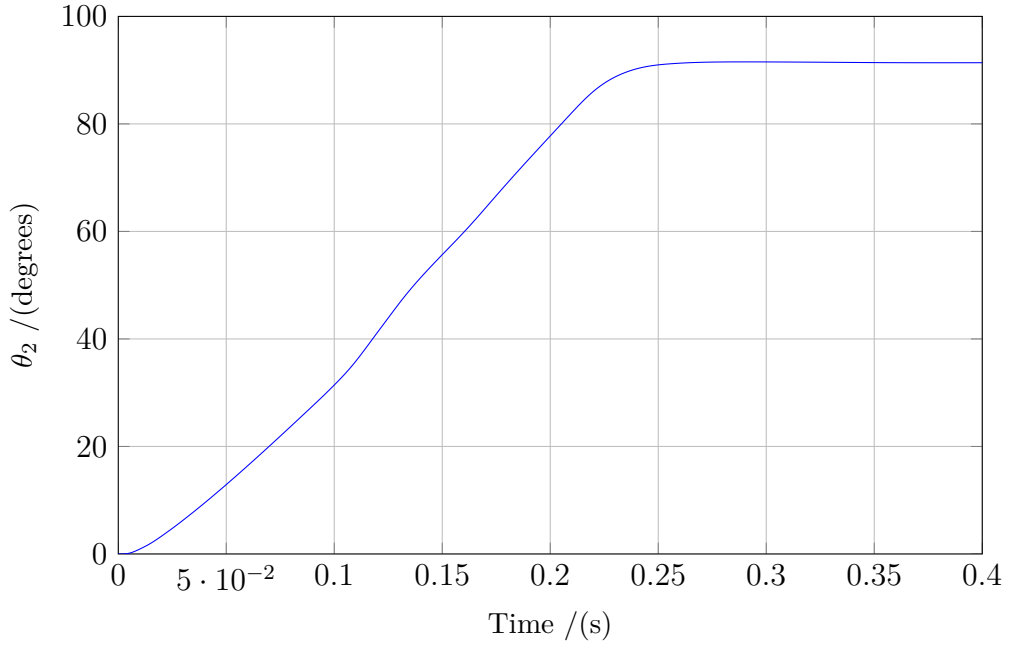

(b) Joint angle of actuator 2

Figure 2.8: Actuator joint angles

The variation of x- position produces a damped response while the y-position produces an overshoot in its response. When it settles to a final value, there will be no steady state error. The variation of actuator joint angles over time is shown in Fig. 2.8. The first joint angle will change from 0° to 32.3° and reach its steady state. Similarly, the angle of second joint angle will reach 91.5° from 0° reaching a steady state.

The variation of angular velocity of the joint angles over time is shown in Fig. 2.9. It is clear from the graph that the angular velocity could reach high values at times. According to the figure, the first joint angle could reach up to 372°/s and the second joint angle could reach up to 544 °/s. These are very large angular velocities considering the fact that this robot is moving a considerable load. The enormous power available in hydraulic systems allows rapid accelerations and decelerations. This is evident with the sharp positive and negative gradients seen in the angular velocity vs time graph. The angular acceleration and deceleration of the robot is shown in Fig. 2.10. These figures show rapid fluctuations in the angular acceleration of the links before it finally settles. As with the angular velocity, the angular acceleration of the second link is much higher compared to the first link. This is due to the fact that the second link is moving a much lower load compared to the first one. During the operation, its angular acceleration can reach up to -14,885 $°/s^2$ in the first actuator and 35,100 $°/s^2$ in the second actuator.

The hydraulic actuators are capable of producing extremely high torques. The variation of torque with time in the two actuators when the EE moves from a point in the work envelope in response to the step input is illustrated in Fig. 2.11. The torque in actuator 1 is generally greater than that of actuator 2 as it has to drive both links

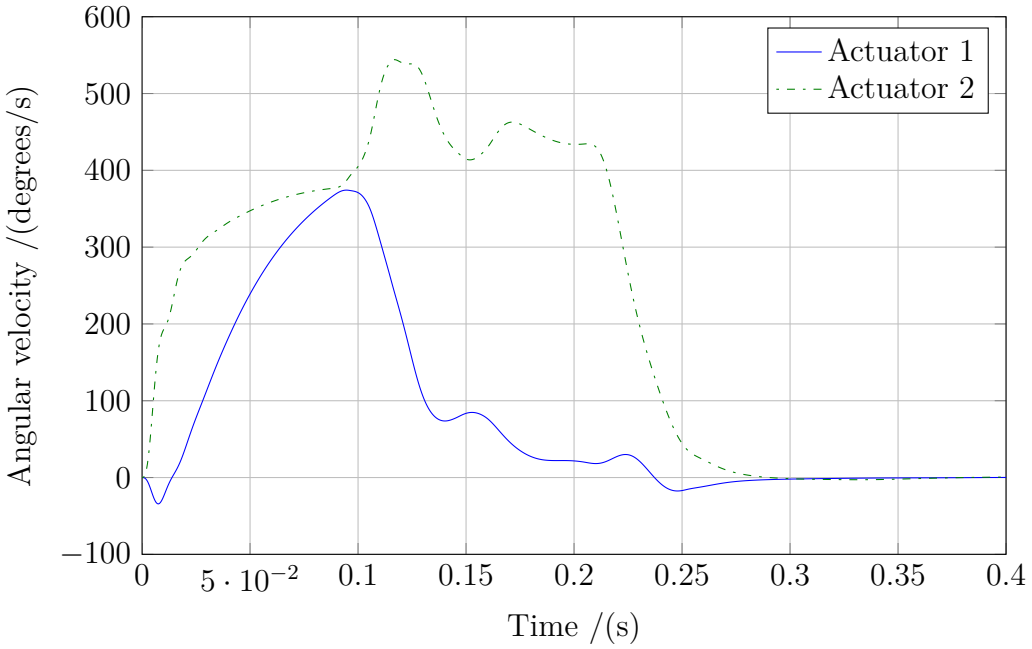

Figure 2.9: Variation of angular velocity of the actuators

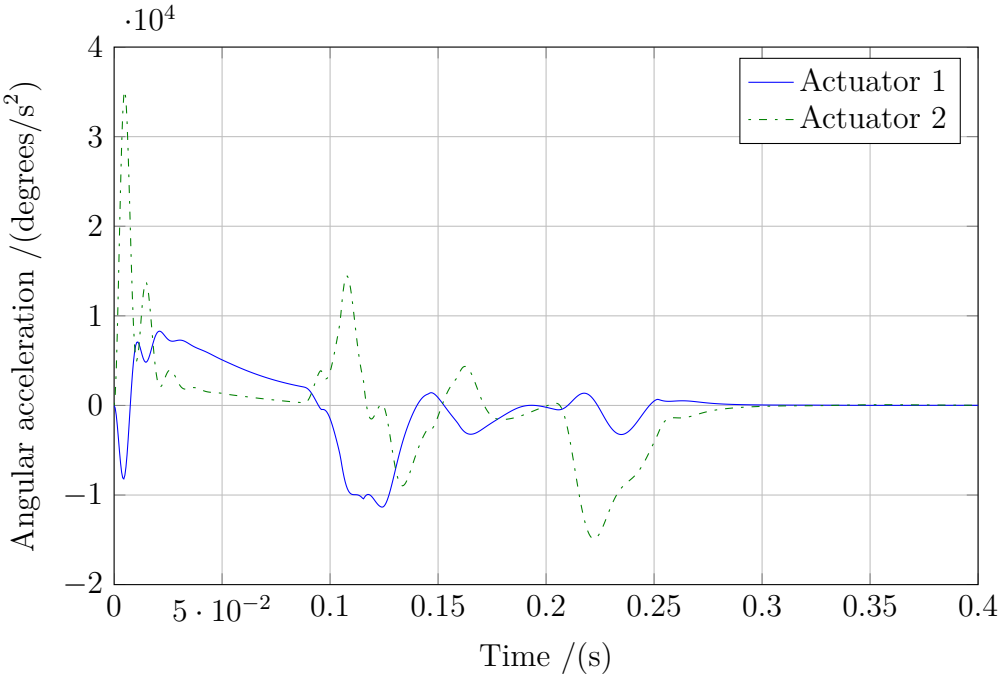

Figure 2.10: Variation of angular acceleration of the actuators

as well as the EE. In the first joint, the forward torque could reach up to 771 Nm in 15 ms and the breaking torque could reach up to 934 Nm in 124 ms. In the second joint,

the corresponding values would be 283 Nm and 247 Nm, respectively. An electric motor capable of producing a similar torque performance would be much larger in size and heavier in weight. For example, the high performance novel in-wheel electric drive motor developed by Protean Electric® for hybrid vehicle applications produces a peak torque of 800 Nm. However, this motor is 420 mm in diameter, 115 mm in width and 31 kg in weight [59]. This shows that, for producing high torques, large motors have to be used introducing much higher inertia to the system.

The hydraulic fluid flow rate into the chambers of the actuators is shown in Fig. 2.12.

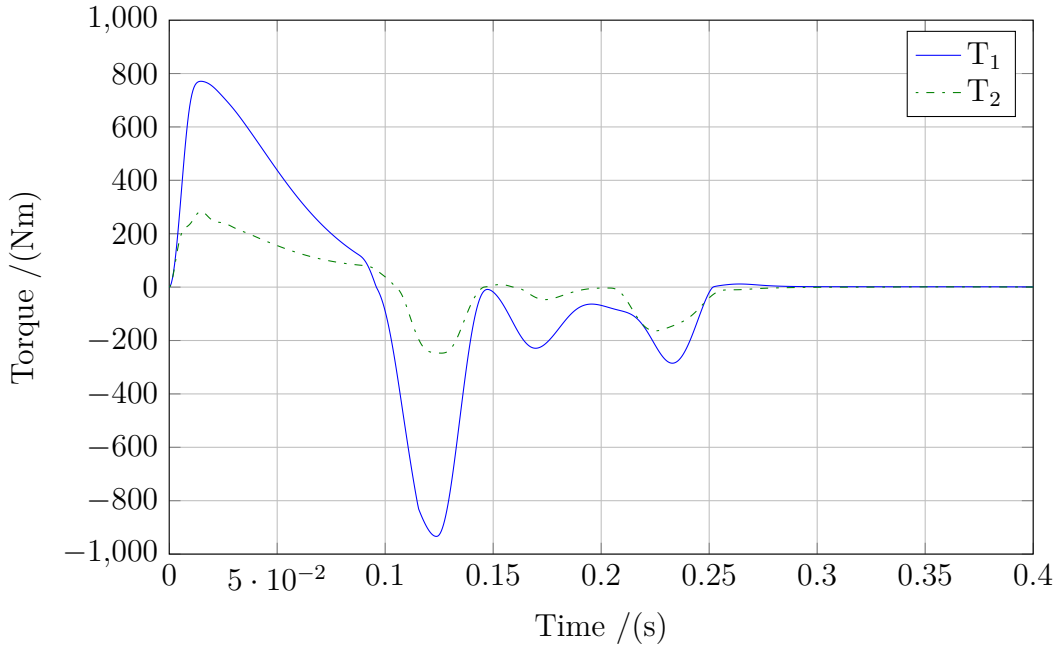

Figure 2.11: Variation of actuator torque with time

The flow rate into actuator 2 is higher than that of the flow rate into actuator 1. This is because actuator 2 moves at a higher angular velocity due to its low inertia. The highest flow rate of 275 ml/s to the first actuator occurs at 88 ms. This will decrease to 0 ml/s in another 82 ms and continue to decrease until the flow rate becomes a negative as it tries to correct for the overshoot. In actuator 2, the maximum flow rate

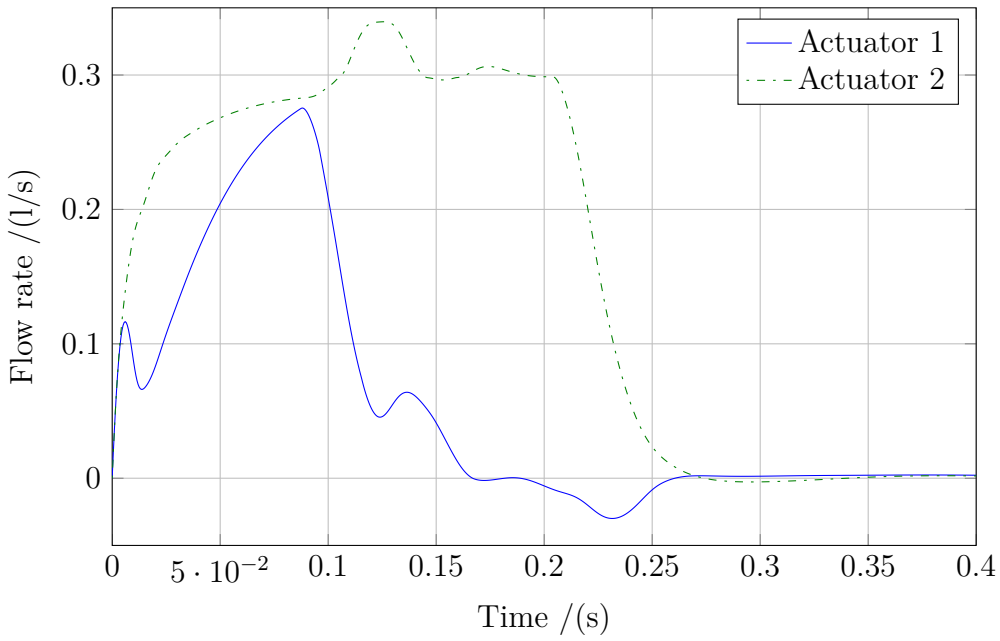

Figure 2.12: Variation of actuator flowrate with time

of 340 ml/s occurred at 125 ms. It continued to decrease until it reached close to zero at 275 ms. The maximum flow rate gives an indication of the capacity of the servo valves required for driving the actuators. For the current application, a servo valve with a capacity of 30 liters per minute or higher should be selected.

These actuators operate at very high pressures. The pressure difference between the actuator chambers result in hydraulic fluid leaking from one chamber to the other. The leakage of hydraulic fluid reduces the operating efficiency of the actuator. The leakage flow rates of the two actuators are shown in Fig. 2.13. As can be seen the leakage of actuator 1 is higher than that of actuator 2. This is because actuator 1 produces a higher torque which is the result of a larger pressure differential. The higher pressure difference result in a higher leakage rate of 70 ml/s. The leakage flow of actuator 2 reached a maximum of 38 ml/s.

The variation of pressure in actuator chambers over time is shown in Fig. 2.14,

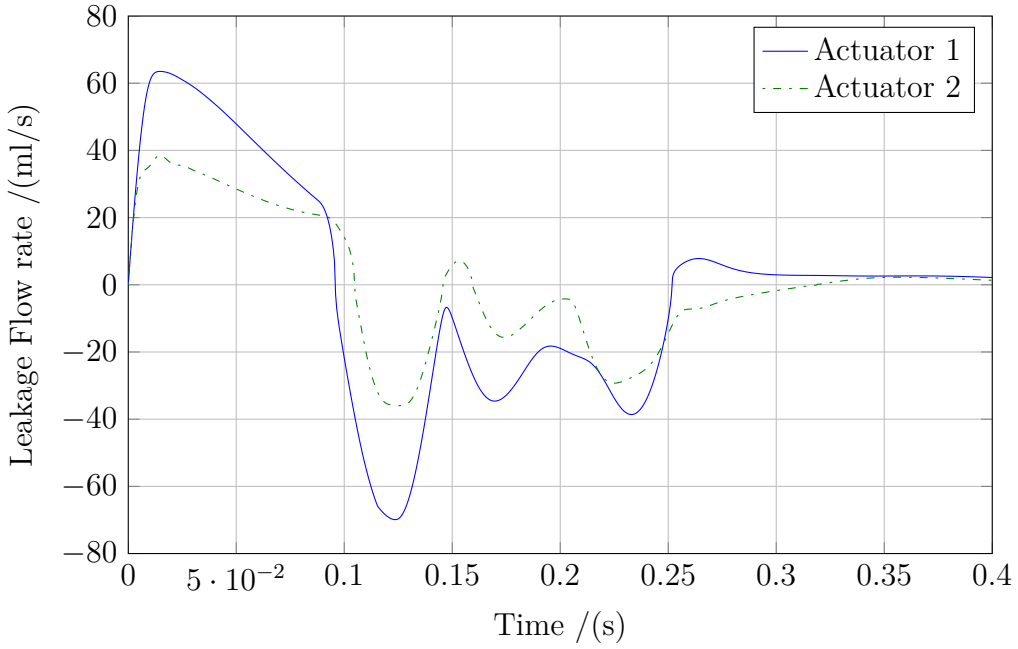

Figure 2.13: Variation of actuator leakage flowrate with time

2.15. The pressure in the first actuator reaches a maximum at 15 ms and will change rapidly and produce a vacuum in 100 ms. As a result, the opposite chamber pressure will rise rapidly from 720 kPa to 20.7 MPa. Pressure in one chamber of the actuator 2 will have a peak value of 13.8 MPa in 15 ms. This will change to 7.27 MPa in 111 ms. Following an opposite trend, the pressure in the opposite chamber will increase from 6.8 MPa to 13.4 MPa during this period. The figures obtained by simulation results show that the pressure in one actuator chamber is nearly the inverse of the pressure in the opposite actuator chamber. This is because it was assumed that the supply pressure and tank pressure remain constant throughout the operation. The minor difference of this value is attributed to actuator leakage.

The power output of the actuators over time is shown in Fig. 2.16. This was cal-

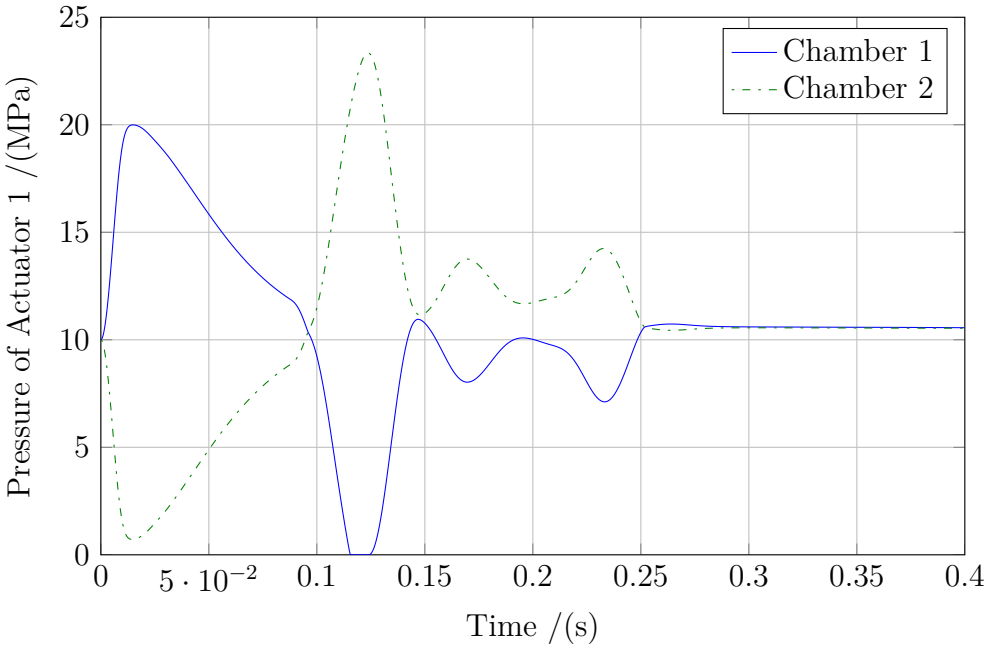

Figure 2.14: Variation of pressure in actuator 1

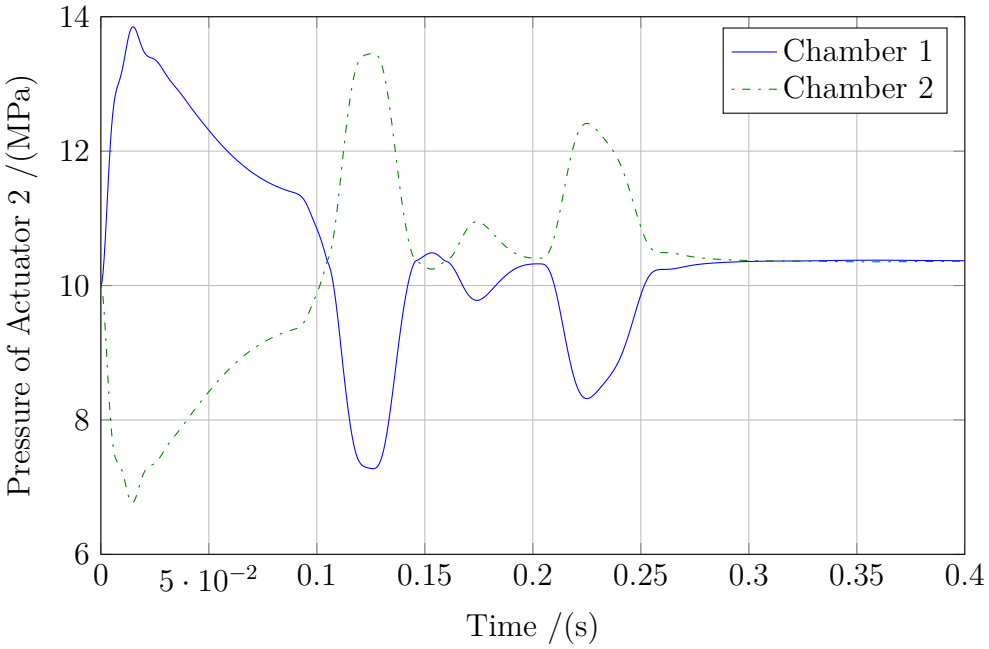

Figure 2.15: Variation of pressure in actuator 2

culated using the output torque and angular velocity. The power output of the first actuator is higher than that of the second actuator since it carries both second actuator and the load. It can be seen that the actuator power output is higher during the braking phase. In actuator 1, the highest power output of 1860 W occurs in 40 ms for accelerating and 3750 W occurs in 118 ms for braking. The same values for actuator 2 correspond to 1220 W in 22 ms and 2315 W in 125 ms. This gives an idea of the power rating of the actuators that are used to drive the links of the robot.

The velocity of the EE is shown in Fig. 2.17. The EE will accelerate rapidly until it reaches a maximum velocity of 5.9 m/s. It would take 109 ms for the EE to obtain its maximum speed before it starts to decelerate to come to a rest. The acceleration of the EE is shown in Fig. 2.18. As seen from the figure EE encounters rapid acceleration and deceleration during its operation. It reaches a maximum acceleration of 178 m/s^2 in 5 ms during its starting phase. The maximum acceleration amounts to 18 times the gravitational acceleration. This value is remarkable considering the fact that it carries a 10 kg payload. It then fluctuates rapidly until the EE decelerates before it settles.

2.5.2 Manipulator Response to a Single Step Input with Variable Mass on End Effector

In the next case, an analysis was carried out to study the effect of EE payload on the performance of the robot. A range of masses were considered for the EE payload. A step input as in the earlier case from point (0.9 m, 0 m) to point (0.2 m, 0.6 m) was considered as this allowed the EE to cover a sufficient distance. Masses that range from 2 kg to 20 kg were used in the analysis.

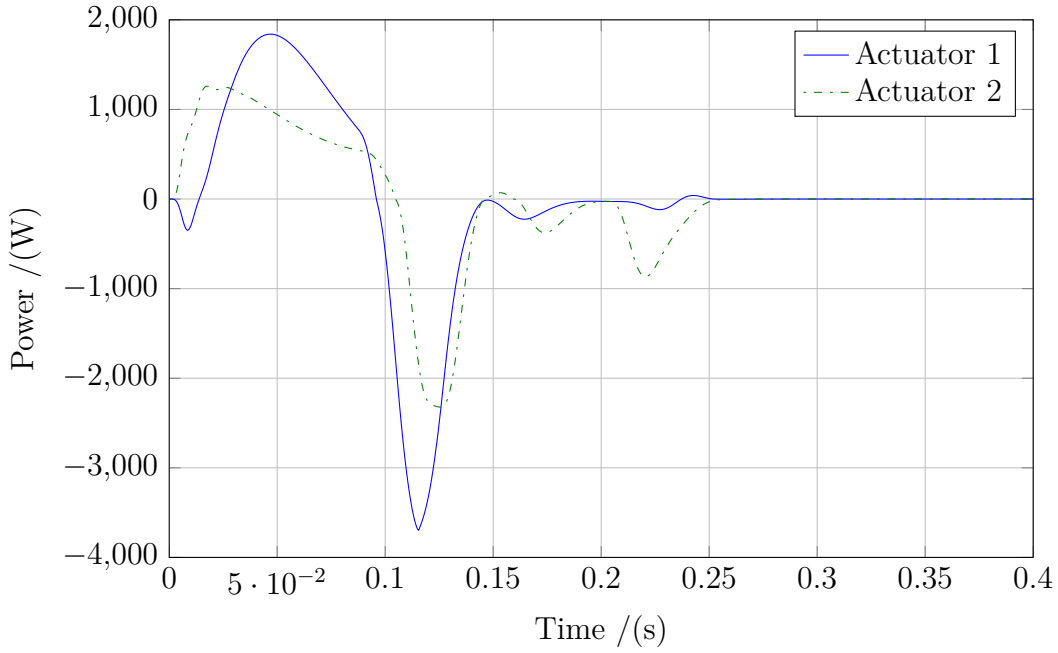

Figure 2.16: Variation of power output of actuators with time

The EE attains a stable position for each of these payloads showing a satisfactory control performance. The speed and settling time are two important parameters for a high-speed robot. The settling time of the robot for these masses is shown in Fig. 2.19. In the case of the first actuator, the settling time was increased from 242 ms with a payload of 2 kg to 326 ms with a payload of 20 kg. In the second actuator, the settling time was increased from 232 ms with a payload of 2 kg to 308 ms with a payload of 20 kg. This shows that the settling time of the actuators increases when higher payloads are introduced. This is because it increases the system inertia slowing the response of the two actuators. Although the EE payload increased 10 times, the settling time increased by only 1.35 times for both the actuators.

Although the EE carries a large mass as the payload, it is still capable of reaching high velocities. This is illustrated in Fig. 2.20. As seen here, the maximum velocity of the EE will decrease from 6.24 m/s with a 2 kg payload to 4.69 m/s with

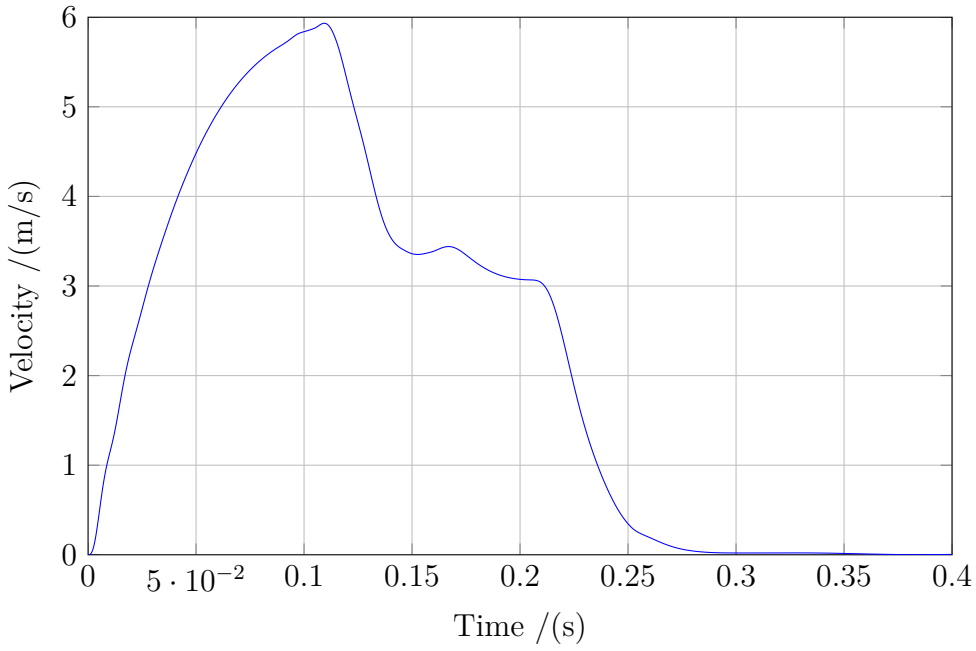

Figure 2.17: Variation of the EE velocity with time

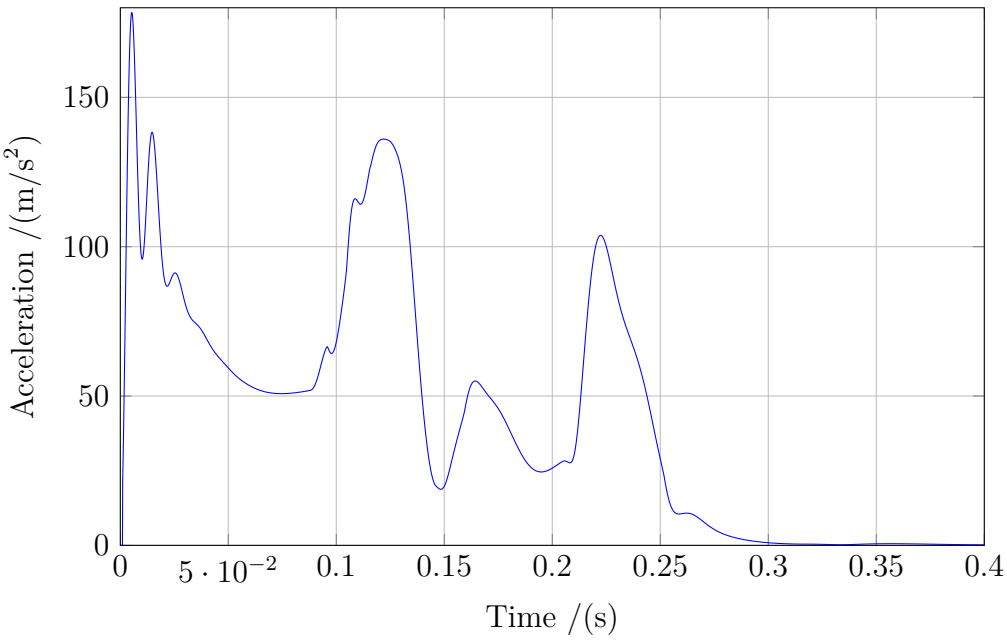

Figure 2.18: Variation of the EE acceleration with time

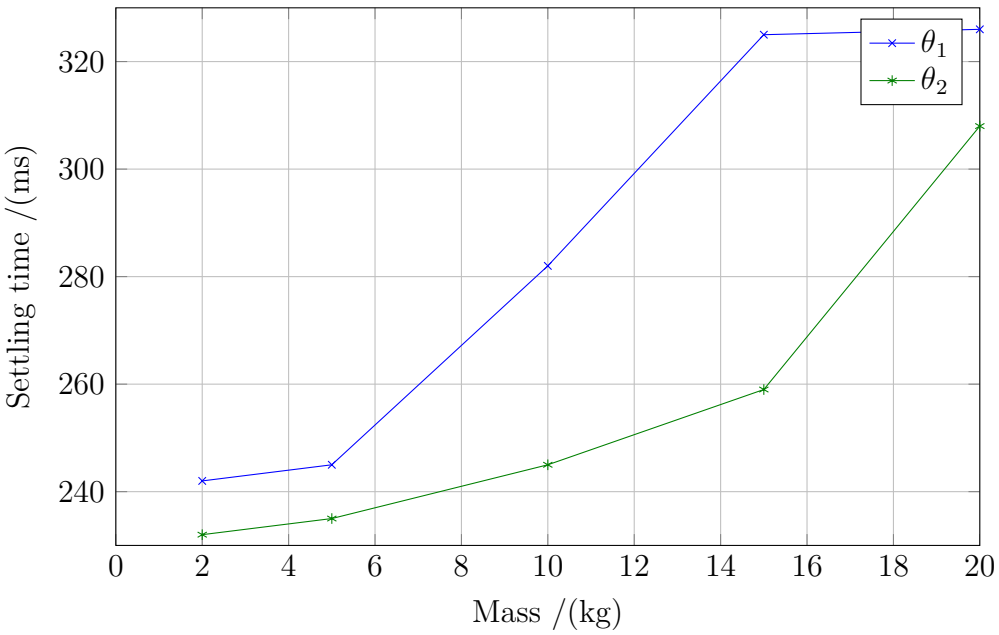

Figure 2.19: Variation of actuator settling time with mass

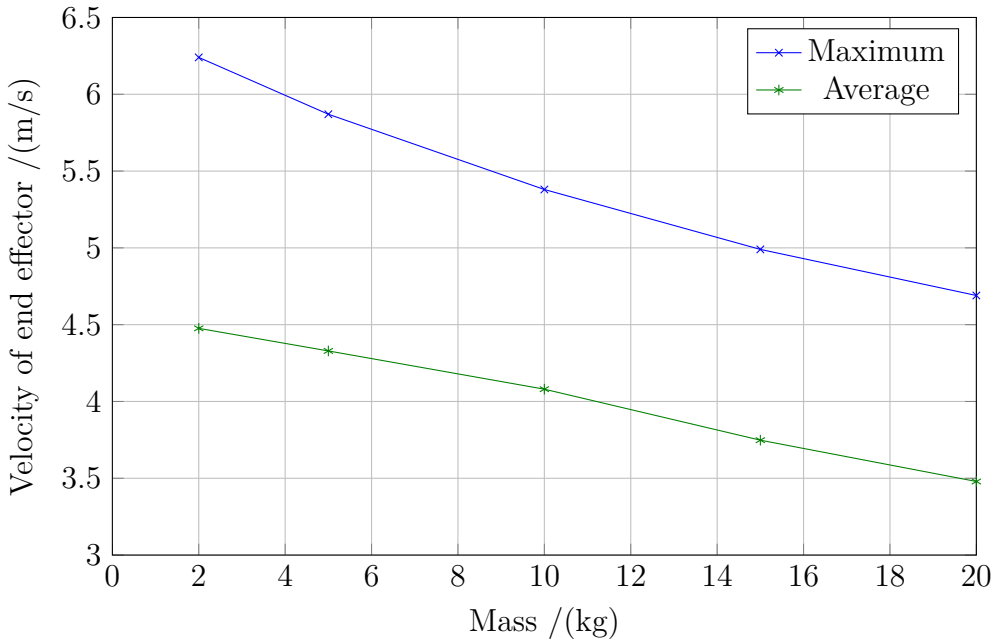

Figure 2.20: Variation of EE velocity with mass

a 20 kg payload. The average velocity will decrease from 4.48 m/s to 3.48 m/s for the same payload values. Thus it is evident that even with very high payloads, such

as 20 kg, the EE can reach considerable velocities compared to its electrical counterparts. For example, the Adept® Cobra s800 is a widely used SCARA type robot in the industry. It is a conventional robot with two electric motors driving the revolute joints. The time required to complete one Adept cycle, which consists of a 25 mm up/down movement of the prismatic joint and a linear displacement of 305 mm in the horizontal plane, is 0.54 s with a payload of 2 kg [2]. Assuming the prismatic joint of the robot operates at 0.250 ms^{-1} it takes 0.34 s to cover the 305 mm distance. This implies a burst velocity of 0.9 ms^{-1}. Similarly, it could also be shown that the Epson® G6 SCARA arm is capable of achieving a controlled speed of only 0.92 ms^{-1} when it follows the Epson cycle with a payload of 2 kg [17].

2.5.3 Robot Response to a Range of Step Inputs

The response of the robot over a range of desired positions for the EE were considered. These values included 0, 0.2, 0.4 and 0.6 m in x-direction and 0.2, 0.3, 0.4, 0.5 and 0.6 m in y-direction. It was assumed that the EE payload is 10 kg. This would help analyze the performance of the robot in workspace.

The EE position in x- and y- directions for the given step inputs are shown in Fig.s 2.21 and 2.22. These figures show that the EE reaches stability for each of the values considered. Between some of these points the transition is not a smooth one (e.g. between 2 s and 2.3 s). A smoother control performance could be obtained using a predetermined set of transition points between each x- and y- points. Over the range of values considered the settling time is a minimum of 155 ms when t=4 s and a maximum of 307 ms when t=0 s. The minimum occurs when the EE moves a minimum distance from x=0.6 m to x=0.4 m. The maximum occurs when the position changes from x=0.9 m to x=0.4 m. In the case of y- direction, the minimum of 80 ms

occurs at t=4 s when the EE moves from 0.5 m to 0.6 m. The maximum settling time in y- direction is 337 ms at t=0 s when the EE moves from 0 m to 0.2 m in y- direction.

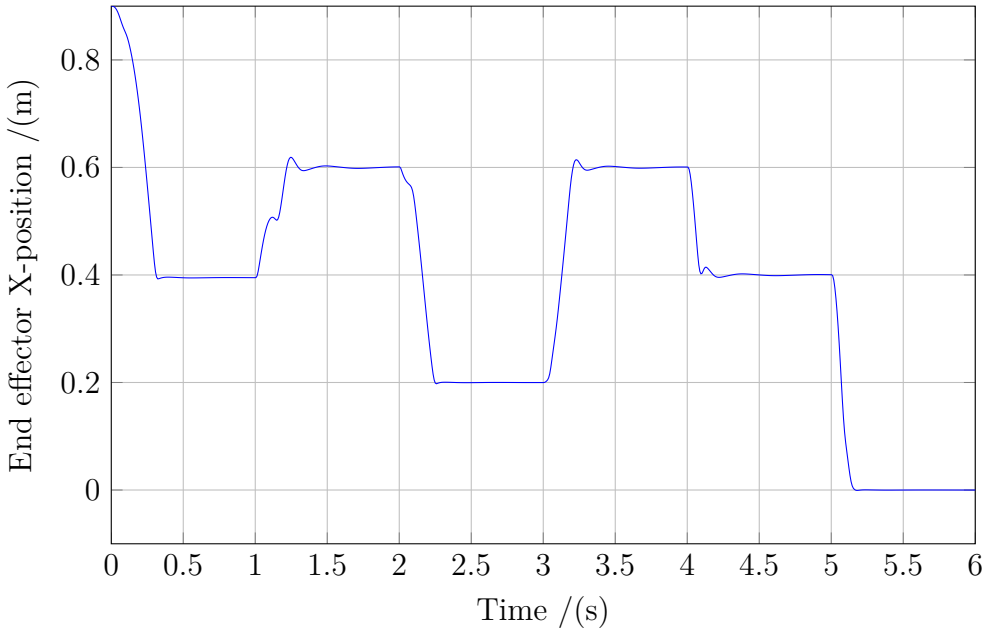

Figure 2.21: Variation of the x- position of the EE with time

The torque provides an indication of the required sizing for the actuators so that it would allow a sufficient flow rate into the chambers. The torques of the two actuators are shown in Fig.s 2.23 and 2.24. Similar to the earlier case, the torque of the second actuator is less than that of the first actuator for all other instances. During the periods of each step response, the magnitude of the maximum torque will vary between 730 Nm at 3.045 s and 1230 Nm at 4.088 s in the first actuator. This is a very large torque considering the comparable electric motors. For the second actuator, the magnitude of the maximum torque will vary between 465 Nm at 3.015 s and 563 Nm at 5.152 s. The output power gives an indication of the size and speed of the payload. The power output of the two actuators are shown in Fig.s 2.25 and 2.26. The output

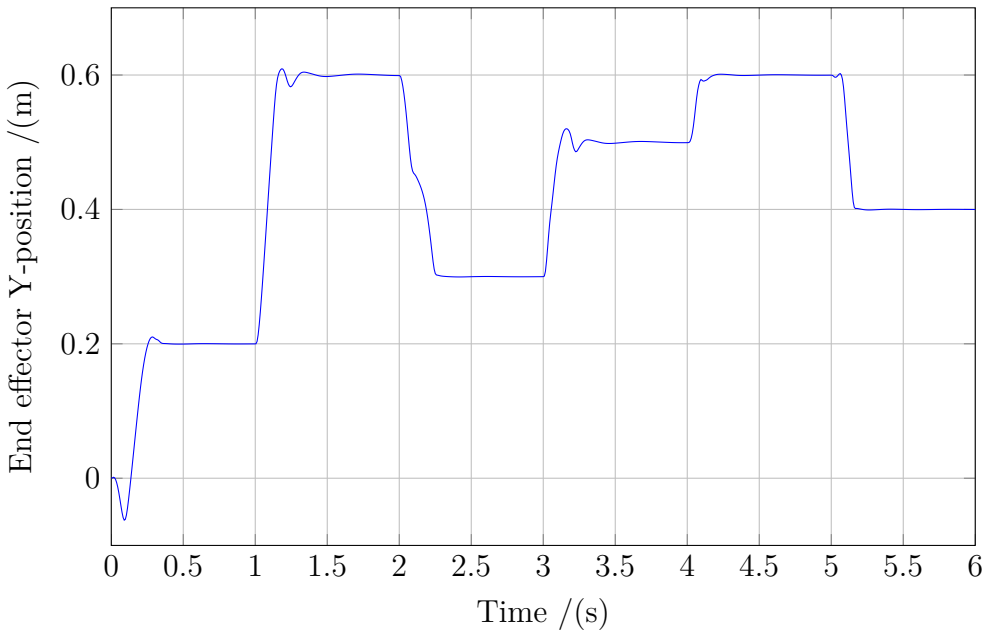

Figure 2.22: Variation of the y- position of the EE with time

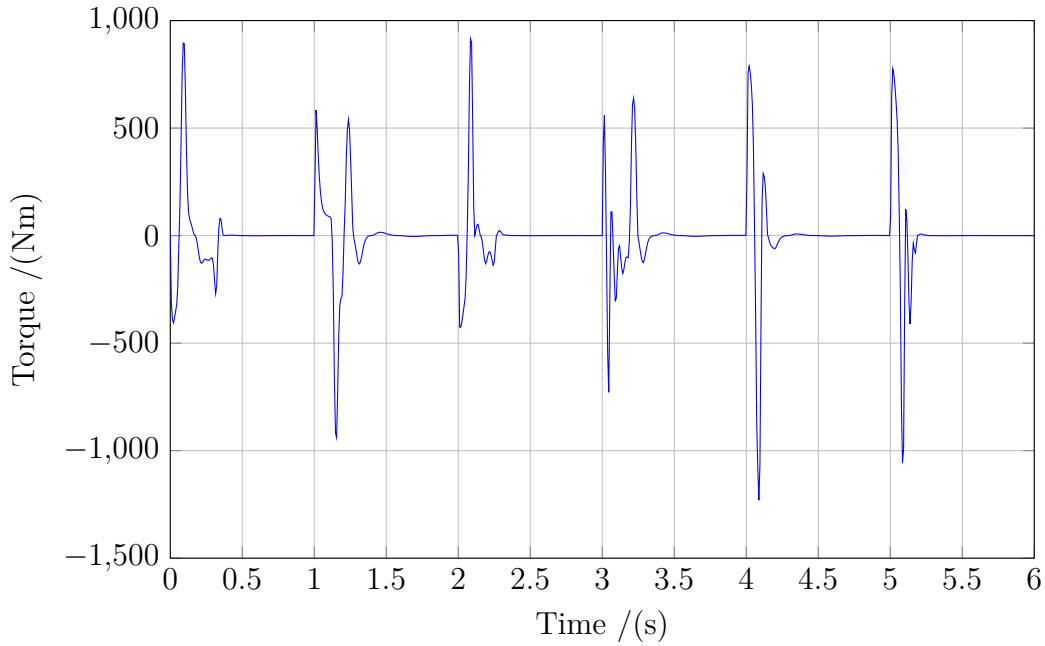

Figure 2.23: Variation of torque in first actuator (T_1)

power of the first actuator reaches its maximum of 3427 W at 1.140 s. The output power is a maximum for the first actuator when it rotations through its largest angle

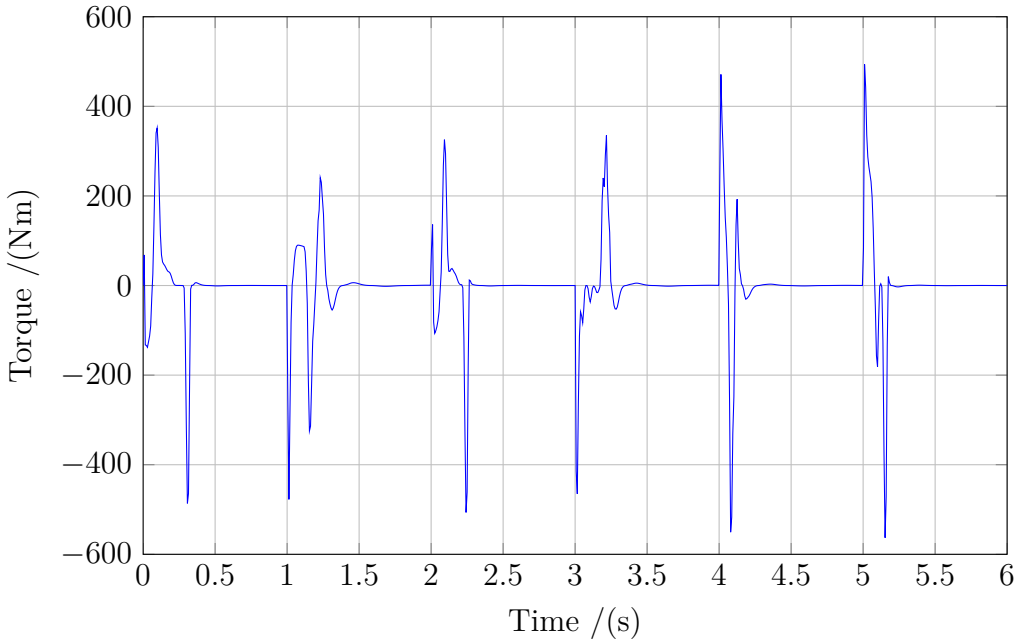

Figure 2.24: Variation of torque in second actuator (T_2)

from -28 degrees to 27 degrees. This is because the spool valve opens for a longer period of time and the higher flow of hydraulic fluid results in higher power. The maximum power output for the second actuator was 2387 W at 5.145 s. This occurs when the second actuator turns from 74 degrees to 129 degrees. In all cases, the power output is higher during the braking phase compared to that of the acceleration phase.

The acceleration allows the EE to reach higher speeds during the operation. The variation of the EE acceleration is shown in Fig. 2.28. During its response to each step input the EE accelerates until it reaches its maximum velocity. The maximum acceleration of the EE varies between 116 m/s^2 at 4.013 s and 240 m/s^2 at 1.013 s. Then it starts to decelerate so that it achieves stability. In the braking phase it reaches a maximum deceleration before it settles in the desired position. This maximum deceleration of the EE varies between 93 m/s^2 at 3.045 s and 148 m/s^2 at 5.152 s. The variation of the EE velocity over time is shown in Fig. 2.27. The EE velocity

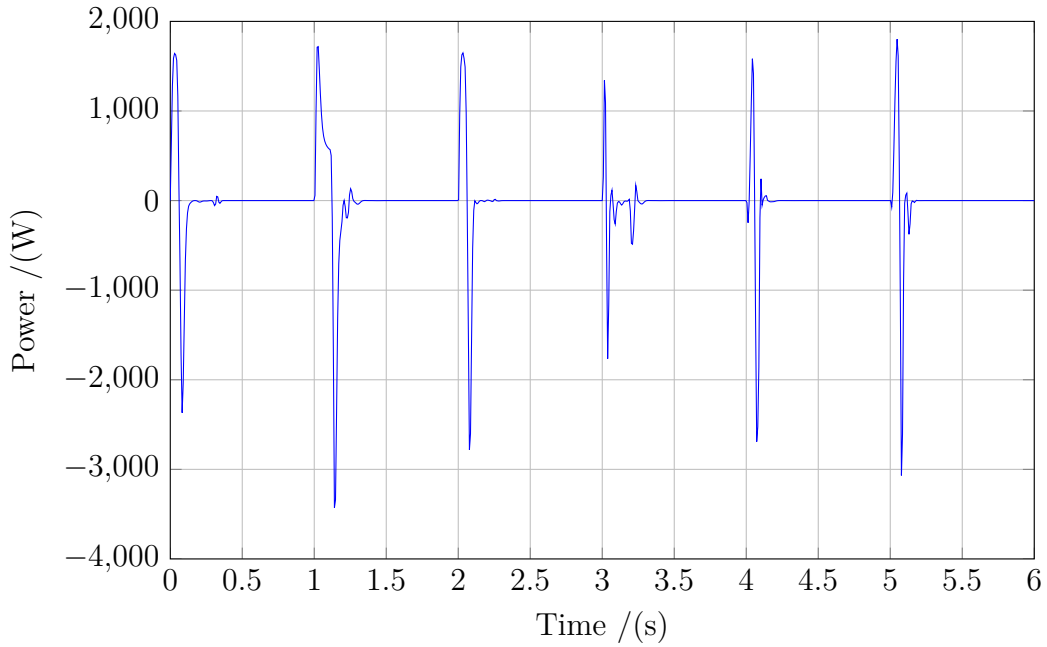

Figure 2.25: Variation of power output of first actuator with time

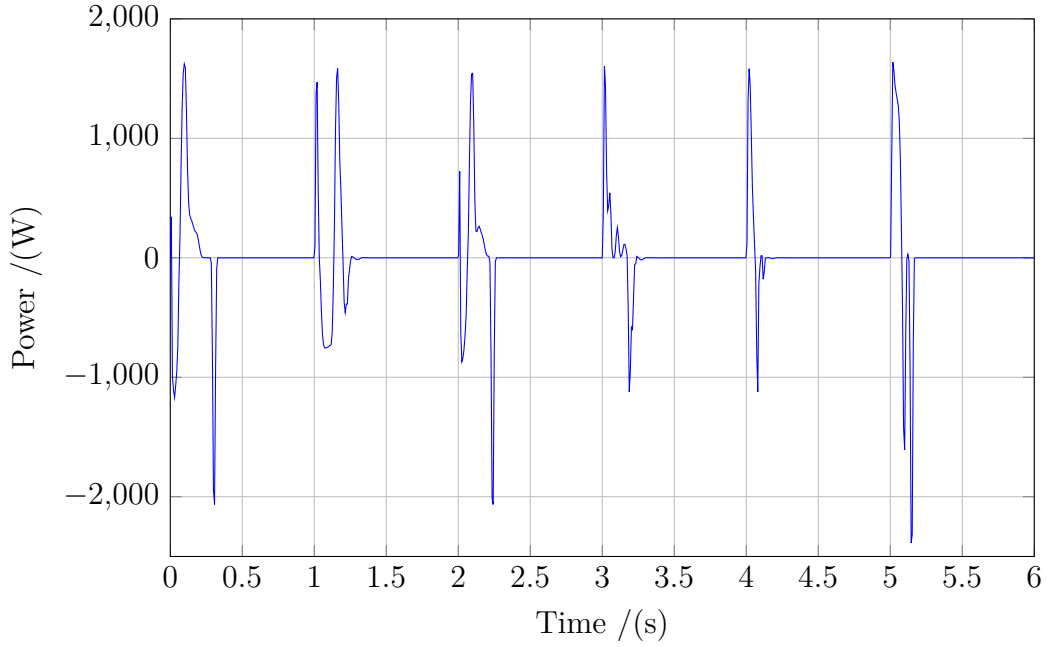

Figure 2.26: Variation of power output of second actuator with time

has the highest value with 5.097 m/s at 1.05 s. As a result of this peak velocity, it overshoots the EE before reaching its final position. In each case, the maximum velocity would reach values of much greater than 2.6 m/s. The proposed robot is capable of reaching these unprecedented speeds even with significant payloads.

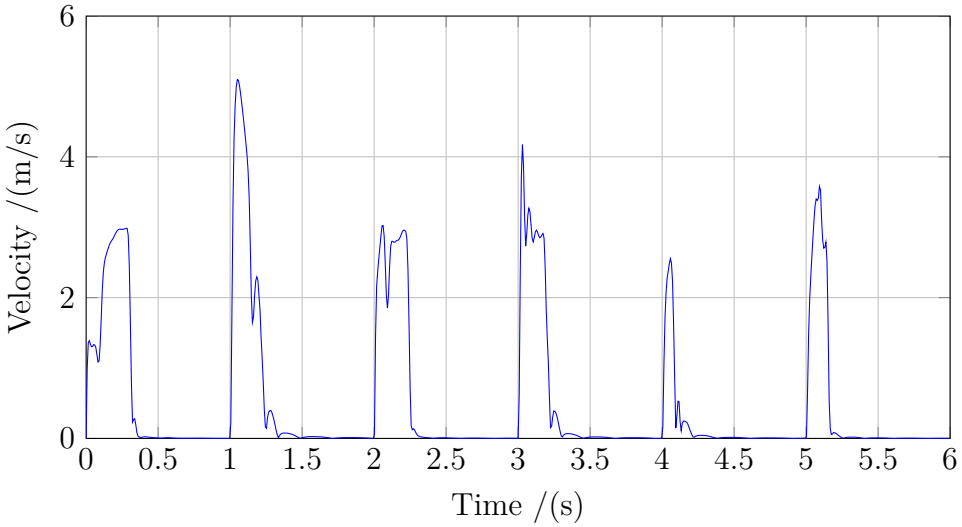

Figure 2.27: Variation of the EE velocity to the step inputs

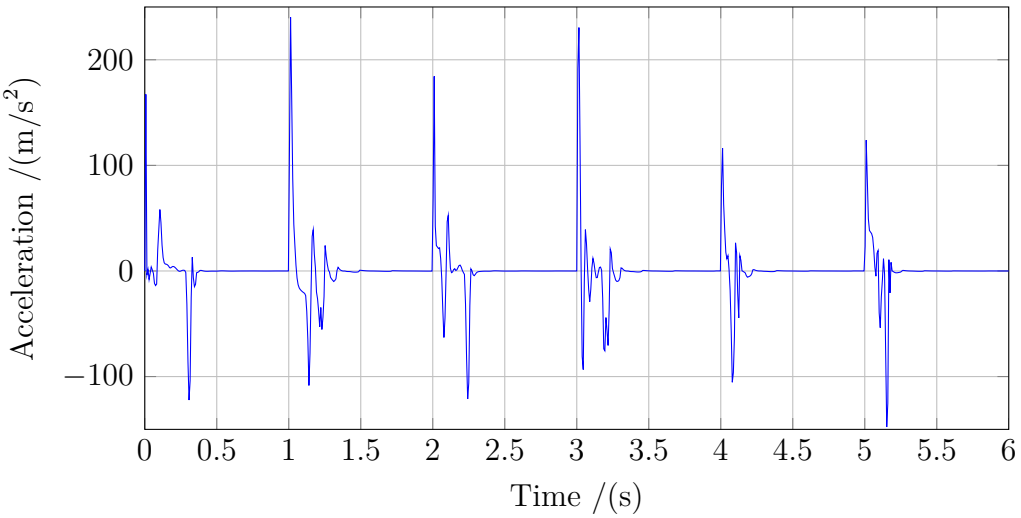

Figure 2.28: Variation of the EE acceleration to the step inputs

2.6 Performance of the Modeled System

This chapter presented the modeling, simulation and results of a SCARA type robot employing novel rotary hydraulic actuators. It considers double vane rotary type actuators for the revolute joints of the robot. The system was divided into different sub-components for developing the mathematical model. It comprised models for servo valve, rotary actuator, robotic manipulator and the control system. These sub-components were integrated into a single model for analyzing the performance of the arm. The Matlab®-Simulink toolbox was used to model and simulate the proposed system. A hydraulic system pressure of 3000 psi was considered for the simulation. The summarized performance is given for a robot which has actuators with a displacement coefficient of 4.0 x 10^{-5} m^3/rad (2.44 in^3/rad). This is an important parameter in determining the size of actuators.

The discussion of performance parameters of the robot is given for a case with a 10 kg payload for a given step input. An analysis of the performance of the robot was carried out over a range of EE masses varying from 2-20 kg and a range desired EE displacements. The key performance parameters of this robot are summarized in Table 2.1.

Table 2.1: Summary of the performance parameters of the SCARA robot according to the simulation

Parameter	*Value*
Rated Payload/(kg)	10
Power output/(kW)	3.7
Max. torque/(Nm)	1235
Max. velocity/(m/s)	5.1
Max acceleration/deceleration/(m/s^2)	245

In this study, PD-based independent joint control was used for controlling the joints

of the robot. A trial-and-error method was used to tune the system and obtain the proportional and derivative parameters of the controller. The system was capable of achieving satisfactory control even with a basic PD type controller.

Chapter 3

Design of a SCARA Type Manipulator With Rotary Hydraulic Actuators

3.1 Introduction

The main objective of this study was to develop a high speed visual servoing system. The main component of this system is a high speed manipulator capable of performing operations in two dimensional space. The goal is to be fast, accurate and non-oscillatory while accommodating comparatively large loads. There are two types of robotic configurations that could be considered for performing two dimensional operations. The Cartesian coordinate type configuration is frequently used in three dimensional printers and gantry cranes. It has the advantage of being able to handle large loads but not necessarily at high speeds. The SCARA type configuration has frequently been used for robotic manipulators due to its simplicity and its ability to reach high speeds during operation.

There are several major manufacturers (Eg. Adept®, Epson®, Toshiba®) of SCARA type robots. Almost all these SCARA type robotic manipulators use brushless servo motors to drive the revolute joints. As a result, these robots are only capable of handling payloads that are limited in size. Electric actuators can produce only limited speeds while handling loads. This study proposes the design and development of a custom made rotary hydraulic actuator which is capable of achieving high speeds even with large payloads. In Chapter 2, a mathematical model was developed to model the proposed system. This simulation provided some of the key parameters required for the system design.

An actuator that uses hydraulic power runs on high pressure hydraulic oil. Therefore, the strength of the internal components must be sufficient to withstand excessive forces generated during operation. Most importantly, the system should be adequately sealed in order to prevent leakages. As the second actuator will be moving with the first link, it should be of minimum weight. Therefore, the material selection plays an important part in the design. Aircraft grade of Aluminum (2024-T6 alloy) was used to design lightweight components. This Aluminum alloy also has a high strength to weight ratio and good fatigue resistance as compared to other alloys. Brass, which has wear-resistant properties, was used in places where mechanical wear is encountered.

The proposed robotic arm has two links and an EE. The actuators will be coupled directly to the links. This eliminates the need to have a gear drive. It will also prevent delays, backlashes and other losses. This unit will be powered by hydraulic power. Thus, a hydraulic supply and a return will be connected for the hydraulic fluid. The hydraulic flow will be controlled using electro-hydraulic servo valves. This arm will

have a nominal operating pressure of 20 MPa (3000 psi). The joints of this arm will be instrumented with joint encoders to provide the angular position of the links. A schematic diagram of the hydraulic circuit is shown in Fig. 3.1. This chapter considers the design and development of the horizontal positioning of the two links. It does not cover the design of the EE which is application-dependent.

The design of the SCARA arm was considered in several different stages. First

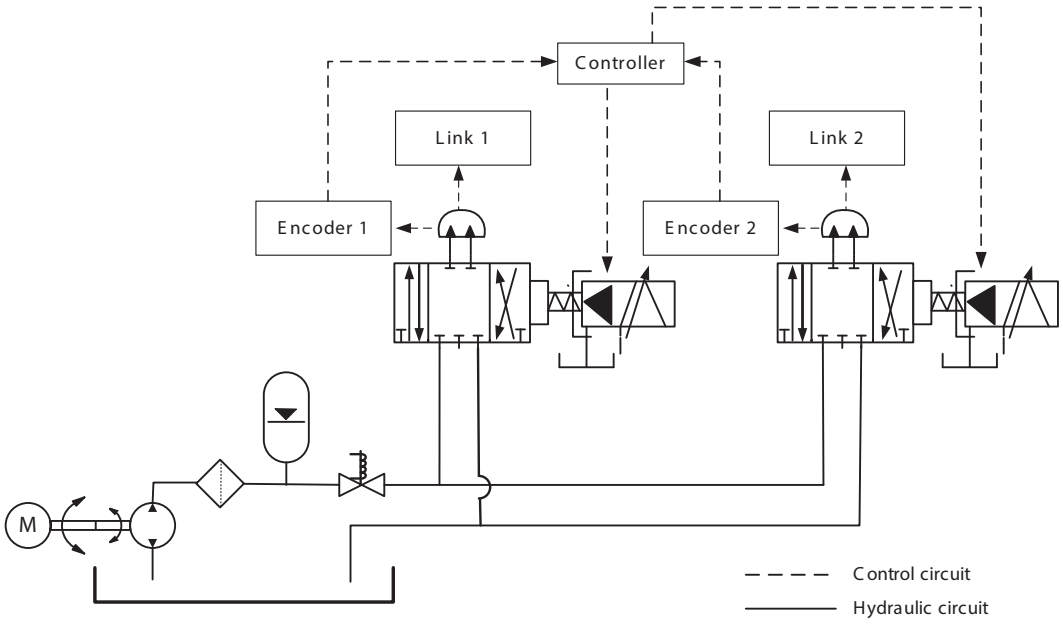

Figure 3.1: A schematic diagram of the hydraulic circuit

the rotary hydraulic actuator was designed. Based on this actuator, the overall arm was developed. Modeling and simulation of the system in Chapter 2 provided the actuator displacement coefficient. This was used to estimate the basic sizing of the actuator and its components. The system was designed using Solidworks® mechanical design software. The package Cosmosworks was used to check the strength and deformation of each of these components.

3.2 Design of a Rotary Hydraulic Actuator

The actuator is the most important component of the robotic arm. It will operate with a hydraulic pressure of 20 MPa. A Moog® G761 servo valve is used to control the flow into the actuator. Since the operating pressure of the actuator is very high, it should be able to withstand excessive forces generated from the flow of hydraulic fluid. This system should be enclosed in such a way that it is fully leak-proof. Rapid oscillatory movement of the spool of the servo hydraulic valve would result in large bi-directional flows in and out of the actuator. These may create large fluctuations in the stresses on internal components of the actuator. Therefore, in order to mitigate any vibration from unbalanced shaft forces, a double vane rotary type actuator was considered in the design. Another advantage of this type of double vane rotary actuator was that it could provide higher torques without excessive shaft forces.

This type of actuator would essentially consist of two vanes fitted to a shaft. This shaft vane assembly is enclosed within a housing and endcaps. There has to be a set of side caps to contain the fluid in the space. The hydraulic actuator is divided into two chambers by separation using wedges. The two vanes will divide these chambers into two compartments. In place of external piping, the housing comprises a series of drilled passageways which channel the hydraulic oil. Passageways located in the housing channel the oil flow in and out of these two compartments. Based on the direction of spool displacement, the pressure port is connected with one of the compartments, which creates a clockwise or counter-clockwise rotation.

The pressure inside the chambers will reach very high levels during the operation and there is an imminent possibility of hydraulic fluid leaking from the actuator. In order to prevent such leaks, a side cap, an o-ring and a seal are incorporated into

the design. The shaft is mounted on two bearings in order to produce a smooth, balanced motion. Two end caps are bolted on either sides to the housing. This will further reduce any chances of hydraulic leaks. The servo valve will be mounted via a separate manifold which is designed as a part of this actuator. There were no seals used between the vanes and housing to minimize static friction. The leakage flow is minimized by closely controlling the manufacturing tolerances. A schematic diagram of the exploded version of the actuator is shown in Fig. 3.2. This actuator has a span of 100 degrees as the angular displacement. The components of the actuator design are as follows.

1. Housing
2. Shaft
3. Vanes
4. End caps
5. Side caps
6. Separators
7. Manifold
8. Stops

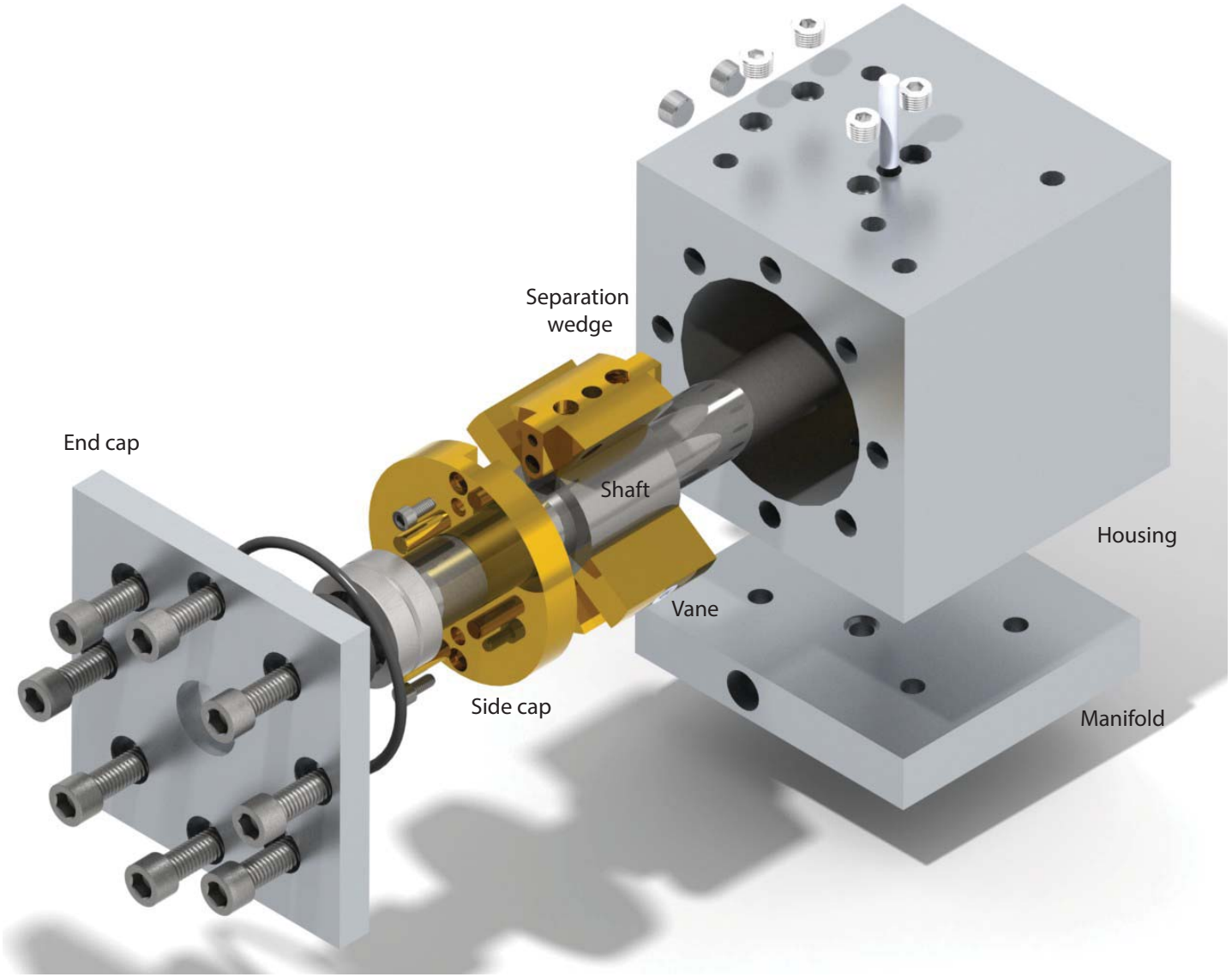

Figure 3.2: An exploded view of the proposed actuator in real view graphics

3.2.1 Housing

The housing was used as an enclosure for the shaft vane assembly and other components. It is also used to facilitate the flow of hydraulic oil in and out of the chambers. The servo valve is also connected to the housing via a manifold. The housing was designed to have a cubic outer shape. Aluminum (2024-T6) alloy was used as the material for the housing in order to minimize weight. The size of the housing was determined based on the actuator displacement coefficient. This was estimated from the earlier simulation as 2.44 in^3/rad. Considering the actuator displacement coefficient and the shaft/vane dimensions, actuator housing requires a cylindrical volume of 3 in. in diameter and 4.5 in. in length. The outer dimensions of the housing were estimated to be 4.5 x 4.5 x 4.5 in..

A series of drilled passageways with a diameter of 0.312 in. were used to channel the flow of hydraulic oil. It was determined based on the specifications given by the servo valve manufacturer. These drilled passageways which channel the flow to the separation wedges are located 180 degrees apart. Steel NPTF plugs (Mcmaster-carr® model number: 4534K41) with a diameter of 1/8 in. and a length of 0.25 in. are used to close the openings on the sides of the housing. These plugs are precision-machined with a 7/8 in. taper with 27 thread per inch. These steel plugs not only install flush, but also have the ability to withstand higher pressure than standard steel plugs. The robotic arm will consist of two actuators. One will be fixed while the other one will be moving together with the first link. Therefore, the second actuator will consist of an extruded surface to hold the second link.

The actuator housing that was designed is shown in Fig. 3.3. The left side figure shows an isometric view of the housing. The right side figure shows the passageways

of the housing in dotted lines. The holes that are used to mount the first actuator will be inserted with heli-coils to hold the bolts in place, since Aluminum is a soft material. When heli-coils are installed into tapped holes, they provide permanent conventional internal screw threads that accommodate any standard bolt or screw. These have a very high wearing tensile strength, low thread friction with tight tolerances, and a high surface quality as well as anti corrosive and heat-resistant properties.

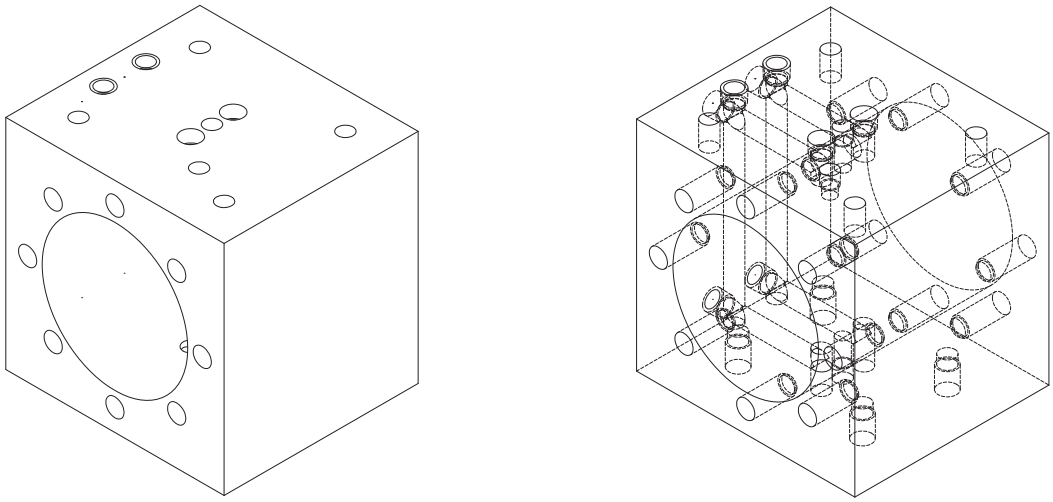

Figure 3.3: Normal and detailed views of the actuator housing

3.2.2 Shaft and Vanes

The forces generated on the two vanes from the hydraulic fluid result in the turning of the shaft. Therefore, the vanes should be sized so that an adequate area is provided for generating the required force from the hydraulic oil while being able to withstand the stresses. The sizes of the vanes were determined based on the stresses. The Cosmosworks software was used to check the stress levels generated during the operation. The horizontal cross section of the vane was 0.5 x 1.5 in. to meet the

required conditions. The vanes are continuously in contact with the side caps and the actuator housing. Therefore, the vanes should be made out of a wear-resistant material. Hence, brass was used as the material for the vanes. In addition to this, if the vanes happen to collide with the separation wedges, both these vanes and wedges should be of adequate strength to avoid damage.

The shaft will be fitted with two vanes on opposite sides, 180° apart from each other. It will have a socket to hold the vanes. This socket on the shaft will be of 1 x 1/2 x 1/2 in. in size. The shaft is provided with a flat section where the vane fits. These are bolted to the shaft so that it is firmly held in place. The shaft will have a diameter of 1.5 in. in the middle section and 1.0 in. on the sides. The links of the robotic arm will be mounted on to the shaft of the actuator. Therefore, the overall length of the shaft should be sufficient enough to hold the connectors. The overall length of the shaft was 7.5 in.. The 4140 alloy steel was the material used for making the shaft. It is an alloy steel that is supplied in either an annealed or pre-hardened condition. It is stronger and has excellent fatigue-resistant properties. A diagram of the shaft and vane is shown in Fig. 3.4.

3.2.3 End Cap and Side Cap

The actuator is provided with two side caps and end caps on each side. These are used to seal the system while withstanding the high operating pressures of the hydraulic fluid. While the side caps close the chambers on either sides, the end caps are used to close the entire actuator. The side cap is basically shaped like a disk and has two pockets to locate the chamber separators. It has a diameter of 3.0 in. with a thickness of 0.5 in.. The vanes will be constantly rubbing the side caps during the motion. Therefore, these should be made out of a wear-resistant material. Thus, side caps

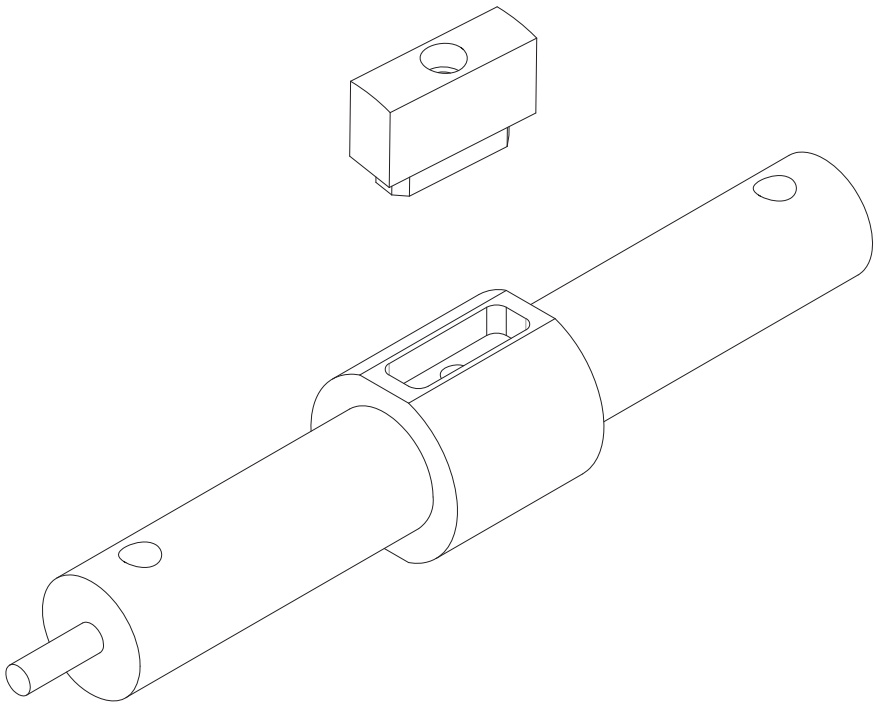

Figure 3.4: The shaft and the vane of the actuator

were made out of brass. The front and back views of the end cap are shown in Fig. 3.5. The end caps are used to hold the components in place. The thickness of the end cap was estimated considering the stresses that it would encounter during the operation. The end cap has a square, 4.5 x 4.5 in. shape. The thickness of the end cap is 0.5 in.. It has a through hole with 1 in. diameter on one side. On the other side, there is a cylindrical extrusion which has a 3 in. diameter and a length of 0.75 in.. This cylindrical part will be completely inserted into the housing. There is a space to hold a set of roller bearings so that a shaft can be mounted. It also carries a groove to hold an oil seal and an o-ring. These are rated at an operating pressure of 3000 psi will prevent any leakages during the operation. The number of bolts required to fit the end cap to the housing was determined from the forces created by the hydraulic pressure of the fluid. Based on the strength required, eight (8) 5/16 in. (8-32) socket

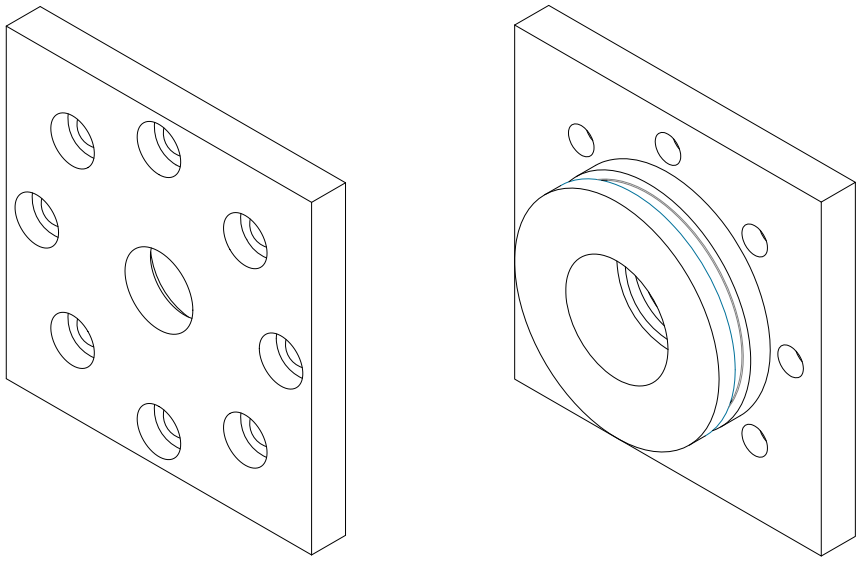

Figure 3.5: The end cap

head cap screws were used on either side. Aluminum (2024-T6) alloy was used for the endcaps. A diagram of the side cap used to close the sides is shown in Fig. 3.6.

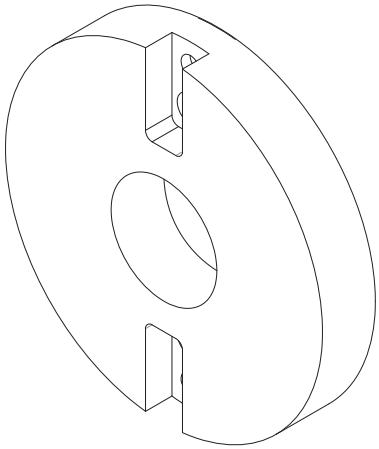

Figure 3.6: The side cap

3.2.4 Separation Wedge

The housing must be divided into two sections, since this is a double vane actuator. Separation wedges are used to divide the housing into two chambers. These wedges have a trapezoidal cross section. The separation wedge has an angle of 69 °, a normal distance of 0.75 in. between the upper arc and lower arc and a width of 1.5 in.. It has a series of drilled holes used to channel the hydraulic fluid from the housing to the chambers. They are fixed to the housing using 1/4 in. dowel pins. The separators also have 0.25 in. protrusions on either side so that they can be inserted into the side caps. These wedges will be held in place using a dowel pin and a 8-32, 3/8 in. screw fitted through side caps. Brass is used as the material for separation wedges as it has a high impact resistance. The separation wedge that was designed for the actuator is shown in Fig. 3.7. The right side figure shows the passageways used to channel the flow.

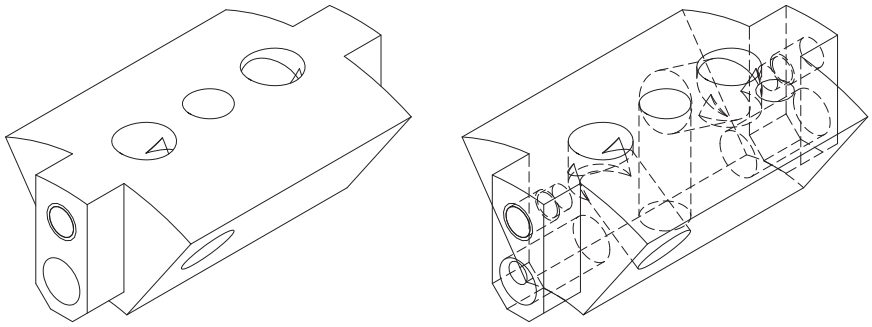

Figure 3.7: The separation wedge which divide the housing

3.2.5 Electro Hydraulic Servo Valve

This actuator requires a valve to control the hydraulic fluid flow from the actuator. The Moog® G761 series electro-hydraulic servo valve is used for regulating the oil flow. This is a high-response valve which has a flow rate of 10 gallons per minute. An illustration of this valve was given in Chapter 2. It will be fixed to the actuator using a manifold. The valve requires an electrical connection and a hydraulic connection.

3.2.6 Manifold

The servo valve will be mounted onto a manifold which in turn is mounted onto the housing. The manifold provides flexibility to change the servo valve without making modifications to the housing. The dimensions of the manifold are 4.5 x 4.0 x 0.75 in.. It consists of a series of passageways to connect the hydraulic fluid from the servo valve to the actuator housing, the hydraulic source and the tank. In order to minimize weight, Aluminum (2024-T6) alloy is used. The manifold that was designed for the servo valve is shown in Fig. 3.8.

The manifold connects the hydraulic supply to the valve. The regulated flow from the servo valve (both pressure and return) is supplied via the manifold. A schematic of the manifold mount is shown in 3.9. There is a locating pin to indicate the orientation of the servo valve. The holes P, T are connected to the pressure and return of the hydraulic supply. The holes A,B are connected to the actuator. O-rings are used between the housing and the manifold to prevent any leaks. A cross-section of an o-ring installation is shown in the same figure.

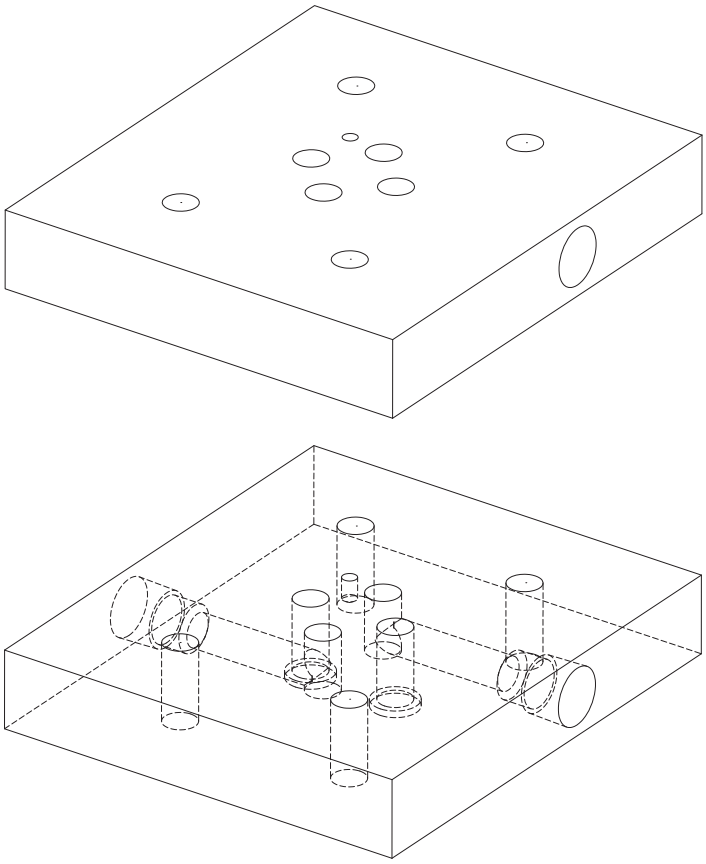

Figure 3.8: The manifold that was designed for connecting the servo valve

3.2.7 Stops

Two stops are used on the actuator to prevent the imminent possibility of vanes striking the separation wedges at high speeds. This could damage both the vanes and the separation wedges. These stops will be mounted to the end caps. The stops that we designed are shown in Fig. 3.10. One of these stops will be used to mount the optical encoder. Steel sleeves will be used along with bolts in order to absorb the energy during any impact. Aluminum (2024-T6) alloy is used as the material for the stops.

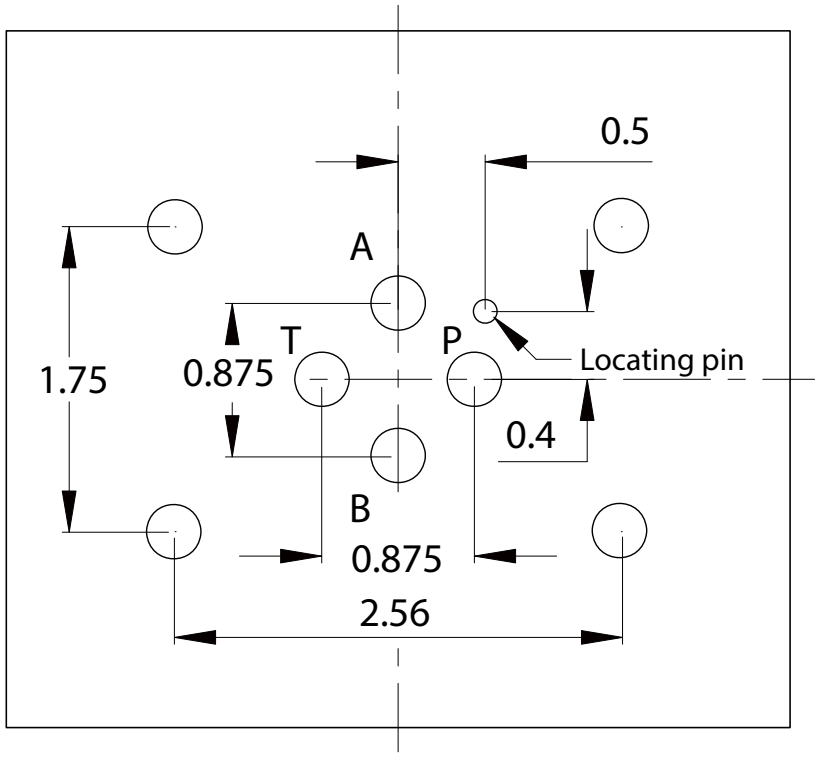

Figure 3.9: A schematic of the hole pattern of the manifold

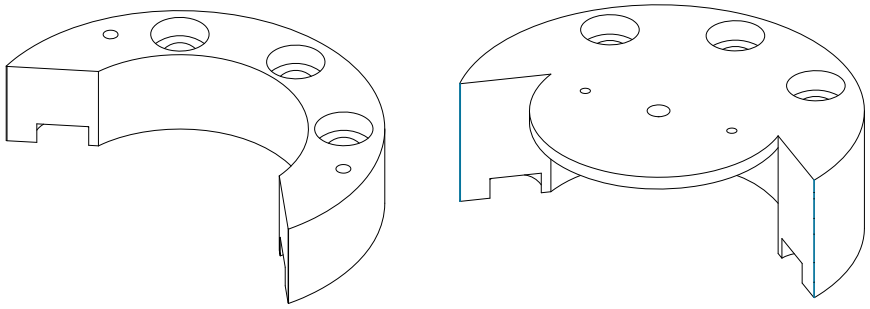

Figure 3.10: The stops used for preventing damage of the internal components

3.2.8 Encoders

The actuators are instrumented with encoders to measure the angular position of the robot links. The Accu-coder® model 755A type encoder is used in this study. It is 1.5 in. in diameter and 1.5 in. in length. This encoder is provided with a through

Figure 3.11: An optical encoder from Accu-Coder® with shaft

hole for mounting the shaft. This through hole design eliminates the requirement for a coupling to mount the encoder. The encoder we used is a high-precision, high-performance encoder. It has an angular resolution of 2000 pulses per revolution. By using quadrature decoding, angles can be measured with accuracies of up to 0.045 degrees (8000 pulses per revolution). An optical encoder is shown in Fig. 3.11.

The encoder has 5 wire connections. These include a Channel A, Channel B, Power, Ground and an index. The power is connected to +5 V. The Channels A,B can be used to measure the magnitude and the direction of the angles. Pull up resistors should be used during interfacing of these channels.

3.3 Simulation of Stresses and Strains of the Actuator Components

The rated operating pressure of the actuator is 20.7 MPa (3000 psi). This results in very high stresses on the the internal components of the actuator. Therefore, during

the design process, it was necessary to ensure that that the components were within the critical stress and strain levels of the specific materials. Cosmosworks was used to test these stress and strain values.

It is important to limit the weight of the second actuator in order to minimize its inertia. Reduced weight contributes to an increase in the speed of the robot. Hence, some of the components of the actuator were fabricated using Aluminum 2024-T6 alloy. This is an aircraft-grade Aluminum alloy. It uses copper as the primary alloying agent. It has a high strength-to-weight ratio and good fatigue resistance.

Brass was used as the material for the components which encountered continuous wear. However, brass is not a very lightweight material. It contributed to an increase in the weight of the actuator. Alloy steel 4140 is a versatile steel which is used in a variety of tooling and other industrial applications. This is available in pre-hardened and annealed condition. The 4140 alloy steel was used where strength of components was a critical factor. The annealed steel was used in other places since it is easy to machine. The properties of the materials used for the actuator components are given in Table 3.1.

Table 3.1: Mechanical properties of the materials used. Source: Shigley et. al[1]

Material	Density $/(kg/m^3)$	Yield Strength $/(MPa)$	Shear Modulus $/(GPa)$
Aluminum	7800	220	79
4140 Alloy Steel	2780	325	28
Brass	8500	240	37

The stress-strain distributions of the housing, end cap, side cap, lock and shaft-vane assembly were analyzed. These are the major components that have to bear the ex-

treme stresses during the operation of the manipulator. The lock is used to prevent the vane from striking the separator at a high velocity. Therefore, the lock is tested for impact when the system runs at its peak torque of 800 Nm. In order to carry out the simulation, these components had to be assumed fixed to a restraint and the corresponding pressure had to be applied on the effective surface. The component was then divided into mesh elements. The Cosmosworks software package was used to calculate the stress distribution along with the deformations using finite element analysis. Each of the components was assumed to be fixed and subjected to an operating pressure of 20.7 MPa (3000 psi). Based on the results, specific modifications were introduced into the design. The simulation results of the stress and strain distributions of these components are shown in Fig.s 3.12 and 3.13.

The key results of the simulation are presented in Table 3.2. These show that the critical stresses under extreme operating conditions do not exceed the Von Mises stress by a reasonable margin. It is also seen that the deformation of these components is negligible under the operating conditions. The maximum stress is concentrated on the inlet and outlet positions of the flow channels. Elsewhere, the stresses rarely exceed 16 MPa. When the housing is subjected to rated pressure, the highest deformation of the housing occurs in its cylindrical section, although it too is negligible. The end cap will encounter its maximum stress (110 MPa) where the bolts are fixed. The stresses and deformations are negligible in quantity elsewhere. The stress and strain distribution of the side cap shows that the dimensions are adequate to avoid failure. The lock is also safe for a force generated on its surface at its peak torque. The stress will be a maximum (174 MPa) at the bottom end of the cap screws.

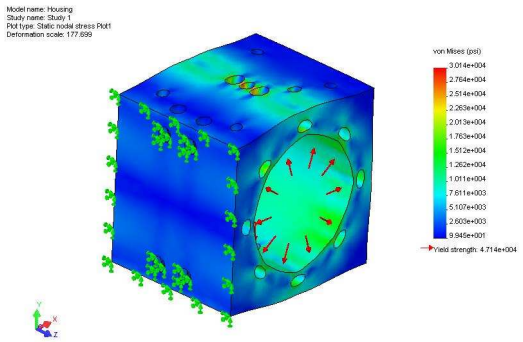

(a) Stress distribution of the housing

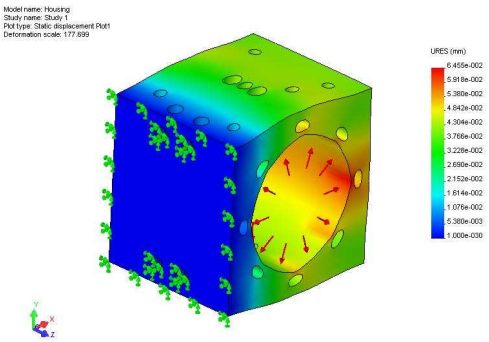

(b) Deformation of the housing under the stress

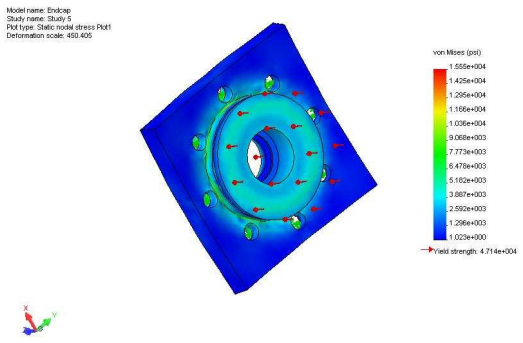

(c) Stress distribution of the end cap

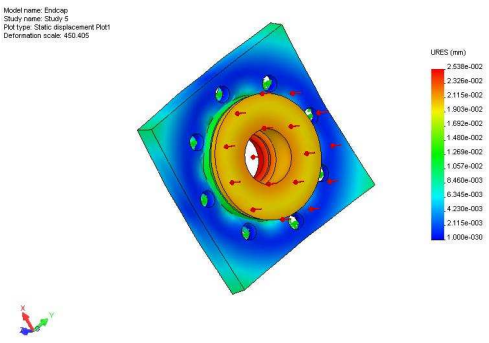

(d) Deformation of the end cap under the stress

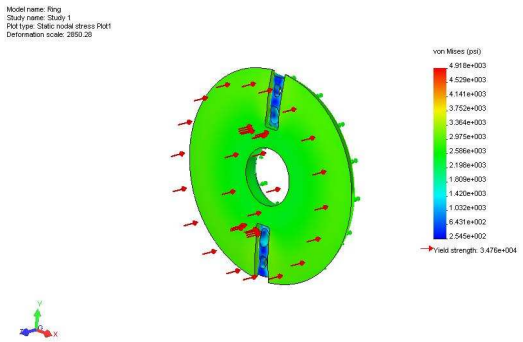

(e) Stress distribution of the side cap

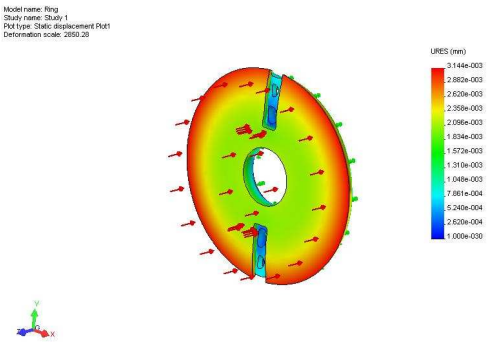

(f) Deformation of the side cap under the stress

Figure 3.12: The distribution of stresses and strain

3.4 Actuator Assembly

The assembly process of the actuator has to be performed very carefully in order to prevent leaks. The vanes were inserted into the shaft and fixed in place using

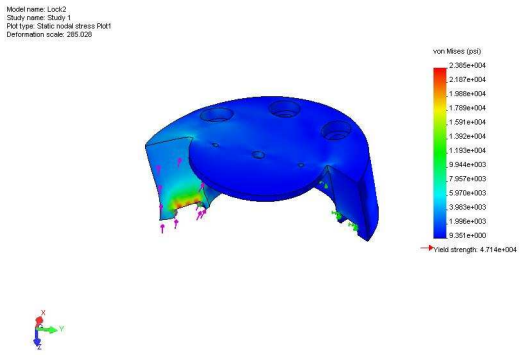

(a) Stress distribution of the lock

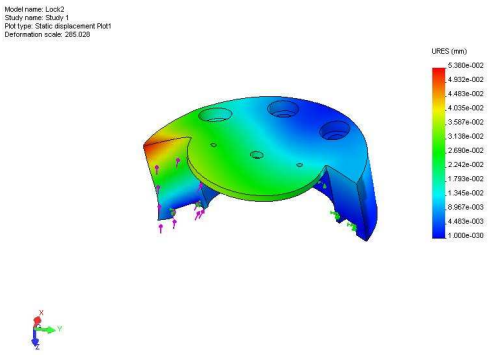

(b) Deformation of the lock under the stress

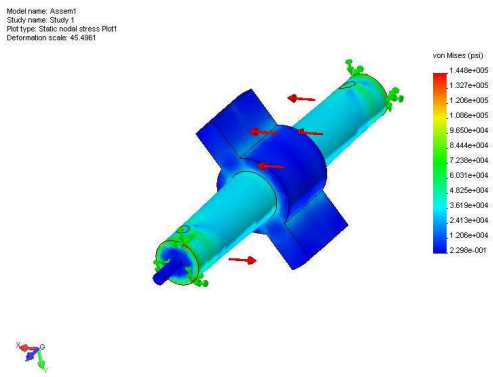

(c) Stress distribution of the shaft vane assembly

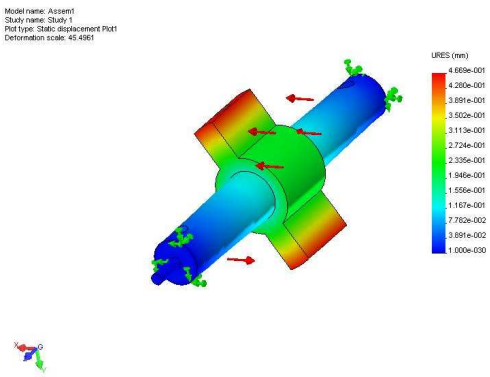

(d) Deformation of the shaft vane assembly under the stress

Figure 3.13: The distribution of stresses and strain

the socket head cap screw. Then the separation wedges were fixed to the housing using steel dowel pins 1/4 in. in diameter. The side caps were pinned to the separation wedges using a dowel pin 3/8 in. in diameter and a 3/16 in. (8-32) socket head cap screw on each side. An o-ring and a seal was inserted into the end cap in order to prevent hydraulic leaks. The o-ring and the seal used for this purpose, along with installation details of the o-ring and seal, are shown in Fig.s 3.14(a) and 3.14(b). The groove for the installation should be made to a surface roughness value of 32 μin..

The end caps are secured to the housing using eight 3/8 in. (8-32) socket head cap screws to bear the forces generated from the hydraulic oil. NPT plugs having a

Table 3.2: Maximum stress-strain values of the components

Component	Von Mises Stress $/(MPa)$	Yield Strength $/(MPa)$	Displacement $/(mm)$
Housing	210	325	0.064
End cap	110	325	0.025
Side cap	34	240	0.003
Lock	164	325	0.054

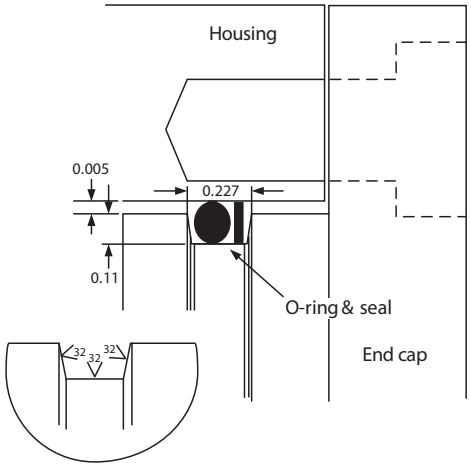

(a) Installation of o-ring and seal on the endcap to prevent hydraulic leaks

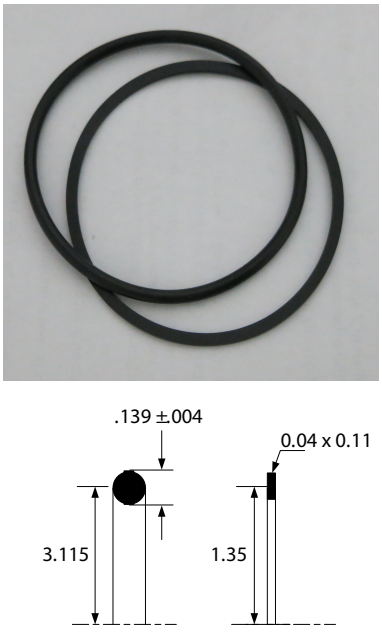

(b) The o-ring and seal used

Figure 3.14: The o-ring and the seal for end cap

diameter of 3/8 in. are used on the housing in order to close the drilled passageways. The shaft is also mounted on two needle bearings to support the weight and cantilever moment of the manipulator (i.e., forces in the z direction).

The servo valve is installed on to the manifold. There will be four o-rings between

the manifold and the housing to prevent any leaks. The actuator is then fitted with a set of external stops. Cylindrical sleeves are used with socket head cap screws of the stops to absorb the energy during any high speed impact. The end cap will be tightly secured using eight (8) 5/16 in. (8-32) socket head cap screws.

The clearances between the components should be tightly controlled in order to minimize leakage and friction. The nominal manufacturing clearance between the housing and the vane was 1.5 mil. The manufacturing tolerance between the side cap and vane was 3 mil.

3.5 The Design of the Robotic Arm

The proposed SCARA type robotic arm consists of two links. These will be directly driven by the rotary hydraulic actuators. Gear drives will not be used, in order to prevent the possibility of delays, backlash and interference. The links of the robot are assumed to be of 0.5 m and 0.4 m. The links of the arm will be connected to the actuator via connectors. The Aluminum (2024-T6) alloy is selected as the material for fabricating the links and the connectors. This is to minimize the weight of the system while providing adequate strength.

Connectors are used between the links and actuators. These connectors are fabricated out of 1/2 in. thick Aluminum plates. There are two connectors pinned to the actuator shaft on top and bottom. These are connected using two vertical plates. These plates are connected to the links. The connectors of this arm are shown in Fig. 3.15. Square Aluminum tubes (3 x 3 in.) with a 1/8 in. wall thickness are used for designing the links. Material is removed from these tubes in places where there are no

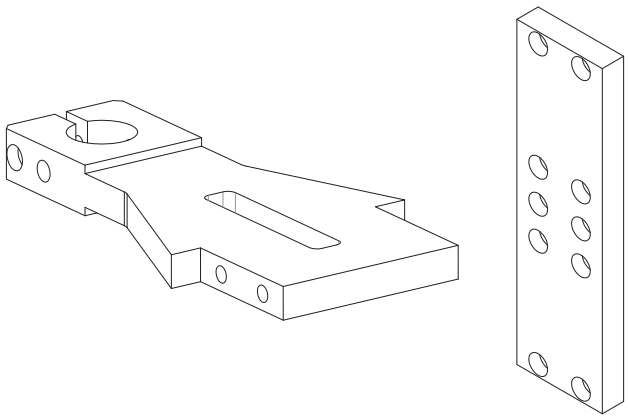

Figure 3.15: The link connectors of the robot

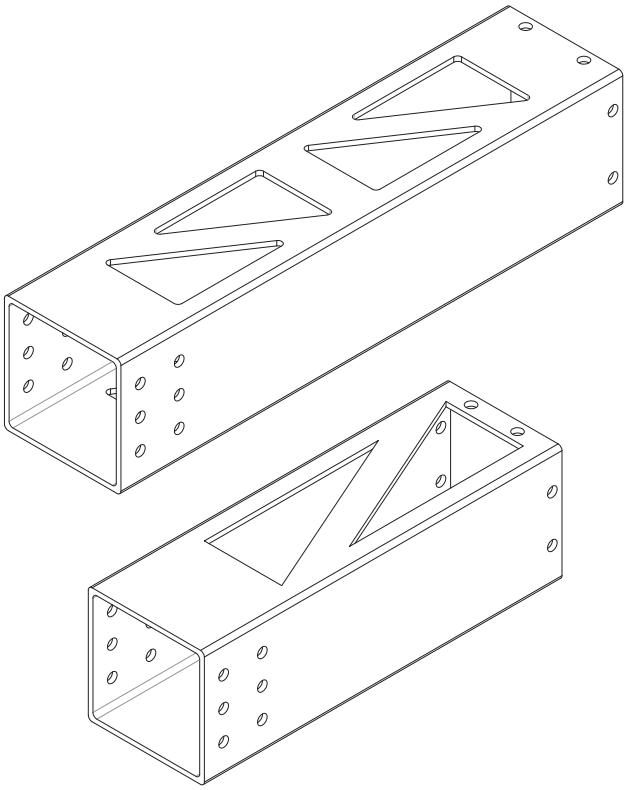

Figure 3.16: The two links of the proposed robot

stresses in order to reduce the weight. In order to meet the length requirements the links must be of 12.92 in. and 9.38 in. in true length. These links are shown in Fig. 3.16. The top figure shows link 1 and the bottom figure shows link 2. The first link is fixed to the housing of the second actuator. The second link and the EE was mounted onto the second actuator. The servo valve was fitted directly onto the manifold. The inlet and the outlet of the hydraulic supply was connected to the manifold. The final design of the SCARA arm in Solidworks® Real View graphics is shown in Fig 3.17.

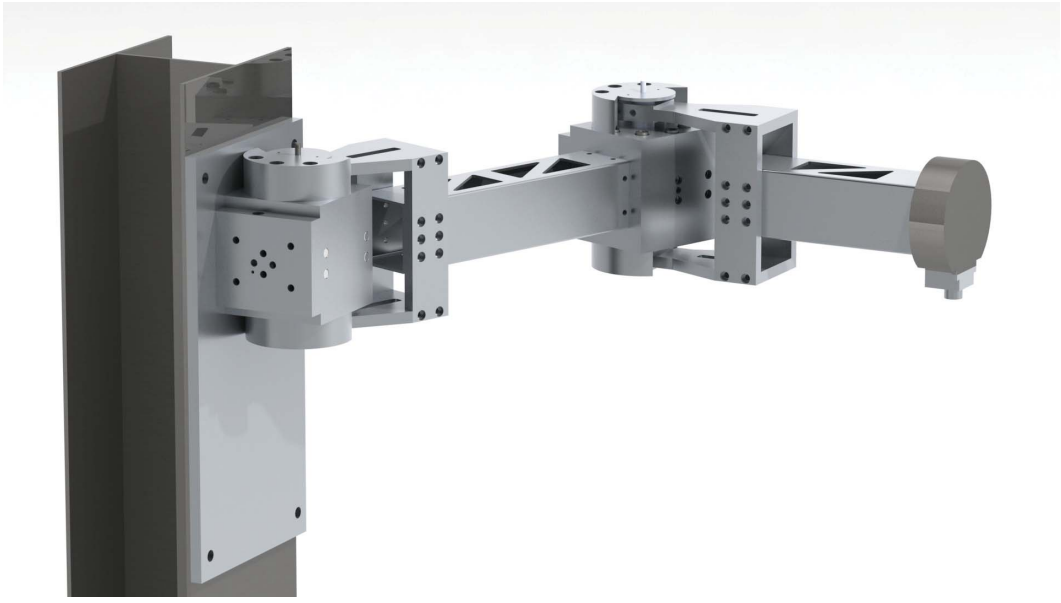

Figure 3.17: View of the SCARA arm proposed for fabrication in Solidworks Real View Graphics

3.6 Fabrication of the Robotic Arm

The drawings for the designs were made using Solidworks® CAD software. The actuator and robotic arm were fabricated and assembled by the Technical Services Division of Memorial University. Fabrication requires precision machining, since the dimensional tolerances are a critical factor. The tolerances between the components had to be maintained so that they would fit ideally with each other, preventing hydraulic

leaks. All manual operations required the craftsmanship of a skilled machinist. The CNC, end mill and lathe were used for making the parts. The accuracy of the components was maintained up to 1/2 mil.

The actuator housing was the most complex part to fabricate. This is because the dimensional tolerances had to be maintained within tight limits. The clearance between the external wall of the housing and the passageways is less than 0.15 in. at certain points. The separation wedges and the housing should fit perfectly with each other. The vanes and the housing should be within the required clearance. The actuator once fabricated is shown in Fig. 3.18. The robotic arm once fabricated is shown in Fig. 3.19.

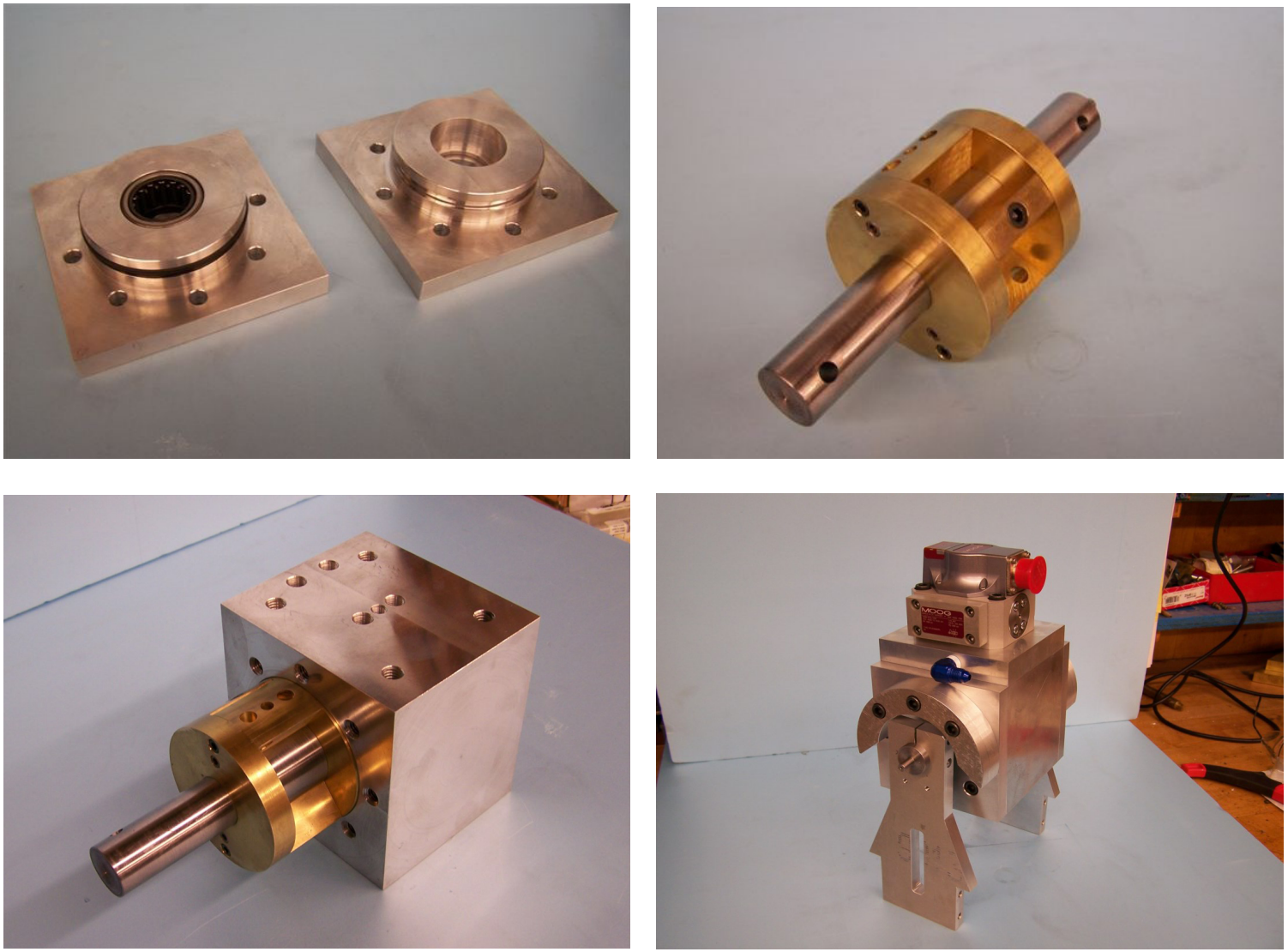

Figure 3.18: The proposed actuator after fabrication

Figure 3.19: The proposed robotic manipulator after fabrication

Chapter 4

Bond Graph based Modeling of a High Speed Visual Servoing System

4.1 Introduction

This study considers the control of the EE of a high-speed SCARA type manipulator. This manipulator uses two custom designed double vane rotary actuators with servo hydraulic valves driving the links. This manipulator is designed to handle payloads of up to 15 kg. During the high speed operation, the EE is subjected to the torsional vibration of the support column and flexing of the robot links. This results in deflecting the EE effector of the robot by a considerable amount. The joint encoders will provide the joint angles from a relative frame of reference. However, in order to account for these effects and disturbances, this robotic manipulator needs to obtain the feedback from an external frame of reference. This feedback from an external sensor can be obtained by a visual exteroceptive sensor.

Visual servoing is the integration of vision based feedback in the robot control loop in order to mitigate the effects of disturbances and achieve increased accuracy and robustness. Vision is a useful form of robotic sensor feedback since it mimics the human sense of vision. In robotics visual feedback is usually obtained using a camera. With the advancement in high-tech camera systems, visual servoing has often been used for robotic applications in recent years [60], [61], [62]. It provides a non-contact measurement of the environmental parameters [63]. It has a great potential to provide a controller feedback for some of the mechatronic systems operating in less changing and unstructured environments [64].

The problem of fine position control of a flexible manipulator has been extensively researched but it is seldom resolved using visual servoing techniques. One possible exception is in the field of space robotics where lightweight, slender designs result in appreciable link deflections that must be compensated through dynamic modeling and control, or through a combination of proprioceptive and exteroceptive sensors [65],[66],[67]. Visual servoing is a viable option especially in cases where the EE velocities of the manipulators are low. This is evident in the International Space Station Mobile Servicing System where the EE velocities are typically on the order of 2 cm/s with payloads [68]. Vision-based feedback is used by Jiang and Eguchi [69] for EE tracking control of a flexible manipulator. These robots are simpler and moves at much lower speeds (40 mm/s).

In the case of high speed applications, researchers have devised a number of strategies to circumvent the bandwidth and computational challenges associated with quick response visual servoing. Liu et al. [70] proposed a hybrid, multi-sensor approach for

accurate, high speed robot positioning. In their study, an image loop is proposed exclusively for coarse positioning. Then a laser pointer fixed to the EE and the high resolution feedback from a PSD is used for fine position control. Bascetta et al. [65], [71] adopted a two time scale visual servoing strategy for flexible manipulators. In this approach, specific natural vibration modes are actively dampened by a fast controller that employs feedback from proprioceptive sensors which comprise strain gauges and operate at a maximum loop rate of 500 Hz. The visual control law is executed every 40 ms (25 Hz) in order to ensure smooth tracking of the desired trajectory. Several researchers have adopted similar two time scale control strategies [72],[73],[74],[75].

This chapter considers the development of a visual servoing system for a high speed SCARA type manipulator. The proposed system comprises hydraulic, mechanical and electronic sub-components. It is important that in a multi-domain system, the dynamics of systems that exchange power and energy in various forms should be clearly understood. The bond graphs provide a unified approach to model electrical, mechanical and hydraulic subsystems. Through bond graph theory, graphical depictions of dynamic systems that have been derived could be automatically translated into complex mathematical models for computer simulation [76]. The visual servoing system will be modeled using bond graph theory. There have been a number of studies using bond graph theory. Bilodeau and Papadopoulos [46] presented the modeling and identification of a hydraulic servo actuator system. This model considered line losses, nonlinear orifice areas, hysteresis, friction, leakage, and load dynamics. It was used for developing a force controller. In the current study, the servo valves, hydraulic actuator, SCARA robot and support column were modeled using the bond graph theory. A controller architecture for this robot was also proposed using feedforward-based set point modification to compensate for support column vibration.

4.2 Related Studies

Visual servoing techniques have been widely investigated in the last three decades. Machine vision has been used for closed-loop position control for a robot EE as early as 1979 [77]. This study uses vision to obtain a non-contact measurement position or environmental parameters. With the development of modern camera systems, robot controllers have frequently been integrated with vision systems. Visual servoing requires the fusion of results from several areas including high-speed image processing, dynamics, control systems theory and the development of real time embedded systems [63]. However, there are many problems that still remain unsolved. The implementation of high-speed visual servoing systems for robotic applications still remain a challenge today. Visual servoing has been used in a wide range of robotic applications including manipulation [78], mobile robotics [79], medical robotics [80], micro-assembly [81], and auto-piloting and automatic surveillance by unmanned aerial vehicles [82], [64].

Visual servoing can be broadly classified into two main categories: image based visual servoing (IBVS) and pose based visual servoing (PBVS) [83]. Most existing IBVS approaches have been developed for serial manipulators, while PBVS has been developed mainly for unmanned aerial vehicles [84]. IBVS is based on the error between current and desired features on the image and does not necessarily involve an explicit estimation of the pose and orientation [85]. IBVS has been considered in several studies [86],[87],[88],[89], [90]. In contrast, PBVS involves estimating the position and orientation of a target relative to the image sensor in six degrees-of-freedom [83]. Generally latter is relatively faster, however both these methods are computationally expensive. Hence, they have not often been considered for high speed applications. There have been many studies considering PBVS for controls [90], [91], [92], [93], [94],

[95].

IBVS involves image pre-processing, image feature extraction and sequence control design [96]. Traditional image-based control schemes use the image coordinates of a selected set of points for implementing the controller [97], [83]. Collewet and Marchand [98] considered the luminance of the pixels in an image instead of using classical geometric features such as points and straight lines. Unlike other methods it did not require any tracking or matching of the features during the process [98]. IBVS does not require a model of the target object. It is also robust to the errors in the parameters of the camera model. Therefore, the camera calibration process will not significantly affect the accuracy of this method. It is also much simpler since, in the image plane, the trajectories of image features are controlled, approximately straight lines [96].

PBVS uses the pose and orientation of the camera with respect to a reference coordinate system [83]. Therefore, it requires the explicit estimation of relative position and orientation of the EE with respect to the camera. One of the advantages of this method is that it makes it possible to specify the desired and relative trajectories of the EE [99]. Efficiency and robustness are two major challenges associated with the pose estimation problem [100]. PVBS involves the explicit estimation of the position and orientation using either an inertial measurement unit or a camera. If a single camera is used, either markers [91] or a structured lighting system on an untextured environment [101] can be used to estimate position and orientation. If stereo vision is used, triangulation or linear methods can be used [102], [103]. All these methods require rigorous calibration of the camera to estimate the extrinsic parameters. Gratal et al. [104] propose markerless pose estimation and tracking of a robot manipulator

by comparing the virtual image with the real image in terms of visual features.

A number of control strategies have been used in studies in the past. Lee et al. [105] used image-based visual servoing (IBVS) with an adaptive sliding mode controller to track a two dimensional landing target and land a quadrotor. Shi et al [106] used a hybrid approach to control a space robot. They employed both IBVS and PBVS to control the position of a space robot. PBVS controllers were used when IBVS did not provide any control over the specific position or velocity of the camera. Sim et al. [107] proposed a position-based approach to control a SCARA type manipulator with 5 DOF. Their approach used a modified Smith Predictor control scheme to take account of the delays outside the feedback loop. Leonard and Jagersand [108] presented a preliminary learning-based approach to address the problem of visual servoing. This method used neither any pose estimation from the image space, as with PBVS, nor any model representing the variations between the image and motor spaces as with IBVS. The control signal will be generated for a specific task by using a reinforced learning technique. Sharifi and Marey [91] proposed a novel Kalman Filter based method for the pose estimation in visual servoing, integrating the mechanisms for noise adaptation and iterative-measurement linearization. This method was proposed to address the problem of erroneous assumptions that lead to a weak pose estimation during visual servoing. Akella [109] proposed an adaptive control scheme for manipulators with visual servoing to address the issues of uncertainty through linearized inertia parameters and non-linearity in camera calibration parameters. Other controllers proposed in the literature include feedforward approach [110], model predictive control [111], [112], fuzzy adaptive [113] and H_∞ [114].

A two time scale approach has been considered in several studies as the vision loop op-

erates at a much lower frequency. It employs a fast control loop for coarse positioning and a slow control loop for fast positioning of the system. An eye-in-hand approach for flexible manipulators was used in [115]. The main objective of this strategy is to avoid the computationally expensive operations of obtaining the inverse and time derivative of the Jacobian. It consisted of a slow controller which is based on task space inverse dynamics. The fast controller was designed with singular perturbation theory using image features as feedback. It is used to dampen the mechanical vibrations. Using a similar approach, a control framework for a visual alignment system was proposed by Kwon et al. [116]. It used a fast vision loop for coarse alignment. Then a vision loop which runs at a lower frequency is used for the accurate of alignment mark is to compensate for the mask-panel misalignment. It used a set of degraded images for coarse alignment which was the faster loop. The Kalman filter was used to further improve the accuracy of the points.

4.3 Proposed High Speed Visual Servoing System

The SCARA manipulator considered in this study consists of two links and an EE. It is mounted onto a compliant support that has an $'I'$ shaped cross section. The typical length of the links of this manipulator are 0.49 m and 0.36 m. The EE is 12 kg in weight. This study proposes a PBVS technique for controlling the EE of the manipulator. Two methods methods are proposed in this study for EE control. Both these methods use joint encoders as proprioceptive sensors and a high speed camera as the exteroceptive sensor. The joint encoders will provide a relative angular measurement while the high speed camera will provide the position of the EE relative to an external frame of reference. This is required to mitigate any external disturbances from EE vibration and beam flexing.

Two methods are proposed in this study for joint control. The first method is called the Set Point Modification Control (SPMC). It estimates the torsional vibration of the support column in real time and accounts for the EE deflection. In the second method a single time scale IBVS controller is proposed. It uses both the encoders and high seed camera as feedback, simultaneously to estimate the control signal.

This robotic manipulator is designed to operate at a very high speeds. Hence the camera used to obtain feedback should be fast and accurate. Therefore, a two dimensional PSD is used as the image sensor of the proposed camera. These sensors are capable of measuring position at very high speeds. The proposed system also needs the hardware that is capable of implementing the controller at high speeds. An embedded system was designed using a Field Programmable Gate Array (FPGA) to perform these functions. It provides a low level implementation of the controller with a single chip solution offering parallel processing. A schematic diagram of the proposed high-speed visual servoing system is shown in Fig. 4.1.

This chapter covers the development of a dynamic model for the visual servoing system. The details of the high speed camera system's development will be covered in Chapter 5. It will also include the calibration process of the two dimensional PSD and camera. The development of an embedded system which consists of the input/output interface and controller implementation will be covered in Chapter 6.

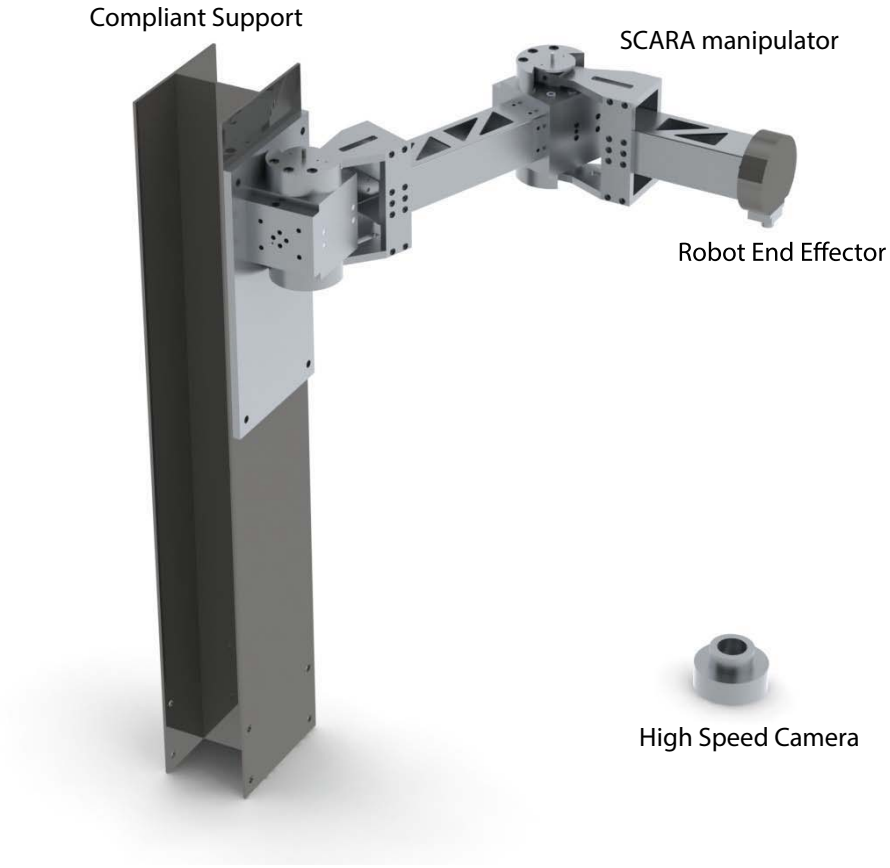

Figure 4.1: The schematic diagram of the proposed system

4.4 Modeling of the Proposed System

The total visual servoing system comprises several subsystems including a hydraulic system (servo valves and rotary actuators), a SCARA robot arm, controllers and the compliant support. These involve hydraulic, mechanical and electronic sub components. Bond graphs provide a unified way of graphically representing energy flows associated with a multi-domain system using a single representation. In the current system, the servo valve and the actuator belong to a hydraulic subsystem, the SCARA arm and the compliant support belongs to a mechanical subsystem and the controller belongs to an electronic subsystem. This section presents the development of a bond graph for the entire system representing its dynamic characteristics. Bond graphs are

developed for each of the sub-components and finally connected together to represent a single system.

4.4.1 Modeling of the Hydraulic Actuator

The hydraulic actuator used for this robot is a double vane rotary type actuator. A cross section of this actuator is shown in Fig. 2.5. The hydraulic actuator consists of two main compartments that are separated using wedges. The vanes of this actuator are fitted to the shaft so that they are 180° from each other. These vanes further divide the compartment into two chambers. The actuator housing consists of a series of passageways to channel the oil flow in and out of the actuator. A servo valve is fitted to the actuator in order to channel the oil flow. When the spool of the servo valve opens, one of the chambers is connected to the supply pressure while the other is connected to the reservoir. When one side of the chamber connects to the pressure, the other side connects to the tank and vice versa. This creates a pressure differential in the vane. In a similar manner, the other compartment creates an opposite force, resulting in a torque.

The torque on the shaft is proportional to the pressure differential between the vanes. Pressure differential could be transformed into torque using a transformer. The transformation ratio is the amount of torque produced per unit of difference in pressure across the vanes per unit of rotation of the shaft. This corresponds to the actuator displacement coefficient (D_M). Therefore the torque on the shaft is:

$$T = D_M(P_1 - P_2); \tag{4.1}$$

where T is the actuator torque and P_1 and P_2 refer to pressure in chambers 1 and 2.

The control volume considered for analysis consists of the fluid volume trapped in the chambers of the actuator. The hydraulic fluid which is used to run the actuator is subjected to compression under high pressure. Hence, the effects of fluid compression cannot be neglected. For a control volume of fluid which is subjected to compression [8]:

$$\frac{\delta P}{\delta V} = \frac{\beta}{V} \tag{4.2}$$

where P is the pressure of the fluid under compression, V is the control volume and β is the effective bulk modulus of the fluid. Considering the compressibility effects of the fluid in both chambers:

$$P_1 = \frac{\beta}{V_1} \int \Delta Q dt \tag{4.3}$$

$$P_2 = \frac{\beta}{V_2} \int \Delta Q dt \tag{4.4}$$

where V_1 and V_2 correspond to the initial volume of the two chambers of the actuator. Q corresponds to the change in the volume of the fluid. Fluid compressibility is represented as a capacitive element in the bond graph diagram of the actuator.

Defects during manufacturing, expansion of the pressurized housing and wear during the operation of the actuator could leave a gap between the actuator housing and the vane. This results in fluid leaks across the vanes as high pressure fluid is moved within the chambers. The fluid leakage is considered as a resistive element. The

inverse square law can be used to estimate the leakage flow. It is given by:

$$Q_L = c_d A_L \sqrt{\frac{2}{\rho} |(P_1 - P_2)|} sign(P_1 - P_2) \tag{4.5}$$

Where Q_L is the oil leakage rate, C_d is the coefficient of fluid discharge and A_L is the effective cross sectional area of the vane clearance and ρ is the density of the hydraulic fluid.

The principles of fluid continuity apply to the control volume considered in the analysis. Therefore, the rate of fluid flow into the chamber should be the same as total amount of fluid which flows out of the chamber minus the fluid which leaks through the vanes together with the volume change due to compression. The fluid continuity principle could be applied to both chambers of the actuator giving fluid flow into the chamber equal to the sum of the fluid into the chamber, change in fluid compressibility and the leakage volume per unit time. Considering fluid continuity principles,

$$Q_{in} = Q_{out} + Q_{comp} + Q_L \tag{4.6}$$

Where Q_{in} is the fluid flow rate in to the actuator, Q_{out} is the fluid flow rate out of the actuator, Q_{comp} is the volume of fluid compressed and Q_L is the leakage flow. The bond graph model for the actuator is given in Fig. 4.2.

4.4.2 Modeling of the Servo Valve

An electro-hydraulic servo valve is used to regulate the flow of the actuator. The actual valve used for the actuators is a MOOG® G761. It consists of the spool, a cylindrical sleeve, flapper and an armature with coils. The spool consists of a set of

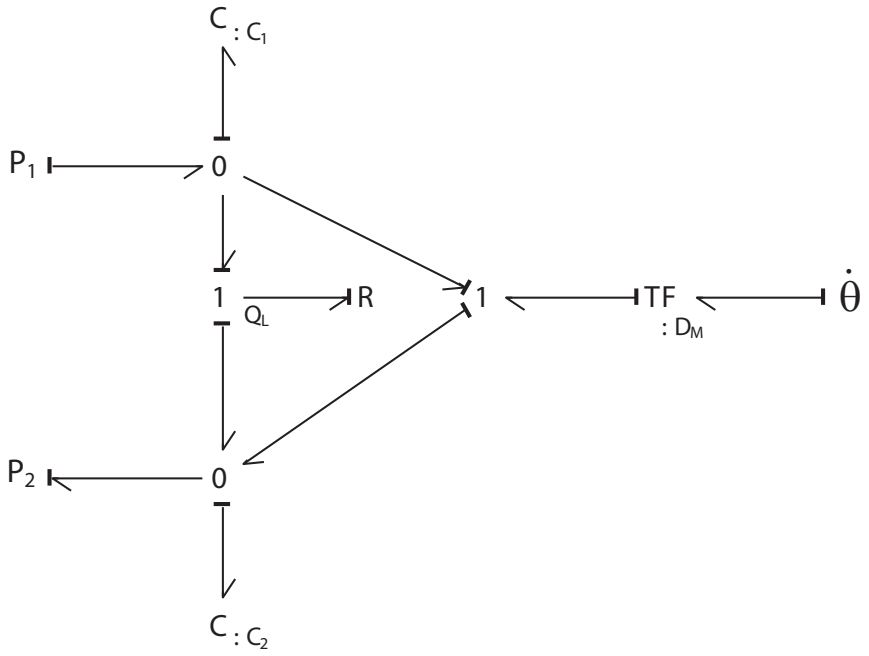

Figure 4.2: The bond graph for the rotary hydraulic actuator

lands. It moves in a cylindrical sleeve. When a current is applied to the armature coils, it creates a force to move the flapper proportional to the current. This regulates the opening of the spool. The movement of the spool progressively changes the exposed aperture size and alters the differential oil flow between two control ports [24].

The armature which moves the flapper consists of two inductance coils that have been placed in series. These coils have a resistance and an inductance. Therefore, the coil of the valve is modeled as a simple LR circuit which has the transfer function shown below:

$$I(s) = \frac{1}{Ls + R} U(s) \tag{4.7}$$

where, $I(s)$ is the induced current, L is the coil inductance, R is the coil resistance and $U(s)$ is the voltage command signal applied to the coils.

Displacement of the spool in a given direction connects the pressure port of the hydraulic supply to a chamber of the actuator while the return port of the hydraulic supply is connected to the opposite chamber. This results in rotating the actuator in a clockwise or counter clockwise direction. When the spool makes a displacement in the opposite direction, opposite ports are connected to the actuator chambers, resulting in rotation in the reverse direction. The bond graph developed for the servo valve is shown in Fig. 4.3.

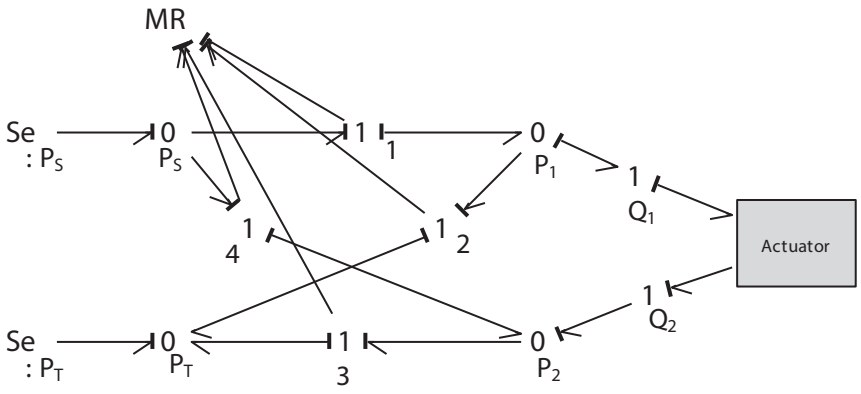

Figure 4.3: A cross section of the double vane rotary actuator

Flow rate through the valve is dependent on displacement of the spool. Displacement of the spool will change the exposed aperture size for fluid flow. Fluid flows through a gap from a high pressure side to a low pressure side. This flow can be modeled as a flow through an orifice. This fluid flow rate can be represented as a modulated resistor ($'MR'$ element in Fig. 4.3). The flow rates are given by:

If $x_v > 0$,

$$q_1 = c_d k_v |x_v| \sqrt{\frac{2|P_s - P_1|}{\rho}} sign(P_s - P_1) \tag{4.8}$$

$$q_3 = c_d k_v |x_v| \sqrt{\frac{2|P_2 - P_T|}{\rho}} sign(P_2 - P_T) \tag{4.9}$$

$$q_2 = 0, q_4 = 0 \tag{4.10}$$

If $x_v < 0$,

$$q_2 = c_d k_v |x_v| \sqrt{\frac{2|P_1 - P_T|}{\rho}} sign(P_1 - P_T) \tag{4.11}$$

$$q_4 = c_d k_v |x_v| \sqrt{\frac{2|P_s - P_2|}{\rho}} sign(P_s - P_2) \tag{4.12}$$

$$q_1 = 0, q_3 = 0 \tag{4.13}$$

where q_1, q_2, q_3, q_4 correspond to the flow rates through the junctions 1, 2, 3 and 4, k_v is the circumference of the cylindrical sleeve, P_s is the supply pressure and P_T is the tank pressure.

The directional flow of the hydraulic fluid based on the direction of the spool movement is modeled using bond graphs, as shown in Fig. 4.3. In the bond graph shown, one of the two bond flows into the left side of the 0-junction will be zero. The half-arrow directions will reverse the sign of Q_1 or Q_2 as necessary. Therefore in the constitutive laws of the modulated resistor, the absolute value of x_v is used.

If x_v moves in a positive direction, then $'1'$ junctions 1 and 3 are activated. Oil

will flow at a rate of q_1 from the source to the actuator's first chamber and a flow rate of q_3 will result from the second chamber to the tank. When x_v moves in a negative direction $'1'$ junctions 2 and 4 are activated. Oil will flow at a flow rate of q_4 from the source to the second chamber and at a rate of q_2 from the first chamber to the tank.

4.4.3 Modeling of the SCARA Arm

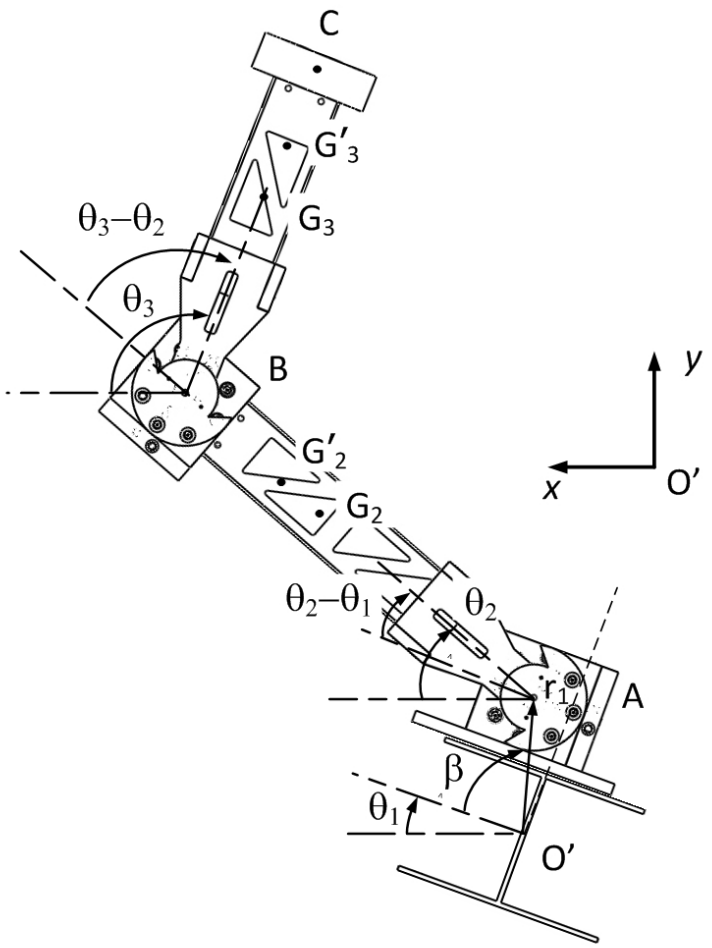

Figure 4.4: The plan view of the manipulator with the support column

The manipulator consists of two rigid links fitted with hydraulic actuators. The plan

view of the manipulator with the vertical column is shown in Figure 4.4. These actuators and the EE are considered as point masses in the analysis. The mass of the actuator has to be distributed between two robot links. When the first link is considered, the rotor of the first actuator is assigned at point A and the stator of the second actuator is assigned at point B. In the case of the second link, the rotor of the second actuator is assigned at point B while the EE is assigned at point C. Hence the center of gravity (COG) needs to be modified for each link. For link AB considering moments, the modified center of gravity will be given by:

$$AG_2^{'} = \frac{m_2 AG_2 + M_S L_2}{M_r + m_2 + M_S} \tag{4.14}$$

where $AG_2^{'}$ is the distance to the modified COG, AG_2 is the distance to existing COG, m_2 is the mass of link AB, M_r is the mass of the rotor of the actuator, M_s is the mass of the stator of the actuator and L_2 is the length of the link AB of the robot. For link BC, the modified center of gravity will be given by:

$$BG_3^{'} = \frac{m_3 BG_3 + M L_3}{M_r + m_3 + M} \tag{4.15}$$

where $BG_3^{'}$ is the distance to the modified COG, BG_3 the distance to the existing COG, m_3 is the mass of the link BC, L_3 is the length of the link BC of the robot.

The moment of inertia (MOI) also needs to be modified for each link. It could be calculated for each link using the parallel axis theorem. The modified MOI for link AB is given by:

$$J_{G_2}^{'} = J_{G_2} + m_2(AG_2^{'} - 0.5L_2)^2 + M_s(L_2 - AG_2^{'})^2 + M_r AG_2^{'2} \tag{4.16}$$

Where $J_{G_2}^{'}$ is the modified MOI inertia about the new COG and J_{G_2} is the MOI of the link AB about G2.

$$J_{G_3}^{'} = J_{G_3} + m_3(BG_3^{'} - 0.5L_3)^2 + M(L_3 - BG_3^{'})^2 + M_r BG_3^{'2} \tag{4.17}$$

Where $J_{G_3}^{'}$ is the modified MOI inertia about the new COG and J_{G_3} is the MOI of the link BC about G_3. J_{G_2} and J_{G_3} for each link was estimated using a CAD model.

Each link is considered separately to develop the bond graph. Link 2 (denoted by AB) has a modified COG $^{'}$. It rotates about point A at an angular velocity of $\dot{\theta}_2$. Considering the velocity of point A:

$$\mathbf{V}_A = \mathbf{V}_{G_2}^{'} + \mathbf{V}_{A/G_2}^{'} \tag{4.18}$$

Where $\mathbf{V}_A$ is velocity of point A, $\mathbf{V}_{G_2}^{'}$ is the velocity of point $G_2^{'}$ and $\mathbf{V}_{A/G_2}^{'}$ is relative velocity of point 'A' w.r.t. $G_2^{'}$. The velocity $\mathbf{V}_{A/G_2}^{'}$ is given by:

$$\mathbf{V}_{A/G_2}^{'} = \omega \times r = \dot{\theta}_2 \hat{k} \times \bar{\mathbf{r}}_{A/G_2^{'}} \tag{4.19}$$

Where $r_{A/G_2}^{'}$ is the vector which is defined by the length AG_2. This length is given by:

$$\bar{\mathbf{r}}_{A/G_2^{'}} = \begin{bmatrix} -AG_2^{'}\cos\theta_2 \\ -AG_2^{'}\sin\theta_2 \end{bmatrix} \tag{4.20}$$

By substituting $r^{'}_{A/G_2}$ in eqn. 4.19:

$$\mathbf{V}^{'}_{A/G_2} = \begin{bmatrix} -AG^{'}_2 \sin\theta_2\dot{\theta}_2 \\ -AG^{'}_2 \cos\theta_2\dot{\theta}_2 \end{bmatrix} \tag{4.21}$$

By substituting $\mathbf{V}^{'}_{A/G_2}$ in eqn. 4.18:

$$\mathbf{V}_A = \mathbf{V}^{'}_{G_2} + \begin{bmatrix} -AG^{'}_2 \sin\theta_2\dot{\theta}_2 \\ -AG^{'}_2 \cos\theta_2\dot{\theta}_2 \end{bmatrix} \tag{4.22}$$

Similarly for point B it can be shown that:

$$\mathbf{V}_B = \mathbf{V}^{'}_{G_2} + \begin{bmatrix} -BG^{'}_2 \sin\theta_2\dot{\theta}_2 \\ -BG^{'}_2 \cos\theta_2\dot{\theta}_2 \end{bmatrix} \tag{4.23}$$

where $\mathbf{V}_B$ is the velocity of point B, $\mathbf{V}^{'}_{G_2}$ is the velocity of point $G^{'}_2$. The bond graph for the link AB is derived from expressions 4.22 and 4.23. Modulated transformers are used to convert the angular velocity to a linear velocity. The mass of the link is considered at the $'1'$ junction corresponding to V_B. The mass of the second actuator which is at B is considered as a point mass acting as an inertia element at G_2. This is connected as an inertia element to the $'1'$ junction corresponding to the angular velocity of the link 2. The bond graph developed for link 2 is shown in Fig. 4.5.

Fig. 4.4 shows how the first actuator is attached to the support column. The angle β is defined considering the angle between the center of support column and the center of first actuator as shown in Fig. 4.4. The angle of twist due to torsional vibration is denoted as θ_1. The vector defined by the axis of the first revolute joint and the point $O^{'}$ on the flange is given by:

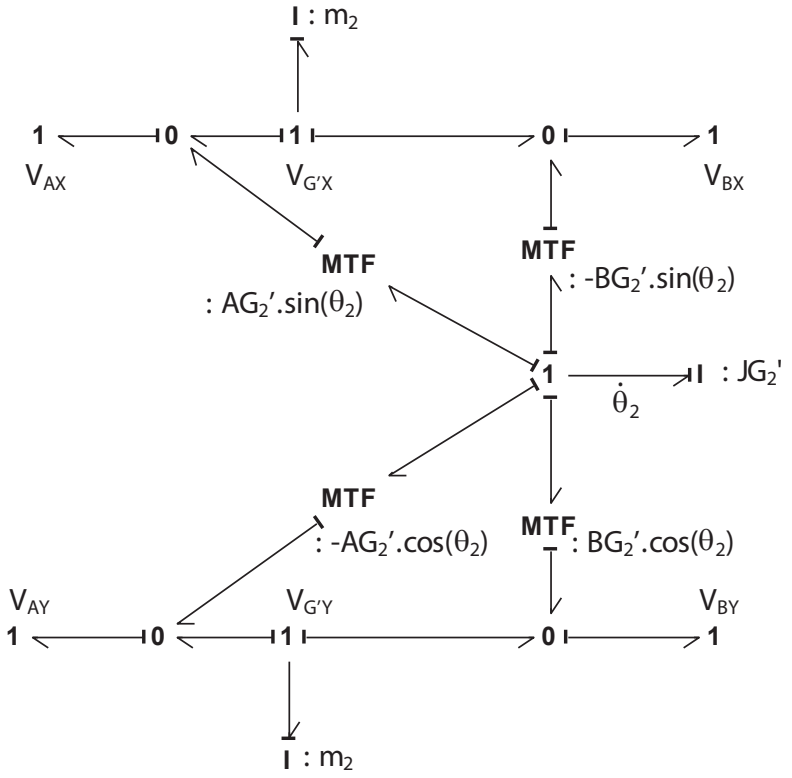

Figure 4.5: The bond graph for first link of the SCARA arm

$$\mathbf{r} = \begin{bmatrix} r_1 \cos(\theta_1 + \beta) \\ r_1 \sin(\theta_1 + \beta) \end{bmatrix} \tag{4.24}$$

Following a similar procedure as link AB, a bond graph can be developed for link BC. The two bond graphs will be connected by considering the velocity vector at point B. In order to remove the algebraic loops, a stiff spring was attached along with a low resistance to point B.

By taking the derivative w.r.t. time,

$$\mathbf{V}_A = \frac{dr}{dt} = \begin{bmatrix} -r_1 \sin(\theta_1 + \beta)\dot{\theta_1} \\ r_1 \cos(\theta_1 + \beta)\dot{\theta_1} \end{bmatrix} \tag{4.25}$$

4.4.4 Modeling of the Support Column

The manipulator is mounted on to a vertical beam. It has an $'I'$ shaped cross section. This column will be modeled as a lumped parameter model. This will simplify the analysis of this continuous column, by assuming that it consists of discrete entities connected by torsional springs and dampers. The support column was divided into 50 lumped segments. A schematic of the lumped segment model is shown in Fig. 4.6.

An analysis of a single lumped-mass segment develops the incremental solution to the total torsional response. A free body diagram of a single torsion element is shown in Fig. 4.7.

Each lumped mass segment is considered as a rotational inertia element connected with a torsional spring and a damper. This element transfers torque and relative twist to the elements adjacent to each other. The bond graph for one such element is developed and shown in Fig. 4.8.

In the bond graph shown, the resistive element corresponds to the material damping factor (R_{mat}) and the inertia element (J_i) corresponds to the mass moment of inertia. The compliance (C_i) is given by:

$$C_i = \frac{\Delta X}{GJ} = \frac{\frac{L_1}{N}}{GJ} \tag{4.26}$$

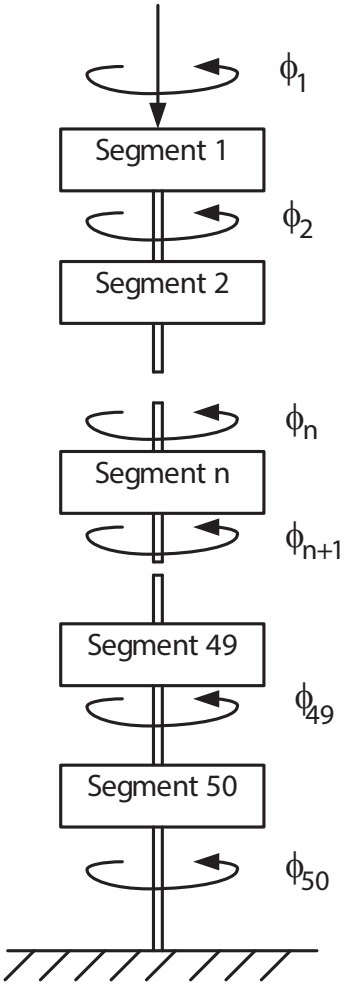

Figure 4.6: The compliant support column divided into torsional elements

where ΔX is the length of a lumped segment, L_1 is the length of the beam, N is the number of segments, G is the shear modulus and J is the polar moment of inertia.

The system was modeled as separate components. It includes the valves, actuators, support beam and robot. Finally, these components were integrated separately as a total system model. This is shown in Fig. 4.9. Bond graph modeling software 20 Sim® was used to develop the bond graph model for the simulation.

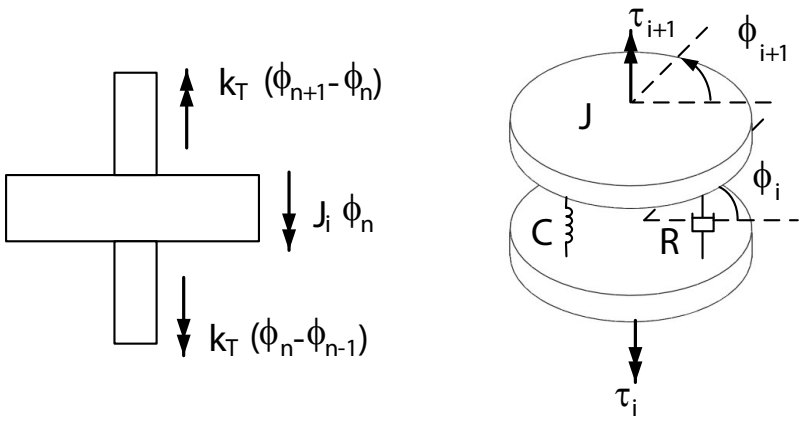

Figure 4.7: The free body diagram of a single torsional element

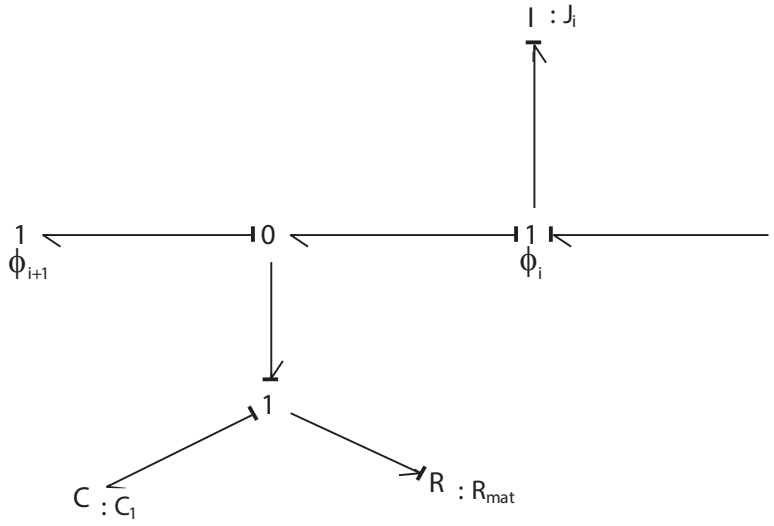

Figure 4.8: The bond graph of a single torsional element

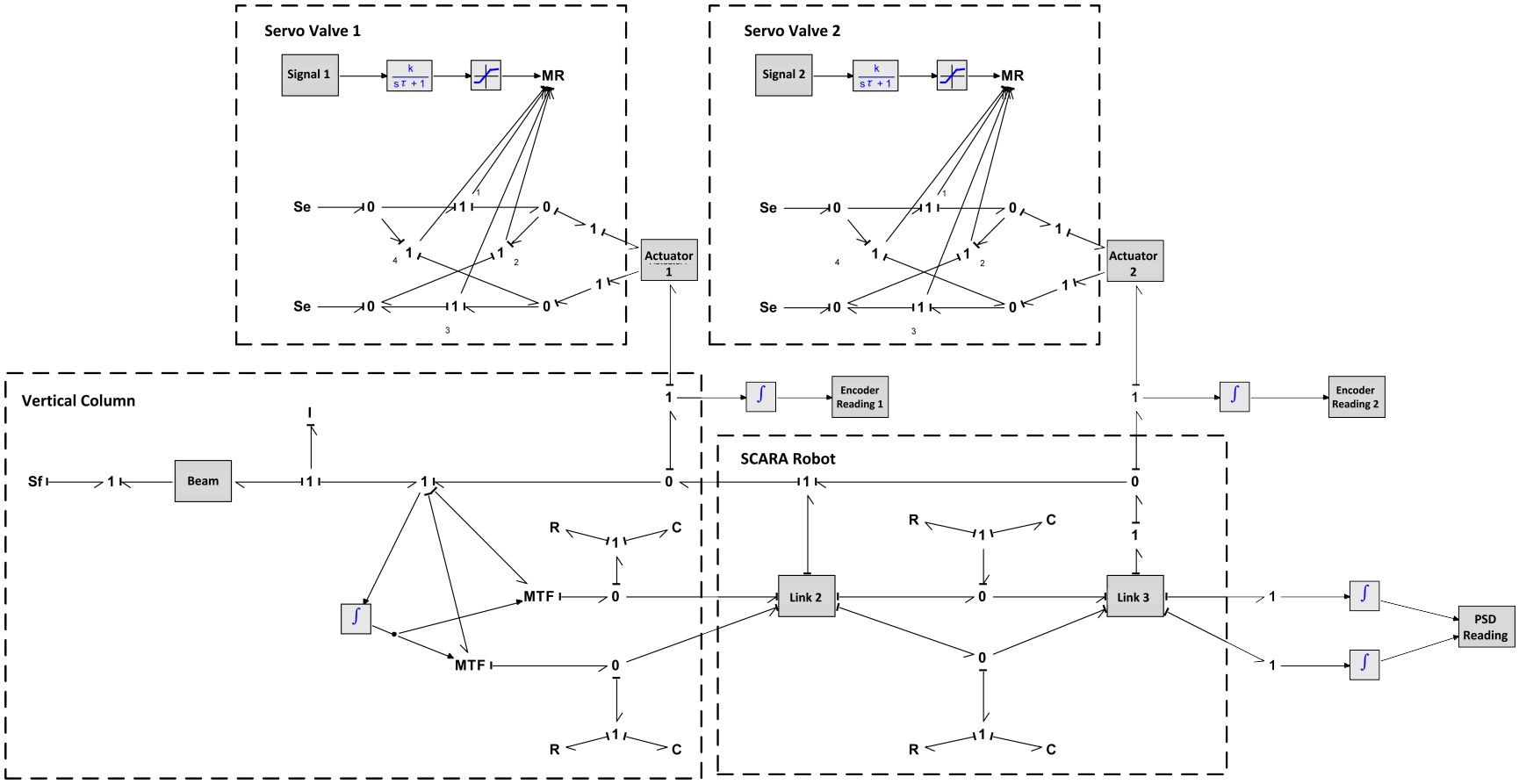

Figure 4.9: The SCARA arm with the compliant support using bond graph representation

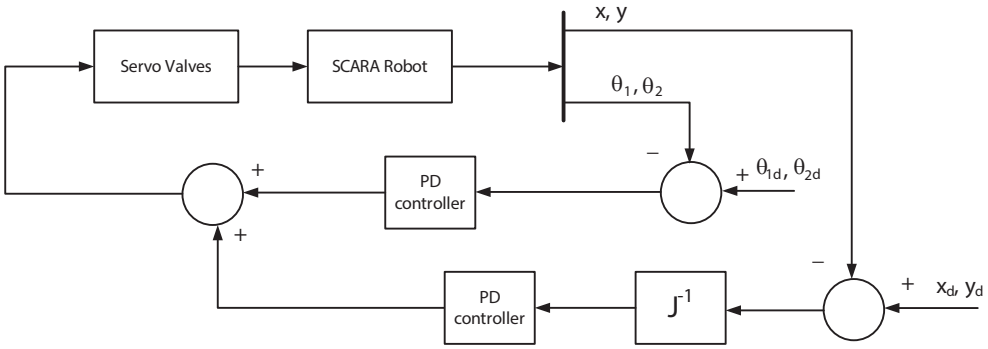

Figure 4.10: A schematic diagram of the proposed single time scale Visual Servoing controller architecture

4.5 Development of a Single Time Scale Visual Servoing System

The feedback for controlling the arm will be obtained using both proprioceptive (encoders) and exteroceptive sensors (high speed camera). The encoder angles will provide the relative position of the links. During the high speed motion of the robot flexing of the links and torsional vibration of the support column could affect the final position of the EE. Therefore, accurate position control of the EE requires to consider the absolute position the EE. A schematic diagram of the proposed controller is shown in Fig. 4.10. The EE position could be related to the joint variables using the manipulator jacobian. It will be given by,

$$\mathbf{\Delta X} = \mathbf{J}.\mathbf{\Delta}\theta \tag{4.27}$$

Where $\mathbf{\Delta X}$ is the EE position vector, $\mathbf{\Delta}\theta$ is the vector with link angles and $\mathbf{J}$ is the manipulator jacobian.

Hence, if the EE position is known the link angles could be calculated using:

$$\mathbf{\Delta}\theta = \mathbf{J^{-1}}\mathbf{\Delta X} \tag{4.28}$$

Using the desired and measured link angles and EE position the above equation could be given as,

$$\theta_{\mathbf{d}} - \theta = \mathbf{J^{-1}}(\mathbf{X_d} - \mathbf{X}) \tag{4.29}$$

Where, $\theta_{\mathbf{d}}$ is the desired link angle, θ is the measured link angle, $\mathbf{X_d}$ is the desired position and $\mathbf{X}$ is the measured EE position.

The link angles of the manipulator could be obtained using the optical encoders. The EE position could be obtained using the high speed camera. The inverse jacobian for a SCARA type manipulator will be given by:

$$\mathbf{J^{-1}} = \begin{bmatrix} \frac{cos(\frac{\pi}{2}+\theta_2+\theta_3)}{l_2.sin(\frac{\pi}{2}+\theta_2)} & \frac{sin(\frac{\pi}{2}+\theta_2+\theta_3)}{l_2.sin(\frac{\pi}{2}+\theta_2)} \\ \frac{-(l_3.cos(\frac{\pi}{2}+\theta_2+\theta_3)-l_2.cos(\theta_2))}{l_2.l_3.sin(\frac{\pi}{2}+\theta_3)} & \frac{-(l_3.sin(\frac{\pi}{2}+\theta_2+\theta_3)-l_2.sin(\theta_2))}{l_2.l_3.sin(\frac{\pi}{2}+\theta_3)} \end{bmatrix} \tag{4.30}$$

The control signal (U) for the servo valves will calculated considering joint angles and EE position. This will be given by:

$$U = K_{P\theta}.E_\theta + K_{D\theta}.\dot{E}_\theta + K_{PXY}.J^{-1}.E_{XY} + K_{DXY}.(J^{-1}.\dot{E}_{XY}) \tag{4.31}$$

Where $K_{P\theta}$,K_{PXY} are a set of proportional gains, $K_{D\theta}$, K_{DXY} are a set of derivative gains, E_θ is the difference between desired and actual link angles, E_{XY} is the difference between the desired and actual position of the EE in Cartesian coordinates with respect to a world coordinate system and J^{-1} corresponds to the inverse of the manipulator Jacobian.

The inverse Jacobian function is evaluated considering the measured encoder angles. It does not result in singularities with in the operating workspace of the robot.

4.6 Development of a Set Point Modification Controller

When the manipulator is in motion, the $'I'$ beam that is used as compliant support twists and produces torsional vibration. It will result in deflecting the EE from the desired position. In formulating the SPMC control strategy only the effects from this torsional vibration was considered to correct the position of the EE. A schematic diagram of the arm under the effect of torsional vibration is shown in Fig. 4.11. The first actuator (A) will move to point A', displacing the manipulator from ABC to $A'B'C'$ through a circular arc. The desired position of the EE is point D. The joint encoders provide a relative measurement of its angles. Hence, they do not have the capability to capture the effects of external disturbances. The novel control strategy proposed in this study will use the data from the high speed imaging system in addition to the relative angles provided by the encoder for controls. The PSD camera was used to measure the position of the EE from a fixed frame of reference.

In this control strategy, set points of the two joint encoders are modified based on torsional vibration experienced by the column. This will compensate for the twisting of the $'I'$ beam. The encoders provide the relative angles of the joints while the PSD camera system provides the position of the EE with respect to a fixed frame of reference. In order to compensate for the effects of vibration, set points for the joint angles are modified. The angle of twist of the $'I'$ beam is estimated using the joint encoder angles. The desired position of the EE with respect to a fixed co-ordinate

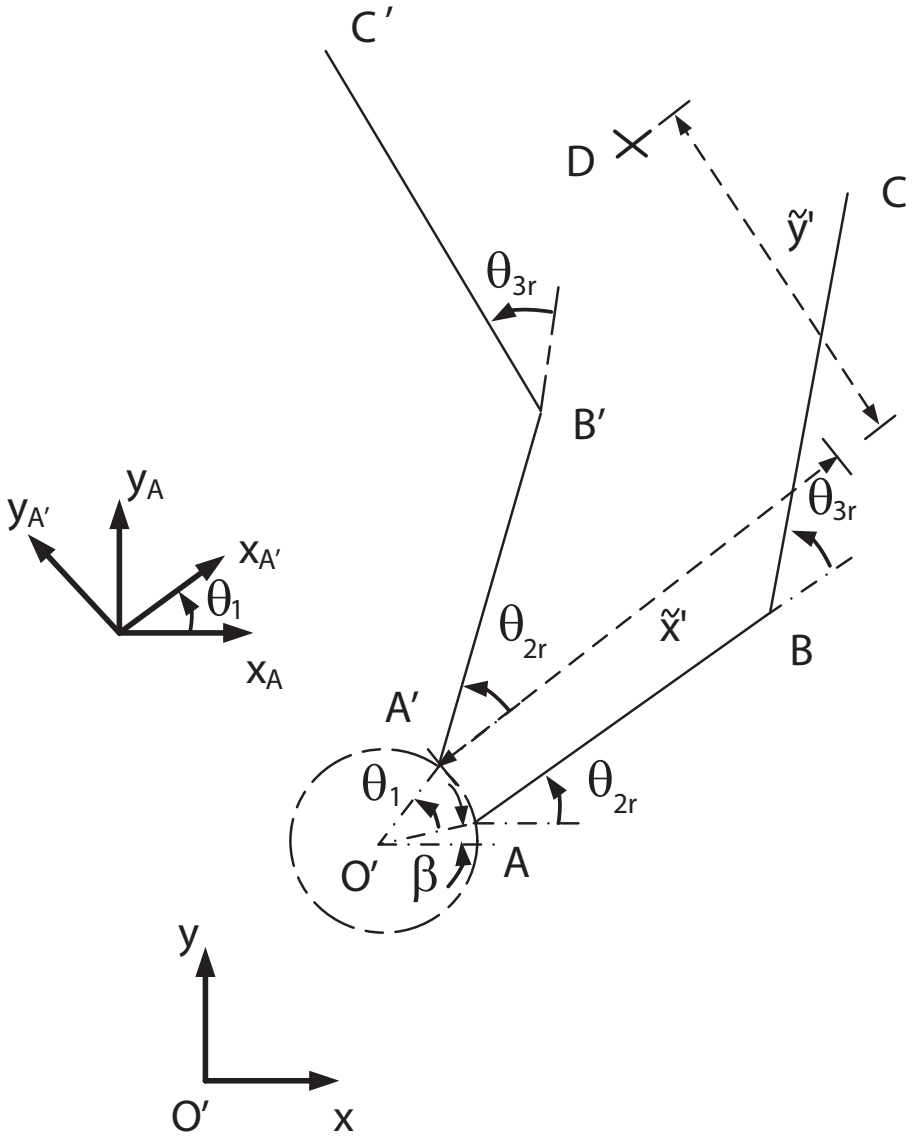

Figure 4.11: The EE position with and without the vibration of the support column

frame at O' is given by $P_{D/O'}$. If there is no torsional vibration, the EE will be at point C due to the controller action. However, twisting of the vertical support column leads the EE to be displaced to point C'. The joint encoders will measure the the relative angles θ_{2r} and θ_{3r} at C' with respect to the coordinate frame $x'y'$. This co-ordinate frame $(x'y')$ at A' forms an angle of θ_1 relative to the inertial frame at O'. In order to estimate θ_1, both points C,C' have to be known. The point C can be estimated using the feedback from the encoders while point C' can be estimated using the position measurement of the imaging system. The position of C w.r.t. O', in coordinates of the inertial frame xy, is given by:

$$\mathbf{P_{C/O'} = P_{A/O'} + P_{C/A}} \tag{4.32}$$

The point $\mathbf{P_{C/O'}}$ is given by:

$$\begin{bmatrix} x_r \\ y_r \end{bmatrix} = \begin{bmatrix} r_1.cos(\beta) \\ r_1.sin(\beta) \end{bmatrix} + \begin{bmatrix} l_2.cos(\theta_{2r}) & l_3.cos(\frac{\pi}{2} + \theta_{1r} + \theta_{2r}) \\ l_2.sin(\theta_{2r}) & l_3.sin(\frac{\pi}{2} + \theta_{1r} + \theta_{2r}) \end{bmatrix} \tag{4.33}$$

Where, r_1 corresponds to the distance horizontal distance between the center of the first actuator and center of the support column.

The position of the EE with respect to the inertial coordinate frame is used to introduce correction for the deflection in real time. The PSD will provide the position of the distorted image coordinates $(\bar{x}'_{dis}, \bar{y}'_{dis})$ on the PSD image sensor. These distorted image coordinates have to be corrected for radial and tangential lens distortion. Along with these, the modified coordinates of the image center have to be used in the estimation. The undistorted image coordinates $(\bar{x}', \bar{y}')$ is given by [117]:

$$\begin{bmatrix} \bar{x}' \\ \bar{y}' \end{bmatrix} = \begin{bmatrix} \bar{x}'_{dis} \\ \bar{y}'_{dis} \end{bmatrix} + \begin{bmatrix} \check{x}_{dis}(k_1 r_{dis}^2 + k_2 r_{dis}^4) + 2p_1 \check{x}_{dis}\check{y}_{dis} + p_2(r_{dis}^2 + 2\check{x}_{dis}^2) \\ \check{y}_{dis}(k_1 r_{dis}^2 + k_2 r_{dis}^4) + 2p_2 \check{x}_{dis}\check{y}_{dis} + p_1(r_{dis}^2 + 2\check{y}_{dis}^2) \end{bmatrix} \quad (4.34)$$

where $\check{x}_{dis} = \bar{x}'_{dis} - u_0, \check{y}_{dis} = \bar{y}'_{dis} - v_0, r_{dis} = \sqrt{\check{x}_{dis}^2 + \check{y}_{dis}^2}$. u_0 and v_0 are the position of the image center obtained from a camera calibration.

The pin hole camera model is used for estimating the position of the EE with respect to a coordinate frame of the camera. Once a measurement is made for EE position using the camera, the backward projection camera model can be used for estimating the EE position with respect to a world coordinate frame [118]. This will be given by:

$$\hat{\mathbf{P}}_{\mathbf{C'/O'}} = \mathbf{R}_{\mathbf{O'/cam}}(\hat{\mathbf{P}}_{\mathbf{C'/cam}} - \mathbf{T}_{\mathbf{cam/O'}}) \quad (4.35)$$

Where, $\hat{\mathbf{P}}_{C'/O'}$ is the measured position of C' w.r.t the inertial coordinate frame at O', $\hat{\mathbf{P}}_{\mathbf{C'/cam}} = \begin{bmatrix} \bar{x}' \\ \bar{y}' \\ z \end{bmatrix}$, measured position of C' w.r.t to the camera ordinate frame, $\mathbf{T}_{cam/O'}$ is the translation vector which describes the position of the camera coordinate frame w.r.t to inertial coordinate frame and $\mathbf{R}_{O'/cam}$ is the rotation vector which describes the position of the inertial coordinate frame w.r.t to camera coordinate frame.

The $\hat{\mathbf{P}}_{\mathbf{C'/O'}}$ corresponds to the position coordinate (x_{camera}, y_{camera}). The vertical column rotates from $O'C$ to $O'C'$ through an angle corresponding to the angle of

twist. Therefore, θ_1 can be estimated by:

$$\theta_1 = atan2(y_{camera}, x_{camera}) - atan2(y_r, x_r) \tag{4.36}$$

The desired position of the EE is point D. If it is to be precisely positioned, the EE will have to move from the current point C' to point D. In order to perform this, the desired relative angles of the links should be recalculated. Hence, position D with respect to A' ($\mathbf{P_{D/A'}}$) are given by:

$$\mathbf{P_{D/A'}} = \mathbf{P_{D/O'}} + \mathbf{P_{A'/O'}} \tag{4.37}$$

where $\mathbf{P_{A'/O'}} = \begin{bmatrix} r_1.cos(\beta + \theta_1) \\ r_1.sin(\beta + \theta_1) \end{bmatrix}$.

The vector $\mathbf{P_{D/A'}}$ should be expressed with respect to the rotated coordinate system A' for performing the inverse kinematics. The modified desired position coordinates $\tilde{\mathbf{P}}_{\mathbf{D/A'}}$ is given by:

$$\tilde{\mathbf{P}}_{\mathbf{D/A'}} = \mathbf{R_{A'}}(\theta_\mathbf{1}).\mathbf{P_{D/A'}} \tag{4.38}$$

where $\mathbf{R_{A'}}(\theta_\mathbf{1}) = \begin{bmatrix} cos(\theta_1) & sin(\theta_1) \\ -sin(\theta_1) & cos(\theta_1) \end{bmatrix}$, which is the rotation matrix about a vertical axis through A'.

Since the desired relative position $(\tilde{x}, \tilde{y})$ of the EE is known, the relative angles of links 2 and 3 can be estimated considering simple geometry and are given by:

$$cos(\tilde{\theta}_{3r}) = N = \frac{\tilde{x}_d'^2 + \tilde{y}_d'^2 - l_2^2 - l_3^2}{2l_2l_3} \tag{4.39}$$

$$sin(\tilde{\theta}_{3r}) = M = \sqrt{1 - N^2} \tag{4.40}$$

$$\theta_{2r} = atan2(M, N) - \frac{\pi}{2} \tag{4.41}$$

Considering Fig. 4.11, using geometry $theta_1$ could be obtained by:

$$\theta_1 = atan2(\tilde{y}'_d, \tilde{x}'_d) - atan2(l_3 sin(\frac{\pi}{2} + \theta_2), a_1 + l_2 cos(\frac{\pi}{2} + \theta_2)) \tag{4.42}$$

The modified desired relative angles for links 2 and 3 are $\tilde{\theta}_{2r}$ and $\tilde{\theta}_{3r}$, respectively.

The error between the measured relative angle of the joints and modified angle for relative set point is fed through a PD type controller for each valve. The controller signal is translated into a voltage signal for controlling each valve. These controllers are tuned using a trial and error method. A schematic diagram of the proposed controller is shown in Fig. 4.12.

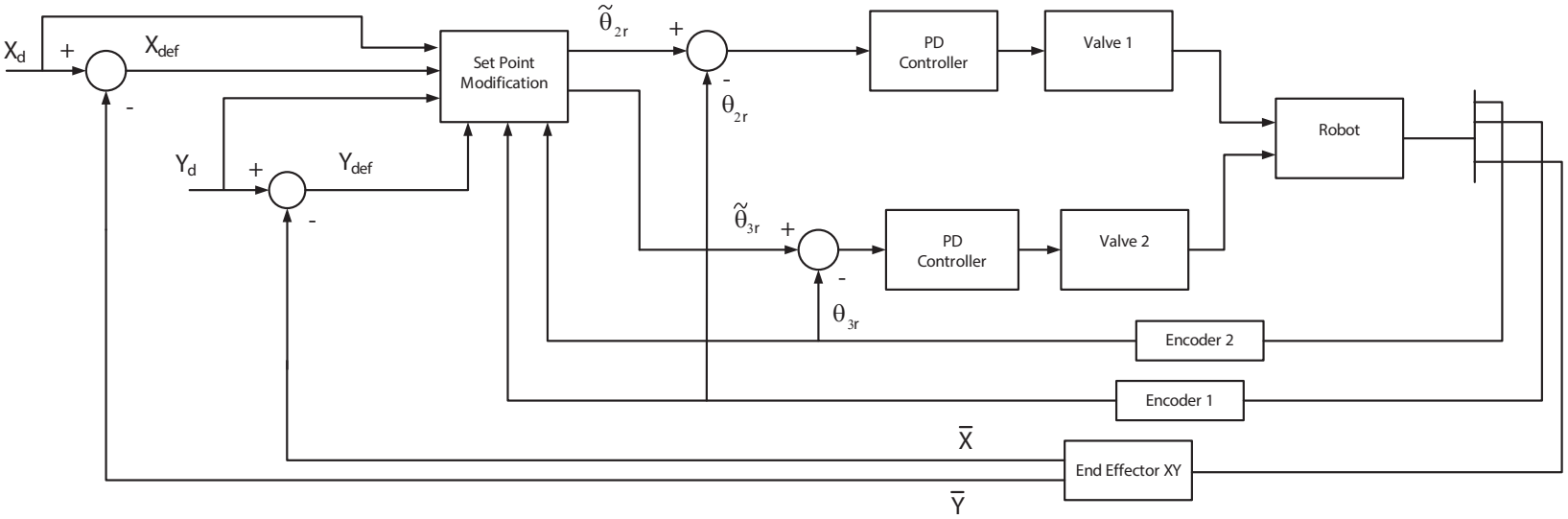

Figure 4.12: A schematic diagram of the proposed control system architecture

Chapter 5

Design and Development of a High Speed Camera System for Position Measurement

5.1 Introduction

In many applications of industrial robots, the EE needs to be controlled to track a desired trajectory or to move to the target positions with speed and accuracy. Precise measurement of the EE position is important for achieving this objective [119]. There are a number of position measuring techniques in practice today [120]. These techniques can be broadly divided into two main categories; direct measurement and non-contact measurement techniques [119]. In the direct measurement techniques, the position information will be acquired directly using sensors mounted on the robot. Non-contact techniques avoid any physical contact between target and sensor. Thus, the measurements must be made with respect to a fixed position on the ground. Non-contact measurement is especially important when the robot is subjected to an

external disturbance such as compliant support vibration, beam flexing, etc.

Non-contact position measurements usually have two common features: They usually employ an emitter and a receiver. This gives the EE position from an external point of reference, providing an absolute measurement. However, one disadvantage of this method is that it may sometimes interfere with the payload during the actual robot operation. These sensors either use light [121], [122], [123] or sound [124], [125], [126], [127] as the medium. Position estimation is usually carried out using time of flight techniques [128], [129],[130], [131], interferometry [132], [121], [133], projection of waves [134], [133] , [135] or signal energy density [136].

The current problem is to develop a 2-D position measurement system for a high speed robotic EE. There are several candidate non-contact position measurement techniques. Among them, time of flight (TOF) cameras are recently reported in literature as an emerging technology. However, these are at a very novel stage in their development. They provide a much lower resolution compared to other cameras and depth distortion of the images occurs, resulting in erroneous measurements [137]. Ziraknejad et al. [138] showed that for a range of distances between $70 - 90$ cm a TOF techniques could provide accuracies up to only 0.77 cm. TOF cameras still have a great number of issues to be resolved, so much further research is needed [131].

Ultra-wide band signals are often used to measure large distances and these have rarely been used for short range indoor applications. Gentile et al. [139] used ultra-wide band based TOF techniques to measure range in some indoor applications. However, the minimum error was reported to be 6 cm for distances up to 45 m. This level of accuracy is far from sufficient. Saad et al. [126] used ultrasonic sensors for de-

veloping a low cost indoor measurement system. They obtained an accuracy of over 0.5 mm using cross-correlation and phase-shift of the signal with the TOF. However, sonar requires multiple sensors and involves complex circuits for signal processing. These have also not yet been proved viable for high speed applications. Laser interferometry has been used for robot EE positioning in some studies [121], [140] and it is capable of producing accurate results. However, in addition to being expensive, laser interferometry based technologies are not capable of carrying out measurements.

Development of a high-speed camera system is the most viable option for carrying out 2-D position measurement. In recent years, motion capture system have been considered in various studies of robot positioning applications. The ARTrack2 motion capture system was used by Tobergte et al. [141] to track and control the EE of a medical light-weight robot (MIRO) intended to perform surgeries in patients. This system uses this off the shelf optical tracking system and inertial measurement unit (IMU) data for position measurement. The ARTrack2 can only achieve a frame rate of 60Hz. The Vikon® motion capture system was used for some of the robot position applications [142], [143]. In a study by Windolf et al. [143] the Vicon® 460 system provided an accuracy of up to 0.129 mm. The Vicon® T10s is an advanced camera developed by the same manufacturer which is capable of reaching speeds of up to 1000 fps. Although this is a much superior frame rate, extra time is needed to carry out image processing to estimate position.

Since the EE of the SCARA arm moves in a plane, a single camera can provide a simple and low-cost approach for measuring its 2-D position. There are a wide range of cameras available in the market to perform this task. High resolution charge coupled device (CCD) cameras have been used for various position estimation ap-

plications [144]. Nakao et al. [145] and Rousseau et al. [135] used a CCD camera mounted on the EE of a robot and employed image processing techniques to estimate its position in 6 DOF. The tests showed that a precision of 0.1 mm could be attained [135]. Complementary metal oxide semiconductor (CMOS) cameras have emerged as an alternative to the conventional CCD cameras. Unlike CCD sensors, in CMOS sensors each pixel consists of its own charge-to-voltage conversion, amplifiers, noise-correction and digitization circuits. Since each pixel carries out the conversion, it results in parallel operation which increases the bandwidth for high-speed transfer. CMOS cameras have been reported to be used in several studies as a replacement for CCD cameras [146], [147], [148]. Fukuzawa et. al [149] used a CMOS camera system for high speed distance measurement of moving vehicles. The system achieved a measurement rate of 1000 frames per second at accuracies higher than 99 percent.

PSDs are used in many industrial position sensing applications. These devices can operate at faster speeds with sampling frequencies of up to 10 kHz. They can also produce resolutions of up to 2 μm [150] and require minimum interfacing for operation. A large number of studies have been reported using PSDs for non-contact position measurement applications. Krouglicof [151], used PSDs to develop a real time position and orientation measurement technique for helmets used by fighter pilots. Inoue et al. [152] used three 1-D PSDs in a triangular shape to cover 360 degrees around a micro robot with wheels. These were used to estimate the position and orientation of the robot. The accuracy of the measurement that was directly made on the PSD was within less than 0.4 mm [152]. In another study, a position measurement system comprised three laser line projectors fixed externally to the robot. A PSD camera was used to estimate the position of the robot using the relative position of the lasers. This system is capable of producing accuracies of up to 0.7 mm in a 60 x 60 mm area

[134].

PSDs provide a very simple and efficient method for non-contact position sensing compared to other available methods. The implementation of these sensors require simple electronic circuits. These devices are capable of operating at much higher speeds. During the operation, not much data processing is required to estimate the position and the orientation. Thus, PSD provide a cost effective method to be used in position measurement applications.

The high-speed imaging device is an important part of the visual servoing system. Since the robot is operating at very high speeds of up to 2.5 m/s, the camera must be able to operate at a speed of at least 1 kHz. This chapter considers the development of this high speed camera using a PSD as the image sensor. It will be used in this study for position estimation. In the first step, an electronic circuit was designed and developed for signal conditioning and high speed data acquisition. Then this electronic circuit was tested for its performance. The 2-D PSD was calibrated next, in order to estimate the relationship between the position of IR marker and the estimated x, y values for the position. After this, the PSD was used as the image sensor to construct a camera with a c-mount lens and an IR filter. The lens/sensor assembly was calibrated once again to estimate the intrinsic parameters of the camera system. Next, the camera assembly was mounted on a rigid platform and used to measure the position of the EE. Finally, an interface was developed to carry out data acquisition through an FPGA.

5.2 Position Sensitive Detector

PSDs absorb optical power and convert it into an electrical charge. These work on the principle of lateral-effect present in all semiconductor junctions. When a semiconductor junction absorbs light, there are two voltages that are induced: a transverse voltage and a lateral voltage. The transverse voltage is commonly used to detect light; the lateral voltage is not often exploited. However, it can be used to estimate the position of the light spot. This concept was presented by Schottky [153] and Wallmark [154]. A schematic diagram showing the principle of the lateral effect can be seen in Figure 5.1. The photo effect of these devices will vary depending on the location of the light source on the sensor. The generated photo currents are proportional to the position and intensity of the centroid of light on the active area. The experiments carried out by Schottky and Wallmark demonstrated that a relationship exists between this lateral photo voltage and the position of a focused light spot [155]. Wallmark also suggested that this effect could be used on a two-dimensional device by simply having an additional pair of leads. Usually, lateral-effect photo diodes are used for the photoelectric effect.

The lateral-effect PSD usually consists of n-type silicon substrate with resistive layers separated by a p-n junction. The front side of the device which is exposed to light has ions implanted with a p-type resistive layer. The rear side of the detector has an ion-implanted n-type resistive layer. The electrodes are placed at opposite ends of the p-type resistive layer. A light spot within the spectral range with peak sensitivity of silicon will generate a photo current that flows from the incident point through the resistive layers to the electrodes. The resistivity of the ion-implanted layer is extremely uniform so that the photo current at each electrode is inversely proportional to the distance between the incident spot of light and the electrodes,

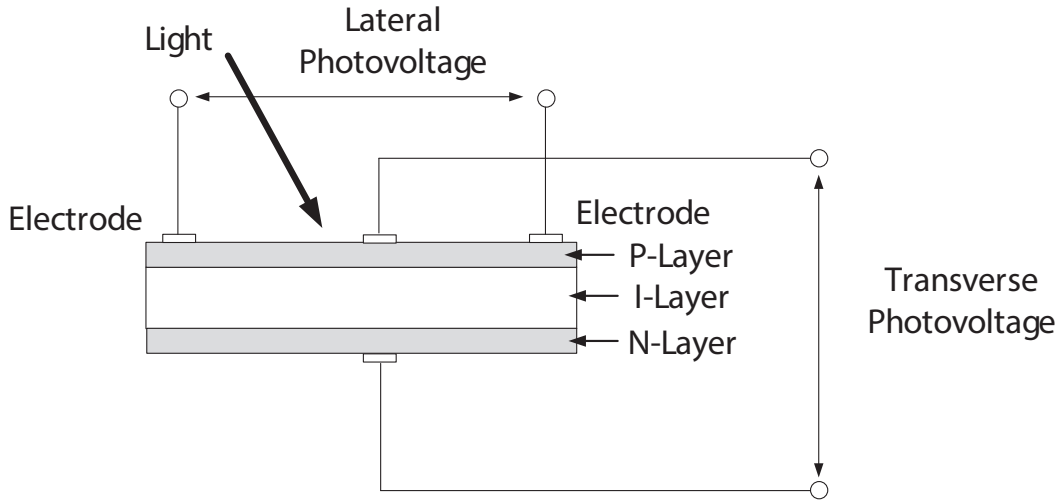

Figure 5.1: A cross section of a 2-D Tetra Lateral PSD

following the principles of a voltage divider. The output of the detector tracks the centroid of the light spot with high resolution and high linearity.

There are three main types of PSDs commonly found in applications. These are namely the duo-lateral, tetra-lateral and pin cushion type PSDs.

5.2.1 Duo-Lateral PSDs

Duo-lateral PSDs have two resistive layers on top and bottom. The front side has a resistive layer with a set of electrodes on the sides. The rear side of PSD has a resistive layer with two contacts on opposite ends as cathodes placed perpendicular to the electrodes on the front side. A schematic diagram of a duo-lateral PSD is shown in Fig. 5.2. The equivalent circuit shows that the position signals are generated by two positioning layers with positioning resistances of R_p. The connection between the layers can be modeled by a current generator (P), an ideal diode (D), a junction capacitance (C_j) and a shunt resistance (R_{sh}). The ion-implanted top and bottom

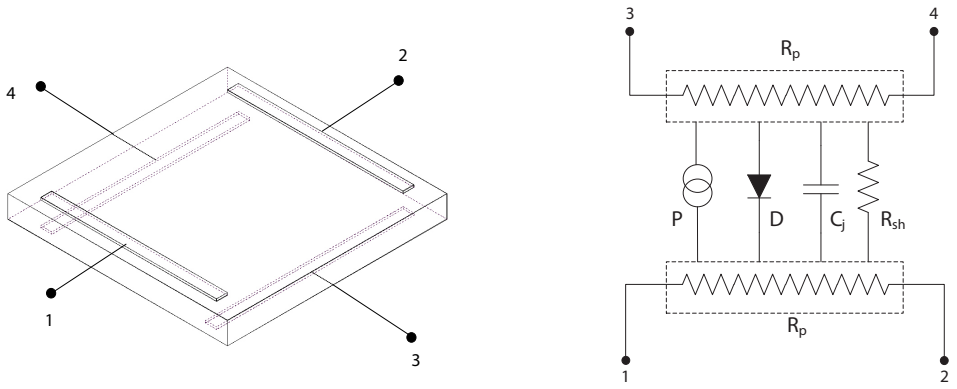

(a) The structure (b) Equivalent Circuit

Figure 5.2: The Duo Lateral PSD

layers are made to be extremely uniform so that it maintains the same resistivity. Since the photo current is divided into only two parts, it increases the resolution and improves the position detection capability compared to other types.

The photo current induced for each pair of electrodes is inversely proportional to the distance between the incident light spot and electrodes providing a superior linear performance over the active area. A reverse bias should be applied to these detectors to achieve optimum current linearity at high light levels. Some of the sensors available in the market provide continuous position sensing accuracies of up to 99 % over 64 % of the sensing area. The complex structure of this PSD makes it more expensive.

5.2.2 Tetra-Lateral PSDs

Tetra-lateral position sensing detectors have a single resistive layer, which consists of an anode and four cathodes for 2-D position sensing. A reverse bias should be applied to these detectors to achieve optimum current linearity with the light signals. A schematic diagram of a tetra-lateral PSD is shown in Fig. 5.3. The tetra-lateral

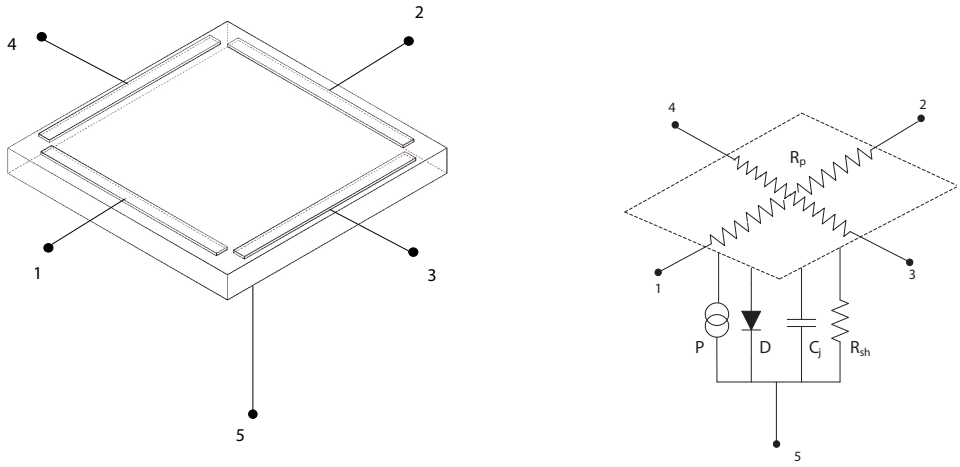

(a) The structure (b) Equivalent circuit

Figure 5.3: The Tetra Lateral PSD

PSD can be modeled by considering a current generator, an ideal diode, junction capacitance and a shunt resistance connected parallel between the front resistive layer and the anode.

Unlike in duo-lateral PSDs, the photo current is divided into four parts by the same resistive layer. This results in a greater distortion in the circumference compared to other types of PSDs. These detectors are ideally suited for applications that require to making measurements over a wide spatial range. They offer a faster response time, low dark current and a high position linearity. Some of the sensors provide linearity over 64 % of the total image sensing area.

5.2.3 Pin Cushion Type PSDs

This is an improved version of the tetra-lateral type. Pin cushion type PSDs have shaped electrodes to increase linearity near the edges. This arrangement greatly reduces distortion in the circumference. A schematic diagram of a pin cushion type

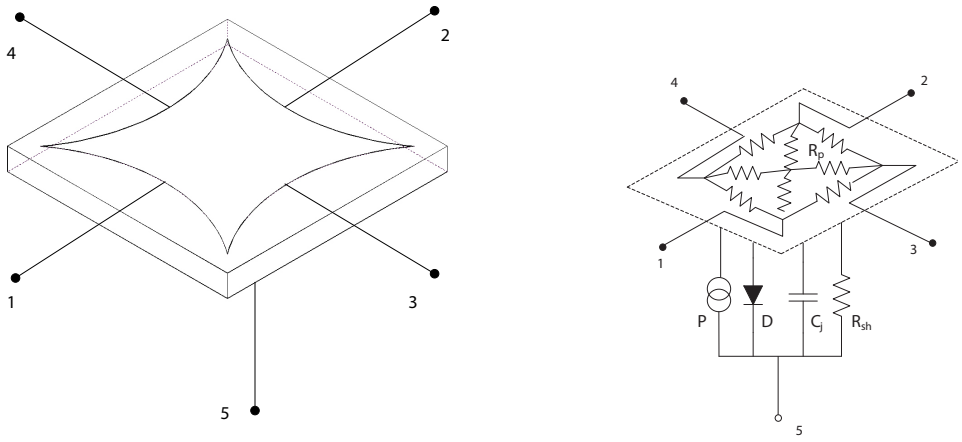

(a) The structure (b) Equivalent circuit

Figure 5.4: The Pin Cushion Type PSD

PSD is shown in Fig. 5.4. In this type of PSD, the positioning resistance of the sensitive surface will be modeled as shown. As with tetra-lateral type PSDs, it also has a smaller induced dark current, fast response time and easy bias application. The main advantage of this type is its superior linear performance over the sensing area.

When the PSD is illuminated by the IR source, a current is induced by the photo-electric effect. Ideally, the PSD should respond to the position of the IR spot and not the intensity. The induced current in the anodes will flow through then such that its magnitude is proportional to the intensity of the source of illumination and the distance between the illuminated point and the four anodes. In order to reduce the sensitivity of the PSD to variations in intensity, the output signals from the anodes should be normalized by the sum of the four currents. Hence, the xy coordinates of the spot of illumination can be calculated using the equation,

$$X_p = \frac{(I_2 + I_3) - (I_1 + I_4)}{I_1 + I_2 + I_3 + I_4} \tag{5.1}$$

$$Y_p = \frac{(I_2 + I_4) - (I_1 + I_3)}{I_1 + I_2 + I_3 + I_4} \tag{5.2}$$

Where I_1,I_2,I_3,I_4 correspond to the induced current in the PSD, and X_p, Y_p are the PSD gains in $-x$,$-y$ directions.

This equation results in dimensionless quantities for both X and Y. These quantities should be related to a physical position in the PSD for position measurement applications. Hence, the PSD should be calibrated to estimate the nonlinear relationship between the currents and the position of the light spot on the image sensor.

5.3 Development of the High Speed Camera System

The PSD is the main part of the camera. It is a non-imaging device which provides position as current signals. Hamamatsu® S5991-01, 2-D PSD was selected for developing the camera. A schematic diagram of this PSD is shown in Fig. 5.5. It has an active area of 9 x 9 mm for spot detection. This is a pin cushion (tetra-lateral) type PSD. It is expected to provide a superior linear performance over the active area and a faster response time for the EE position measurement. It has a cathode and four anodes as electrodes. The anode should be reverse biased with the cathodes and have a voltage of -5 V. The camera will then be mounted on to a camera housing. A c-mount lens which has a nominal focal length of 35 mm is used to focus the IR spot on to the sensor. An IR filter which matches the peak frequency of the IR signal is used to eliminate the noise from sources other than the marker.

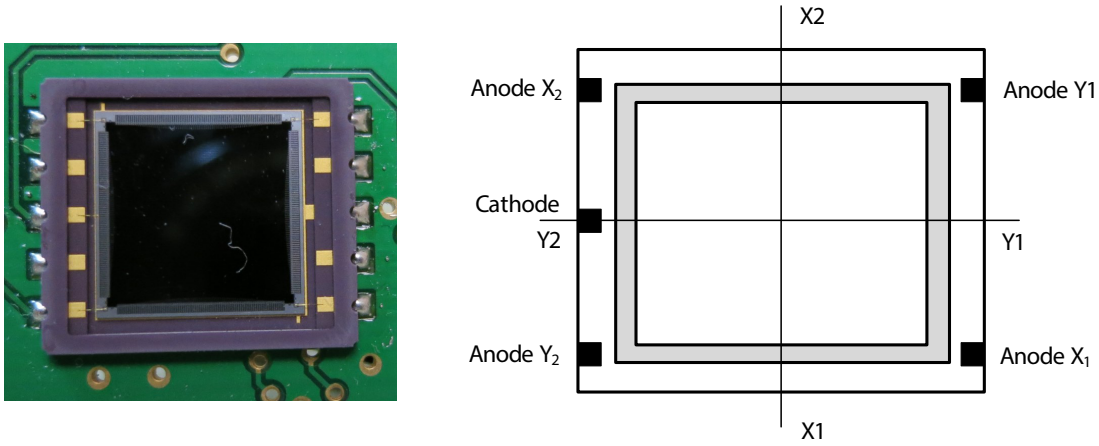

Figure 5.5: Hamamatsu® s5991 2-D PSD

This PSD gives its peak spectral response to light rays with 700-1100 nm in wavelength. Therefore, high power IR light emitting diode (LED) from Vishay (VSMY7850X01) is used as the marker. Fig. 5.6 shows a diagram of this LED. It will be mounted onto the EE of the SCARA arm. This LED emits IR light with a peak wavelength of 850 nm. It uses surface emitter technology with high radiant power and offers high-speed operation with a low rise time. It also allows a continuous direct current flow through the LED up to 1 A, resulting in an intense IR spot. Compared to other IR LEDs, it emits at a wider angle of 120 degrees. This allows the EE to be seen by the camera over a much wider operating envelope.

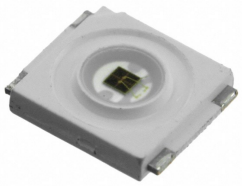

Figure 5.6: Vishay high power Infra Red LED

5.3.1 Design of the Signal Conditioning Circuit for the Camera

This PSD requires the four anodes and the cathode of the PSD to be reverse biased for operation. Therefore, cathode of this PSD will be biased at a voltage of +10 V while the anodes of the PSD will be biased at a voltage of +5 V.

The proposed circuit uses LT1019 precision voltage reference to generate +5 V reference signal. This chip has a highly stable output performance with an accuracy of up to 0.05 % and used to generate the +5 V. An operation amplifier (op amp) stage with a gain of 2 will be used to produce a +10 V voltage. The dual OP295 op amp was selected for this. This is a single supply operational amplifier which features a high DC accuracy and a rail-to-rail output swing. This chip produces a lower output noise in the signal. The op amp and the precision reference will be powered by a regulator supplying +12 V. A schematic diagram of the circuit showing the connections of precision reference and op amp for producing the +5 V and +10 V is shown in Fig. 5.7. The cathode of the PSD will be biased with this +10 V while the anodes of the PSD will be biased with the +5 V.

The circuit that is used to perform the low pass filtering and data acquisition is shown in Fig. 5.8. The current induced in the anodes are very weak signals that requires amplification. In addition, a low pass filter is used to remove noise eliminating the high frequency components from the signal. A 1.5 $M\Omega$ resistor is used to increase the signal amplification. This transforms the weak current signal from the anode to a measurable voltage signal. Using this resistor and a capacitor of 60 pF will introduce an integration time of 90 μs. The operational amplifier circuit is scaled

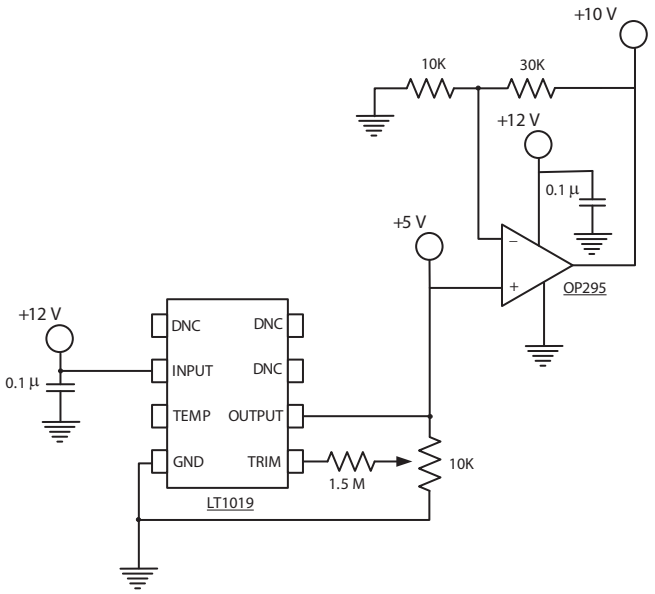

Figure 5.7: The circuit for producing +5 V and +10 V

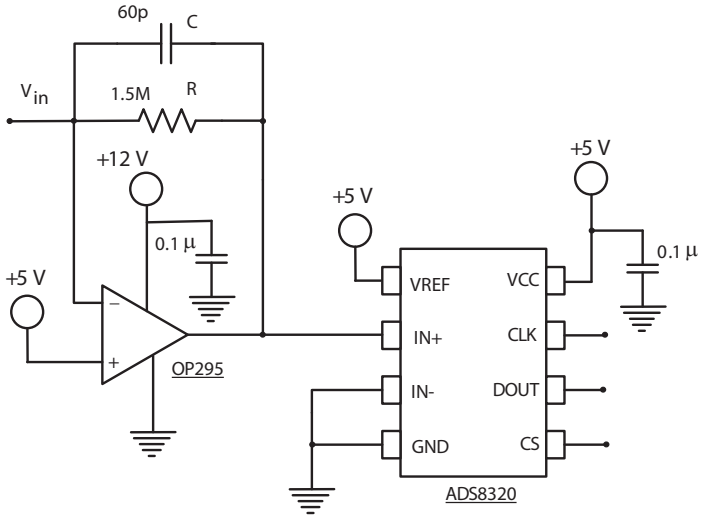

Figure 5.8: The circuit to perform low pass filtering and data acquisition

in such a way that it would induce a voltage signal between 0 V and +5 V depending on the strength of the light spot. The induced voltage signal once the random noise is eliminated is given by:

$$V_f = 5V - i_f . \frac{R}{RCs + 1}, \tag{5.3}$$

where V_f corresponds to the induced voltage of the filtered signal, i_f corresponds to the induced current of the filtered signal, R is the resistance and C is the capacitance across the op amp.

The photo current's analog signals must be converted into digital signals for data acquisition by an FPGA or a microcontroller. Since this camera is used to make position measurements of a highly dynamic system the data acquisition should be fast and accurate. Therefore, a 16-bit analog to digital converter (A/D) (ADS8320) is used for data acquisition. This ADC chip is capable of performing data acquisition at 100 kHz with an accuracy of up to 0.1 mV. A SPI is needed to acquire the data output from this chip.

The total circuit which was designed to use PSD for position measurements is shown in Fig. 5.9. A printed circuit board (PCB) was designed and fabricated with the proposed circuit. A final PCB with the PSD is shown in Fig. 5.10.

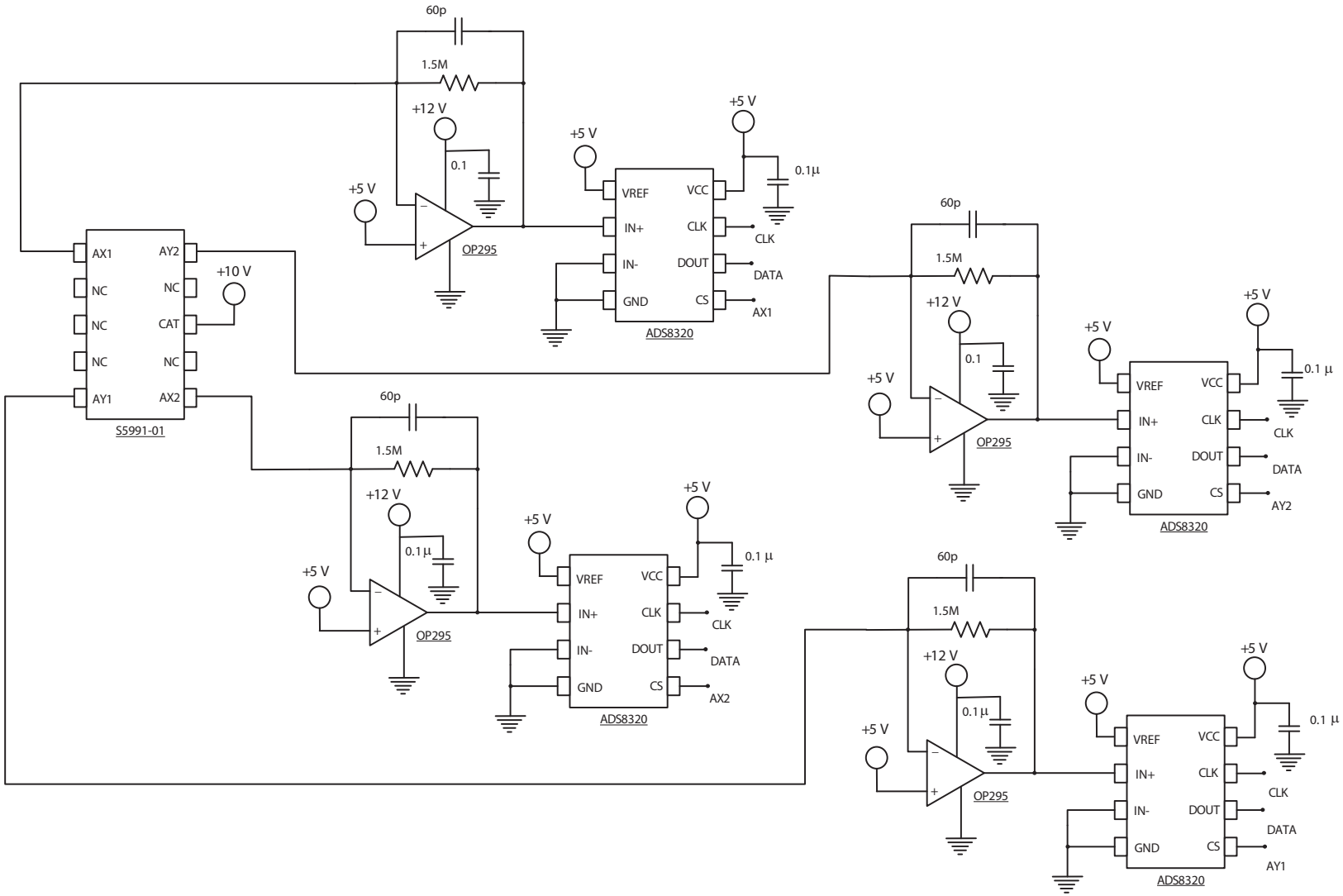

Figure 5.9: The total circuit with the PSD

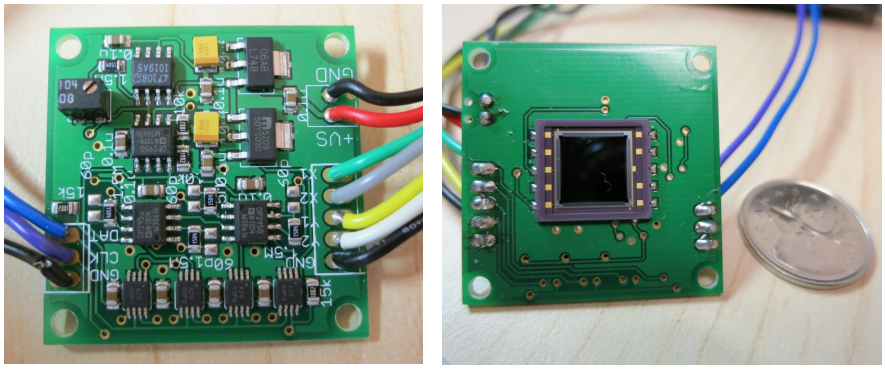

Figure 5.10: A schematic diagram and printed circuit board for PSD signal conditioning

5.3.2 Calibration of the 2-D PSD

A Newport® 406 precision xy translation stage is used for carrying out calibration of the PSD. It consists of a pair of micrometers capable of producing linear translations of up to a 1 μm accuracy in x,y directions. A base plate and a holder assembly is used to mount the LED. The holder consists of a mount and a socket for placing the LED. A laser LED (OPV382) by Optek Technology was used as the source of illumination. This LED emits a wavelength of 860 nm with a narrow beam angle of 6 degrees. A brass aperture which consists of a 100 μm hole is placed on top of the LED. The PCB with the image sensor will be fixed on to a sensor mount which can be screwed into a top plate. The top plate along with the sensor mount is used to cover the setup to prevent light from escaping into it. The sensor mount can be rotated with the image sensor to change the orientation of the PSD. The experimental setup used for the calibration of the 2-D PSD is shown in Fig. 5.11 and Fig. 5.12.

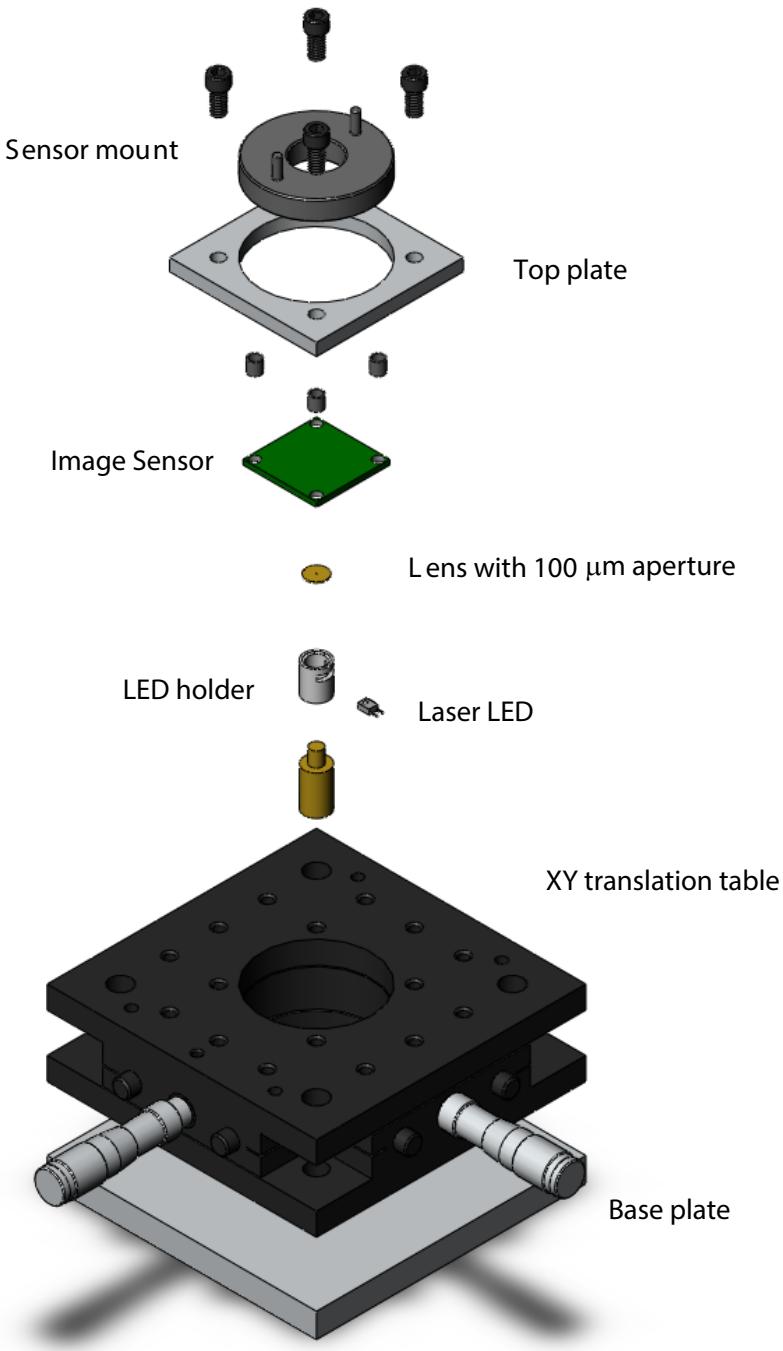

Figure 5.11: The setup used for calibration of the 2-D PSD

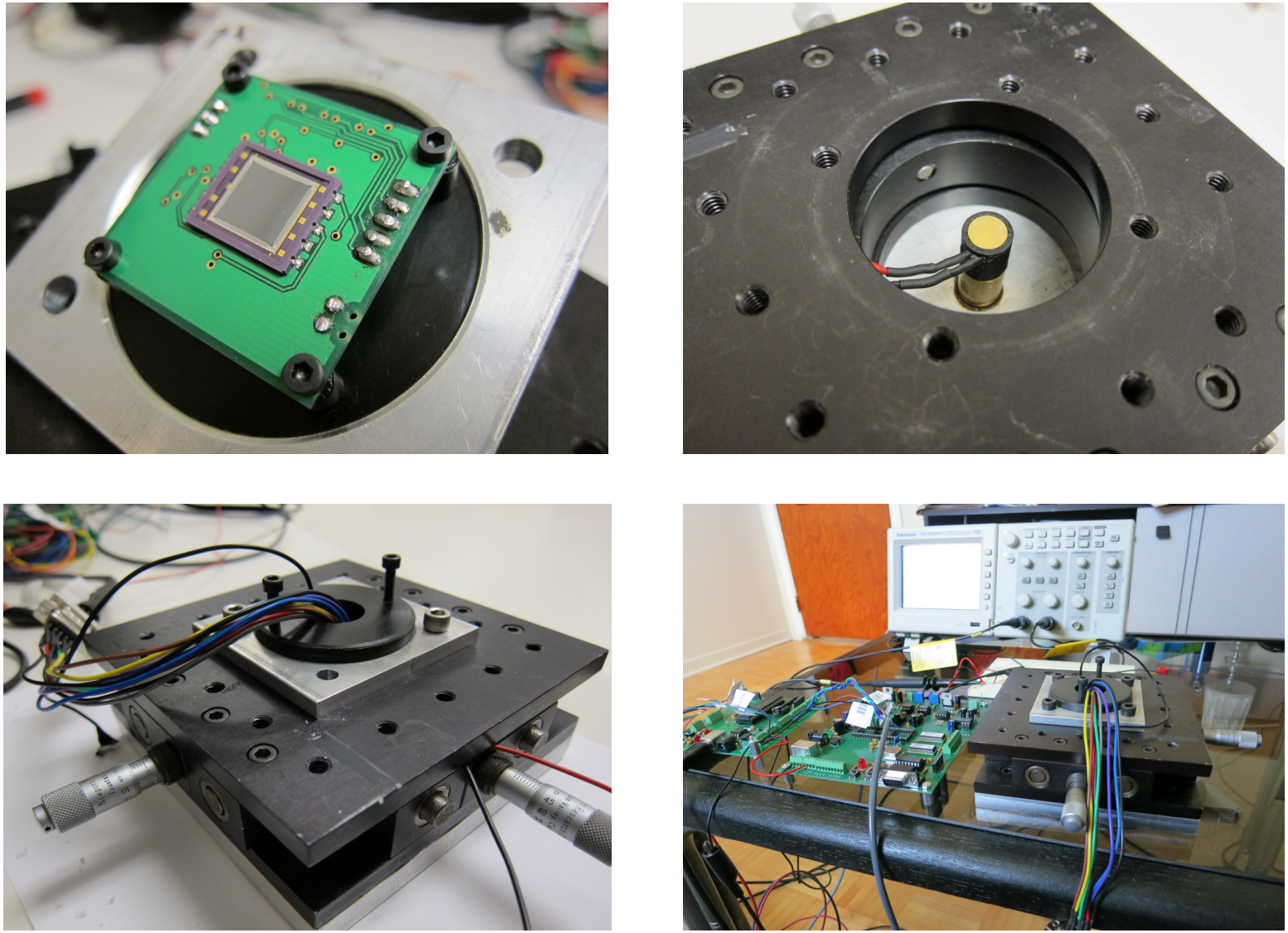

Figure 5.12: Selected photos from the calibration of the 2-D PSD

The sum of the four anode currents indicates the light intensity of the IR spot. This needs to be a uniform value in order to improve the accuracy of the results. Hence, a PID controller was used to maintain the intensity of the LED at a constant value. A schematic diagram of the PID controller is shown in Fig. 5.13. This controller was implemented using a PIC18F4550 microcontroller with a MAX541 DAC converter. The sum of the four currents provided the feedback, while the control signal provided via the DAC indicated voltage level to drive the LED to maintain a constant IR spot. A user interface was developed using the MATLAB Guide software to display the four currents in real time along with the mean and standard deviation. This user interface is shown in Fig. 5.14. This interface communicated with the PIC18F4550 via the USB through an emulated RS232 connection. This interface also provided an option for data acquisition during the calibration process.

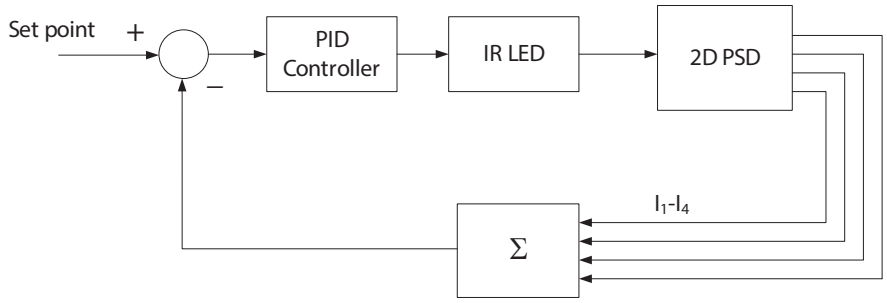

Figure 5.13: A schematic diagram of the LED intensity controller

The first step in the calibration process was to align the axes of the PSD with the axes of the translation stage by rotating it. Once this was completed, a set of 8 x 9 points covering the total 9 mm x 9 mm span of the PSD was obtained for analysis. The calibration results of the PSD are shown in Fig. 5.15. Surface plots that show the variation of X,Y with psdX and psdY for the experimental results are shown in

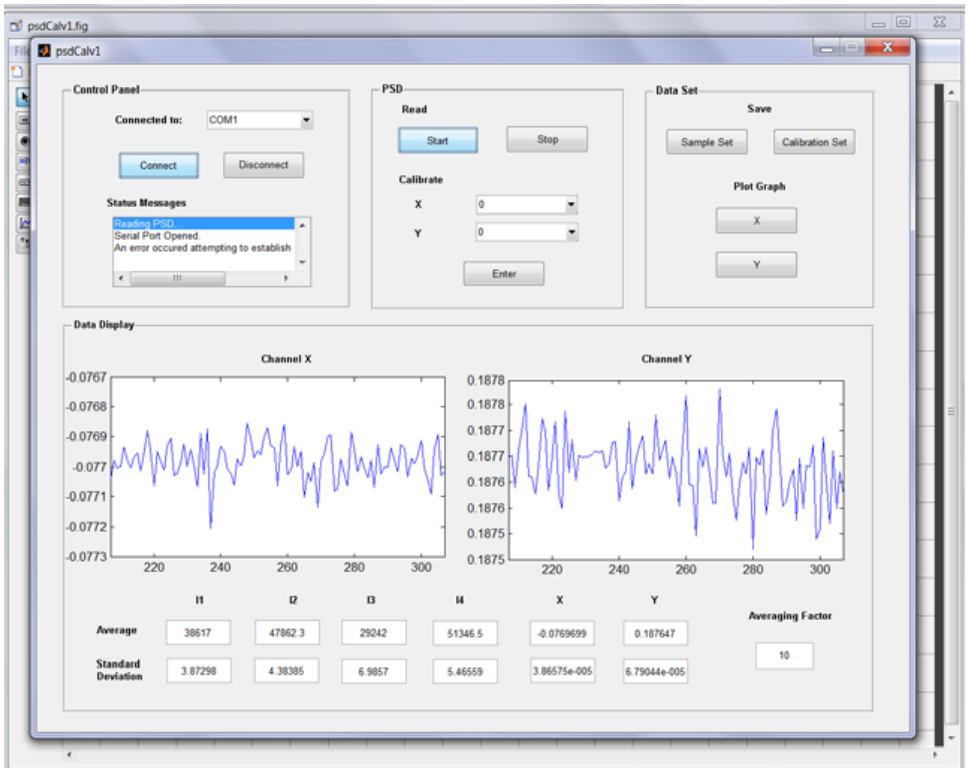

Figure 5.14: A user interface developed for data acquisition

Fig. 5.16 and Fig. 5.17.

The response surface methodology (RSM) in Design of Experiments(DOE) based method was used to analyze the data and obtain the results from the calibration data [156]. DOE techniques enable designers to determine the interaction between the individual and interactive effects of multiple factors which would affect the final output results in a given design. The RSM uses mathematical and statistical techniques to develop a functional relationship between a response variable and a number of input variables or factors. The actual position provided by the micrometer gauges is considered the response, and the x,y positions estimated using the PSD equations in 5.1 and 5.2 are considered as factors. The calibration data was analyzed using the RSM - IV optimal design method [156]. This technique will provide a best fit model for the

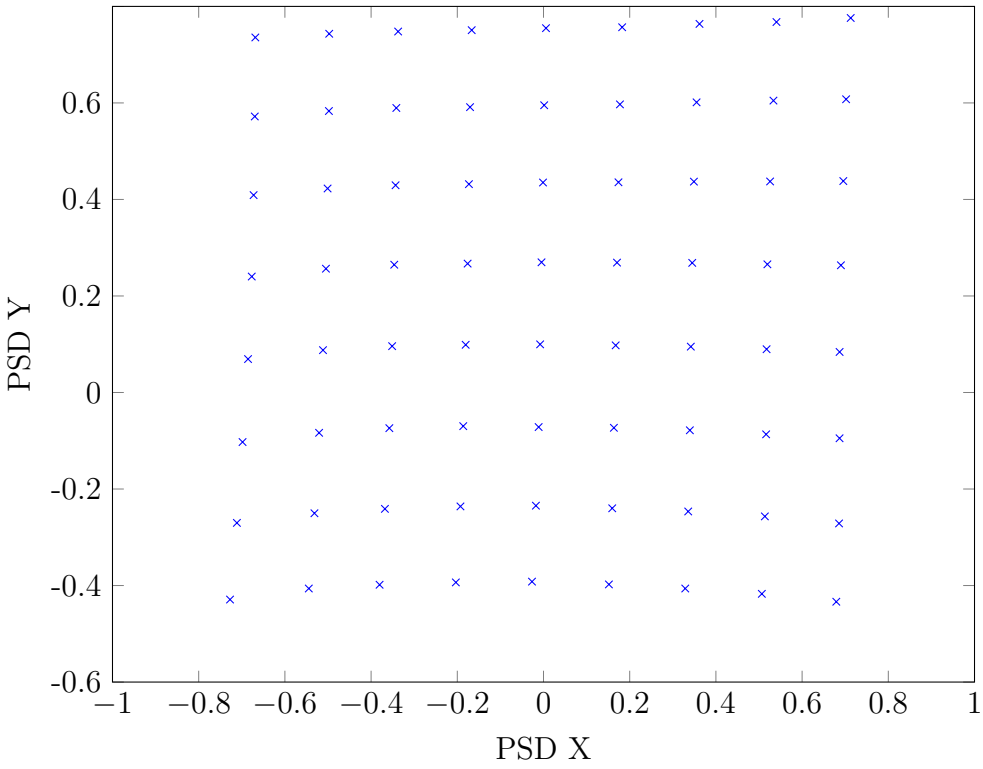

Figure 5.15: x vs y positions obtained using the anode currents for the experimental results

experiments carried out.

The StatEase® (Version 8) software was used as a tool for analyzing the experimental data. The suggested points comprise linear to sixth order models. The best model is determined based on several statistical parameters. In statistics, the $p - value$ provides the probability of obtaining a test statistic at least as extreme as the one that was actually observed. The $F - value$ is used when comparing statistical models that have been fitted to a data set, in order to identify the model that best fits the population. The coefficient of determination (R^2) is used to indicate how well data points fit a statistical model.The best model from the study should produce a lower p, higher F and reasonably agreeing adjusted and predicted R^2 that are high in magnitude with a lower standard deviation. The variation of x,y from the analysis provided a sixth order model for X and a sixth order model for Y. The sixth order models for X and Y that were obtained from the calibration are as follows:

$$\begin{aligned} X = & -0.029208 - 5.72614.X_p + 0.11152.Y_p - 0.064731.X_p.Y_p - 0.03531.X_p^2 \\ & - 0.029152.Y_p^2 + 0.31523.X_p^2.Y_p + 0.44659.X_p.Y_p^2 - 0.70989.X_p^3 + 0.046984.Y_p^3 \\ & - 0.030985.X_p^2.Y_p^2 - 0.33308.X_p^3.Y_p + 0.00571.X_p.Y_p^3 + 2.0147.X_p^4 - 0.10882.Y_p^4 \\ & - 0.016453.X_p^3.Y_p^2 - 0.095985.X_p^2.Y_p^3 - 0.42426.X_p^4.Y_p - 0.41511.X_p.Y_p^4 \\ & + 0.96796.X_p^5 + 0.2577.Y_p^5 + 0.32129.X_p^3.Y_p^3 + 0.22198.X_p^4.Y_p^2 - 0.095201.X_p^2.Y_p^4 \\ & + 0.58163.X_p^5.Y_p - 0.049314.X_p.Y_p^5 - 3.59314.X_p^6 + 0.087.Y_p^6 \end{aligned} \tag{5.4}$$

$$
\begin{aligned}
Y = &- 0.41116 - 0.0009854.X_p + 5.90666.Y_p - 0.22986.X_p.Y_p + 0.16429.X_p^2 + 0.3583.Y_p^2 \\
&- 0.37884.X_p^2.Y_p - 0.088692.X_p.Y_p^2 - 0.10510.X_p^3 + 0.72077.Y_p^3 - 0.059941.X_p^2.Y_p^2 \\
&+ 0.018451.X_p^3.Y_p + 0.094316.X_p.Y_p^3 + 0.17215.X_p^4 - 0.73212.Y_p^4 + 0.23018.X_p^3.Y_p^2 \\
&- 0.15670.X_p^2.Y_p^3 + 0.017811.X_p^4.Y_p + 0.13505.X_p.Y_p^4 - 0.17281.X_p^5 - 0.43507.Y_p^5
\end{aligned}
\tag{5.5}
$$

Where X,Y are the actual position of the IR spot on the PSD.

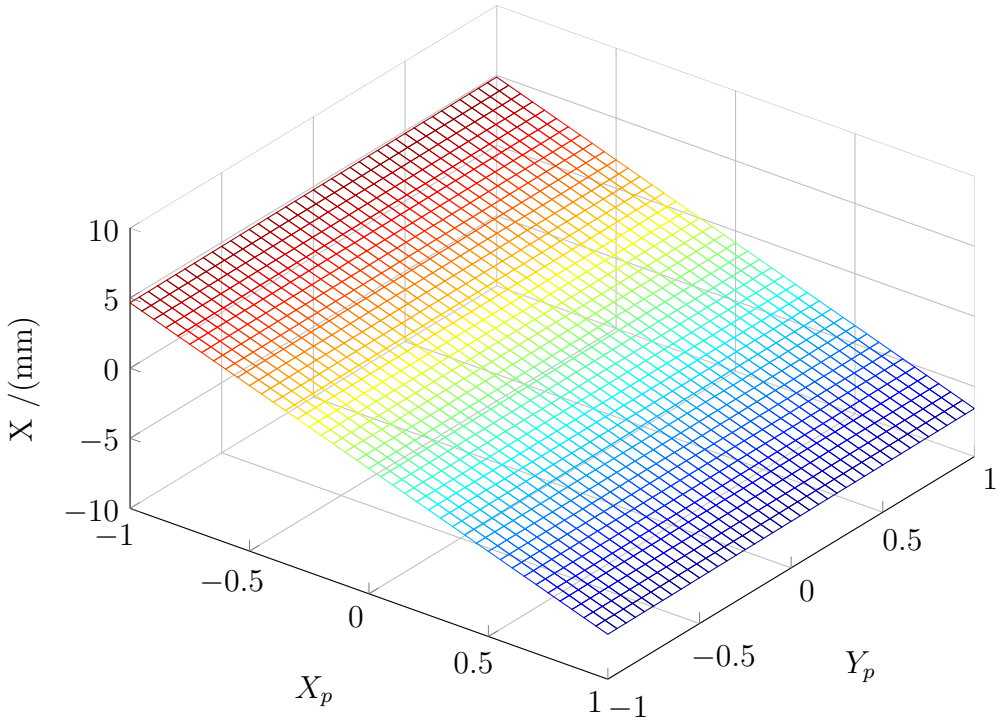

Figure 5.16: The variation between X vs X_p and Y_p

The proposed models should be used to correct the position obtained by the four currents. It will eliminate the non linearites due to the pin cushion effect. The corrected position is obtained using the equations 5.1, 5.2, 5.4, 5.5 and the measured

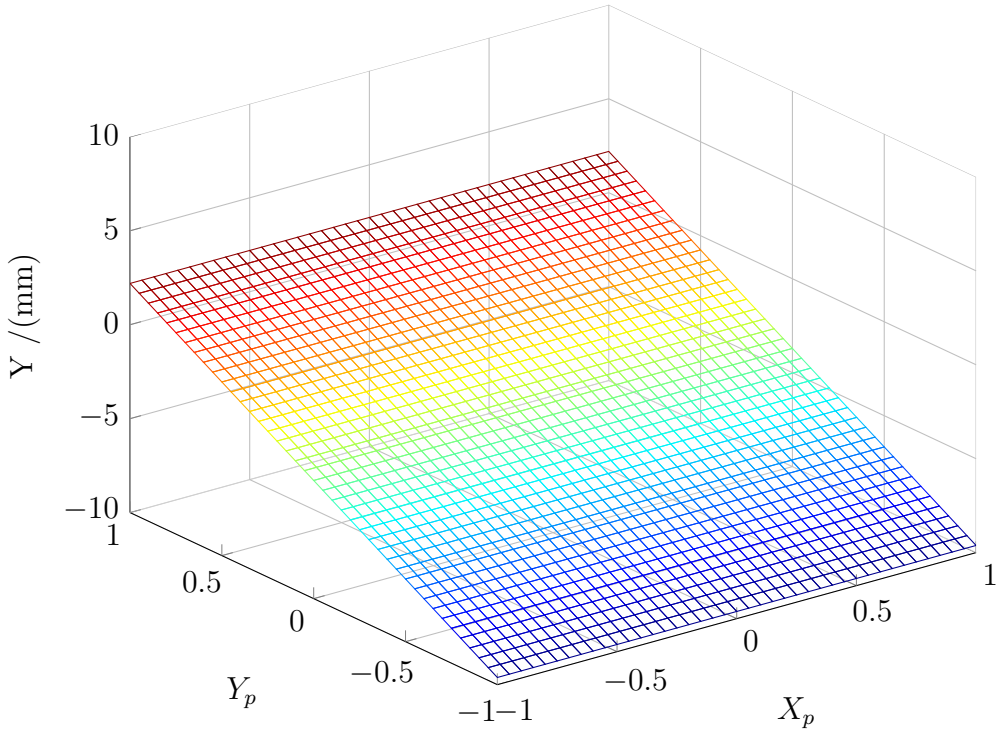

Figure 5.17: The variation between Y vs X_p and Y_p

positions are shown in Fig. 5.18. The reconstructed model shows that the experiment produces an accurate model for estimating the actual position of the IR spot on the image sensor using the induced currents.

Implementation of a sixth order function introduces delay and complexity for a real time controller. Hence, more simpler third order model for X,Y was used during the actual controller implementation.

5.3.3 Design of the Camera

The camera consists of a PCB with the PSD and electronic circuitry, a lens and a filter. A c-mount lens with a nominal focal length of 35 mm is used to focus the light onto the PSD. This lens offers a field of view covering an area of 200 mm x 200 mm at

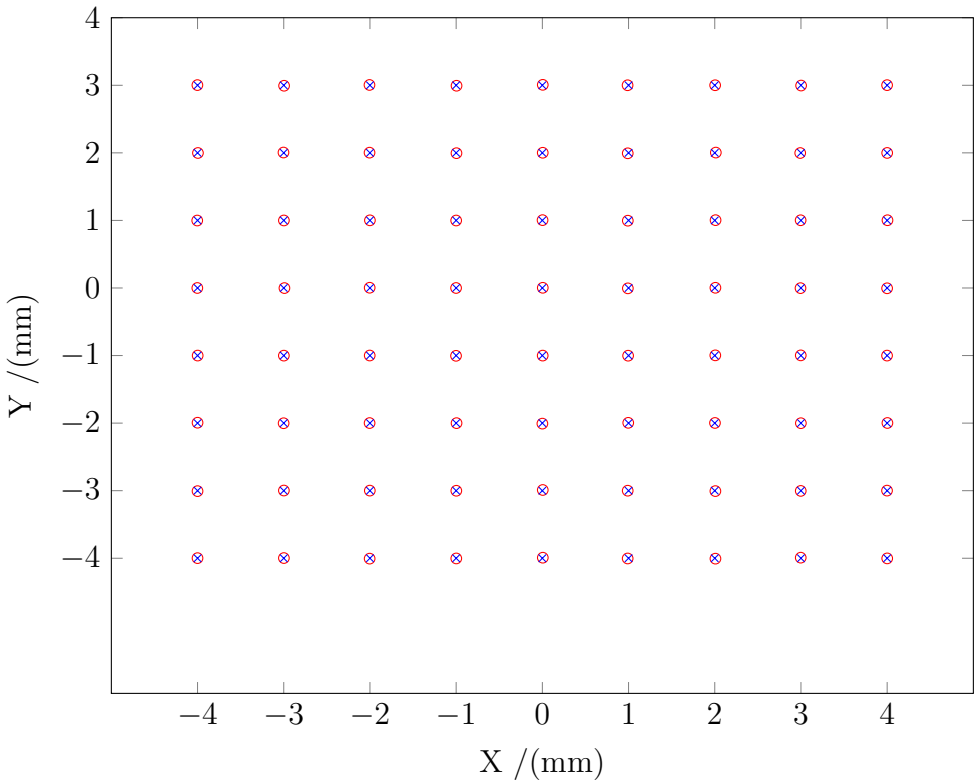

Figure 5.18: The corrected position of IR spot obtained using the four currents

a distance between 800 mm and 950 mm. The aperture of the lens is kept in fully open position during the operation in order to allow the maximum amount of light onto the sensor. An IR filter with a band-pass frequency of 850 nm is used in front of the lens to reduce background illumination and noise other than from the marker. These components are mounted onto a housing made out of ABS plastic. This housing uses a DB9 connector for data acquisition and power. The camera is powered by a 15 V supply. A schematic diagram of the camera design is shown in Fig. 5.19. The final camera once it is fabricated is shown in Fig. 5.20.

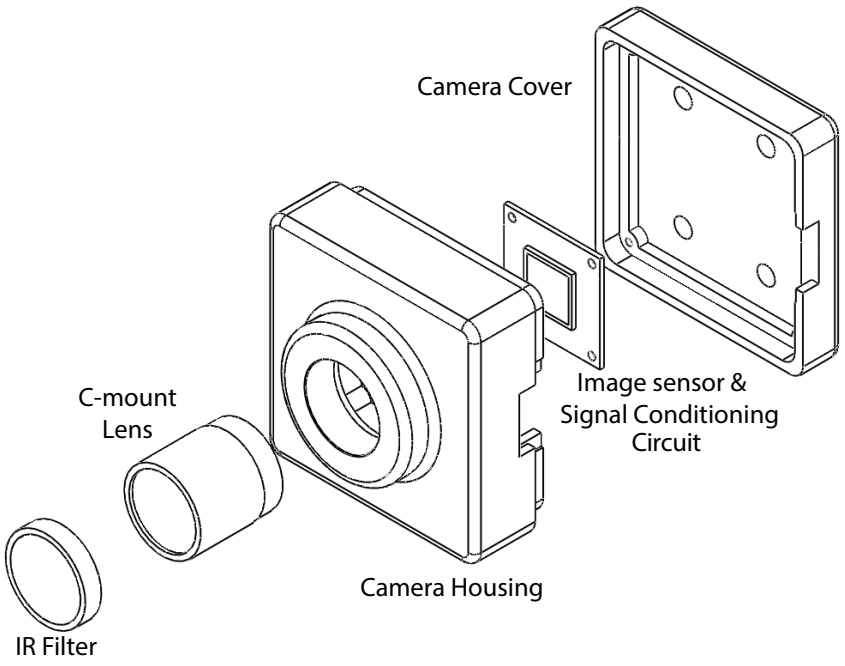

Figure 5.19: An exploded view of the proposed camera

The camera needs to be calibrated before it is able to be used for making measurements. The calibration process relates the point of projection on the image sensor

to the position of the target considering the intrinsic and extrinsic parameters of the camera system. A rigorous calibration process will result in accurate and repeatable results. There has to be more emphasis on the calibration process since the camera is to be used for position measurement as compared with the study by Wang et. al [119].

The calibration process of a camera with a PSD as the image sensor is different from that of a conventional camera. It consists of three stages. In the first calibration stage, the image sensor has to be calibrated. This is to obtain a model of the relationship between the currents and the position of an IR spot on the PSD. This is necessary to account for the non-linearities from the pin cushion effect. In the next stage, the complete camera unit has to be calibrated using a camera calibration setup at Memorial University. This is used to obtain the intrinsic parameters of the camera unit. In the final stage, an on-site calibration is carried out to estimate the extrinsic parameters of the camera once it is mounted near the robot EE.

5.3.4 Calibration of the Camera Unit

The intrinsic parameters of the camera has to be estimated if this unit is used for position measurement. In the field of machine vision, camera calibration refers to the experimental determination of a set of parameters that describe the image formation process for a given analytical model of the machine vision system [117]. In order to achieve high accuracy and robustness of the measurements, the intrinsic parameters of the camera need to be estimated with precision. These intrinsic parameters include effective focal length, image center, radial and tangential distortion parameters and the scale factor. These parameters can be estimated only by a rigorous camera

Figure 5.20: The final camera once fabricated

calibration process. There are several methods proposed in the literature that can be used for calibrating a PSD camera. The methods proposed by Heikkila [118] and Rahman and Krouglicof [117] were used for calibrating this PSD camera.

Heikkila's method considers an array of markers as the calibration target. There are three main steps in this procedure. In the first step, an initial estimate for both intrinsic and extrinsic parameters are obtained. Next, an iterative search method is employed by minimizing the weighted sum of squared differences between the observations and the model to estimate the parameters of the forward camera model. In the third step using a backward projection model, the radial and tangential distortion parameters are obtained. The method proposed by Rahman and Krouglicof minimizes the error between the reconstructed image points and their experimentally determined counterparts in a distortion-free space. In addition to this, unit quaternions are used

for expressing spatial orientation and an analytically derived Jacobian matrix in the numerical solution. According to Rahman and Krouglicof [117], latter method produces accurate and robust results over a wide range of values for lens distortion.

Precision is an important factor if the camera is used for metrological applications [118]. Therefore, this camera is mounted onto a camera calibration setup. The setup comprises a precision XY table with two stepper-motor-driven ball-screw assemblies. This table is capable of producing a translational resolution of up to 0.0005 in. It also provides backlash compensation during its movement. A high power IR LED was used as the calibration target. This provides a point during the calibration. The target LED was displaced every 5 mm, through a predefined square grid of 150 mm x 150 mm. The camera acquired the current values at each of the nodes. Three parallel planes that are 12.7 mm apart were considered and data were collected. This resulted in a total of 2700 calibration points. The calibration setup for the camera is shown in Fig. 5.21.

Once the calibration data was obtained, it was analyzed using the algorithms proposed in Heikkila [118] and Rahman [117]. A summary of the results of a selected calibration run is tabulated in Table 5.1.

Table 5.1: The summary of calibration results

Calibration	Parameter								
Method	SF	f	u_0	v_0	k_1	k_2	p_1	p_2	ϵ
Heikkila	0.9972	34.70	1.60	-0.92	-2.6	0	5	-5.4	9.2
Rahman	1.0403	35.92	2.87	-0.93	-3.2	0	2	-9.9	8.2

SF corresponds to the scale factor; f is the focal length, k_1, k_2 are the coefficients

Figure 5.21: A schematic diagram of the onsite calibration setup

of radial distortions in units of $10^{-3}mm^{-2}$ and mm^{-4}; p_1, p_2 are the coefficients of tangential distortions in $10^{-4}mm^{-1}$ and $10^{-3}mm^{-1}$ units; and (u_0,v_0) are the coordinates of actual position of the image center in mm, ϵ is the standard deviation of error of the reconstructed model.

The reliability of the calibration depends on the repeatability of the results. The discrepancy between the original calibration data and the reconstructed model is indicative of how well the calibrated model fits the calibration data. This is known as the standard error of the calibration model. The standard deviation of the error of the reconstructed model is higher in Heikkila (9.2 μm) compared to Rahman and Krouglicof (8.2 μm). Therefore, the estimated camera parameters from the method proposed in Rahman and Krouglicof [117] were selected for developing the camera model. Multiple calibration runs proved that these calibration results are repeatable.

5.4 On-site Calibration of the Camera

The position and the orientation with respect to a world coordinate frame has to be known for this camera to be used for position measurements. These parameters of the camera can be obtained by using a closed form solution. However, for accurate estimation of the position of the EE, parameters related to the robotic system should also be known with a degree of accuracy. The joint angles of the robot are provided by joint encoders. These measure the joint angles with high accuracy and reliability. However, the link lengths that are obtained through direct measurements may have uncertainties. Therefore, an on-site calibration methodology is proposed in this section to estimate these parameters of the system. This on-site calibration system is based on an iterative procedure to minimize the error between the actual position

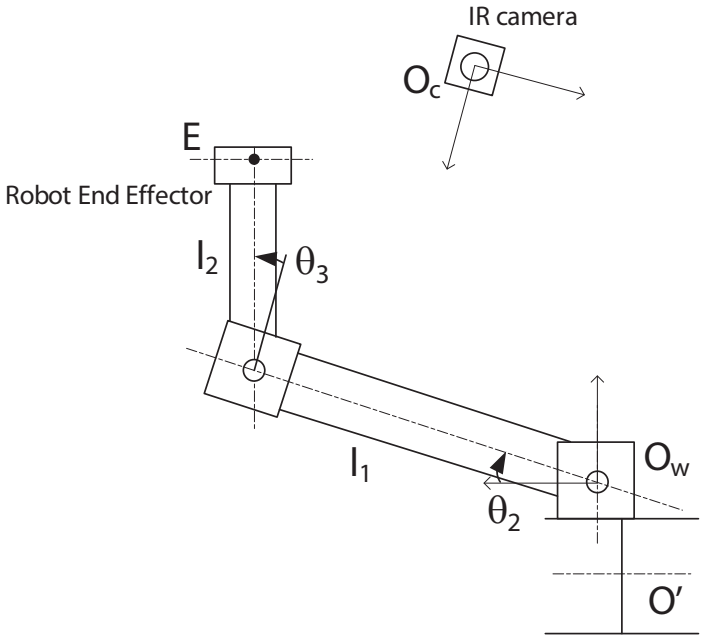

Figure 5.22: A schematic diagram of the onsite calibration setup

obtained by using the encoders and the position obtained using a forward camera model. Due to the nonlinear nature of the problem, an iterative method is used to obtain the required parameters. The on-site calibration offers improved accuracy and efficiency providing the required parameters for an accurate transformation of the measurements made by the camera to a global fixed coordinate system. A schematic diagram of the on-site calibration setup is shown in Fig. 5.22. In the given figure, O_w represents the world coordinate system and O_c the camera′s coordinate system. The current problem considers the EE position E of the SCARA manipulator. An expression for the position of the EE with respect to the global coordinate can be obtained using simple geometry. Joint angles obtained by encoders can be used to estimate the EE position. If the position of the EE w.r.t. to the fixed coordinates is

denoted by ${}^{w}\mathbf{P}$, it could be expressed by:

$$ {}^{w}\mathbf{P} = \begin{bmatrix} l_2.cos(\theta_2) + l_3.cos(\frac{\pi}{2} + \theta_2 + \theta_3) \\ l_2.sin(\theta_2) + l_3.sin(\frac{\pi}{2} + \theta_2 + \theta_3) \\ 0 \\ 0 \end{bmatrix} \tag{5.6} $$

Where θ_2 and θ_3 are the joint angles obtained using the encoders in joints 1 and 2, and l_2, l_3 are the link lengths.

According to the Euler's theorem, the most general displacement of a rigid body with a fixed point in space can be represented using a single rotation of the body about an axis through that fixed point [157]. Therefore, to represent the pure rotation of a body in 3D, three independent rotations about three independent axes should be considered. When these rotations are expressed with respect to the cartesian xyz coordinate system, they are defined in terms of Euler angles. These angles refer to roll (rotation about x), pitch (rotation about y) and yaw (rotation about z). These angles will be used to define the rotation of the camera with respect to the world coordinate frame. The successive rotations around x,y,z axes are given by R_x, R_y and R_z. The rotation of the camera with respect to a world coordinate frame is given by the 3 x 3 Ortho-normal rotation matrix ${}^{c}\mathbf{R}_{w}$:

$$ {}^{c}\mathbf{R}_{w} = R_z.R_y.R_x \tag{5.7} $$

$$ {}^{c}\mathbf{R}_{w} = \begin{bmatrix} cos\theta & -sin\theta & 0 \\ sin\theta & cos\theta & 0 \\ 0 & 0 & 1 \end{bmatrix} \cdot \begin{bmatrix} cos\phi & 0 & sin\phi \\ 0 & 1 & 0 \\ -sin\phi & 0 & cos\phi \end{bmatrix} \cdot \begin{bmatrix} 1 & 0 & 0 \\ 0 & cos\psi & -sin\psi \\ 0 & sin\psi & cos\psi \end{bmatrix} \tag{5.8} $$

The transformation from the world coordinate frame to camera's coordinate frame can be performed by considering a 4 x 4 homogeneous transformation matrix (${}^{c}\mathbf{T}_{w}$) and a camera matrix ($\mathbf{K}_{C}$) to perform the perspective transformation. This is also known as the forward camera model. The estimated position of the EE with respect to the camera (${}^{c}\hat{\mathbf{P}}$) using the encoder data will be given by:

$$ {}^{c}\hat{\mathbf{P}} = K_{C} \times {}^{c}\mathbf{T}_{w} \times {}^{w}\mathbf{P} \tag{5.9} $$

The camera matrix K_{C} is given by:

$$ K_{C} = \begin{bmatrix} sf & 0 & u_{0} & 0 \\ 0 & f & v_{0} & 0 \\ 0 & 0 & 1 & 0 \end{bmatrix} \tag{5.10} $$

Where f is the effective focal length, s is the aspect ratio and (u_{0}, v_{0}) is the position of the image center.

The transformation matrix ${}^{c}\mathbf{T}_{w}$ can be decomposed as:

$$ {}^{c}\mathbf{T}_{w} = \begin{bmatrix} {}^{c}\mathbf{R}_{w} & {}^{c}\mathbf{t}_{w} \\ 0 & 1 \end{bmatrix} \tag{5.11} $$

Where ${}^{c}\mathbf{R}_{w}$ gives the rotation matrix of the camera w.r.t. world coordinate frame and ${}^{c}\mathbf{t}_{w} = [t_x, t_y, t_z]^T$ describes the translation between the camera and the world coordinate frame.

The parameters s, f, u_0, v_0 are the intrinsic parameters and the parameters l_1, l_2, ϕ, ψ, θ, t_x, t_y, t_z are the extrinsic parameters of this model.

Due to the nonlinear nature of the forward camera model, there are no direct estimators of the parameters so that it would produce an optimal solution in a least square sense [118]. Therefore, an iterative search technique minimizing the weighted sum of squared differences between the observations and the model is used. A cost function is formulated to minimize error between the EE position estimated using equation 5.9 and the actual position measured by this camera. If $\mathbf{C}$ is the total cost, it will be given by:

$$\mathbf{C} = argmin \sqrt{\sum_{\forall i} ({}^{c}\hat{P}_i - {}^{c}P_i)^2} \tag{5.12}$$

A schematic diagram showing the proposed optimization problem can be seen in Fig. 5.23. The Levenberg Marquardt (LM) algorithm [158] is employed to solve the optimization problem and obtain the parameters which minimize the given objective function. If the initial values are efficiently selected, only a few iterations will be needed to arrive at the optimum solution. The intrinsic parameters were obtained during the previous calibration. However, if the root mean square error (RMSE) returns a higher value some of the intrinsic parameters need to be re-estimated considering the values from the previous calibration stage as the initial values so that the

RMSE returns a lower value.

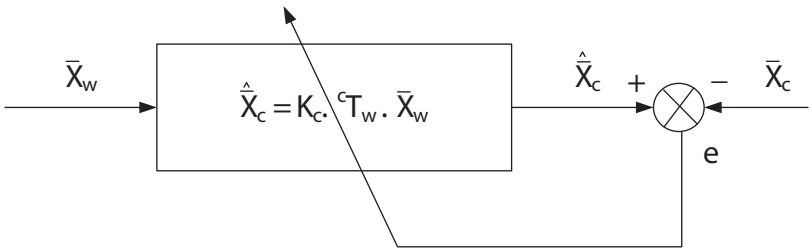

Figure 5.23: A schematic diagram of the on-site calibration setup

The proposed algorithm was validated by conducting an on-site calibration with the proposed visual servoing system. The details of these experiments and a discussion of results are presented under Section 7.3.1.

Chapter 6

FPGA Based Embedded Controller for a High Speed Visual Servoing System

6.1 Introduction

Motion control systems play a major role in the control of different types of industrial automation devices [159]. For most robotic applications, a controller which is compact sized and easily reconfigurable is preferred. In recent years, FPGAs are preferred to ASICs in industrial control applications. The rapid progress of very large scale integration (VLSI) technology and electronic design automation techniques in recent years has created an opportunity for the development of complex and compact high-performance controllers for industrial electronic systems [160], [12]. System-on-a-Programmable-Chip (SoPC) architectures have been increasingly used for robotic applications. These architectures integrate the tasks of different chips onto one chip which produce a more compact version of a control chip [161]. The fact that a virtual

processor can be configured together with the hardware design provides these designs with a much greater flexibility. This allows the powerful features of hardware designs to be integrated with complex software algorithms. Motion controllers that use the features of both hardware and virtual processor technology are still at a novel stage.

Most applications that require high-performance on board processing and reconfigurable electrical hardware to carry out different missions can use FPGAs [162]. FPGAs are capable of performing a range of operations, such as signal acquisition, signal conversion and data communication along with the implementation of control laws. Their ability to perform parallel computations is useful in handling large computational loads [163]. The advantages of FPGAs include low cost, confidentiality of a specific architecture, limited power consumption, low heat production reliability and improved control performance [12]. Execution time of algorithms can be dramatically reduced by designing dedicated parallel architectures, allowing FPGA-based controllers to reach the level of performance of their analog counterparts without the same drawbacks [12]. In recent years, FPGAs have been used in a wide variety of areas including image processing ([164]), machine vision ([165], [166], [167]), telecommunication systems ([165],[166]), digital signal processing ([168]), video decoding ([169]), medical applications ([170]), space applications ([171]), traffic control applications ([172]), multimedia applications ([173]), remote sensing and mapping ([174]), 3D map development for autonomous navigation ([175]) and robotics ([176], [177]).

Since the FPGAs implement functions using low level hardware, they are capable of providing considerable bandwidth and speed to the controllers. A closed loop current controller proposed by Zhou et al. [178] consisted of two loops that could reach sample frequencies of up to 40 kHz with a bandwidth reaching up to 5 kHz.

In another study, Jezernik and Rodic [179] implemented a discrete-event controller in digital logic which had a very high rate of execution. When compared to conventional second-order controllers implemented with traditional amplifiers, the design proposed in this study resulted in increased performance, better efficiency and improved load estimation since the logic operations are executed simultaneously.

There have been a number of studies in recent years using FPGAs for control system applications. These include a number of control system applications. A control of a permanent magnet alternating current servo motor using FPGA technology was proposed by Tzou and Kuo [180]. Programmable logic arrays were used for the position, velocity, torque and current control of the servo motor. Li et al. [181] implemented a fuzzy logic controller for wall-following, corner control, garage-parking and parallel-parking using an FPGA chip for an autonomous car-like mobile robot. Zuhang et al. [182] demonstrated the implementation of a pulsed neural network with a non linear look up table using an FPGA. It used no multipliers in order to improve the compactness of the hardware circuits. The performance of this system was demonstrated for estimating friction in a precision linear stage.

Chan et al. [183] proposed a novel distributed-arithmetic (DA) based proportional-integral-derivative (PID) controller algorithm. It used an FPGA design to accommodate more logic elements and arithmetic functions. It was also designed to reduce power consumption. This controller was demonstrated to have 80 % savings in hardware utilization and 40 % savings in power consumption compared to a multiplier-based scheme. In another study, Chakravarthy et al. [162] developed a PID based control system to drive miniature DC motors using FPGAs. This system comprises a hardware module for counting encoder pulses to estimate the angular position of

the motor, and a hardware module for producing the pulse width modulation (PWM) signal to drive the motor inside the FPGA. The software was developed to implement the PID control algorithm using a hardware module and an on-chip processor.

6.2 Structure of the Proposed Controller

The proposed high speed, PBVS system integrates a 2-D PSD-based optical position sensing system as the exteroceptive sensor, and high resolution joint encoders as proprioceptive sensors. A single chip solution based on reconfigurable hardware was adopted for implementing the complete controller architecture including the interfaces for the sensor suite as well as the computational elements associated with the kinematics and control laws. The entire robot controller was implemented exclusively in a Cyclone III FPGA. A virtual processor was synthesized and implemented in the same FPGA to handle the computationally intensive elements of the controller. The high speed SCARA arm with the visual servoing system is shown in Fig. 6.1.

FPGAs allow hardware based implementation of various input/output (IO) functions. The input interfacing consists of encoder signals and the input channels of the camera. The output interfacing comprises controller signals to the DAC. A NIOS II virtual processor system was configured with a timer, an on-chip memory, JTAG UART, system identification and input/output pins.

Input interfacing of the controller consists of feedback from encoders and a high speed camera. The feedback from joint encoders consists of two pulse trains. Quadrature decoding is implemented in hardware to calculate the joint angles and obtain the direction of rotation. The high speed camera provides the position measurement using

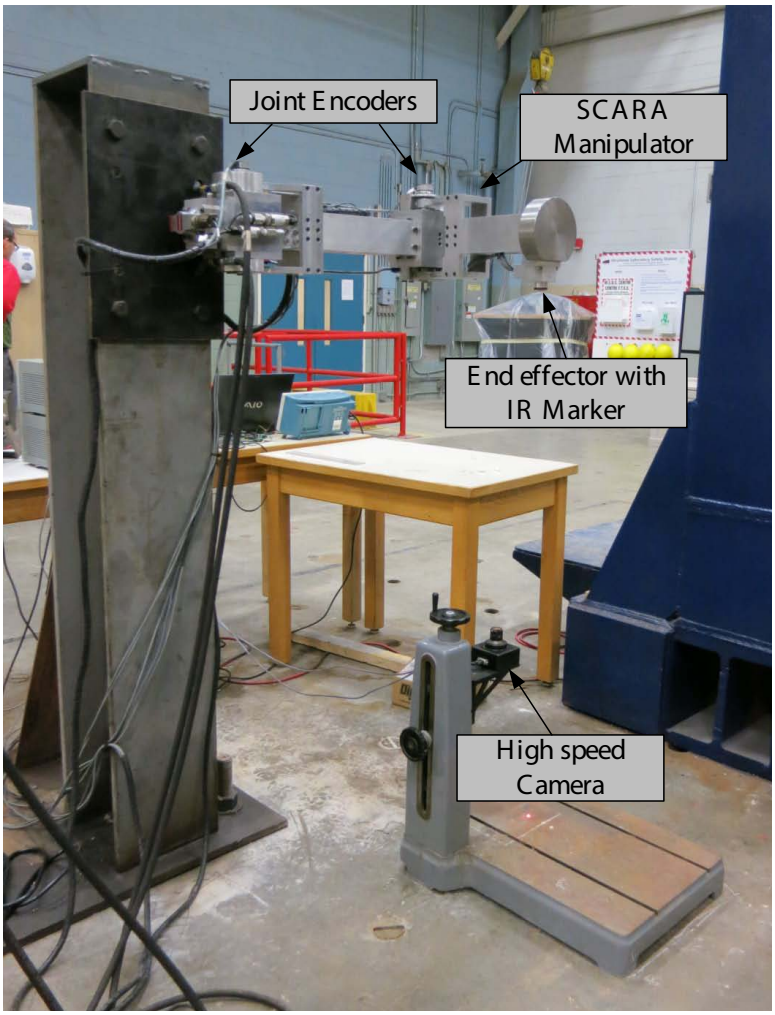

Figure 6.1: Proposed high-speed visual servoing system

four digital channels. These consist of the outputs from four 16-bit analog to digital converters (ADC). The output of the ADCs are obtained via SPI/In interface implemented in hardware. The EE position is estimated in the virtual processor using these signals.

Four different controllers are implemented using the FPGA for controlling the robot. These include software based PD, hardware based PD, set point modification and single time scale visual servoing type controllers. The PD control strategy used only the encoder feedback for estimating the control signal. The SPMC used the EE position and encoder angles as feedback. It uses the estimated angle of twist due to torsional vibration of the support column to introduce a correction in the control signal. Single time scale viusal servoing requires the feedback from both optical encoders and high speed camera. It uses the manipulator Jacobian along with the EE position to estimate the control signal. Except for the hardware based PD controller, all controller algorithms were implemented using the NIOS II virtual processor system.

The electro-hydraulic servo valves require an analog voltage between ± 5 V. The control signal is converted into an analog signal using a 16-bit DAC. Therefore, an SPI/Out module is implemented in the hardware to output the digital signal. The signal to drive the servo valve has to be amplified using an op amp circuit.

The proposed motion controller used dedicated software and hardware modules to implement the controller. This system was integrated and implemented in an Altera® DE0 series FPGA by Terasic. The Altera® DE0 is a low end FPGA, shown in Fig. 6.2. The analog electronics which consist of a DAC and an op amp circuit for the servo valve voltage is implemented in a conventional analog printed circuit board.

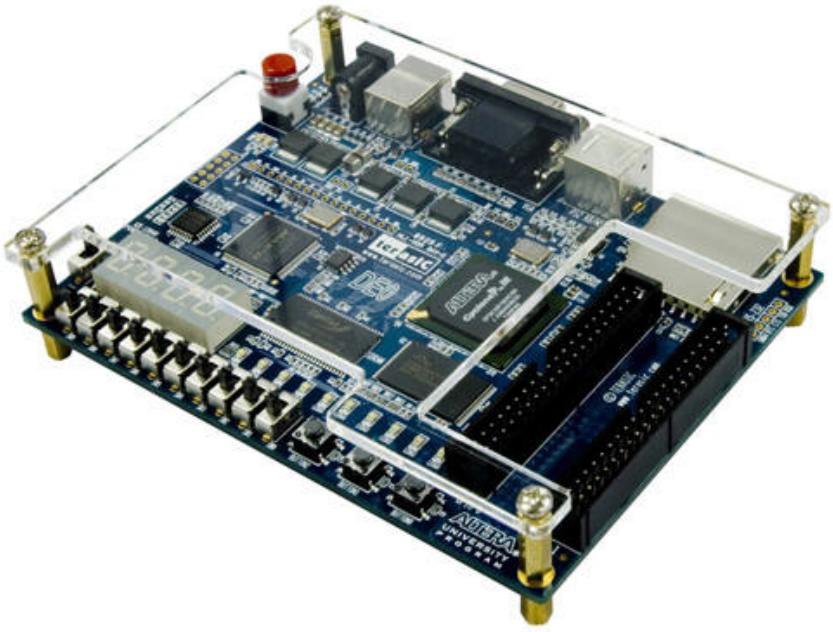

Figure 6.2: The DE0 development board

This chapter details the details the development of hardware based embedded system for controlling the robot.

6.3 Development of the Sub-components of the Motion Controller

6.3.1 Implementation of Quadrature Decoders for Estimating Encoder Angles

The quadrature decoders were implemented in the FPGA using the methodology proposed in Krouglicof [184]. The joints of the SCARA robot are instrumented with encoders. In digital closed loop motion control systems, optical encoders are often used to translate the rotary motion into a digital signal. Optical encoders consist

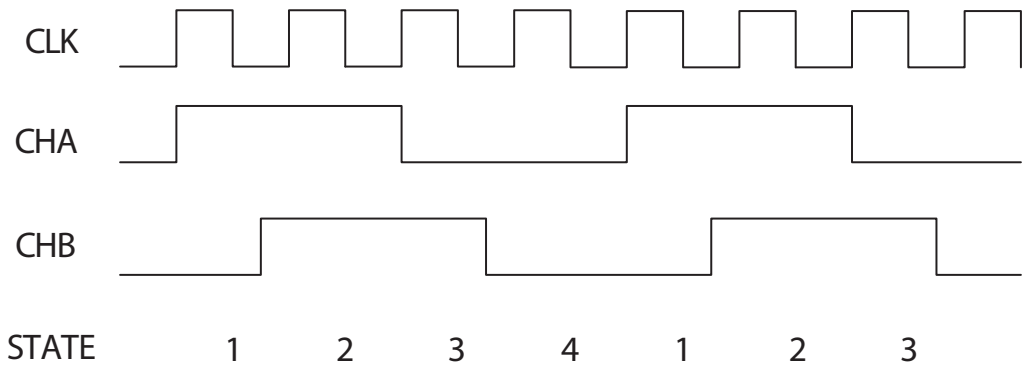

Figure 6.3: The channels of the encoder

of an emitter and detector. The emitter is usually a LED while the detector is a photo diode. There is a code wheel between the emitter and the detector. This code wheel comprises a series of radial slots which interrupt the light from the emitter. The angular displacement can be estimated by counting the number of slots that pass through the emitter. However, if the direction of the rotation is needed, a second set of slots is required. In a typical encoder, the emitter/detector pairs are placed on the circumference of the code wheel in such a way that the first detector (channel A) reads the slot and the second detector (channel B) reads the bar so that Channel A is quadratic (shifted by 90°) to channel B. These signals are usually detected with reference to a clock signal. This is illustrated in Figure 6.3.

Channels A and B could comprise four possible states with respect to the clock signal. These four states are further illustrated in Table 6.2. Therefore, considering the past binary state and the present binary state of the two signals, it can be established whether the angle should be incremented or decremented. As the signals from both channels produce four different states, it results in a resolution of four times the basic

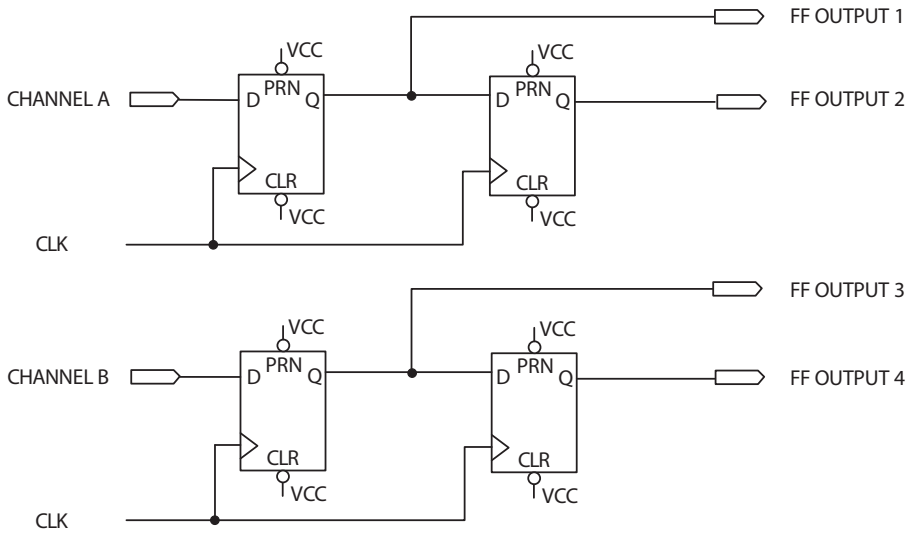

Figure 6.4: Edge detection circuitry for quadrature decoding

resolution of the code wheel. Hence, the 2000 pulse/rev encoder results in a total angular resolution of 8000 pulses/rev. These four states were implemented using four

Table 6.1: State transitions of the encoder

State	Channel A	Channel B
1	1	0
2	1	1
3	0	1
4	0	0

D-type flipflop modules. Edge detection circuitry for quadrature decoding is shown in Fig. 6.4. By using two flip flops per channel, a 2-bit register can be implemented. The 2-bit register will store the possible states. By using state transition, it can be determined whether the encoder count is incremented or decremented. The truth table for carrying out this logic operation is shown in Table 6.2. In order to perform the quadrature decoding operation, the edge detectors should operate by sampling the incoming channels at a frequency significantly higher than the fundamental natural frequency of the encoder. As in Krouglicof [184], the state machine for counting the

Table 6.2: State transitions of the encoder

State transition		Flipflop outputs				Count
Past State	Present State	1	2	3	4	
1	2	1	1	1	0	UP
2	3	0	1	1	1	UP
3	4	0	0	0	1	UP
4	1	1	0	0	0	UP
1	4	0	1	0	0	DOWN
4	3	0	0	1	0	DOWN
3	2	1	0	1	1	DOWN
2	1	1	1	0	1	DOWN

number of pulses is implemented by means of a truth table. It was coded using the Verilog hardware description language.

6.3.2 Implementation of the Interface for the High Speed Camera

The control algorithm uses the feedback of the EE position using a high speed imaging system. This imaging system consists of a camera with a 2-D PSD as the image sensor. It provides the position signal in terms of four voltage signals. It requires signal conditioning prior to data acquisition. A low pass filter is used to eliminate high frequency noise from these channels. Then the voltage signal is amplified using an operational amplifier circuit. A 16-bit ADC is used to convert this signal to a digital signal for data acquisition. A schematic diagram of the PSD is shown in Fig. 6.5.

The data acquisition from this chip is carried using the standard SPI/In mode. Three logic signals are required to perform this operation: the clock signal (SCLK), chip select (CS) and data signal (DAT). The data transfer is initiated by setting the

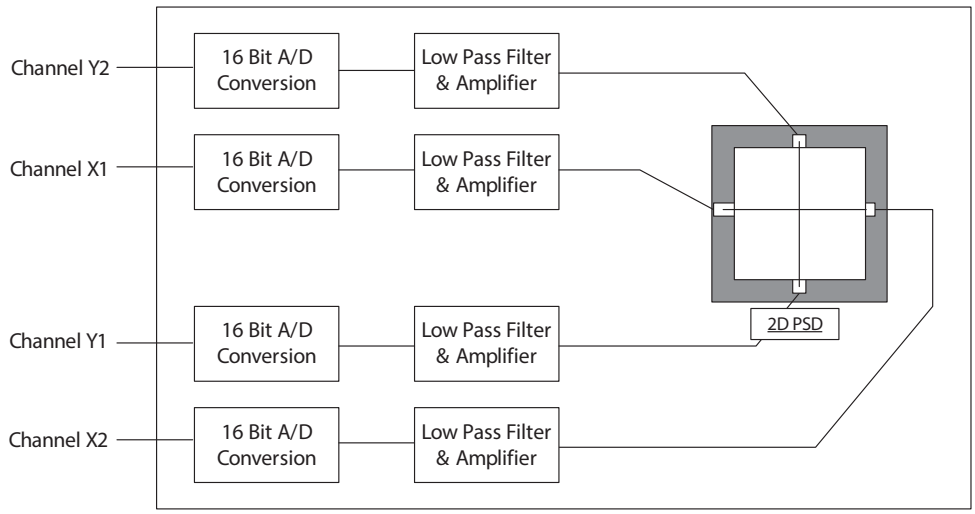

Figure 6.5: The schematic diagram of the PSD

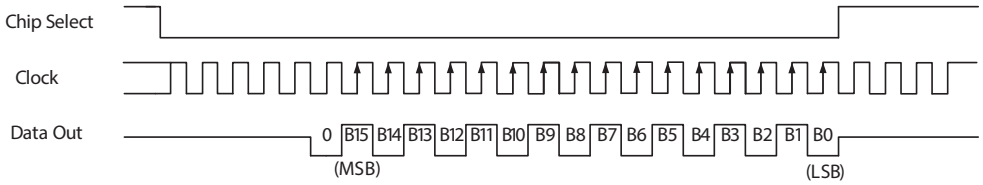

Figure 6.6: The schematic of the timing diagram of ADS8320 chip

CS signal from a high state to a low state. When the clock signal is configured at a suitable frequency, it will clock the data signal bit by bit in digital logic form on the corresponding rising edge. The basic timing diagram for the SPI/In interface for the ADC (ADS8320) is shown in Fig. 6.6.

The camera output consists of four voltage channels from separate ADCs. Multiple SPI/In protocol is used for data acquisition in the proposed design with a common CLK and DAT and a CS for each ADC. The timing diagram for the multiple SPI In interface for the PSD is illustrated in Fig. 6.7. This was implemented in hardware using the Verilog HDL. The clock was configured at a frequency of 98 kHz. Once the

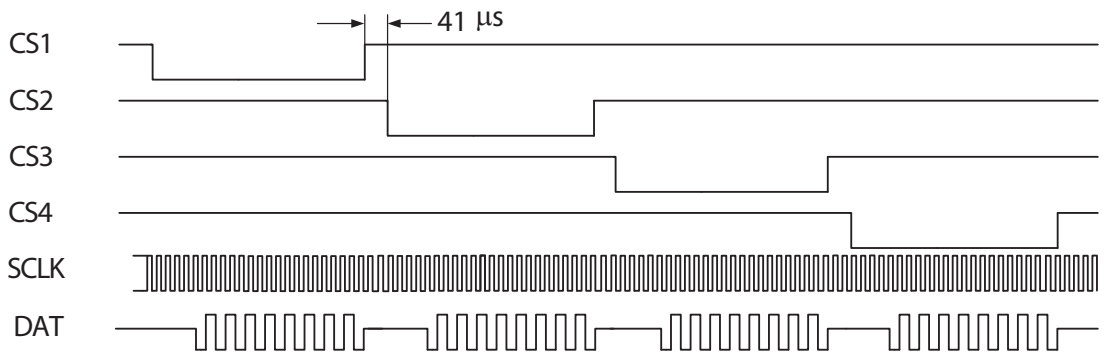

Figure 6.7: The schematic of the timing diagram of Multiple SPI/In interface for the high speed camera

chip select is set to low, the data signal is clocked with MSB first into a data register. Once a data bit is acquired a shift register will move each data bit by one position towards the left side of the array. This is repeated for the next 23 clock cycles before the chip select is set to high. The last 16 bits of the data array correspond to the value of the 16-bit digital voltage signal. The data is read after 2 clock cycles (20.5 μs) when CS is set to low. After 4 clock cycles (41 μs) the CS of the next ADC is set to low and the process is repeated until the next data point is acquired. This is repeated for all the ADC converters. At the clock speed considered, data acquisition is carried out at a sampling rate of 825 Hz. The data signal consists of 2-3 bits of noise at times. Therefore, one more stage of signal conditioning is required. This is carried out using a median filter for noise removal.

6.3.3 Implementation of the Servo Valve Driver Interface

The Moog G761 servo valve is used to control the flow from the actuators of the robot. The control signal is a 16-bit digital signal. It must be converted into an analog voltage signal to drive the servo valve. Therefore, Max541 was used to convert this control signal into an analog voltage signal. The MAX541 has a resolution

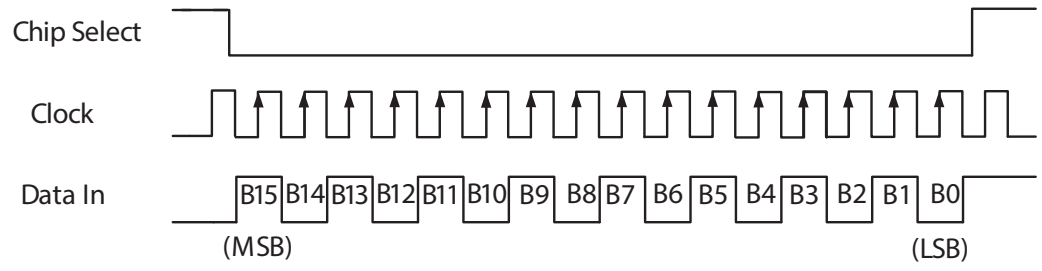

Figure 6.8: The schematic of the timing diagram of MAX541 chip

of 16 bits with an accuracy up to ± 1 bit. A standard 3-wire SPI/out interface is required to load data on to the latch of the DAC. The three signals are CS, SCLK and DAT. The data transfer begins immediately following a high-to-low transition of the CS signal. The 16-bit DAT signal is shifted synchronously from the FPGA pin and latched into the data input pin of the DAC on each rising edge of the SCLK. Once the 16 bits of data have been loaded into the data register of the input pin its contents are transferred to the DAC's latch on low-to-high transition of the CS. This value will then be converted into an analog voltage signal and it will be retained until it receives the external value. Once this task is completed, a new value is loaded into the DAC's latch. The timing diagram for the MAX541 chip is shown in Fig. 6.8.

The robot consists of two servo valves with actuators. Hence, it requires two simultaneous control signals. Since two DACs are used, the data communication is performed using multiple SPI/out protocol. This would serially transfer the two control signals from the FPGA to the two DACs. In order to perform this task it uses common signals for SCLK and DAT along with two signals for CS. The module for the SPI/out interface was implemented in FPGA using Verilog HDL. The frequency of SCLK was configured at 390 kHz. It uses two 16-bit data registers to store the

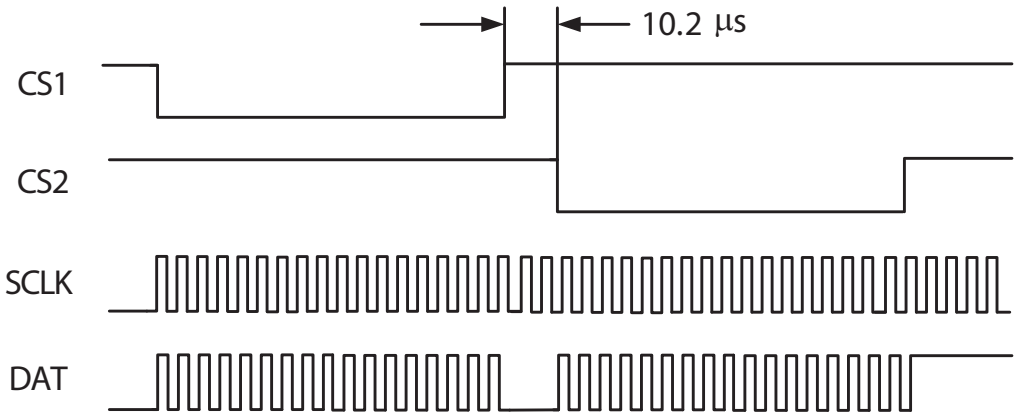

Figure 6.9: The schematic of the timing diagram of multiple SPI/Out for servo valve driver circuit

control signals. The transition of CS from a high logic level to a low logic level on the first chip will activate data transfer. It will latch the DAT signal into the DAC on every rising edge of the SCLK. Once it repeats for 16 clock cycles, CS is set to a high logic level once again. After an interval of 10.2 μs, the second CS will be set to a low logic level. The above described process will be repeated. Once the data transfer is complete, the logic level of the second CS will be set to high. There will be an interval of 563 μs before the first CS is set to a low logic level once again. The overall data transfer rate of the operation is 1.5 kHz. The timing diagram of the multiple SPI/out interface is shown in Fig. 6.9.

This DAC converts the 16-bit digital voltage signal into an analog control signal between 0 - 2.5 V. The servo valve requires an analog voltage signal between -5V to +5V. Thus, the output signals from the DAC should be re-scaled in order to drive these signals. This operation is performed using two operation amplifier stages as shown in Fig. 6.10. The op amp TL072 from Texas Instruments was used in the first stage. It has low input bias with low offset currents with a fast slew rate. In the first

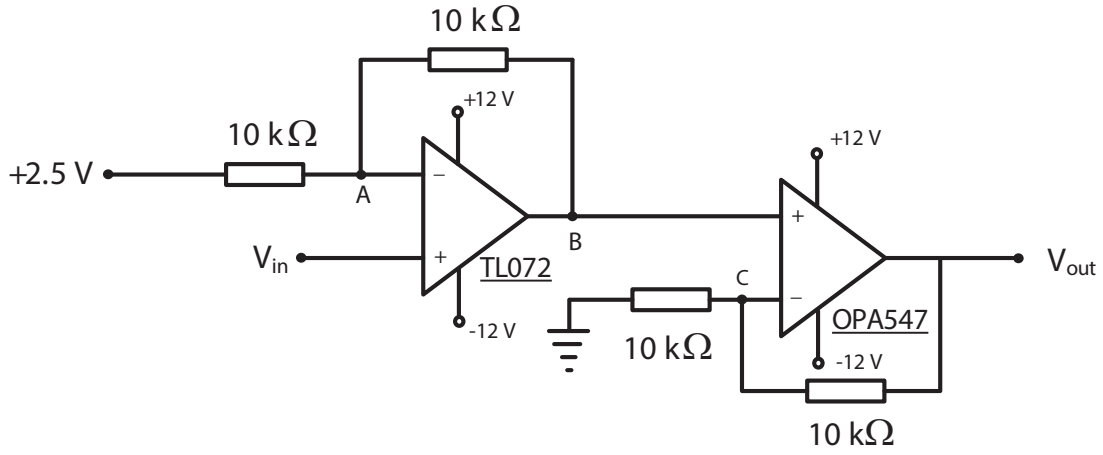

Figure 6.10: The servo valve driver operational amplifier circuit

operational amplifier stage:

$$\frac{2.5 - V_{in}}{10k} = \frac{V_{in} - V_B}{10k} \tag{6.1}$$

$$V_B = 2.V_{in} - 2.5 \tag{6.2}$$

The first op amp stage will linearly scale the output of the Max541 chip from 0 - +2.5 V to -2.5 V and +2.5 V.

The Moog® G761 servo valve will require a current of up to 20 mA. Therefore, a high current op amp (OPA547) is used in the final stage. This op amp is capable of driving any load which requires a continuous current of up to 500 mA. Since this op amp stage provides a gain of two, the corresponding voltage for driving the valves would be between ± 5 V. Therefore, in the second op amp stage:

$$\frac{V_B - 0}{10k} = \frac{V_{out} - V_B}{10k} \tag{6.3}$$

$$V_{out} = 2V_B \tag{6.4}$$

$$V_{out} = 4V_{in} - 5 \tag{6.5}$$

6.3.4 Development of the NIOS II Virtual Soft Processor System

A virtual processor can be integrated with the hardware designs of an FPGA. This provides a greater flexibility for the designers to integrate powerful features of hardware with complex software algorithms. Motion controllers that use the features of both hardware and virtual processor technology are still at an early stage in their development. Altera Corporation developed the Nios II virtual soft processor, which can be instantiated on any Altera FPGA device. The NIOS II soft processor is fundamentally a high performance 32-bit Reduced Instruction Set Computing (RISC) architecture embedded computer. It delivers unprecedented flexibility for real-time, ASIC-optimized applications and processing needs. A Nios II processor system consists of a processor core, on-chip memory, a set of peripherals and interfaces implemented on a single device [13]. Similar to contemporary microcontrollers and microprocessors, it uses a consistent set of instructions and a programming model. The NIOS II processor system was used to implement the EE position estimation and proposed set point modification based controller. The PD control algorithm was also implemented in this processor.

A common interface is required to facilitate communications between the processor and peripherals. The Avalon Memory-Mapped (Avalon-MM) interface is used for this purpose [14]. The peripherals are connected to the Avalon bus which supports dynamic bus sizing. This allows peripherals with different data widths to be connected on a single bus. It is designed to facilitate the integration of on and off chip processors

and peripherals into a system on a programmable chip.

Hence, the Avalon Memory-Mapped (Avalon-MM) interface provides a basis for implementing the address-based read/write interfaces found on master and slave peripherals such as microprocessors, memory, UART, timer, etc. This allows any master-type peripheral to be connected to any slave-type peripheral without a priori knowledge of either the master or slave interface. The Avalon-MM interface defines the signal type, the behavior of the signals and the types of transfers supported by these signals.

The Qsys system integration tool is provided in Quartus IDE version 11.1 for designing the virtual processor system [14]. It saves a significant amount of time and effort in the FPGA design process by automatically generating the interconnect logic of the intellectual property (IP) functions and subsystems. Qsys provides a powerful FPGA-optimized network-on-a-chip (NoC) technology which can deliver a higher performance, improved design reuse and faster verification.

A NIOS II soft processor and a set of peripherals were used for implementing the proposed controller. The design of the proposed processor system is shown in Fig 6.11. It uses a processor, a timer, an on-chip memory, JTAG UART, system identification and input/output pins. A standard variant of the NIOS II processor core (NIOS II/s) was selected for the current application. The Nios II/s standard core is a processor with a smaller core size. The On-chip logic and memory resources are conserved in this processor at the expense of execution performance. An instruction cache of 2 kBytes was configured for the 32-bit Avalon-MM master port. It performs the function of fetching instructions to be executed by the processor. The cache memory units can also improve the average memory access time. This processor is

capable of accessing up to 2 GB of external address space. It is also enabled with a feature for exception handling which includes software traps, unimplemented and illegal instructions.

On-chip memory is the simplest type of memory that can be implemented in an FPGA-based embedded system. This is because it is implemented in the FPGA itself and so external connections are not necessary. The on-chip memory has the fastest access time as compared to off-chip memory. A maximum on-chip memory of 40,560 bytes was configured as the C code to include complex trigonometric functions and data arrays.

The processor requires a JTAG debug module to perform communications. The JTAG UART core with the Avalon Interface provides a method to communicate between a host PC and the System on a Programmable Chip. The host PC is connected to the FPGA via the Altera USB Blaster. The JTAG eliminates the need for a RS-232 serial communication interface for the simple character IO. Altera provides JTAG terminal software running on the host PC that manages the connection with the target, decodes the JTAG data stream and displays messages on screen. The JTAG UART is used for data acquisition. It also facilitates the data transfer from the FPGA to the host computer. The JTAG UART establishes the connection with the host PC and downloads C code into the FPGA.

The Interval Timer core with Avalon interface is an interval timer for Avalon-based processor systems. It provides the controls to start, stop, and reset the timers. These timers can be used to implement interrupt service requests (IRQs), watch dog timers or simple periodic pulse generators. The proposed controller needs to execute func-

tions and calculate the control signals at a specific interval. An IRQ can be used to execute functions at a given interval. An interval timer is used to trigger an IRQ at a 1 ms interval. The interval timer core is builder-ready and integrates easily into any Qsys builder-generated system.

A set of programmable input/output (PIO) pins were configured in the design to facilitate data communication between different modules of the program. The PIOs were used as both input and output buses. The input buses were configured for obtaining readings from encoders and from the four output channels of the high speed camera. When the PD control algorithm is executed in the Nios processor, the controller signals need to be transferred to the SPI/Out module. A data bus was configured for this. The output buses provided set points of the EE (x,y) position, theta 1 and theta 2, controller gains and some of the reset signals. The buses used for feedback and for providing the control signal had a bus width of 16 bits. The P,D gains of the controller were assigned in the Nios processor. These were transferred to the hardware controller modules via 32-bit buses. In addition to these, single bit output pins were configured for resetting the encoder readings to zero and to select the mode of operation (whether hardware or processor based) for the control algorithm.

A system identification peripheral was used in the design to prevent accidental downloading software compiled for a different Nios II system. It allows the Nios II Flash Programmer to validate the target design before downloading it. The Qsys integration tool was used to develop the virtual processor system. It provides these components as a set of blocks and presents a visual interface in which various components can be dragged into the design to complete the connections. Then the design is compiled to generate the Verilog HDL file to be included in the hardware design.

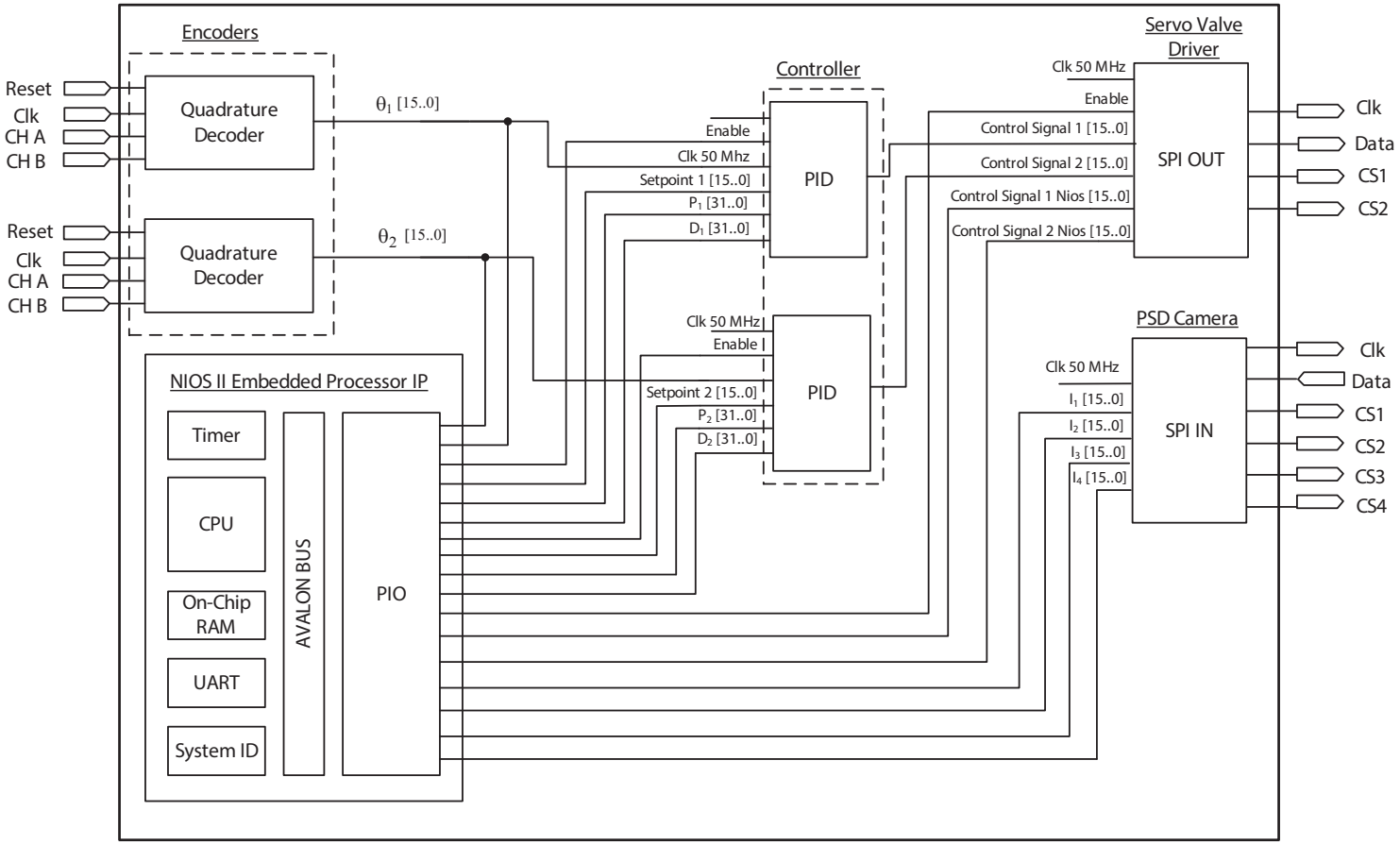

Figure 6.11: Structure of the FPGA with the NIOS II processor

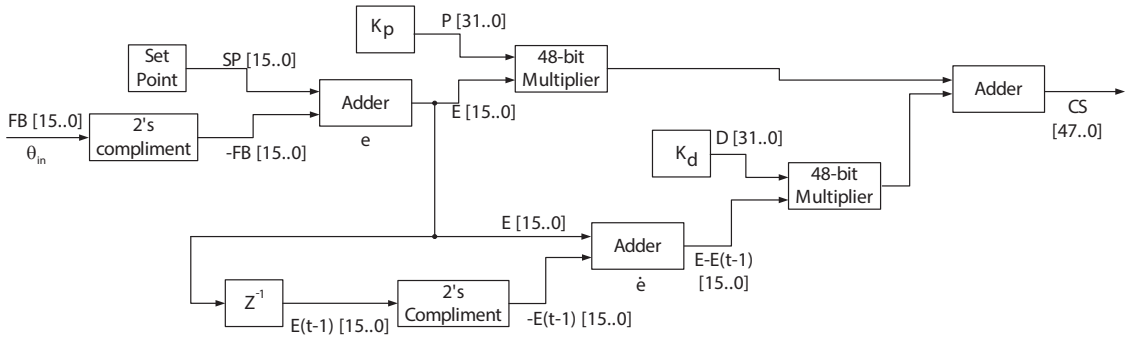

Figure 6.12: The schematic of the Hardware PD controller

6.3.5 Implementation of the Hardware PD Controller

In this study, the PD control algorithm for controlling the robot was implemented in both hardware and software. The hardware version controller uses basic logic operations comprising adders and multipliers to implement the PD control algorithm. Fig. 6.12 shows a schematic diagram of different blocks which constitute the hardware based PD controller for a given joint.

The error is obtained by subtracting the set point from the feedback signal. This is implemented in logic operations as an addition between the set point and the 2's complimented encoder signal. Since the set point and feedback encoder angle were considered as 16-bit binary numbers, the resulting error will also be a 16-bit binary number. The proportional and derivative gains of the controller are considered as 32-bit binary numbers. The first 20 bits of this binary number correspond to the integer portion of the number and the trailing 12 bits correspond to the decimal portion of the number. In the algorithm, proportional gain will be multiplied by the error. Since the proportional gain is a 32-bit binary number and the error signal is a 16-bit binary number, a 48-bit binary multiplication operation is carried out between these variables.

The error signal is considered with the error at the previous instant of time for the next operation. This error signal is subtracted with the previous error using an operation similar to the above one. This will result in a 16-bit binary number. Similar to the earlier case, the derivative gain will also be considered as a 32-bit binary number with 20 bits for the integer portion and 12 bits for the decimal portion. Next, the error rate is multiplied by the derivative gain in a 48-bit binary multiplication operation. The two 48-bit binary numbers which is a result from the multiplication of proportional gain with the error and derivative gain with the error rate are added together making the result a 48 bit binary number. The operations implemented in the hardware based logic elements are given by:

$$e = SP - FB \tag{6.6}$$

$$CT = P.e(t) - D.[e(t) - e(t-1)] \tag{6.7}$$

Where $e(t)$ is error at time t, $e(t-1)$ is error at time t-1, SP is setpoint, FB is encoder angle, P and D are the proportional and derivative gains and CT is the control signal.

The control signal requires a 16-bit binary signal. Therefore, the first 36 bits of the control signal are considered ignoring the decimal bits. Depending on the most significant bit (MSB) of the binary number, a comparator is used to check whether the value of the control signal has reached saturation. If the value of the MSB is 0 and if the control signal exceeds 32,767 in decimal value, the control signal is considered to be 32,767. If the value of the MSB is 1 and if the control signal exceeds 32,768, in decimal value, it is considered as 32,768 since the negative numbers are represented

based on 2's complement binary operations.

The software based PD controller was deployed in the NIOS processor. It was softcoded using the C language. The PD controller which is softcoded is given by:

$$e = SP - \theta \tag{6.8}$$

$$CT = K_p.e + K_d.\frac{de}{dt} \tag{6.9}$$

Where θ is joint angle, K_p and K_d are the proportional and derivative gains and CT is the control signal, respectively.

6.3.6 Implementation of the Single Time Scale PBVS Controller

The structure of the single time scale PBVS controller was presented in Section 4.5. It consists of two separate loops. This controller requires the feedback from the encoders for angular position and high speed camera for EE position. It uses the link angles obtained from the encoders to calculate the manipulator Jacobian. This was used in one of the loops to transform the position based error to an angle based error. This position related error is then fed through a PD type controller. In the other loop the error between the desired and the current link angles is estimated and fed though another PD type controller. The control signal is the sum of these two values. This algorithm was implemented in the NIOS II processor. If the latter loop is ignored only the visual loop is used to run the controls of the manipulator. In this single time scale

visual servoing system, both feedbacks from the encoder and vision system operate at the same speed. A schematic diagram of the FPGA implementation of this single time scale visual servoing is shown in Fig. 6.13.

6.3.7 Implementation of the Set Point Modification Controller

This study implemented the SPMC in the FPGA. The SPMC algorithm was presented in Section 4.6. This algorithm uses the feedback from the high speed camera and encoders. Using the EE position and links angles, the angle of twist is estimated for the compliant support column. Then the deflection of the origin of the first actuator is estimated using this. Using the new position of the origin of first actuator and EE a modified set of desired link angles have to be estimated. This is estimated by performing the inverse kinematics for the manipulator. The obtaining feedback, calculation of the amount of torsional vibration and estimation of the modified desired angles were carried out using the NIOS II virtual processor. Once the modified desired link angles were estimated these were used as set points for the hardware based PD controller. A schematic diagram of the proposed controller architecture for SPMC is shown in Fig. 6.14.

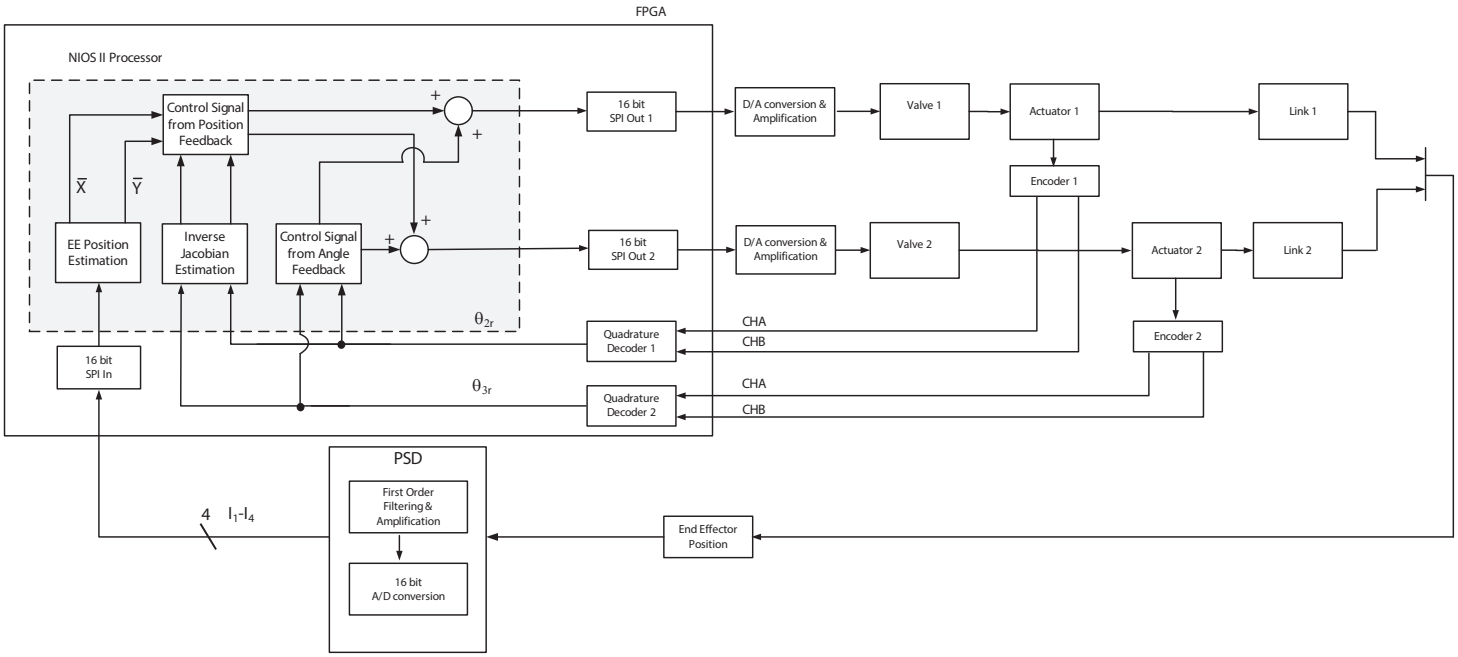

Figure 6.13: Architecture of the proposed single time scale visual servoing system

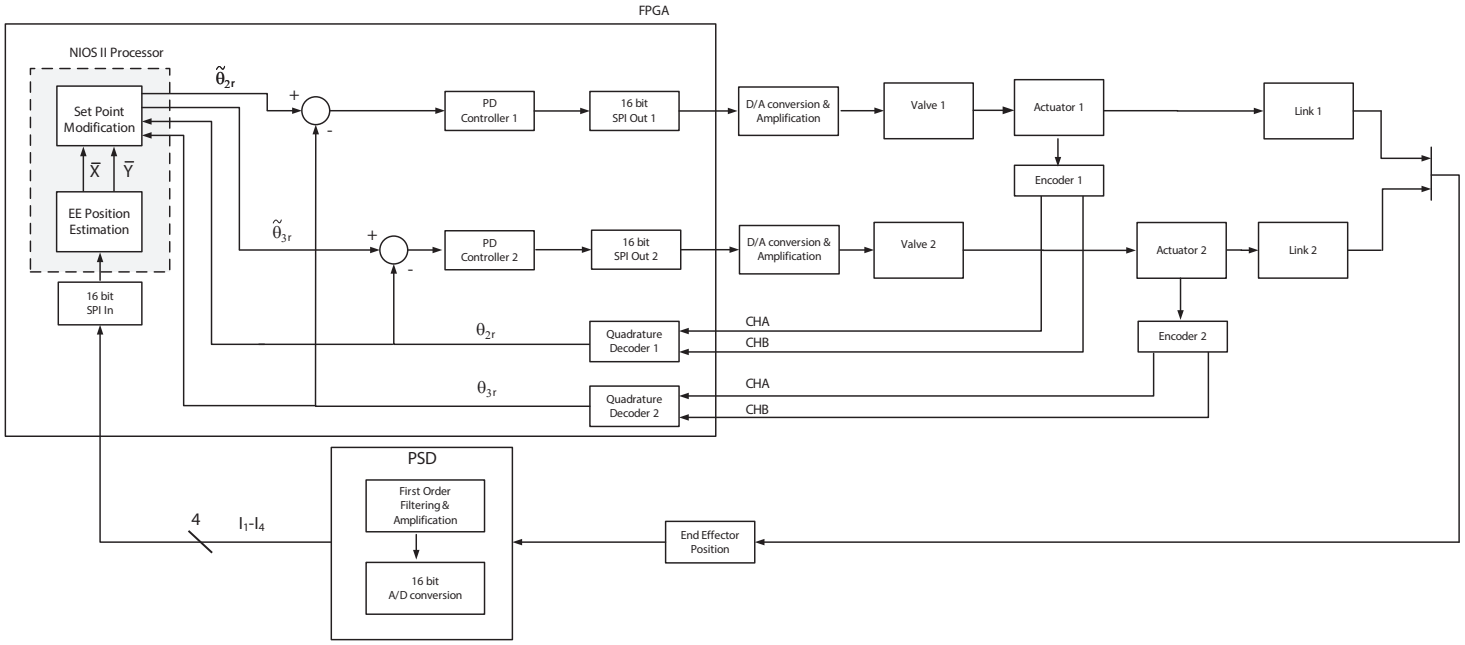

Figure 6.14: Architecture of the proposed SPMC

Chapter 7

Experimental Results

7.1 Results from Testing of the Actuator

Preliminary testing was carried out using an MTS® 407 controller by MTS Systems, Ltd. This is an analog controller specifically used for hydraulic systems. As this controller accepts only analog feedback devices, a potentiometer coupled to the end of shaft is employed to provide feedback on the angular position of the actuator. A basic PD type controller was used for controls. The actuator torque was obtained using the pressure difference across the vanes. Analog pressure transducers were used to measure the pressure in actuator compartments during the experiments.

A figure of the experimental setup of a single actuator with a mass of 6.5 kg is shown in Fig. 7.1. A schematic diagram of the experimental setup with the MTS® 407 is shown in Fig. 7.2. The system performance was evaluated for different step inputs and a range of controller gains. Satisfactory control performance of the actuator was achieved with simple proportional type controller. The feedback signal

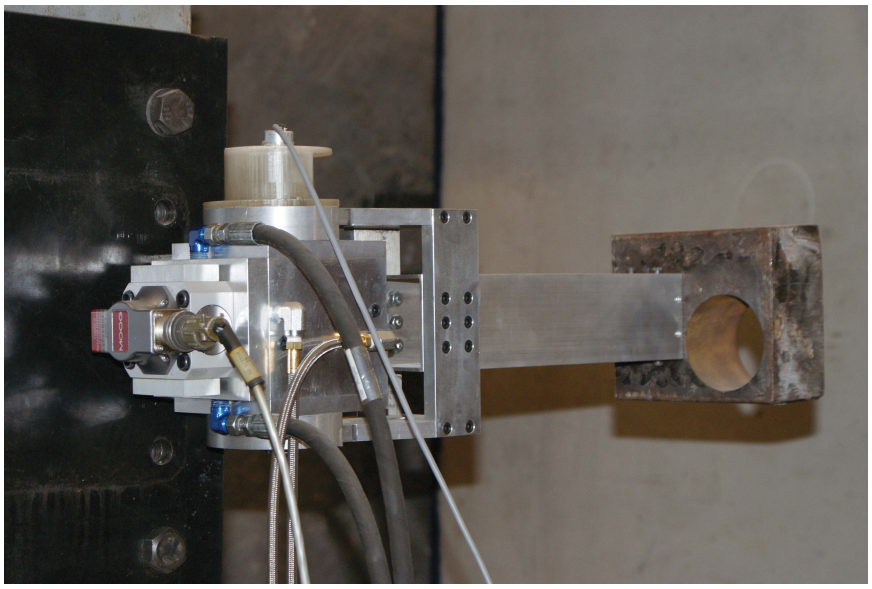

Figure 7.1: The experimental setup with a single actuator

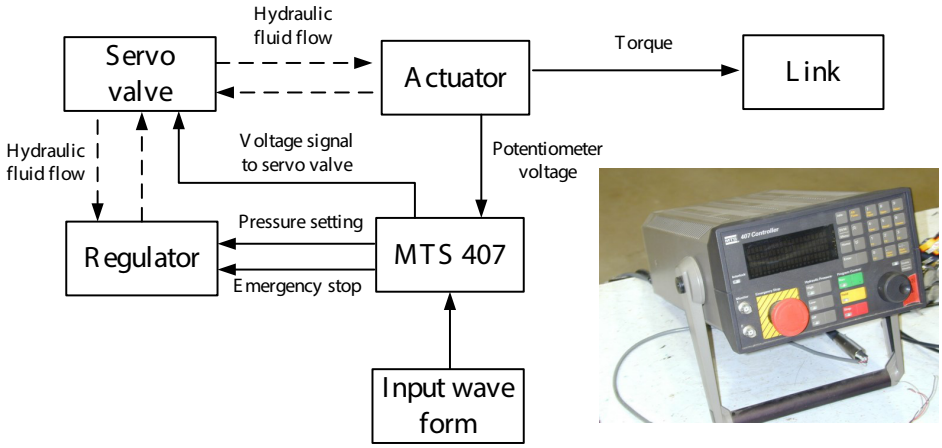

Figure 7.2: A schematic diagram of the experimental setup with MTS® 407

of the potentiometer and control signal to servo valve over time were recorded using an oscilloscope. Actuator torque was calculated by the measured pressure difference between actuator chambers. A mass of 13 kg was considered at the end of the link to represent the mass of the manipulator. The actual pressure of the hydraulic supply during experiments was 14.9 MPa (2160 psi).

The system response was obtained for a square waveform which has a peak to peak amplitude of 18° and duration of 5 s. Three different values were considered for proportional gain in three separate cases. The gain values considered were 0.5 V/V, 1 V/V and 1.5 V/V. These are denoted as cases 1, 2 and 3 (C1, C2 and C3), respectively. The variation of angular displacement and torque over time for these controller gains are shown in Fig.s 7.3, 7.4, 7.5. These figures provide a comparison between the reference angular displacement and torque between experimental and simulation values. The simulation values have been obtained using the MATLAB model proposed in Chapter 2.

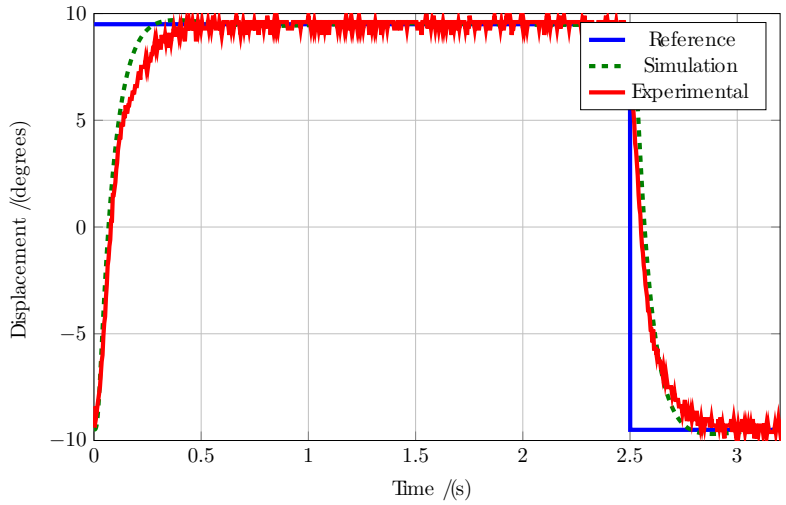

(a) Position response in case 1

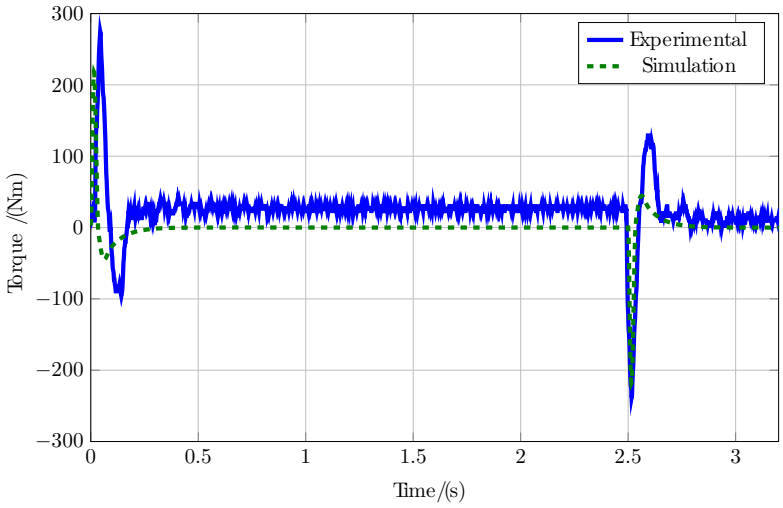

(b) Torque in case 1

Figure 7.3: The system response and actuator torque to a given step input in case 1

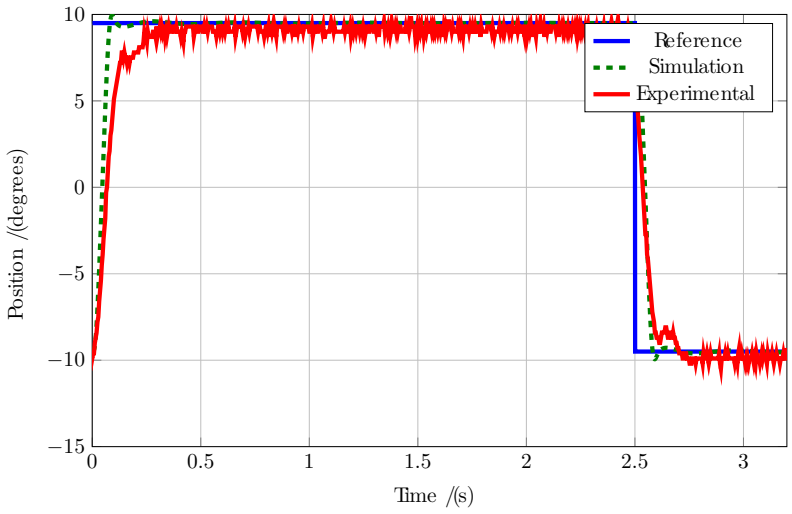

(a) Position response in case 2

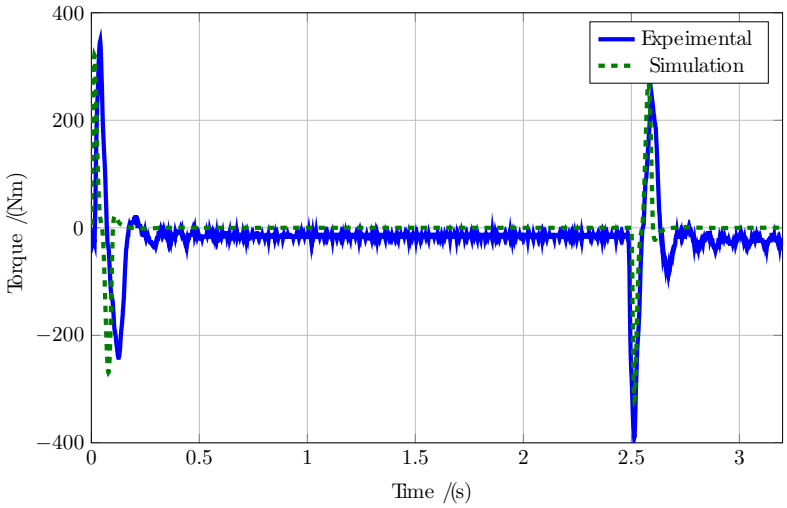

(b) Torque in case 2

Figure 7.4: The system response and actuator torque to a given step input in case 2

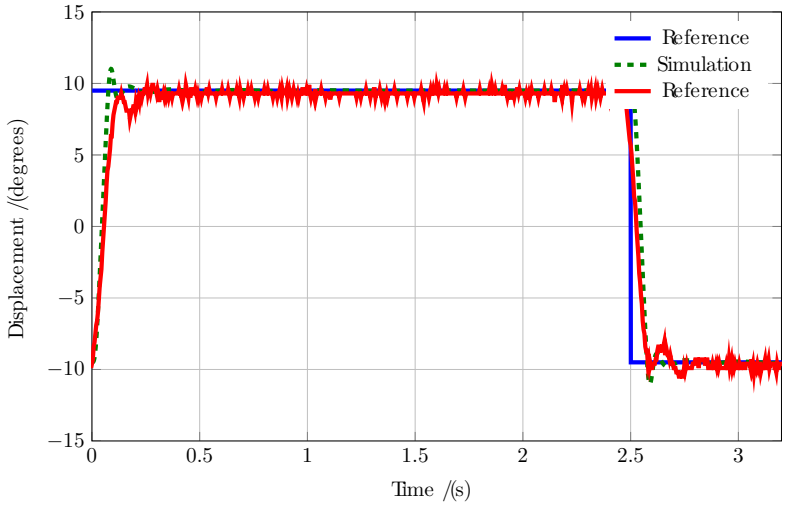

(a) Position response in case 3

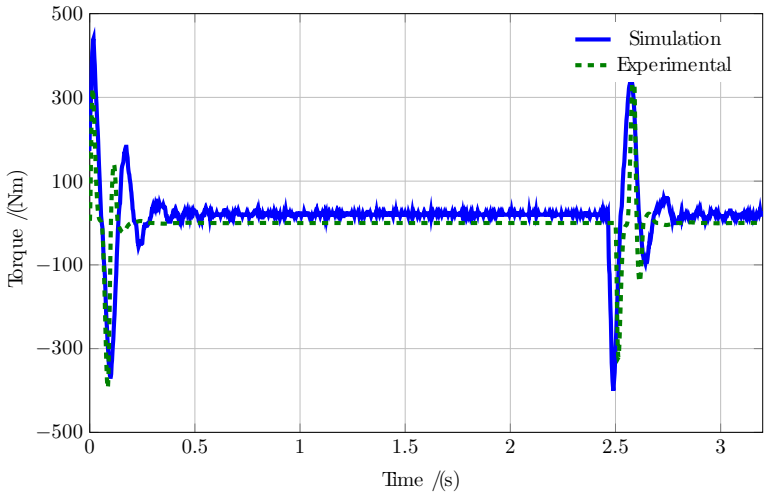

(b) Torque in case 3

Figure 7.5: The system response and actuator torque to a given step input in case 3

The actuator response to this step input is shown in Fig.s 7.3(a), 7.4(a) and 7.5(a). According to the simulation, system reaches steady state in 0.217 s, 0.077 s and 0.074 s in cases 1, 2 and 3 respectively. Experimental results showed that it would take 0.32 s, 0.239 s and 0.117 s for cases 1, 2 and 3, respectively in order to reach the same

position. The results show a stable performance of the manipulator for a range of controller gains.

The variation of actuator torque with time is shown in Fig. 7.3(b), 7.4(b) and 7.5(b). The negative values for torque in these figures represent the actuator breaking torque. According to the simulation, the actuator torque reaches a maximum of 220 Nm, 320 Nm and 395 Nm in cases 1, 2 and 3, respectively. The experimental results indicate that the actuator is capable of producing torques of up to 270 Nm, 390 Nm and 440 Nm in the respective cases 1, 2 and 3.

The peak torque here is given considering the total time horizon and not the corresponding values for experimental and simulation cases. The negative torque basically acts as a braking torque to stop the output shaft. It can be seen from these figures that when there is an overshoot in the system it results in a higher number of torque oscillations. The actuator has produced very large torques. Hence, the proposed actuator has a much higher power to weight ratio. It is not possible to produce such high torques in electric motors of comparable size. The experimental results have a close resemblance with the mathematical simulation over the range of values considered for proportional gain. Therefore, the simulation results appear to validate the mathematical model.

However, there are a few discrepancies between the actual and simulated values. There may be a number reasons behind this variations. Although it was considered that the supply pressure was constant during the experiment in a real hydraulic supply this is not the case. The tank pressure was assumed to be negligible in the model; however, this may not be the case in an actual hydraulic power unit, particularly

if it is not in close proximity to the actuator. The mathematical model developed was based on several assumptions. Some of the parameters assumed for modeling the servo valve were considered without a proper system identification study. There were also assumptions made for the value of the bulk modulus and the leakage area. The noise produced by the potentiometer is also relatively high as seen in the experimental response curves. Pressure transducers were not calibrated prior to experiments and these could have an initial error in these.

7.2 Testing of the Robotic Arm

7.2.1 Results From Testing of the Robotic Arm With a Microcontroller

A custom designed PCB with a PIC 18F4550 microcontroller was used in initial testing. This board consisted of MAX 541 DAC and operational amplifiers. The MAX 541 chip was used to convert the 16-bit digital signal to an analog signal between 0-5 V. The operational amplifier circuitry will convert the analog signal between +5 V and -5 V for the servo valves. The joints of the arm were instrumented with optical encoders for feedback. These provided the angular measurement up to an accuracy of 0.045°. Although the system is rated at 20.7 MPa (3000 psi), the actual hydraulic system pressure was 14.4 MPa (2100 psi) during the experiments. The initial tests were carried out using only a proportional controller. The robot was tested for a range of inputs covering the entire workspace with and without payloads. The chamber pressures were measured using pressure transducers. Based on these readings, actuator torque could be estimated from the pressure difference.

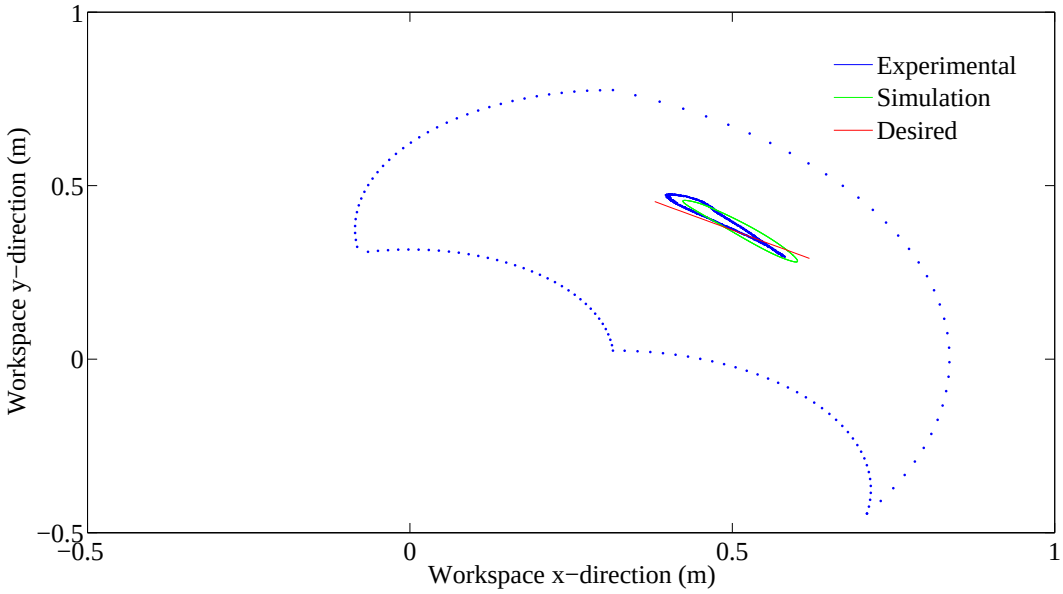

Figure 7.6: The trajectory of the end effector of the manipulator

Fig. 7.6 shows the response of the robot when it follows a linear trajectory from point (0.39,0.45) m to point (0.62,0.29) m in the workspace. The payload on the EE was 5.3 kg. The figure also provides a comparison between the actual and simulation values. The simulation results have been obtained from the Matlab© model in Chapter 2. It is seen that the experimental and simulation values follow a similar pattern.

The torque produced by the actuator is compared with the Matlab© simulation is shown in Fig. 7.7. It can be seen that with the actual supply pressure of 14.4 MPa (2100 psi) and the exact payload, the first actuator achieves torques of up to 597 Nm in magnitude. It was experimentally determined that the actuator torque varies from -597 Nm to 297 Nm in 175 ms. According to the simulation results, the actuator torque varies from -548 Nm to 260 Nm in 190 ms. Since the second actuator only drives the 5.3 kg payload, the actual torque produced by this actuator varies from -90 Nm to 76 Nm. According to the simulation results, the second actuator pro-

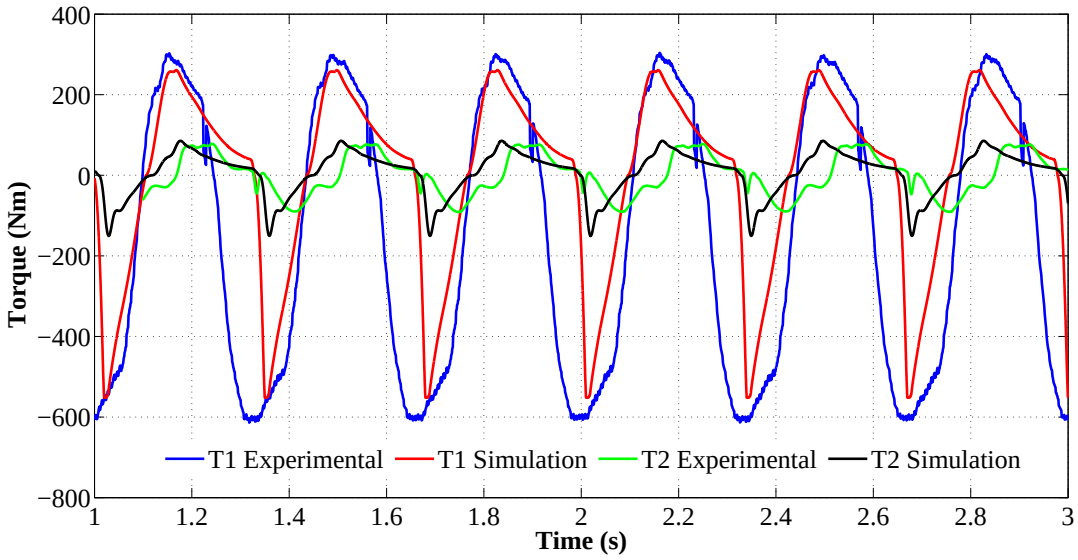

Figure 7.7: The actual and simulated torque of actuators of robot

duces torques between -145 Nm to 85 Nm while maintaining the desired trajectory. Therefore, the experimental results closely follow the simulation results with a few discrepancies.

The length of the assigned trajectory is 0.28 m. The EE traverses this distance in 175 ms. The average velocity of the EE is 1.6 ms^{-1}. In another test, the EE was programmed to follow a linear trajectory from (0.27,0.49) m to (0.65,0.20) m with an EE mass of 5.3 kg. The time required was 178 ms to traverse a linear distance of 0.48 m. This implies that the robot is capable of reaching even higher velocities; up to 2.7 ms^{-1}. This is due to the fact that the servo valve stays opens longer compared to the earlier case, resulting in higher oil flow into the actuator chambers.

There could be several reasons behind the discrepancy between the simulation and experimental results. Some of these contributory factors include those described ear-

lier for the case with actuator testing. Additionally, there are unmodeled dynamics in the system that were not considered in the simulation. It includes the effects of beam flexing and support column vibration.

7.3 Testing of the High Speed Camera

The main focus of this thesis is to propose a high speed visual servoing system. It consists of high speed SCARA type hydraulic manipulator. The joints of this robot are instrumented with rotary encoders as proprioceptive sensors. A camera with a 2-D PSD as the image sensor is used as the exteroceptive sensor. This camera is used to track an IR marker mounted on to the EE of the robotic arm. The experimental setup of the proposed high speed visual servoing system is shown in Fig. 6.1. The results from some of the tests carried out are as follows.

7.3.1 Accuracy of the High Speed Camera System

Using the pin hole camera model for accurate estimation of the EE position requires the knowledge of both the extrinsic and the intrinsic parameters of the camera. The intrinsic parameters, which consist of the focal length, image center, radial and tangential distortion parameters were obtained during the calibration process of the camera. However, once the camera is mounted near the robot, it requires the estimation of the extrinsic parameters of the camera. These parameters include the rotation parameters roll, pitch and yaw and the translation parameters x,y,z of the camera.

The process used to estimate the extrinsic parameters is similar to the process carried out to estimate the intrinsic parameters of the camera. For this, the EE is moved over a grid which consists of points 10 mm x 10 mm apart. The position provided by

the joint encoders is considered as the true position. The position of the IR marker on the PSD is provided by the four voltages. These voltage signals are converted into position signals taking into account the non-linearities of the image sensor. The position of the EE measured using the camera and the true position obtained using the encoder signals in an experiment are shown in Fig. 7.8. These points clearly show that the camera is subjected to a rotation about its axes and a misalignment of the image sensor.

The encoders provide the EE position w.r.t. a world coordinate system. The

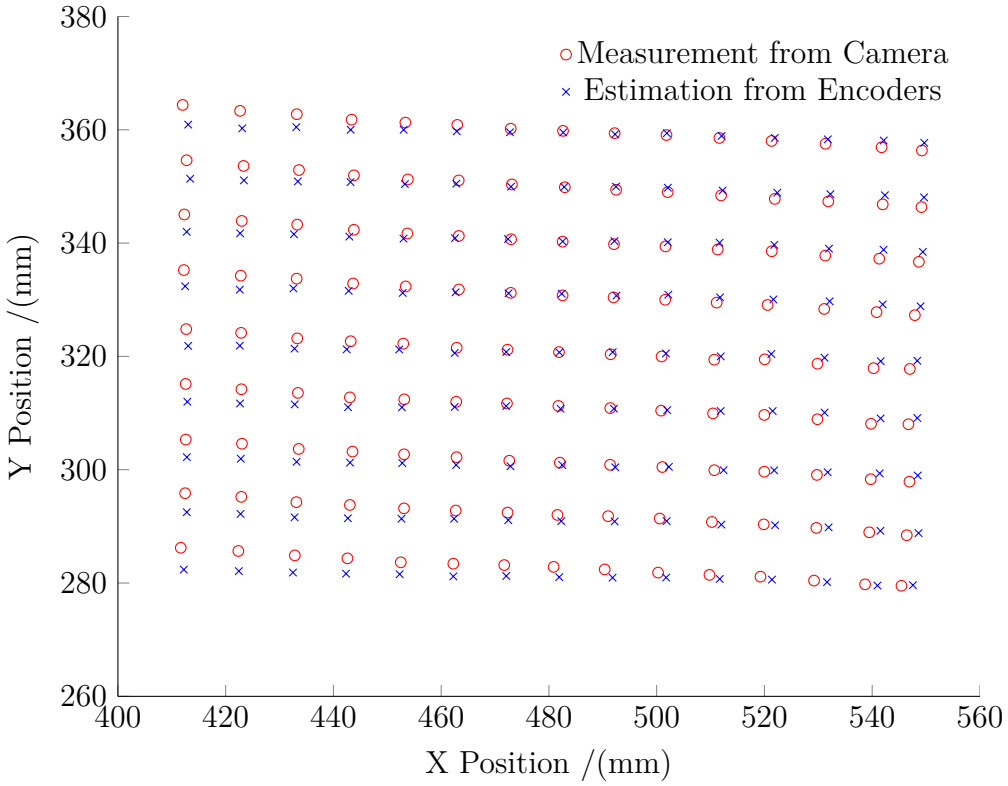

Figure 7.8: The EE position obtained from encoders and camera

projected position of the EE on the PSD was obtained with respect to the camera's coordinate system. A forward camera model was used to project the EE position onto the image coordinates. This transformation considers the rotation and translation of

the camera position. If it is assumed that the camera is not subjected to any rotation, it represents the position measurement error if extrinsic parameters are not considered. The translation vector will correspond to $[-l_2\ -l_3\ tz]^T$, where l_2, l_3 are the link lengths while tz is the distance between the camera and EE. The rotation vector will be a unit vector since it considers no rotation.

Fig.s 7.9, 7.10 (a) show plots of the root mean squared error (RMSE) between the measurements in x and y directions before and after the on-site calibration. An accurate measurement would result in points that are concentrated around (0,0). However, it is seen that these points are mainly concentrated in 2nd and 3rd quadrants. This offset indicates that the position of the image center has to be re-estimated. Fig.s 7.9, 7.10 (b),(c) show plots of the absolute value of the RMSE in x,y directions. It is seen that the error follows a fairly repetitive pattern as the accuracy of the position measurements decrease with the distance from the image center. The error in the measurements in x direction is higher compared to that in y direction.

The on-site calibration algorithm is presented in Section 5.4. It uses an iterative scheme with Levenberg-Marquardt method to optimize a cost function which consists of the RMSE in x,y directions. This algorithm can be used to estimate the extrinsic parameters of the camera. If there is an uncertainty in the intrinsic camera parameters estimated during the camera calibration process, these values can also be re-estimated during the on-site calibration. This will further improve the robustness of the results. The results obtained after the calibration are shown in Fig 7.10. It can be seen that the measurement error decreases with the calibration.

If the extrinsic parameters are not considered, the absolute error could be as high

as 3.7 mm in x direction and 2.34 mm in y direction, respectively. The absolute average RMSE in x direction will decrease from 1.43 mm to 0.31 mm and in y direction it will decrease from 0.73 mm to 0.37 mm after the calibration. The absolute RMSE will not exceed 1 mm in both x,y directions. For the calibration points considered the maximum absolute error was 0.93 mm in x direction and 0.95 mm in y direction, respectively. The on-site calibration produces a significant improvement in the accuracy of the measurement.

Fig. 7.9 and Fig. 7.10 (d) show the absolute value of the cost function for each data point. This represents an error in the distance measurement from the origin of the Cartesian coordinate frame. The cost function has an average RMSE of 1.71 mm before the calibration. The RMSE of the cost function could be as high as 3.71 mm at times. However, with the calibration, the average RMSE reduces to 0.54 mm.

This camera is robust in its performance of carrying out position measurements once it is calibrated. The experiments show that in x direction the camera is capable of providing measurements with an average accuracy of up to 0.31 mm with a standard deviation of 0.26 mm. In y direction the average accuracy was up to 0.37 mm with a standard deviation of 0.24 mm. This is reasonably high accuracy for a camera which is intended to provide distance measurements at 1 kHz.

7.4 Testing of the Robot with FPGA Based Hardware PD Controller

A hardware based PD type controller was implemented in the FPGA for controlling the robot. The feedback is obtained using encoders. Using this feedback, the angular

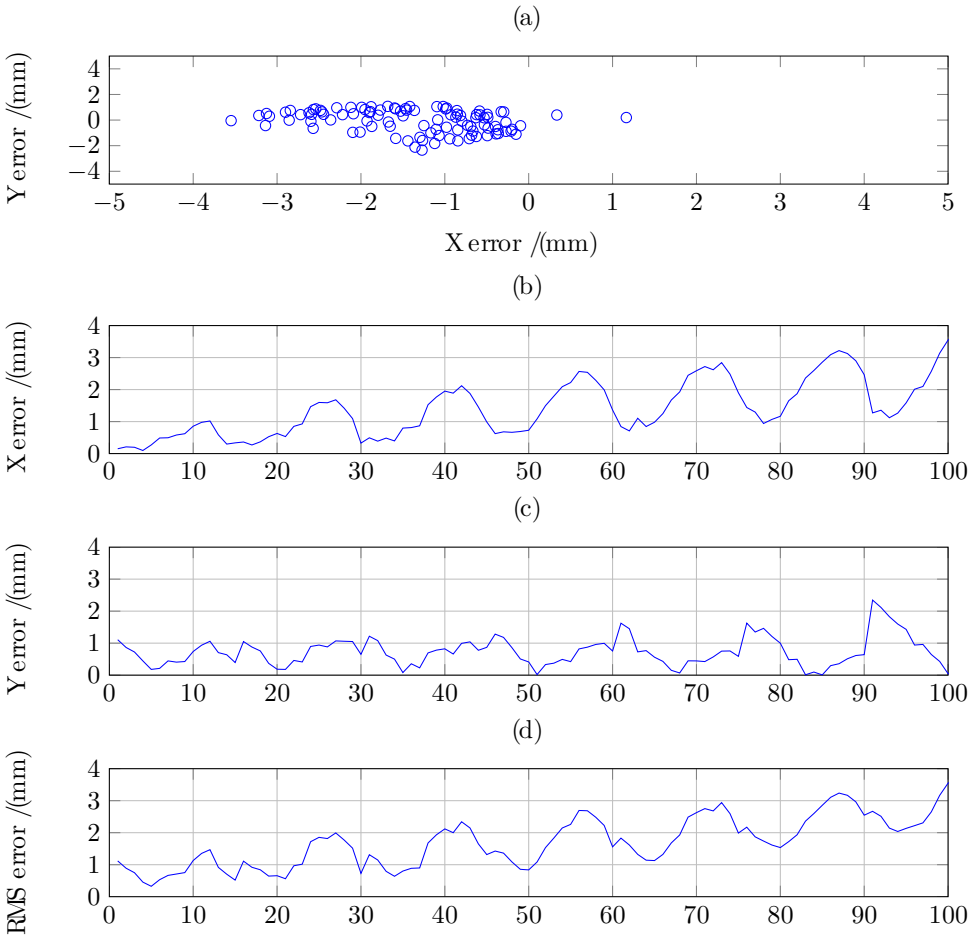

Figure 7.9: The root mean squared error of measurements in x and y directions before on-site calibration

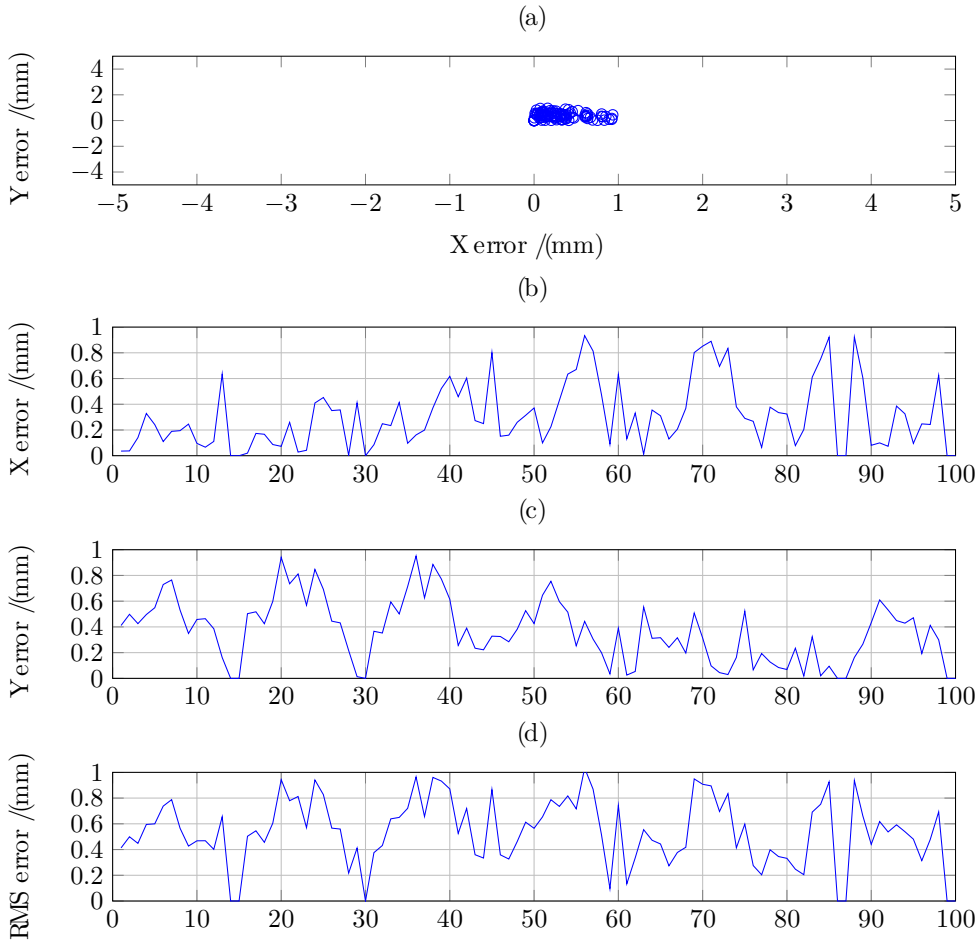

Figure 7.10: The root mean squared error of measurements in x and y directions after on-site calibration

position is estimated using quadrature decoding. The control signal is estimated using fixed point integer operations which include addition and multiplication. The control signal is given to the servo valves using an SPI/out interface. All these operations are implemented in hardware using logic gates. Therefore, this controller is capable of updating the control signal at very high rates.

The response of the robot to a step input of the joint angles from -15^o to $+15^o$ is considered to evaluate the performance of the controller. The variation of the robot angle with time is shown in Fig.s 7.11, 7.12. The response of the robot has been shown for a range of proportional gain values. These gains produce an over damped response to an under damped response which results in an overshoot of the links before it reaches stability. The angle of the first link will have a larger steady state error when the proportional gain is less than 10. In order to reach the steady state, it will take 325 ms with a proportional gain of 15. However, the time it takes to reach steady state decreases as proportional gain increases. Therefore, steady state is reached in 180 ms with a proportional gain of 25. Following a similar pattern, during the above test second link angle does not reach the desired value even in 1 s, when the proportional gain is less than 10. This would take 270 ms with a proportional gain of 15 and 178 ms with a proportional gain of 25. During this experiment, the controller operated at a frequency of 1.5 kHz.

The controller was implemented in both hardware and the NIOS II virtual processor. In both these cases the feedback and SPI/out interface is implemented in hardware. However, in the latter controller the PID control algorithm is implemented using a soft processor configured in the FPGA. This processor is programmed using the C

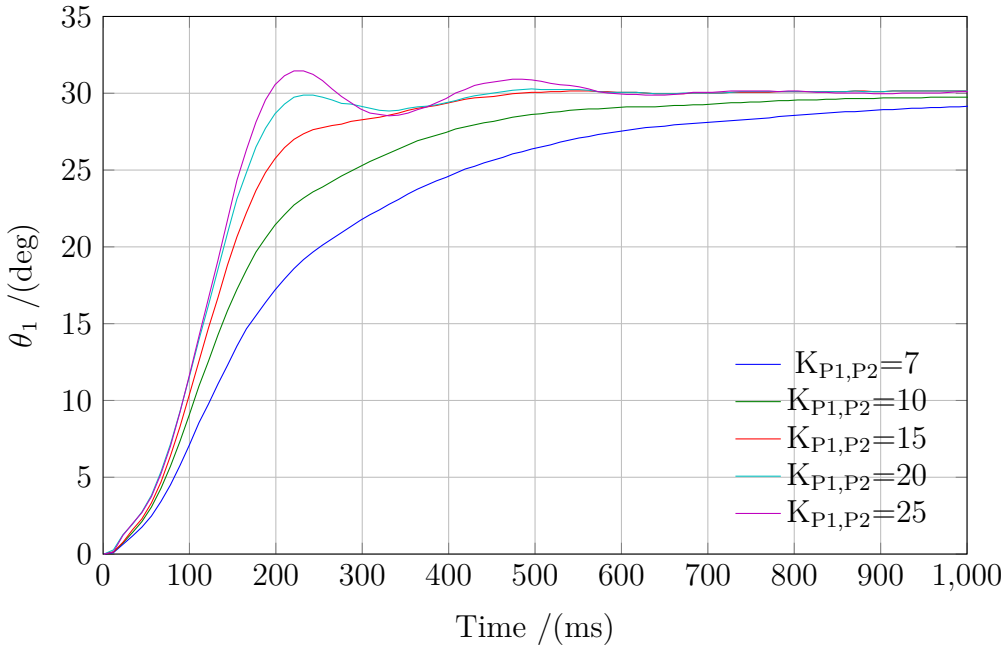

Figure 7.11: The response of θ_1 to a step input from -15^o to -15^o (The units of K_{P1} and K_{P2} are in bits/pulse)

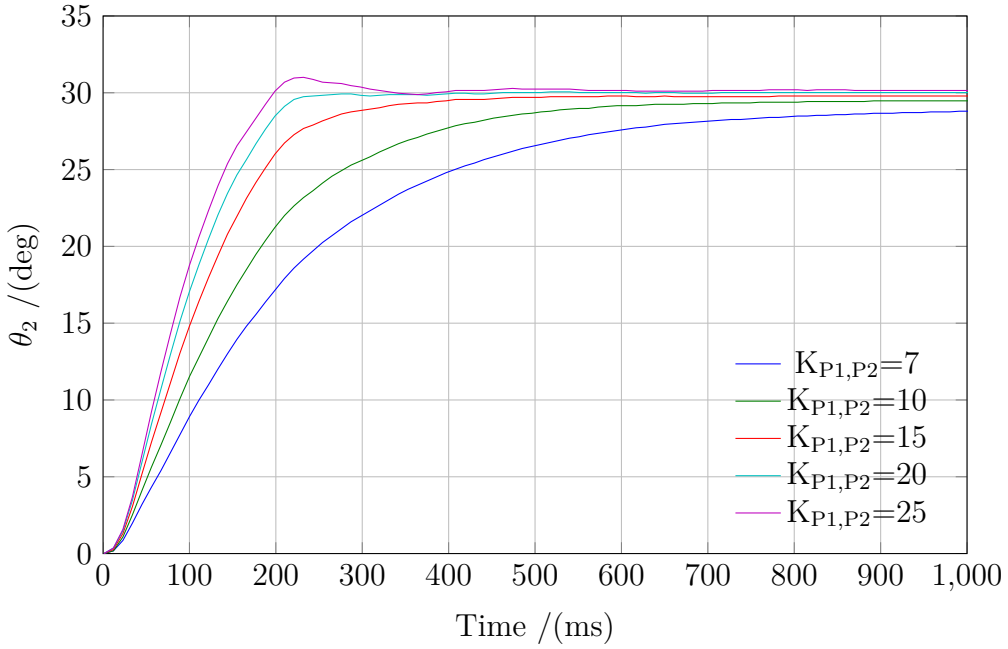

Figure 7.12: The response of θ_2 to a step input from -15^o to -15^o (The units of K_{P1} and K_{P2} are in bits/pulse)

programming language. Although an FPGA is used, it is programmed similarly to a microcontroller or a microprocessor when the NIOS processor is used. Fig. 7.13 displays the performance of the controller implemented using hardware and the NIOS II processor. It shows that both these controllers have a similar performance.

7.4.1 Performance of the FPGA Controller

The speed of these algorithms is important for the performance of the control system. Since the arm could move at high speeds, it is important that the control signal is updated frequently. Some of the calculations in the proposed algorithm involve complex functions. Sometimes the control algorithm has to perform computationally expensive mathematical operations such as forward kinematics, inverse kinematics, estimation of the Jacobian matrix, etc. In the proposed controller, the interface for obtaining feedback and sending the control signal to the valves has been implemented in hardware. It would be worthwhile to explore the time taken to execute some parts of code and the functions. It would provide an indication of the performance of the proposed hardware based controller.

This study used PD based independent joint control strategy for controlling the EE of the robot. This algorithm was implemented using both the microcontroller and an FPGA. The microcontroller consisted of an 8-bit PIC 18F4550 from Microchip technology. A DE0 educational board which consists of an Altera® Cyclone III chip was used as the FPGA. The time it takes to execute the PD joint control algorithm is shown in Table 7.1. The results show that the FPGA based implementation (both hardware and Nios) is much faster than the 8-bit microcontroller.

The PD control algorithm involves obtaining feedback, making calculations and

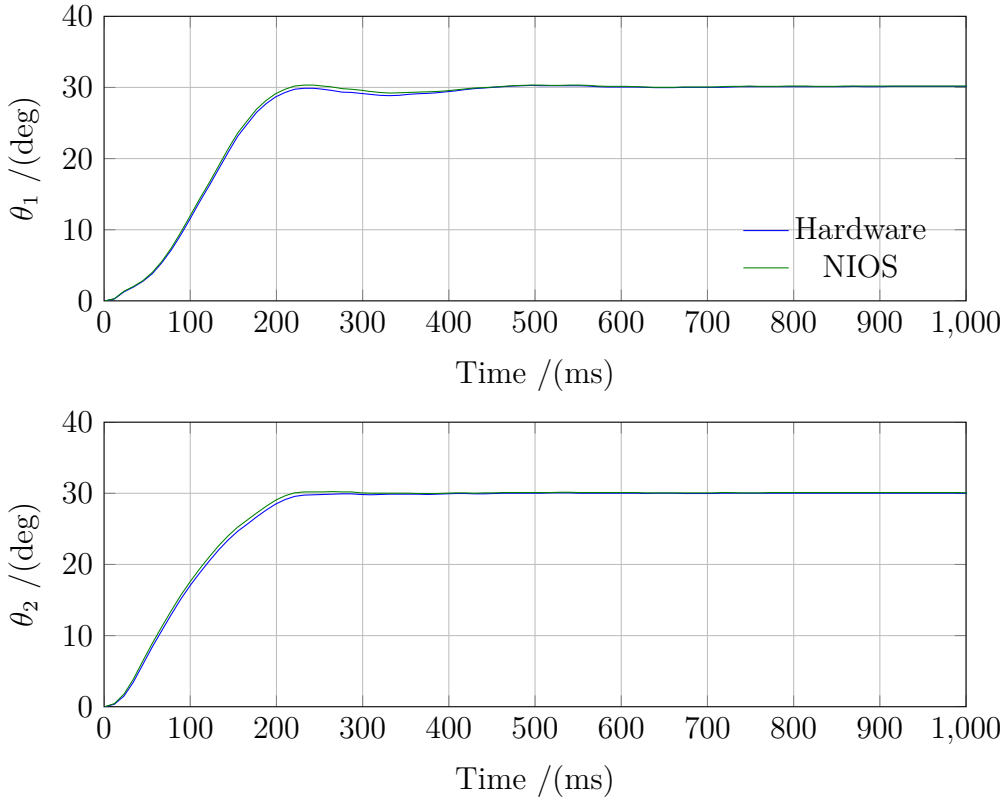

Figure 7.13: The performance of the controller implemented using hardware and NIOS processor

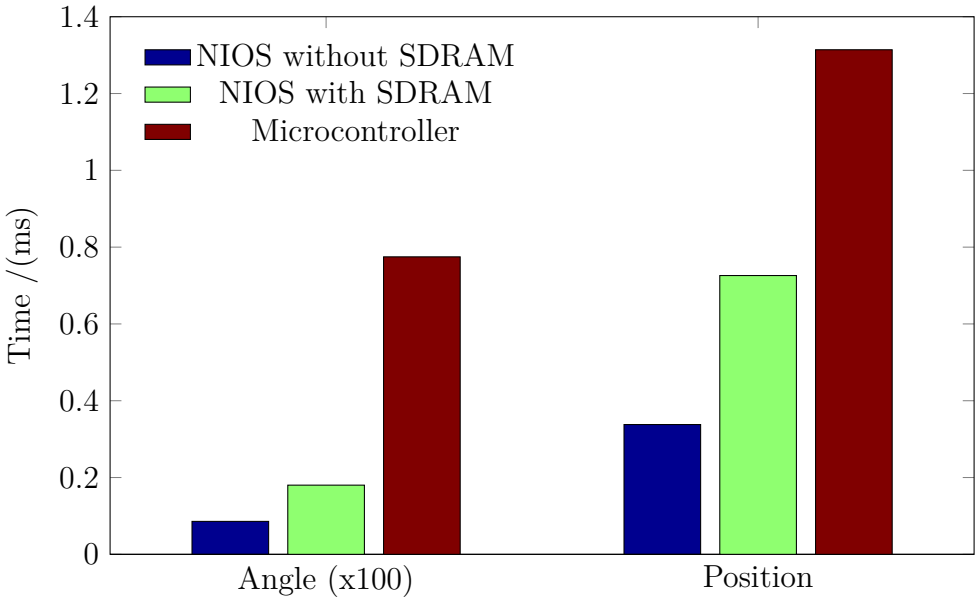

Figure 7.14: Speed of obtaining 100 encoder readings and a position reading as feedback

updating the control signal. The feedback consists of the input from the encoders. Therefore, quadrature decoding has to be carried out for a more accurate measurement of the angular position. The CMOS IC HCTL−2017 was used for quadrature decoding. The 8-bit microcontroller will obtain the reading as 2, 8-bit parallel signals which gives a resolution of 16 bits. In the case of the FPGA, quadrature decoding has been implemented in hardware. In the 8-bit microcontroller's case, by contrast, the calculation of the control signal is performed by the software. With the FPGA it is performed by both software and hardware, as shown in the two cases. The output is sent to the valves using a Max 541 16-bit DAC. This chip requires SPI/in interface. In the 8-bit microcontroller, the SPI/in interface has been implemented in software; in the FPGA it was implemented in hardware.

The hardware implementation provides the most basic logic level implementation of various functions. This is the simplest form of implementation of any function. Hence,

it provides much faster speeds of execution. Thus, hardware based implementation provides an almost 100 times faster implementation of the PD control algorithm compared to the software implementation. The feedback of the visual servoing system is

Table 7.1: Speed of execution of the PD algorithm

	Time \(μ s)
Hardware	1
Nios II	3
Microcontroller	102

obtained using encoders and a camera. The process of obtaining the encoder feedback was explained earlier. The feedback from the high speed camera is obtained using four 16-bit ADCs in parallel operation. The data acquisition from the ADC requires an SPI/in interface. This is implemented in software for the 8-bit microcontroller where as it is implemented in the hardware for the FPGA. The signal from the camera requires median filtering for removing noise. This has been implemented using software in both cases. In the FPGA, median filtering has been implemented in the Nios processor.

The time it takes to obtain a single feedback reading is shown in Fig. 7.14. It can be seen that the FPGA is much faster compared to the 8-bit microcontroller. The FPGA uses a Nios II virtual processor for the implementation of some of the complex functions. In this study, the processor considers both SDRAM and on chip memory as options for carrying out the arithmetic and logic operations. Although the SDRAM provides a much larger memory for the operations, it is much slower compared to the on chip memory. Angular measurements from the encoders are almost 9 times faster and the position measurement from the camera is almost 4 times faster with the FPGA using on-chip memory, as compared to the 8-bit microcontroller. The

results also show that the SDRAM is almost 2 times slower than the on chip memory in both cases. With the FPGA using the hardware implementation it takes 0.858 μs for a single encoder reading and 0.338 ms for obtaining the position of the IR marker on the image sensor.

The implementation of the SPMC requires the execution of several different functions. Some of these functions include estimation of the absolute position of the EE, estimation of the support column deflection and inverse kinematics. The time taken to perform the functions is shown in Fig. 7.15.

The estimation of EE position requires obtaining the x,y position of the IR marker on the PSD (similar to position measurement above), application of the pin hole camera model and accounting for the rotation and translation of the camera. These operations involve floating point calculations and trigonometric functions. The FPGA, if it uses only the on chip memory, takes only 0.742 ms to estimate the EE position. However, if the FPGA uses SDRAM as memory it would take 1.53 ms; it would take 1.764 ms with a 8-bit microcontroller. These results also show that the camera is capable of operating at 1350 Hz for carrying out the position measurement. This is a very high frequency compared to existing technologies.

The SPMC requires the estimation of deflection of the support column. This requires obtaining the feedback from the encoders and the camera, the application of forward kinematics and performing some of the algebraic manipulations and trigonometric calculations. The results show that it takes 2.79 ms for the FPGA with on-chip memory to perform these operations and estimate the angle of deflection due to torsional deflection of the support column. It is also seen that performing this operation

using a 8-bit microcontroller is more than two times slower.

The time taken to perform inverse kinematics of the arm can also be seen. This involves the calculation of several inverse tangent functions. In case of the FPGA, the Nios processor will carry out inverse tan operations. Hence, the inverse kinematics involves only a software implementation. It is seen that the Nios processor with on chip memory and the 8-bit microcontroller take 3.163 ms and 3.242 ms, respectively. Hence, both these devices take almost the same amount of time to perform the inverse kinematics of the arm. However, the FPGA takes almost double this time if SDRAM is used as memory in the configuration.

The FPGA with on-chip memory has a much better performance as compared to the 8-bit microcontroller. This is because hardware based implementation uses logic level implementation and thus works at much faster speeds.

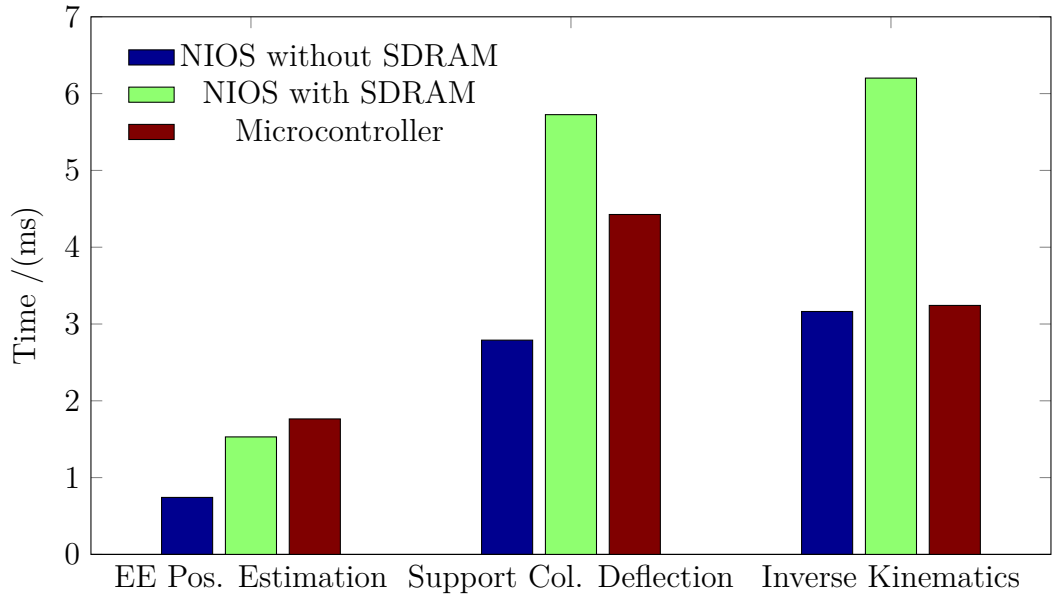

Figure 7.15: The performance of the controller implemented using hardware and NIOS processor

7.5 Validation of the Bond Graph Simulation with Experimental Results

During tests, the robot EE position is expected to move on a desired linear trajectory from (425 mm, 333 mm) to (550 mm, 232 mm) in the robot work space. Three separate cases were considered for testing the manipulator. These cases consider desired average EE velocities of 1.1, 0.8 and 0.6 ms^{-1}. These are denoted as $C1$, $C2$ and $C3$, respectively. The EE payload was 12 kg.

Fig.s 7.16, 7.17 and 7.18 show a comparison between results from the 20 Sim simulation and experimental results for EE position for the three cases considered. SPMC strategy was used to control the manipulator in these simulations and experiments. It could be seen that the experimental results closely match the simulation results only at lower speeds of the EE (Case 2 and 3). When the manipulator operates at high speeds there are considerable discrepancies between the simulated and experimental results (Case 1). The controller performed control signal updates only at a frequency of 140 Hz. If the control signal was updated at a much higher frequency it would have resulted in simulation results being closer to experimental values even at high speeds of the manipulator. There may be also be other reasons behind this variation. During the simulation, it was assumed that the controller was continuous one. However, in reality it operates as a discrete digital controller. This discrepancy could also be attributed to the errors in camera measurement. These errors were not considered in the simulation. There are also inherent non-linearities in hydraulic systems. Therefore, these could also could result in different simulated and experimental results.

The support column of the manipulator consists of an I-shaped cross section. The

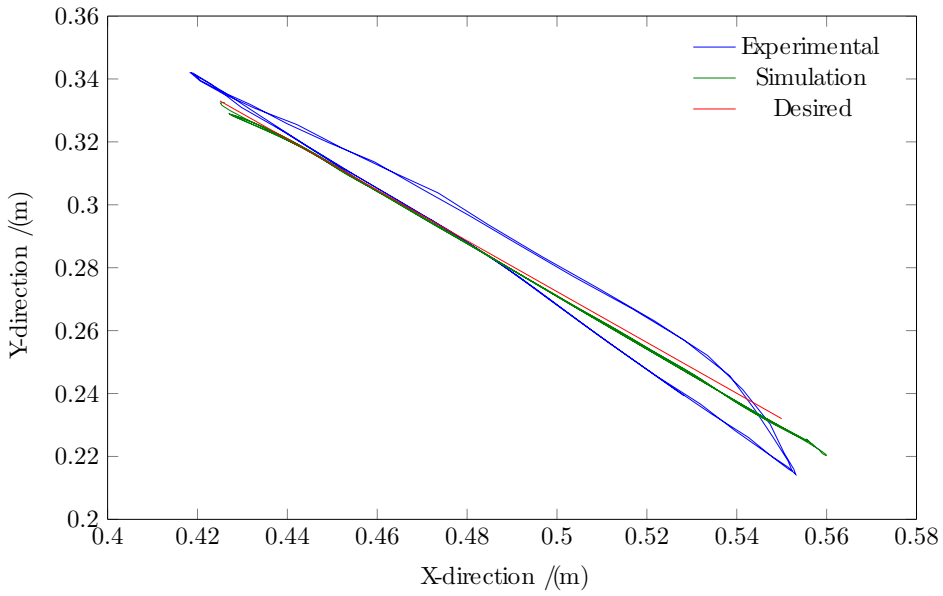

Figure 7.16: A comparison between simulation and experimental values with SPMC for EE position for case 1

estimation of angle at which the support column twists under torsion is an important part of the SPMC algorithm. The methodology for calculating the angle of twist was presented in Section 4.6. The angle of twist for the compliant support column during experiments and simulation results are shown in Fig.s 7.19, 7.20 and 7.21. It is seen that these two follow each other with minor discrepancies between the simulation and experimental results. There could be several reasons for the variation between the two. In modeling this column it was considered as a simplified lumped-segment model. It was also assumed that the beam has homogeneous properties uniformly distributed along the column and that the first actuator is symmetrically attached to the 'I' beam. These assumptions could have contributed to differences between the two.

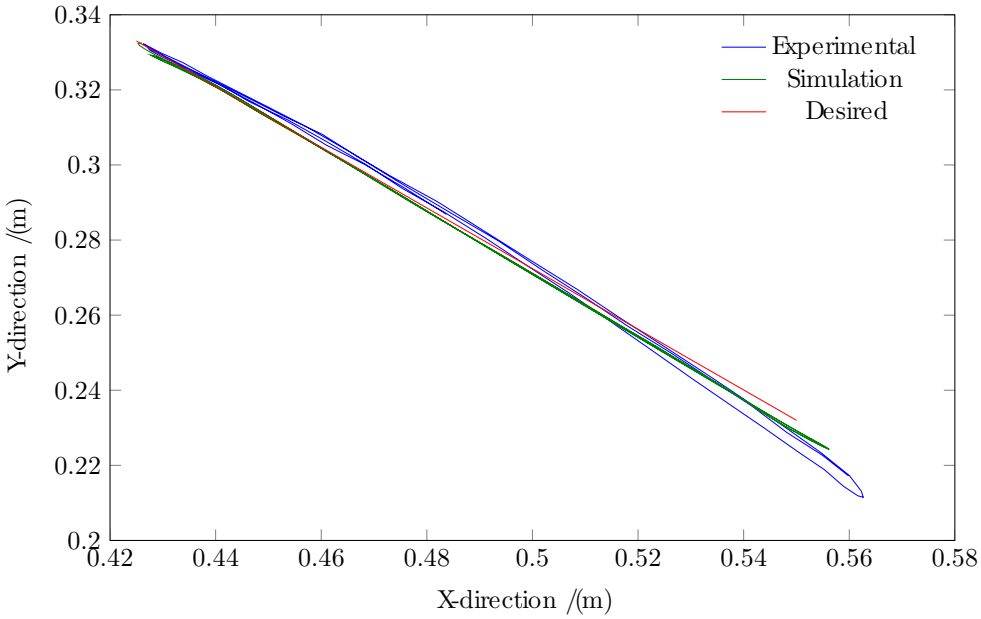

Figure 7.17: A comparison between simulation and experimental values with SPMC for EE position for case 2

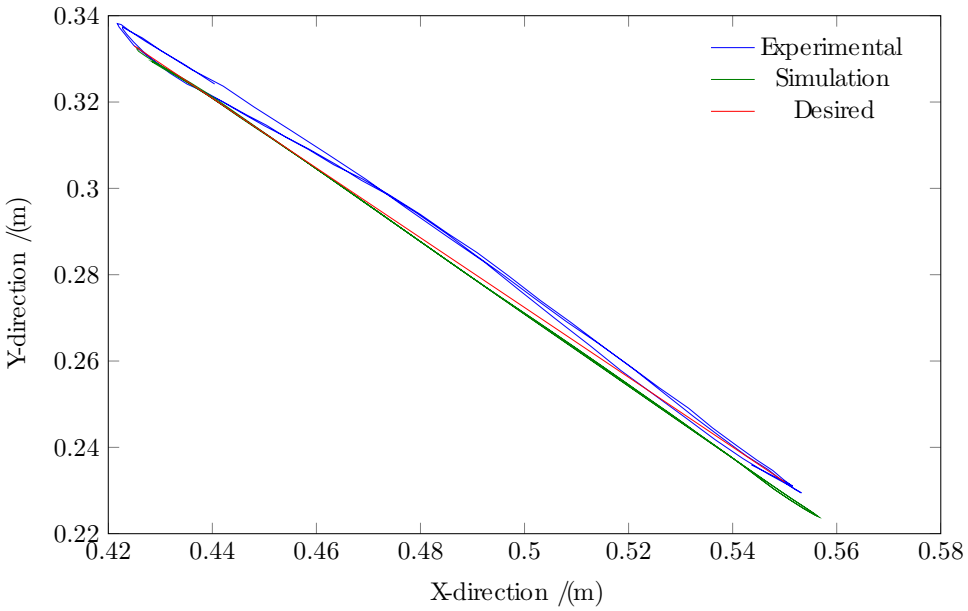

Figure 7.18: A comparison between simulation and experimental values with SPMC for EE position for case 3

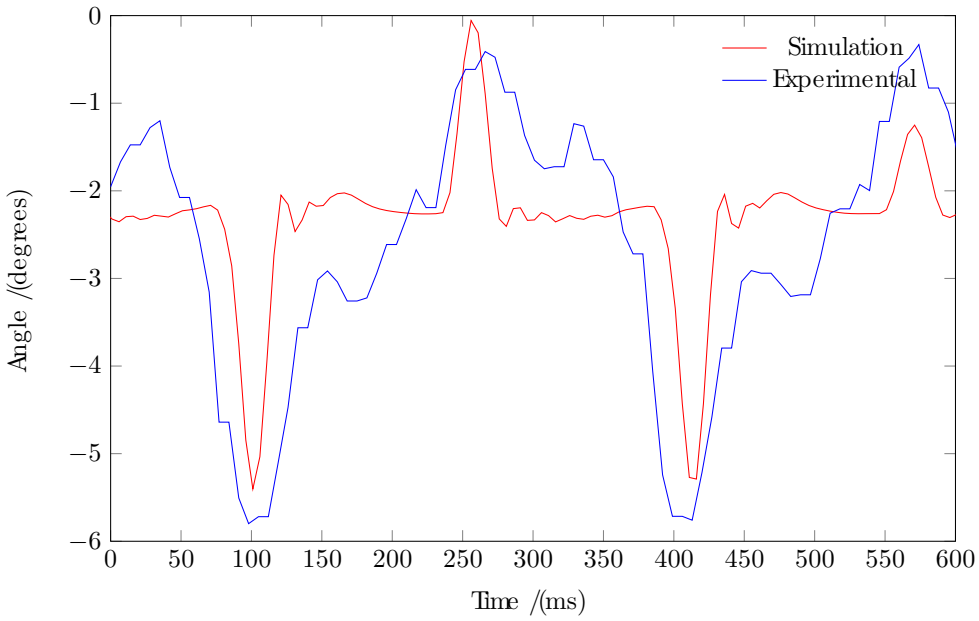

Figure 7.19: A comparison between the simulation and experimental values with SPMC for support column deflection for case 1

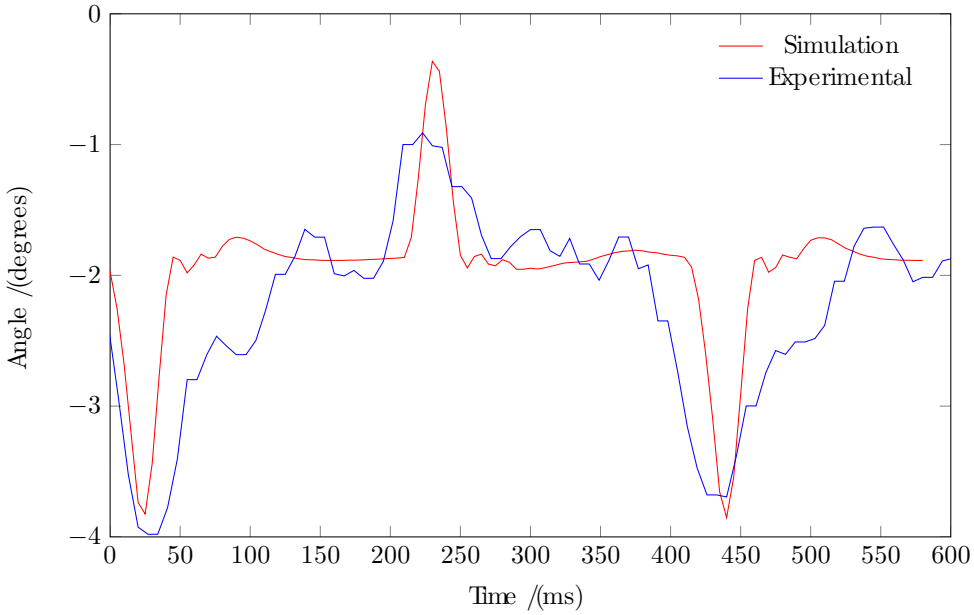

Figure 7.20: A comparison between the simulation and experimental values with SPMC for support column deflection for case 2

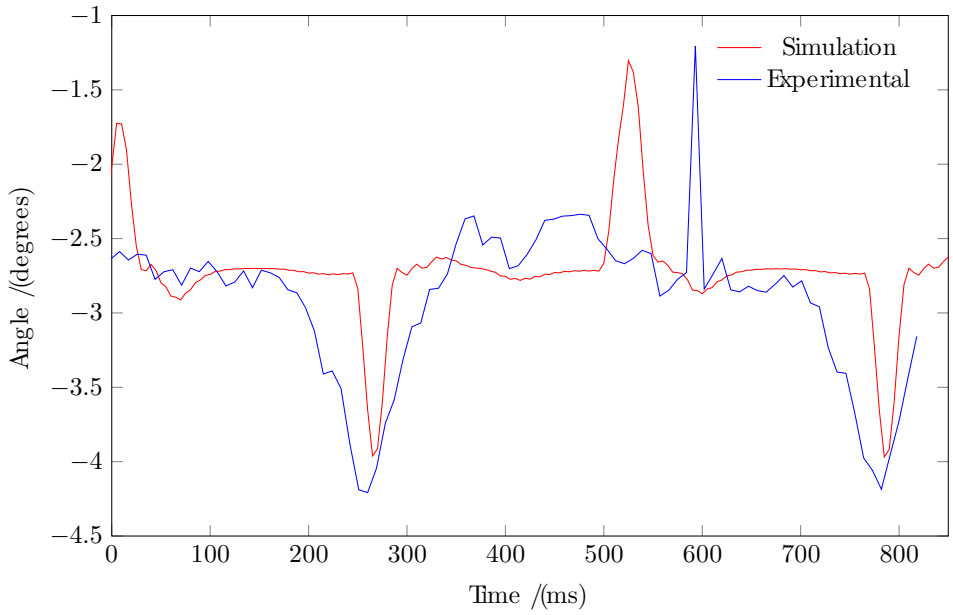

Figure 7.21: A comparison between the simulation and experimental values with SPMC for support column deflection for case 3

7.6 Testing of the High-Speed Visual Servoing System

7.6.1 Proposed Single Time Scale Visual Servoing System

The proposed single time scale visual servoing system was presented in an earlier Section. It integrates the feedback from the 2-D PSD based optical position sensing system as the exteroceptive sensor and high resolution joint encoders as proprioceptive sensors. The FPGA was used to implement the complete controller along with the interfaces for sensors, computational elements associated with kinematics and control laws. The control algorithm was implemented using the NIOS II processor. The objective of the proposed control algorithm is to implement a single time scale visual servoing system. The main objective is to simultaneously use feedback from both

encoders and the high speed camera for calculating the control signal. The proposed controller should be robust to the effects from support column vibration and flexing of the links.

In the first experiment, only the camera was considered as feedback for controlling the EE. Fig.s 7.22, 7.23 show the desired and actual EE, x,y position for these three cases. Fig. 7.24 show the results for xy workspace.

During the tests the EE was subjected to a maximum velocity of 0.93 ms^{-1} in case $C1$, 0.73 ms^{-1} in case $C2$ and 0.61 ms^{-1} in case $C3$, respectively. From the results, it can be seen that there is a time lag between the desired and actual values of the EE position. This time lag is 80 ms in case $C1$ and 50 ms in cases $C2$ and $C3$. It could be attributed to the frequency of the control system and system dynamics. If the controller operates at a much higher frequency this phase difference could be a minimum. It can also be seen that, compared to case C1, case C3 is closer to the desired response. These results show that a satisfactory control performance can be obtained by using the feedback from the high speed camera.

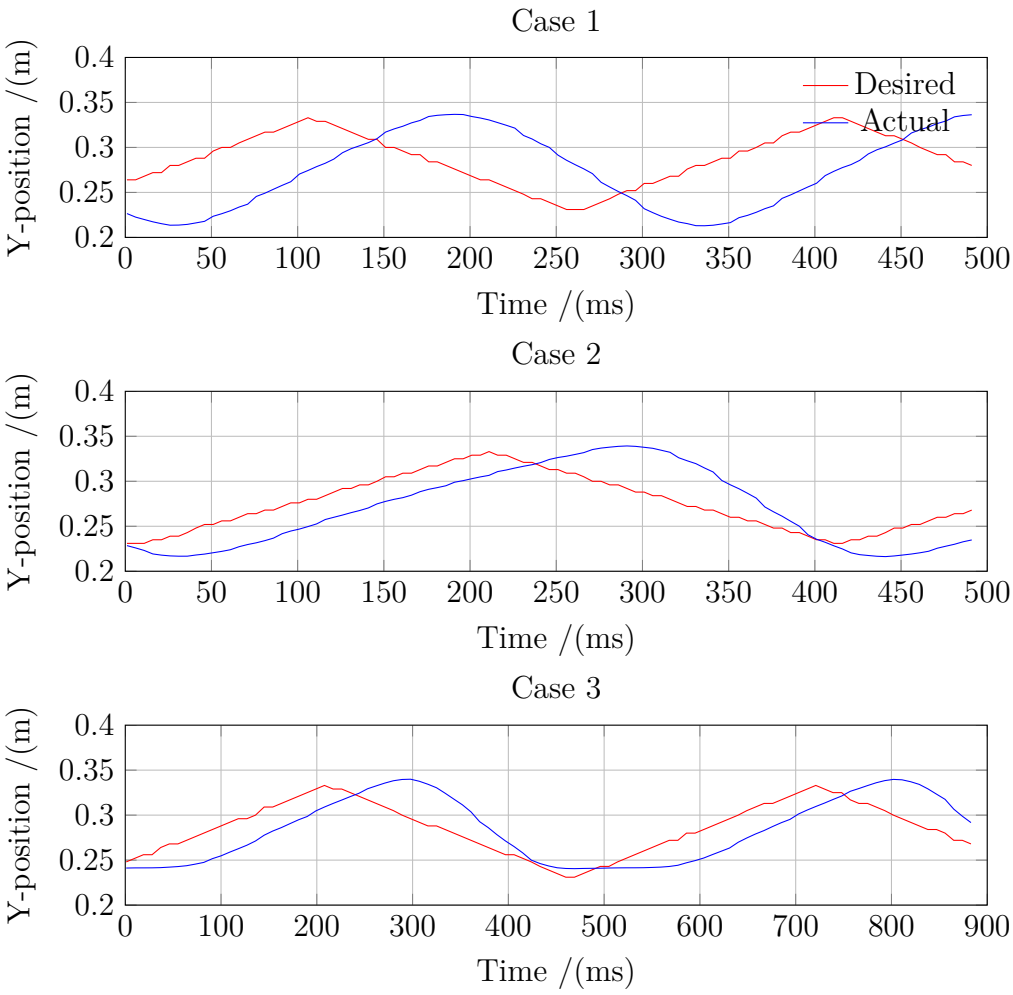

Figure 7.22: Position of EE in x-direction with only the high speed camera as feedback

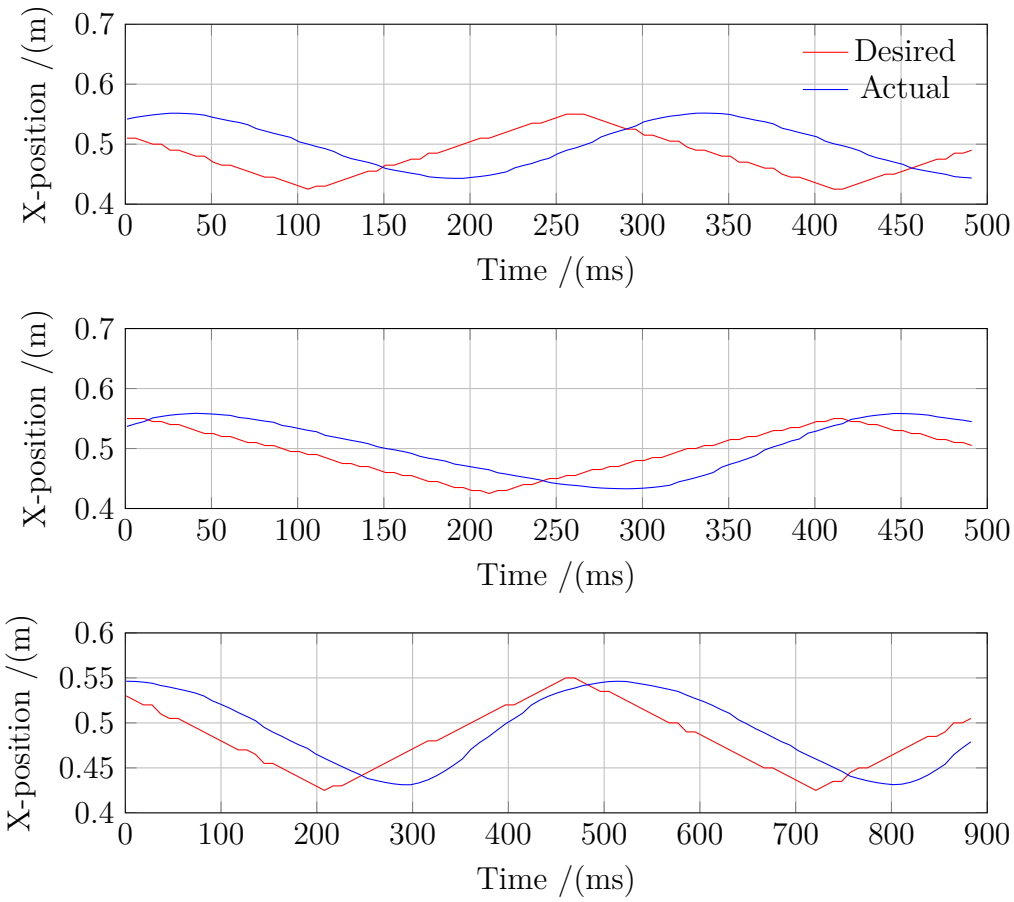

Figure 7.23: Position of EE in y-direction with only the high speed camera as feedback

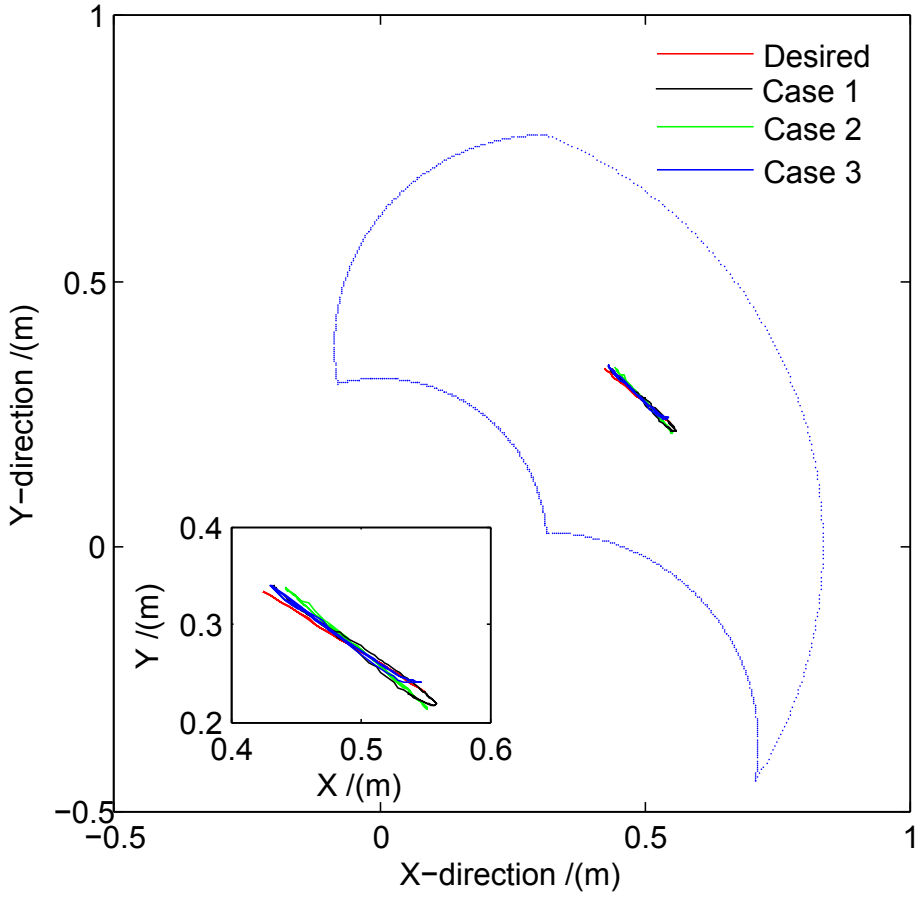

Figure 7.24: Position of EE in robot workspace with only the high speed camera as feedback

In second experiment, the feedback was obtained from both the high speed camera and optical encoders. It considered the same desired trajectory along with the three cases (C1, C2 and C3) as above. The controller performed single time scale visual servoing at a frequency of 330 Hz. The position response for x,y directions of the workspace are shown in Fig.s 7.25, 7.26. These graphs show the desired position of the EE along with the experimental and simulated values. The simulation results were obtained from the 20 Sim model that was developed in an earlier chapter. It is seen from the results that the simulation values are somewhat closer the desired position. However, there is a phase shift between the desired and experimental values. The phase delay in case C1 is 80 ms and in case C3, 40 ms.

The position of the EE in the xy workspace for the three cases are given in Fig.s 7.27, 7.28 and 7.29. According to these figures, the EE response from the 20 Sim simulation closely follows the desired trajectory. However, there is a small deviation between the desired and experimental results for the EE position. The difference between the experimental and desired values is lower in case 3 compared to case 1.

There may be several reasons for the discrepancy between the simulated and desired response. The assumptions made during the model development also would contribute these discrepancies as discussed earlier. The 20 Sim model considered the controller that is in a continuous time domain. However, the actual controller that was implemented using the FPGA is a digital controller. The SCARA arm considered in this study operates at speeds of up to 1.1 ms^{-1}. Therefore, the control signal needs to update at much higher frequencies. The frequency of the clock used in the FPGA is 50 MHz. Therefore, using an FPGA that has a 3 or 4 times faster clock frequency could result in the control algorithm reaching frequencies of up to 1 kHz.

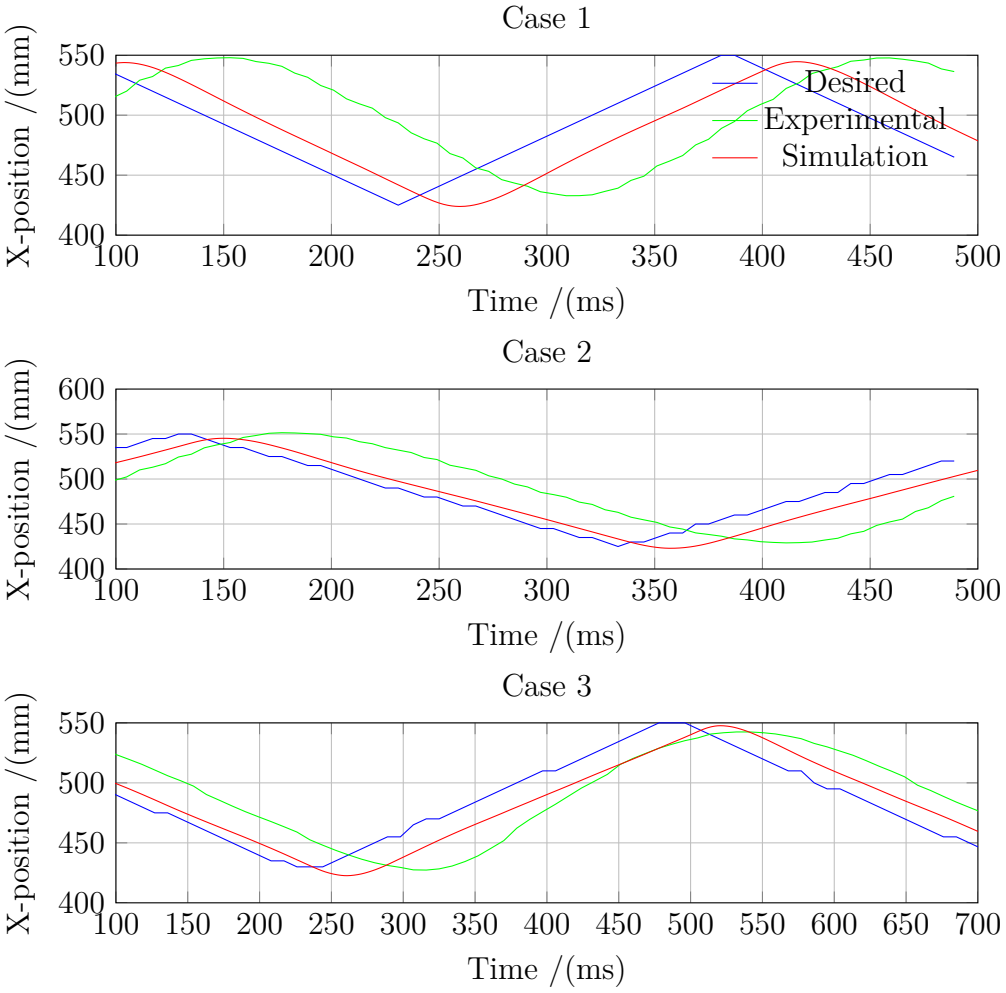

Figure 7.25: Position of EE in x-direction with the high speed camera and encoders as feedback

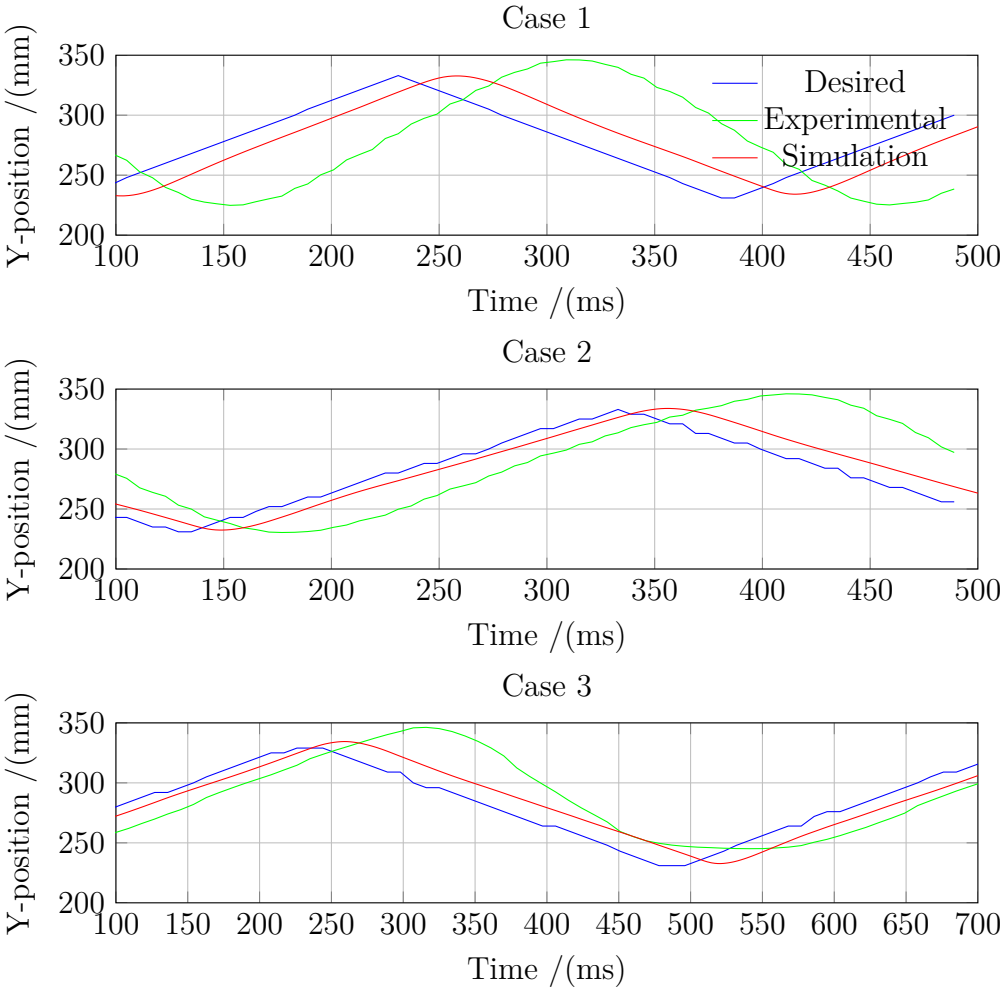

Figure 7.26: Position of EE in y-direction with the high speed camera and encoders as feedback

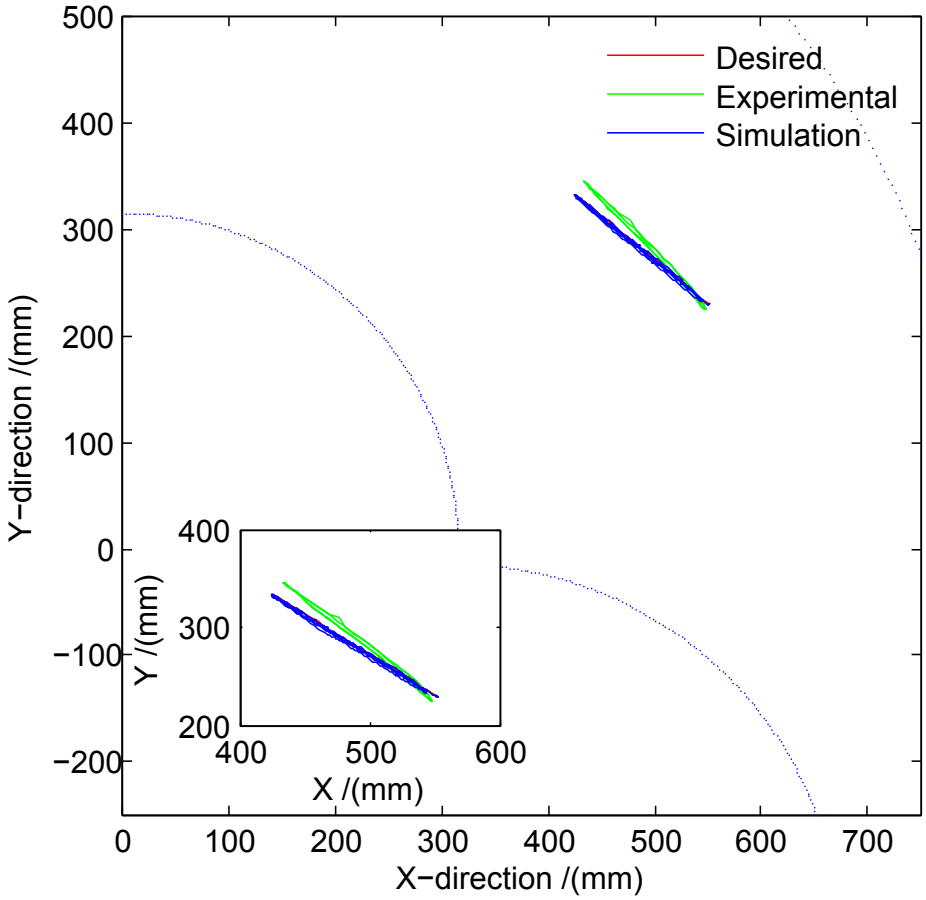

Figure 7.27: Position of EE in workspace for case 1 with the high speed camera and encoders as feedback

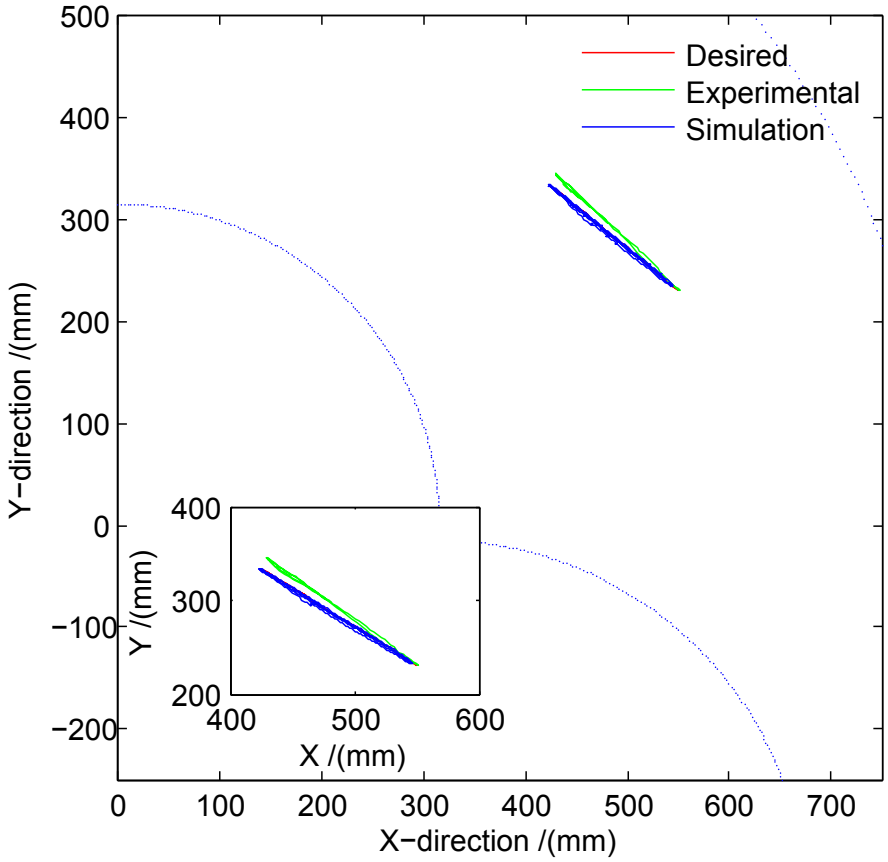

Figure 7.28: Position of EE in workspace for case 2 with the high speed camera and encoders as feedback

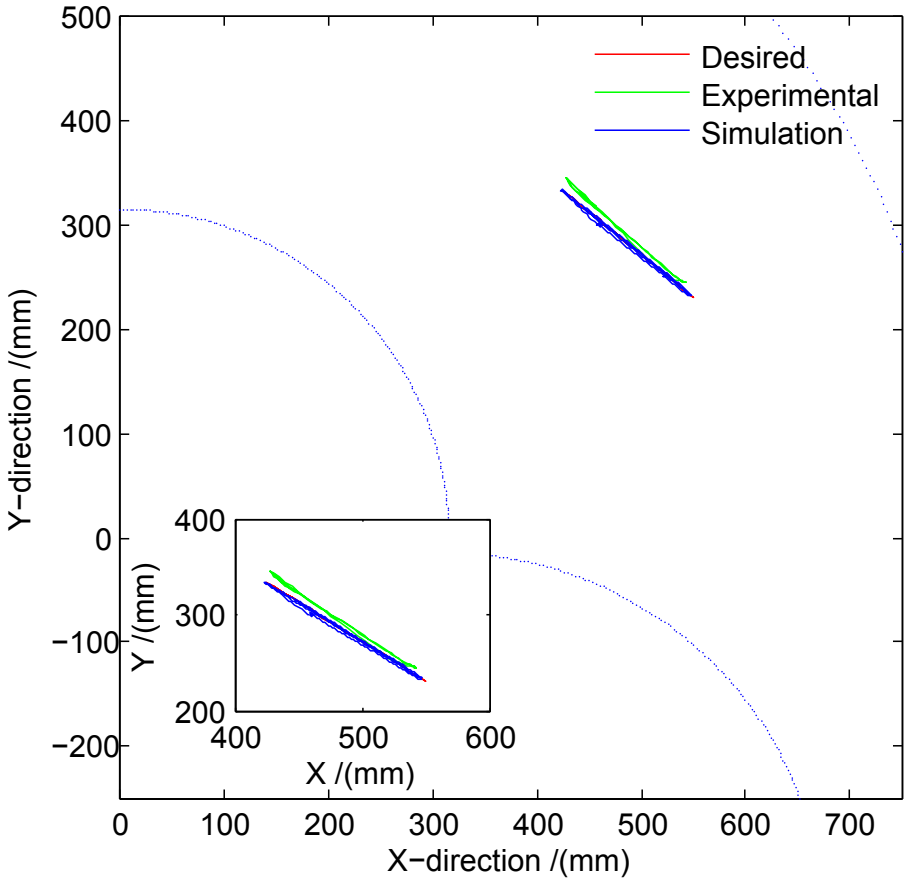

Figure 7.29: Position of EE in workspace for case 3 with the high speed camera and encoders as feedback

7.6.2 Performance of the Set Point Modification Controller

The PD controller uses only relative link angles obtained by the optical encoders for controlling the arm. The feedback from a set of proprioceptive sensors do not mitigate any effects from compliant support vibration and flexing of the links. The SPMC was proposed in this study to counteract the effects of torsional vibration of the compliant support column. Under this control strategy, the set point is modified based on the measured position of the EE by the camera.

A comparison of between the performance of PD and SPMC controllers for cases 1, 2 and 3 are shown Fig.s 7.30, 7.31 and 7.32. It can be seen that in all the cases the proposed SPMC control strategy provides a much superior performance as compared to PD control. It can also be seen that EE is closer to the desired trajectory in case 3 as compared to that in case 1. The EE reached very high speeds during the experiments. In case 1, it reached velocities of up to 2.4 ms^{-1} for SPMC control and 1.6 ms^{-1} for PD control. The same values for velocity in case 3 were as high as 1.1 ms^{-1} for SPMC control and 0.8 ms^{-1} for PD control. Therefore, visual servoing based SPMC control strategy produced a superior control as compared to PD control strategy at these speeds.

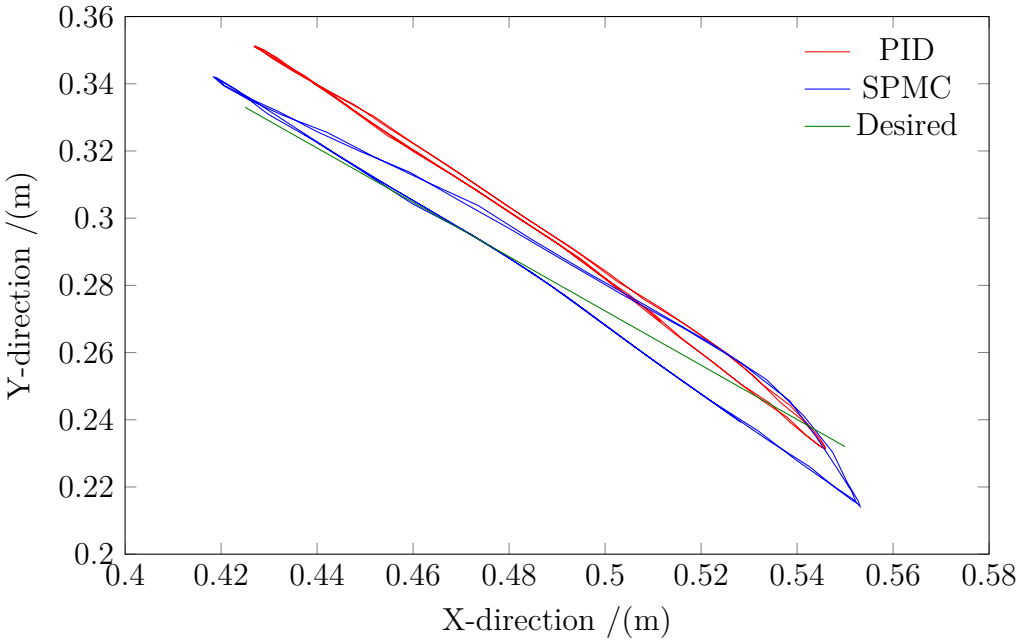

Figure 7.30: The Position of EE in the workspace with SPMC and PID controller for case 1

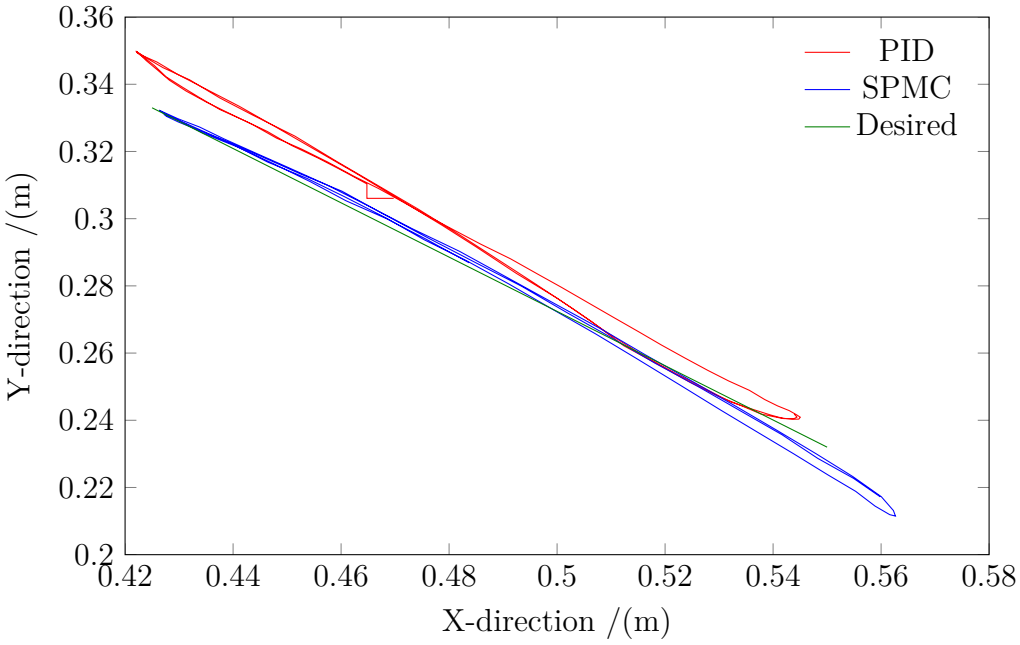

Figure 7.31: The Position of EE in the workspace with SPMC and PID controller for case 2

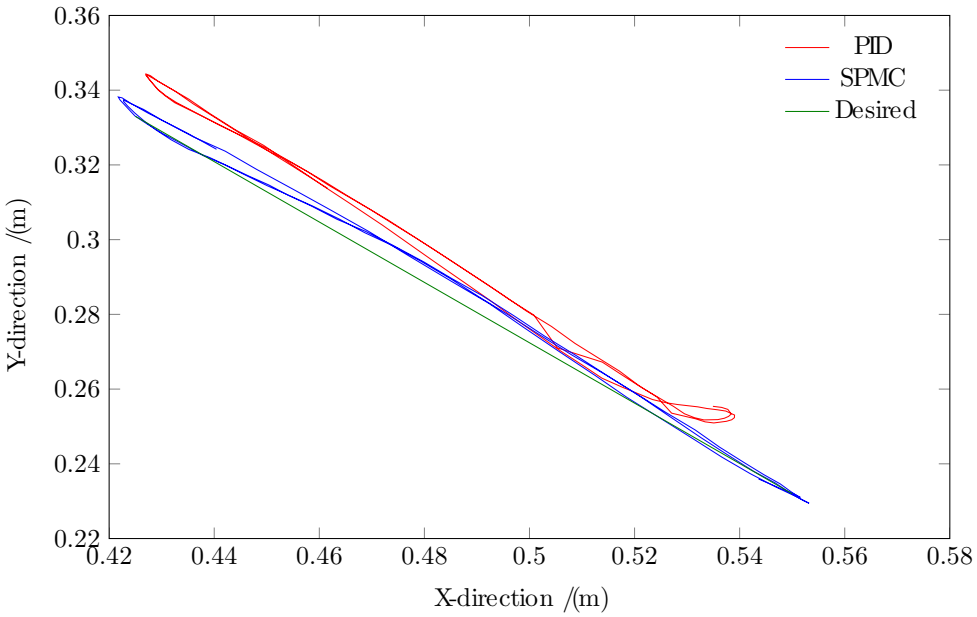

Figure 7.32: The Position of EE in the workspace with SPMC and PID controller for case 3

Chapter 8

Conclusions and Future work

The objective of this thesis is the design, development and fabrication of a high speed visual servoing system. This system is intended to be used in industrial applications such as pick and place, defect removal, industrial assembly, painting, etc. The main contributions of this work are summarized below. The future research and potential improvements to the study are presented next.

8.1 Contributions from this Study

The components of the high speed visual servoing system include a high speed manipulator, a high speed camera system and an embedded controller. The proposed manipulator has a SCARA type configuration. It is ideally suited for operations in a 2-D work space. Unlike its contemporary counterparts, the joints of this robot are driven with rotary hydraulic actuators in order to achieve unprecedented speeds. The development of the 2-D positioning system was the main emphasis of the study. The high speed camera system uses a 2-D PSD as the image sensor. The control system was implemented using an FPGA based embedded system. This was used to develop some of the input and output interfaces in hardware. A virtual processor was also

configured in the FPGA to implement some of the functions that could not be easily implemented in hardware.

The proposed system was first modeled and simulated to analyze the performance. This also revealed some of the parameters required for the design. Two different approaches were used for modeling. In the first technique, a mathematical model of the system was developed using MATLAB®-Simulink software. This mathematical model included hydraulic, robotic and control subsystem characteristics. The components modeled from this technique included the valve, actuator, SCARA robot and the controller. Simple PD control law was used to control the hydraulic manipulator. The simulation results showed that even a very basic controller could provide satisfactory controls. The simulation results showed that the actuators proposed for this arm are capable of producing torques as high as 860 Nm in 104 ms. The model developed using Matlab also did not consider external disturbances such as compliant support vibration, etc.

The double vane rotary hydraulic actuators are used to drive the links of the robot. A novel rotary hydraulic actuator was custom designed for robotic applications. It uses the double vane configuration to eliminate unbalanced shaft forces and suppress vibration. This actuator comprised components which included shaft, vanes, housing, separation wedges, side and end caps. Aircraft grade Aluminium 2024-T6 alloy was used for the housing and endcaps to minimize weight. Steel was used for the shaft because it would encounter very high shaft forces. Brass was used as the material for the vanes and side caps as it has excellent wear-resistant properties. The actuator consists of a locking mechanism which prevents the vanes from hitting the separation wedges inside the actuator chambers. It also includes a fail safe mechanism with

two shear pins so that other parts of the actuator will not be damaged if there are excessive forces. The proposed actuator was designed using Solidworks® and tested for failure using the finite element package Cosmosworks. It was fabricated at the Technical Services Division of Memorial University of Newfoundland. The fabricated weight of the actuator was 6.9 kg. The actuator was rated for operation at a hydraulic system pressure of 3000 psi.

The actuator was experimentally tested to verify its performance. The tests showed that a proportional controller alone could provide satisfactory control of the single actuator system. The test results demonstrate that the prototype actuator is capable of producing torques of up to 440 Nm at a hydraulic system pressure of 14.9 MPa (2160 psi) and with a load of 13 kg. The test results also validated the proposed mathematical model for the actuator. Electric counterparts of these actuators do not have high power to weight ratios. For example the Kollmorgen®-DH143M electric motor has a power-to-weight ratio of 2.8 Nm/kg, while the prototype actuator's is 63.8 Nm/kg. In terms of hydraulic actuators, the commercially available Micromatic® (SS-1 model) double vane rotary hydraulic actuator has a comparable displacement coefficient and is approximately 9.75 kg in weight. However, it does not have external stops, an integrated servo valve or a feedback device. The integration of these components could significantly increase its weight. The prototype actuator is also compact (114.3 x 114.3 x 127.0 mm) in size and light weight (6.9 kg) compared to other commercial actuators of similar configuration. It is also custom built to suit its application for a SCARA type robotic arm.

As the actuator tests provided a satisfactory performance, the design of the robotic arm was carried out next. Extruded Aluminum tubes were used as the links of the

robot. The final dimensions of the links of the SCARA arm were 0.49 and 0.36 m. The actuators of this robot were instrumented with joint encoders to provide the link angles to an accuracy of up to 0.045°. This manipulator was controlled with a custom designed controller board with a PIC® 18F4550 microcontroller using quadrature decoders and 16-bit DAC for analog signal output. A PD type independent joint controller showed satisfactory control. The initial test results showed that the EE was capable of reaching velocities of up to 2.7 ms^{-1} with a 5.3 kg payload. This is a much higher value compared to 0.9 ms^{-1} with a similar payload produced by the Adept® Cobra s800 commercial robot, which is a commonly used robot for similar industrial applications. Initial tests showed that high speed movement of the robot could produce considerable deflection of the support column. Therefore, a more advanced control strategy had to be implemented for more accurate controls. This could be done only by considering the actual position of the EE in the control algorithm.

Mechatronic systems are multi-domain systems. Bond graph theory provides a unified way of modeling multi-domain systems in a single graphical representation. The system considered in this study consists of servo valves and actuators which constitute a hydraulic subsystem. The SCARA arm and the compliant support column comprise a mechanical subsystem and the controller is included as an electronic subsystem. Bond graphs were developed for each of the sub-components in this study and finally they were connected together to represent a single system. The complete visual servoing system was modeled and analyzed using bond graph theory.

The development of the high speed camera system was carried out next. An improved tetra lateral type 2-D PSD was selected as the image sensor. This PSD has a very low rise time and high photo sensitivity. The operation of the PSD required reverse

biasing of the cathode by 5 V and signal conditioning to eliminate noise. A printed circuit board was designed for performing these operations. It included circuitry for reverse biasing, implementing a low pass filter and performing data acquisition. This PSD has inherent non-linearities on the sensor surface. Thus, the PSD itself required calibration before it could be used for position measurements. The calibration provided the relationship between the actual position of an IR spot on the image sensor and the currents induced.

The printed circuit board with the PSD was mounted onto a camera housing. The camera comprised a c-mount lens and an IR filter. In order to use this camera the estimations of both extrinsic and intrinsic parameters are required. To estimate the intrinsic parameters, the camera was mounted onto a camera calibration setup in Memorial University. Heikilla and Rahman are two popular camera calibration techniques in use today. The method proposed by Rahman provided a lower re-projection error. This calibration provided effective focal length of the camera, position of the image center and lens distortion parameters. Subsequently, the camera was mounted onto a stand near the robot overlooking the EE which comprised an IR marker. An on-site calibration was required to estimate the extrinsic parameters of the camera. An algorithm to carry out this was developed as a part of this study. The on-site calibration algorithm provides the position and orientation of the camera w.r.t. a world coordinate frame. It also provides flexibility to estimate the intrinsic parameters of the camera if there are uncertainties associated with the earlier estimation.

An embedded controller for this robot was developed using an FPGA. Using contemporary FPGA technology, a powerful virtual processor can be synthesized and integrated with custom hardware to create a dedicated controller. The virtual soft

processor provided the flexibility to implement complex functions in a hardware platform. The embedded system developed comprises input/output interfacing and controller implementation. DE0 educational board with Altera®'s Cyclone III processor which is a low end FPGA was used to demonstrate implementation. The feedback for controlling the robot was obtained using joint encoders and a high speed camera. The quadrature decoding which is required to estimate the joint angles was implemented in hardware. A SPI-In interface is required to obtain the signal from the PSD camera. The SPI-In interface required to obtain the camera input was also implemented in hardware. The servo valves require an analog control signal for operation. This signal is output via a 16-bit DAC. This DAC required an SPI-out interface which was also implemented in hardware. This camera was capable of providing position measurements at speeds of up to 1350 Hz. This is a much higher rate compared to some of the existing cameras used for similar purposes. The measurements made by this camera will have an average RMSE of 0.31 mm in x direction and 0.37 mm in y direction. This is a high accuracy considering that the camera operates at very high frequencies.

The hardware design consisted of a Nios II soft processor. In order to implement this soft processor, peripherals such as onchip memory, input/output pins, timers, UART and system id were included in the design. This processor was used to implement complex functions and some of the calculations. Performing the forward kinematics, inverse kinematics and jacobian estimation of this manipulator involves trigonometric functions and other complex mathematical operations. This processor provides much flexibility for complex trigonometric functions and dividing operations that are usually difficult to implement in hardware.

It was seen that the hardware implementation provided much faster feedback. Measurement of the joint angles was 9 times faster and the position measurement from the camera was 4 times faster with the FPGA using onchip memory as compared to a PIC® 18F4550 microcontroller. The FPGA provided a logic level implementation of various functions. This resulted in much faster speeds of execution. Implementation of the PD control algorithm in hardware is 100 times faster than the same implemented in software using a microcontroller. It would take only 1 μs for a single execution of the PD control algorithm.

Several control algorithms were considered in this study for controlling the robot. These comprise basic PD based independent joint controllers to more complex control algorithms. The PD based joint control algorithm was implemented in both hardware and software. The Nios II processor was used for the implementation of the software based PD controller. In addition, a number of other controllers were used in this study. These included feed forward based SPMC and single time scale VS. These controllers were implemented in the Nios II processor. The SPMC calculated the deflection of the EE in real time and introduced a correction for deflection due to torsional vibration of the support column. Single time scale VS considered the feedback from the encoders and a high speed camera simultaneously for calculating the control signal. This was capable of updating the control signal at 330 Hz.

8.2 Limitations of this study and future work

The main focus of this study was the development of a high speed SCARA arm. It uses two double vane rotary hydraulic actuators to drive this arm. These actuators have a span of only 100 degrees. Therefore, it limits the robot workspace as compared

to contemporary electric manipulators. These actuators require a hydraulic supply for operation. Therefore, a hydraulic power unit has to be used for this. It adds complexity and also results an expensive option. In addition to this, hydraulic systems are associated with potential leakages making it difficult to maintain a fluid free, dirt free environment. However, it could be prevented by carefully designing a leak proof casing for this arm.

The proposed manipulator is a 2 DOF arm capable of performing operations in 2-D workspace. In future studies, it should consider extending the current principle towards the development of high speed 6 DOF systems. This manipulator has used only custom built servo hydraulic actuators. Some of 6 DOF configurations such as the Stanford arm require actuators for driving prismatic links. This would require the development of novel custom built high speed linear actuators using hydraulics.

This study only covered the design and the development of the horizontal positioning mechanism of the SCARA arm. Future studies should also consider the design and development of the EE for the arm. The configuration of the EE will largely depend on the application. The dynamics of this manipulator needs to be considered with a real and a moving EE on the arm with a considerable weight. The positioning of this EE to perform a specific industrial operation also needs to be studied.

The current study considers only a narrow field of view of its workspace. It would be more useful if the camera could cover a larger portion of the workspace. However, a camera with a larger field of view would introduce additional non-linearities due to lens distortion. As a result, additional calibration parameters and other modifications to address these issues need to be considered. The 2-D PSD used in this study

is a tetra-lateral type PSD. It introduces considerable non-linearity further away from the center of the PSD. The calibration provided a sixth order function to correct the non-linearities on the image sensor surface. However, only a third order function was used in the controller for speed. Using such a simplified model reduces the accuracy of the measurements. Duo-lateral type PSDs would be more suitable to be considered in future studies. The duo-lateral PSDs are more linear and much larger induced current, which would result in improving the accuracy of measurements. This study considered high speed position measurement of a 2-D target. The same camera could be used for estimating 3-D trajectories in workspace at a high speed. This could be done with a single camera using monocular vision or two cameras using stereo vision.

A controller development required both hardware and software with the FPGA. The hardware platform offered greater speeds of execution. Functions that are difficult to be implement in hardware were implemented in software using a virtual processor environment. However, developing some of these functions such as trigonometric and other complex functions in hardware would provide more robust and faster executing controllers. This will allow the controller to update the control signal at much higher frequencies. However, it should also be acknowledged that FPGAs are an emerging technology. Currently available Intel® i5/i7 and ARM®-Cortex processors offer greater speeds and flexibility for control system implementation.

There has to be a greater emphasis on the controller design of the robot. This was not possible in the current study due to time limitations. Although the robot produces a nonlinear response, it is controlled using a linear controller. Therefore, a more robust nonlinear controller should be designed for controlling the robot. This study also did not consider detailed state space modeling of the system and analysis of issues such

as controllability and stability of the control algorithms.

The research completed in this thesis on the design, development, and fabrication of a high speed visual servoing system demonstrates a comprehensive evaluation and contributes to the advancement of the automation of production processes.

8.3 Publications from this Study

The following conference proceedings were published from this study. Co-authors of these papers (Dr. Nicholas Krouglicof, Dr. Raymond Gosine and Dr. Geoff Rideout) have contributed in a supervisory capacity.

1. Liyanage Migara H., Krouglicof N., 2014, A Single Time Scale Visual Servoing System for a High Speed SCARA Type Robotic Arm, 2014 IEEE International Conference on Robotics and Automation (ICRA), 2-5 June, 2013, Hong Kong, China.

2. Liyanage Migara H., Rideout G., Krouglicof N., Modeling and Analysis of the Dynamic Performance of a High Speed Selective Compliant Assembly Robotic Arm (SCARA) on a Compliant Support, 10th International Conference on Bond Graph Modeling And Simulation (ICBGM), July 8-11, 2012, Genoa, Italy.

3. Liyanage Migara H., Krouglicof N., Gosine R., 2011, Development and Testing of a Novel High Speed SCARA Type Manipulator for Robotic Applications, 2011 IEEE International Conference on Robotics and Automation (ICRA), 9-13 May, 2011, Shanghai, China.

4. Liyanage Migara H., Krouglicof N., Gosine R., 2010, High Speed Electro-Hydraulic Actuator for a SCARA Type Robotic Arm, IEEE/RSJ International Conference

on Intelligent Robots and Systems (IROS) 2010, 18-22 October 2010, Taipei, Taiwan.

5. Liyanage Migara H., Krouglicof N., Gosine R., 2009, Design and Control of a High Performance SCARA Type Robotic Arm, 22nd IEEE Canadian Conference on Electrical and Computer Engineering, 3-6 May 2009, St Johns, Newfoundland, Canada.

Bibliography

[1] J. Shigley, C. Mischke, and R. Budynas, *Mechanical engineering design*. McGraw Hill Engineering, 7 ed., 2003.

[2] I. Adept Technology, *Adept Cobra s800 Technical Specifications*. Adept Technology, Inc., September 2010.

[3] M. Inc., "G761 series installation and operation instruction," tech. rep., Moog Inc., East Aurora, NY, 2002.

[4] C. P. and S. D., "A high-frequency first-principle model of a shock absorber and servo-hydraulic tester," *Mechanical Systems and Signal Processing*, vol. 25, no. 6, pp. 1937 – 1955, 2011. Interdisciplinary Aspects of Vehicle Dynamics.

[5] I. F. of Robotics, "IFR world robotics industrial robots 2012 executive summary," annual Report, International Federation of Robotics, 2012.

[6] I. F. of Robotics, "Ifr world robotics 2012 industrial robots," annual report, International Federation of Robotics, 2012.

[7] L. Tsai, *Robot Analysis: The Mechanics of Serial and Parallel Manipulators*. New York: John Wiley & Sons, 1999.

[8] H. Merrit, *Hydraulic control systems*. John Wiley & Sons, Inc., 1967.

[9] H. Hahn, A. Piepenbrink, and K. Leimbach, "Input/output linearization control of an electro servo-hydraulic actuator," pp. 995–1000, IEEE, Proceedings of the 3rd Conference on Control Applications, August 1994.

[10] M. Sirouspour and S. S.E., "Nonlinear control of hydraulic robots," *IEEE Transactions on Robotics and Automation*, vol. 17, pp. 173–182, April 2001.

[11] X. Shao and D. Sun, "Development of a new robot controller architecture with FPGA based IC design for improved high speed performance," *Industrial Informatics, IEEE Transactions on*, vol. 3, pp. 312 –321, November 2007.

[12] E. Monmasson and M. Cirstea, "FPGA design methodology for industrial control systems; A review," *Industrial Electronics, IEEE Transactions on*, vol. 54, pp. 1824 –1842, August 2007.

[13] Altera, "Nios II processor reference handbook," Application Report NII5V1-11.0, Altera Corporation, May 2011.

[14] Altera, "Quartus II handbook version 12.1," Application Report QII5V1-12.1.0, Altera Corporation, November 2012.

[15] K. Chao, Y. Chen, and D. Chan, "A spectroscopic system for high-speed inspection of poultry carcasses," *Applied Engineering in Agriculture*, vol. 20, no. 5, pp. 683–690, 2004.

[16] F. Pierrot, V. Nabat, O. Company, S. Krut, and P. Poignet, "Optimal design of a 4-DOF parallel manipulator: From academia to industry," *Robotics, IEEE Transactions on*, vol. 25, pp. 213 –224, April 2009.

[17] Epson, *Epson G-series SCARA Robots Technical Specifications*. Epson Robots, http://www.robots.epson.com/products/g-series.htm, February 2011.

[18] F. Ltd., *Fanuc Robot M-430iA Series*. Fanuc Ltd., October 2008.

[19] F. Ltd., *Fanuc Robot M-710iC Series*. Fanuc Ltd., October 2012.

[20] J. Li, Y. Liu, C. Wang, and L. Sun, "Optimal kinematic design of a planar parallel manipulator with high speed and high precision," pp. 1888 –1892, June 2006.

[21] K. Nagai, M. Matsumoto, K. Kimura, and B. Masuhara, "Development of parallel manipulator NINJA with ultra-high-acceleration," in *Robotics and Automation, 2003. Proceedings. ICRA '03. IEEE International Conference on*, vol. 3, pp. 3678–3685 vol.3, September 2003.

[22] S. Kawamura, W. Choe, S. Tanaka, and S. Pandian, "Development of an ultrahigh speed robot falcon using wire drive system," vol. 1, pp. 215 –220 vol.1, May 1995.

[23] K. Youcef-Toumi and A. Kuo, "High-speed trajectory control of a direct-drive manipulator," *Robotics and Automation, IEEE Transactions on*, vol. 9, pp. 102 –108, February 1993.

[24] R. Poley, "DSP control of electro-hydraulic servo actuators," Application Report SPRAA76, Texas Instruments, January 2005.

[25] J. Hollerbach, I. Hunter, and J. Ballantyne, *A Comparative Analysis of Actuator Technologies for Robotics*, pp. 299–342. The MIT Press, Cambridge, Massachusetts, 1992.

[26] J. Heintze, G. Van Schothorst, A. Van der Weiden, and P. Teerhuis, "Modeling and control of an industrial hydraulic rotary vane actuator," pp. 1913–1918,

IEEE, Proceedings of the 32nd Conference on Decision and Control, December 1993.

[27] V. Hunt, "Industrial robotics handbook," Industrial Press Inc., 1983.

[28] W. Backe, "Hydraulic drives with high efficiency," *Fluid Power Systems and Technology, ASME*, vol. 2, 1995.

[29] J. Mattila and T. Virvalo, "Energy-efficient motion control of a hydraulic manipulator," pp. 3000–3006, IEEE, International Conference on Robotics and Automation (ICRA), 2000.

[30] N. Manring, *Hydraulic Control Systems*. New Jersey: John Wiley & Sons, 1 ed., 2005.

[31] M. Jelali and A. Kroll, *Hydraulic Servo-systems: Modelling, Identification and Control*. Springer, 2003.

[32] D. Newell, D. Hongliang, M. Sain, P. Quast, and B. Spencer Jr., "Nonlinear modeling and control of a hydraulic seismic simulator," pp. 801–805, Proceedings of the American Control Conference, June 1995.

[33] F. Bu and B. Yao, "Nonlinear adaptive robust control of hydraulic actuators regulated by proportional directional control valves with deadband and nonlinear flow gains," pp. 4129–4133, Proceedings of the American Control Conference, 2000.

[34] F. Bu and B. Yao, "Integrated direct/indirect adaptive robust motion control of single-rod hydraulic actuators with time-varying unknown inertia," pp. 624–629, IEEE/ASME, International Conference on Advanced Intelligent Mechatronics, 2001.

[35] W. Owen, E. Croft, and J. McFarlane, "Reducing stick-slip friction in hydraulic actuators," *Advanced Intelligent Mechatronics, 2001. Proceedings. 2001 IEEE/ASME International Conference on*, vol. 1, pp. 642–647 vol.1, 2001.

[36] L. An and N. Sepehri, "Hydraulic actuator leakage quantification scheme using extended Kalman filter and sequential test method," p. 6, American Control Conference, June 2006.

[37] S. He and N. Sepehri, "Modeling and prediction of hydraulic servo actuators with neural networks," pp. 3708–3712, Proceedings of the American Control Conference, 1999.

[38] B. De Jager, "Acceleration assisted tracking control," *IEEE Control Systems Magazine*, vol. 14, no. 5, pp. 20–27, 1994.

[39] S. Tafazoli, C. De Silva, and P. Lawrence, "Tracking control of an electrohydraulic manipulator in the presence of friction," *IEEE Transactions on Control Systems Technology*, vol. 6, pp. 401–411, May 1998.

[40] G. Field and Y. Stepanenko, "Model reference impedance control of robotic manipulators," pp. 614–617, IEEE, Pacific Rim Conference Proceedings, 1993.

[41] B. Yao, T. C. Chiu, and J. Reedy, "Nonlinear adaptive robust control of 1-DOF electro-hydraulic servo systems," in *FPST-Vol.4.*, (Dallas), pp. 191–197, ASME International Mechanical Engineering Congress and Exposition (IMECE'97), 1997.

[42] V. R. and M. Donath, "Dynamic feedback linearization for electro-hydraulically actuated control systems," *ASME J. Dynamic Systems, Measurement, and Control*, vol. 117, no. 4, pp. 468–477, 1995.

[43] S. Habibi, R. Richards, and A. Goldenberg, "Hydraulic actuator analysis for industrial robot multivariable control," pp. 1003–1007, American Control Conference, June 1994.

[44] F. Bu and Y. Bin, "Nonlinear model based coordinated adaptive robust control of electro-hydraulic robotic arms via overparametrizing method," pp. 3459–3464, IEEE, International Conference on Robotics and Automation (ICRA), 2001.

[45] W. Owen and E. Croft, "The reduction of stick-slip friction in hydraulic actuators," *Mechatronics, IEEE/ASME Transactions on*, vol. 8, pp. 362–371, September 2003.

[46] G. Bilodeau and E. Papadopoulos, "Development of a hydraulic manipulator servoactuator model: simulation and experimental validation," *Robotics and Automation, 1997. Proceedings., 1997 IEEE International Conference on*, vol. 2, pp. 1547–1552 vol.2, 20-25 April 1997.

[47] P. Nakkarat and S. Kuntanapreeda, "Observer-based backstepping force control of an electrohydraulic actuator," *Control Engineering Practice*, vol. 17, no. 8, pp. 895 – 902, 2009.

[48] G. P. Liu and S. Daley, "Optimal-tuning PID control for industrial systems," *Control Engineering Practice*, vol. 9, no. 11, pp. 1185 – 1194, 2001.

[49] C. Kaddissi, J.-P. Kenne, and M. Saad, "Identification and real-time control of an electrohydraulic servo system based on nonlinear backstepping," *Mechatronics, IEEE/ASME Transactions on*, vol. 12, pp. 12–22, February 2007.

[50] P. La Hera, U. Mettin, S. Westerberg, and A. Shiriaev, "Modeling and control of hydraulic rotary actuators used in forestry cranes," in *Robotics and Automation, 2009. ICRA '09. IEEE International Conference on*, pp. 1315–1320, May 2009.

[51] Y. Measson, O. David, F. Louveau, and J. P. Friconneau, "Technology and control for hydraulic manipulators," *Fusion Engineering and Design*, vol. 69, no. 1-4, pp. 129 – 134, 2003. 22nd Symposium on Fusion Technology.

[52] E. L. Lewis, C. Abdallah, and D. Dawson, *Control of Robotic Manipulators*. Macmillan Publishing Company, New York, 1993.

[53] T. Tsao and M. Tomizuka, "Robust adaptive and repetitive digital control and application to hydraulic servo for noncircular machining," *ASME J . Dynamic Systems, Measurement, and Control*, vol. 116, pp. 24–32, 1994.

[54] A. Plummer and N. D. Vaughan, "Robust adaptive control for hydraulic servosystems," *ASME Journal of Dynamic Systems, Measurement and Control*, vol. 118, pp. 237–244, 1996.

[55] A. Alleyne and J. Hedrick, "Nonlinear adaptive control of active suspensions," *Control Systems Technology, IEEE Transactions on*, vol. 3, pp. 94–101, March 1995.

[56] B. Heinrichs, N. Sepehri, and A. Thornton-Trump, "Position-based impedance control of an industrial hydraulic manipulator," *Control Systems Magazine, IEEE*, vol. 17, no. 1, pp. 46–52, February 1997.

[57] J. G. Ziegler and N. Nichols, "Optimum settings for automatic controllers," *Trans. ASME*, no. 64, pp. pp. 759–768, 1942.

[58] K. Ogata, *Modern Control Engineering*. Upper Saddle River, NJ, USA: Prentice Hall PTR, 4th ed., 2001.

[59] Protean, *Protean Drive PD18 Performance Characteristics*. Protean Limited, http://www.proteanelectric.com, February 2013.

[60] D. Mellinger, A. Kushleyev, and V. Kumar, "Mixed-integer quadratic program trajectory generation for heterogeneous quadrotor teams," in *Robotics and Automation (ICRA), 2012 IEEE International Conference on*, pp. 477–483, 2012.

[61] B. Tamadazte, N. Le-Fort Piat, and E. Marchand, "A direct visual servoing scheme for automatic nanopositioning," *Mechatronics, IEEE/ASME Transactions on*, vol. 17, no. 4, pp. 728–736, 2012.

[62] D.-H. Park, J.-H. Kwon, and I.-J. Ha, "Novel position-based visual servoing approach to robust global stability under field-of-view constraint," *Industrial Electronics, IEEE Transactions on*, vol. 59, no. 12, pp. 4735–4752, 2012.

[63] S. Hutchinson, G. Hager, and P. Corke, "A tutorial on visual servo control," *Robotics and Automation, IEEE Transactions on*, vol. 12, no. 5, pp. 651–670, 1996.

[64] F. Janabi-Sharifi, L. Deng, and W. J. Wilson, "Comparison of basic visual servoing methods," *Mechatronics, IEEE/ASME Transactions on*, vol. 16, no. 5, pp. 967–983, 2011.

[65] L. Bascetta and P. Rocco, "End-point vibration sensing of planar flexible manipulators through visual servoing," *Mechatronics*, vol. 16, no. 3-4, pp. 221–232, 2006.

[66] M. Tavakoli and R. Howe, "Improving teleoperation performance in the presence of non-ideal robot dynamics," in *Technologies for Practical Robot Applications, 2008. TePRA 2008. IEEE International Conference on*, pp. 128–130, 2008.

[67] M. Attolico, O. Cargnel, R. Cazzoli, A. Davighi, and F. Bernelli-Zazzera, "A visual servoing control system for lightweight robotic manipulator," in *Advanced Intelligent Mechatronics. Proceedings, 2005 IEEE/ASME International Conference on*, pp. 1005–1010, 2005.

[68] O. Ma, J. Wang, S. Misra, and M. Liu, "On the validation of SPDM task verification facility," *Journal of Robotic Systems*, vol. 21, no. 5, pp. 219–235, 2004.

[69] Z.-H. Jiang and T. Eguchi, "Vision feedback based end-effector motion control of a flexible robot arm," in *Systems, Man and Cybernetics, 2007. ISIC. IEEE International Conference on*, pp. 2413–2419, 2007.

[70] Y. Liu, N. Xi, Y. Shen, S. Bi, B. Gao, Q. Shi, X. Li, G. Zhang, and T. Fuhlbrigge, "High-accuracy visual/PSD hybrid servoing of robotic manipulator," in *Advanced Intelligent Mechatronics, 2008. AIM 2008. IEEE/ASME International Conference on*, pp. 217–222, 2008.

[71] L. Bascetta and P. Rocco, "Two-time scale visual servoing of eye-in-hand flexible manipulators," *Robotics, IEEE Transactions on*, vol. 22, no. 4, pp. 818–830, 2006.

[72] X. Jiang, A. Konno, and M. Uchiyama, "Visual servoing experiment using a 3D flexible-link manipulator," in *Intelligent Robots and Systems, 2006 IEEE/RSJ International Conference on*, pp. 1224–1229, 2006.

[73] V. Lippiello, B. Siciliano, and L. Villani, "Position-based visual servoing in industrial multirobot cells using a hybrid camera configuration," *Robotics, IEEE Transactions on*, vol. 23, no. 1, pp. 73–86, 2007.

[74] X. Jiang, Y. Yabe, A. Konno, and M. Uchiyama, "Vibration suppression control of a flexible arm using image features of unknown objects," in *Intelligent Robots and Systems, 2008. IROS 2008. IEEE/RSJ International Conference on*, pp. 3783–3788, 2008.

[75] T. Mansour, X. Jiang, A. Konno, and M. Uchiyama, "Experimental verification on vibration suppression of a flexible manipulator using MPID controller," in *Robotics and Automation, 2008. ICRA 2008. IEEE International Conference on*, pp. 2896–2901, 2008.

[76] D. Karnopp, D. Margolis, and R. Rosenberg, *System Dynamics: Modeling and Simulation of Mechatronic Systems.* John Wiley and Sons, New Jersey, 5 ed., 2012.

[77] J. Hill and W. Park, "Real time control of a robot with a mobile camera," in *9th ISIR, Proceedings of the*, pp. 233–246, 1979.

[78] C. Onal and M. Sitti, "Visual servoing-based autonomous 2D manipulation of micro-particles using a nanoprobe," *Control Systems Technology, IEEE Transactions on*, vol. 15, no. 5, pp. 842–852, 2007.

[79] Y. Wang, H. Lang, and C. de Silva, "A hybrid visual servo controller for robust grasping by wheeled mobile robots," *Mechatronics, IEEE/ASME Transactions on*, vol. 15, no. 5, pp. 757–769, 2010.

[80] A. Krupa, J. Gangloff, C. Doignon, M. de Mathelin, G. Morel, J. Leroy, L. Soler, and J. Marescaux, "Autonomous 3D positioning of surgical instruments in robo-

tized laparoscopic surgery using visual servoing," *Robotics and Automation, IEEE Transactions on*, vol. 19, no. 5, pp. 842–853, 2003.

[81] A. Ferreira, C. Cassier, and S. Hirai, "Automatic microassembly system assisted by vision servoing and virtual reality," *Mechatronics, IEEE/ASME Transactions on*, vol. 9, no. 2, pp. 321–333, 2004.

[82] L. Mejias, P. Campoy, S. Saripalli, and G. Sukhatme, "A visual servoing approach for tracking features in urban areas using an autonomous helicopter," in *Robotics and Automation, 2006. ICRA 2006. Proceedings 2006 IEEE International Conference on*, pp. 2503–2508, 2006.

[83] F. Chaumette and S. Hutchinson, "Visual servo control. i. basic approaches," *Robotics Automation Magazine, IEEE*, vol. 13, no. 4, pp. 82–90, 2006.

[84] N. Guenard, T. Hamel, and R. Mahony, "A practical visual servo control for an unmanned aerial vehicle," *Robotics, IEEE Transactions on*, vol. 24, no. 2, pp. 331–340, 2008.

[85] N. Vahrenkamp, S. Wieland, P. Azad, D. Gonzalez, T. Asfour, and R. Dillmann, "Visual servoing for humanoid grasping and manipulation tasks," in *Humanoid Robots, 2008. Humanoids 2008. 8th IEEE-RAS International Conference on*, pp. 406–412, 2008.

[86] O. Bourquardez, R. Mahony, N. Guenard, F. Chaumette, T. Hamel, and L. Eck, "Image-based visual servo control of the translation kinematics of a quadrotor aerial vehicle," *Robotics, IEEE Transactions on*, vol. 25, no. 3, pp. 743–749, 2009.

[87] H. Fujimoto, L.-C. Zhu, and K. Abdel-Malek, "Image-based visual servoing for grasping unknown objects," in *Industrial Electronics Society, 2000. IECON 2000. 26th Annual Confjerence of the IEEE*, vol. 2, pp. 876–881 vol.2, 2000.

[88] P. Corke and S. Hutchinson, "A new hybrid image-based visual servo control scheme," in *Decision and Control, 2000. Proceedings of the 39th IEEE Conference on*, vol. 3, pp. 2521–2526 vol.3, 2000.

[89] R. Mahony and T. Hamel, "Image-based visual servo control of aerial robotic systems using linear image features," *Robotics, IEEE Transactions on*, vol. 21, no. 2, pp. 227–239, 2005.

[90] F. Le Bras, T. Hamel, and R. Mahony, "Image-based visual servo control for circular trajectories for a fixed-wing aircraft," in *Decision and Control, 2009 held jointly with the 2009 28th Chinese Control Conference. CDC/CCC 2009. Proceedings of the 48th IEEE Conference on*, pp. 3430–3435, 2009.

[91] F. Janabi-Sharifi and M. Marey, "A Kalman-filter-based method for pose estimation in visual servoing," *Robotics, IEEE Transactions on*, vol. 26, no. 5, pp. 939–947, 2010.

[92] S. Hati and S. Sengupta, "A GA-based integrated approach to model-assisted matching and pose estimation for automated visual inspection applications," in *Evolutionary Computation, 2004. CEC2004. Congress on*, vol. 2, pp. 1346–1353 Vol.2, 2004.

[93] H. M. Becerra and C. Sagues, "Exploiting the trifocal tensor in dynamic pose estimation for visual control," 2012.

[94] M. Salehian, S. RayatDoost, and H. Taghirad, "Robust unscented Kalman filter for visual servoing system," in *Control, Instrumentation and Automation (ICCIA), 2011 2nd International Conference on*, pp. 1006–1011, 2011.

[95] V. Lippiello, B. Siciliano, and L. Villani, "3D pose estimation for robotic applications based on a multi-camera hybrid visual system," in *Robotics and Automation, 2006. ICRA 2006. Proceedings 2006 IEEE International Conference on*, pp. 2732–2737, 2006.

[96] S. Liu, W.-F. Xie, and C.-Y. Su, "Image-based visual servoing using improved image moments," in *Information and Automation, 2009. ICIA '09. International Conference on*, pp. 577–582, 2009.

[97] J. Feddema and O. R. Mitchell, "Vision-guided servoing with feature-based trajectory generation [for robots]," *Robotics and Automation, IEEE Transactions on*, vol. 5, no. 5, pp. 691–700, 1989.

[98] C. Collewet and E. Marchand, "Photometric visual servoing," *Robotics, IEEE Transactions on*, vol. 27, no. 4, pp. 828–834, 2011.

[99] W. J. Wilson, C. Williams Hulls, and G. Bell, "Relative end-effector control using cartesian position based visual servoing," *Robotics and Automation, IEEE Transactions on*, vol. 12, no. 5, pp. 684–696, 1996.

[100] W. Wilson, C. Wiliams-Hulls, and F. Janabi-Sharifi, "Robust image processing and position-based visual servoing," in *Proceedings of the IEEE International Conference on Robotics and Automation, ICRA 98, Workshop WS2 Robust Vision for Vision-Based Control of Motion*, pp. 1–24, 1998.

[101] T. Heitzmann, C. Doignon, C. Albitar, and P. Graebling, "Position-based visual servoing using a coded structured light sensor," in *Robotic and Sensors Environments, 2008. ROSE 2008. International Workshop on*, pp. 126–131, 2008.

[102] N. Ziraknejad, S. Tafazoli, and P. Lawrence, "Autonomous stereo camera parameter estimation for outdoor visual servoing," in *Machine Learning for Signal Processing, 2007 IEEE Workshop on*, pp. 157–162, 2007.

[103] Y. Yoon, G. DeSouza, and A. Kak, "Real-time tracking and pose estimation for industrial objects using geometric features," in *Robotics and Automation, 2003. Proceedings. ICRA '03. IEEE International Conference on*, vol. 3, pp. 3473–3478 vol.3, 2003.

[104] X. Gratal, J. Romero, and D. Kragic, "Virtual visual servoing for real-time robot pose estimation," in *18th IFAC World congress*, vol. 18, pp. 9017–9022, 2011.

[105] D. Lee, T. Ryan, and H. Kim, "Autonomous landing of a VTOL UAV on a moving platform using image-based visual servoing," in *Robotics and Automation (ICRA), 2012 IEEE International Conference on*, pp. 971–976, 2012.

[106] Y. Shi, B. Liang, X. Wang, W. Xu, and H. Liu, "Modeling and simulation of space robot visual servoing for autonomous target capturing," in *Mechatronics and Automation (ICMA), 2012 International Conference on*, pp. 2275–2280, 2012.

[107] T. P. Sim, G. Hong, and K. Lim, "A pragmatic 3D visual servoing system," in *Robotics and Automation, 2002. Proceedings. ICRA '02. IEEE International Conference on*, vol. 4, pp. 4185–4190 vol.4, 2002.

[108] S. Leonard and M. Jagersand, "Learning based visual servoing," in *Intelligent Robots and Systems, 2004. (IROS 2004). Proceedings. 2004 IEEE/RSJ International Conference on*, vol. 1, pp. 680–685 vol.1, 2004.

[109] M. Akella, "Vision-based adaptive tracking control of uncertain robot manipulators," *Robotics, IEEE Transactions on*, vol. 21, no. 4, pp. 747–753, 2005.

[110] R. Pieters, A. Alvarez-Aguirre, P. Jonker, and H. Nijmeijer, "Feed forward visual servoing for object exploration," in *Intelligent Robots and Systems (IROS), 2012 IEEE/RSJ International Conference on*, pp. 1702–1707, 2012.

[111] T. Murao, T. Yamada, and M. Fujita, "Predictive visual feedback control with eye-in-hand system via stabilizing receding horizon approach," in *Decision and Control, 2006 45th IEEE Conference on*, pp. 1758–1763, 2006.

[112] C. Copot, C. Lazar, and A. Burlacu, "Predictive control of nonlinear visual servoing systems using image moments," *Control Theory Applications, IET*, vol. 6, no. 10, pp. 1486–1496, 2012.

[113] X. Lv and X. Huang, "Fuzzy adaptive Kalman filtering based estimation of image jacobian for uncalibrated visual servoing," in *Intelligent Robots and Systems, 2006 IEEE/RSJ International Conference on*, pp. 2167–2172, 2006.

[114] L. Cuvillon, E. Laroche, J. Gangloff, and M. De Mathelin, "GPC versus H-infinity control for fast visual servoing of a medical manipulator including flexibilities," in *Robotics and Automation, 2005. ICRA 2005. Proceedings of the 2005 IEEE International Conference on*, pp. 4044–4049, 2005.

[115] L. Bascetta and P. Rocco, "Two-time scale visual servoing of eye-in-hand flexible manipulators," *Robotics, IEEE Transactions on*, vol. 22, no. 4, pp. 818–830, 2006.

[116] S. Kwon, H. Jeong, and J. Hwang, "Kalman filter-based coarse-to-fine control for display visual alignment systems," *Automation Science and Engineering, IEEE Transactions on*, vol. 9, no. 3, pp. 621–628, 2012.

[117] T. Rahman and N. Krouglicof, "An efficient camera calibration technique offering robustness and accuracy over a wide range of lens distortion," *Image Processing, IEEE Transactions on*, vol. 21, pp. 626 –637, February 2012.

[118] J. Heikkila, "Geometric camera calibration using circular control points," *Pattern Analysis and Machine Intelligence, IEEE Transactions on*, vol. 22, pp. 1066 – 1077, October 2000.

[119] C. Wang, W. Chen, and M. Tomizuka, "Robot end-effector sensing with position sensitive detector and inertial sensors," in *Robotics and Automation (ICRA), 2012 IEEE International Conference on*, pp. 5252 –5257, May 2012.

[120] G. Brooker, *Introduction to Sensors for Ranging and Imaging*. Scitech, 2009.

[121] B. Shirinzadeh, P. Teoh, Y. Tian, M. Dalvand, Y. Zhong, and H. Liaw, "Laser interferometry-based guidance methodology for high precision positioning of mechanisms and robots," *Robotics and Computer-Integrated Manufacturing*, vol. 26, no. 1, pp. 74 – 82, 2010.

[122] Z.-H. Jiang and T. Eguchi, "Vision feedback based end-effector motion control of a flexible robot arm," in *Systems, Man and Cybernetics, 2007. ISIC. IEEE International Conference on*, pp. 2413 –2419, October 2007.

[123] W. Xu, S. Tso, and X. Wang, "Conceptual design of an integrated laser-optical measuring system for flexible manipulator," in *Systems, Man, and Cybernetics, 1996., IEEE International Conference on*, vol. 2, pp. 1247 –1252 vol.2, October 1996.

[124] J. Gonzalez and C. Bleakley, "High-precision robust broadband ultrasonic location and orientation estimation," *Selected Topics in Signal Processing, IEEE Journal of*, vol. 3, pp. 832 –844, October 2009.

[125] J. Prieto, A. Jimenez, J. Guevara, J. Ealo, F. Seco, J. Roa, and F. Ramos, "Performance evaluation of 3D-LOCUS advanced acoustic LPS," *Instrumentation and Measurement, IEEE Transactions on*, vol. 58, pp. 2385 –2395, August 2009.

[126] M. Saad, C. Bleakley, and S. Dobson, "Robust high-accuracy ultrasonic range measurement system," *Instrumentation and Measurement, IEEE Transactions on*, vol. 60, pp. 3334 –3341, October 2011.

[127] U. J. *et al.*, "Advanced sensorial system for an acoustic lps," *Microprocessors and Microsystems*, vol. 31, no. 6, pp. 393 – 401, 2007. <ce:title>Special Issue on Sensor Systems</ce:title>.

[128] A. Morris, M. Dickinson, and A. Zalzala, "An enhanced ultrasonic system for robot end effector tracking," in *Control 1991. Control '91., International Conference on*, pp. 352 –357 vol.1, March 1991.

[129] A. Urruela, A. Pages-Zamora, and J. Riba, "Divide-and-conquer based closed-form position estimation for AOA and TDOA measurements," in *Acoustics, Speech and Signal Processing, 2006. ICASSP 2006 Proceedings. 2006 IEEE International Conference on*, vol. 4, p. IV, May 2006.

[130] C. De Marziani, J. Urena, M. Mazo, A. Hernandez, J. Garcia, A. Jimenez, M. Perez, A. Ochoa, and J. Villadangos, "Relative positioning system using simultaneous round trip time of flight measurements," in *Emerging Technologies*

and Factory Automation, 2006. ETFA '06. IEEE Conference on, pp. 602 –605, September 2006.

[131] P. Gil, J. Pomares, and F. Torres, "Analysis and adaptation of integration time in PMD camera for visual servoing," in *Pattern Recognition (ICPR), 2010 20th International Conference on*, pp. 311 –315, August 2010.

[132] K. Pourvoyeur, A. Stelzer, and G. Gassenbauer, "Position estimation techniques for the local position measurement system LPM," in *Microwave Conference, 2006. APMC 2006. Asia-Pacific*, pp. 1509 –1514, December 2006.

[133] H. Gander, M. Vincze, and J. Prenninger, "An external 6D-sensor for industrial robots," in *Intelligent Robots and Systems '93, IROS '93. Proceedings of the 1993 IEEE/RSJ International Conference on*, vol. 2, pp. 975 –978 vol.2, July 1993.

[134] C. Nagata, A. Torii, K. Doki, and A. Ueda, "A position measurement system for a small autonomous mobile robot," in *Micro-NanoMechatronics and Human Science, 2007. MHS '07. International Symposium on*, pp. 50 –55, November 2007.

[135] P. Rousseau, A. Desrochers, and N. Krouglicof, "Machine vision system for the automatic identification of robot kinematic parameters," *Robotics and Automation, IEEE Transactions on*, vol. 17, pp. 972 –978, December 2001.

[136] C. Medina, J. Segura, and S. Holm, "Feasibility of ultrasound positioning based on signal strength," in *Indoor Positioning and Indoor Navigation (IPIN), 2012 International Conference on*, pp. 1 –9, November 2012.

[137] A. Kolb, E. Barth, and R. Koch, "TOF-sensors: New dimensions for realism and interactivity," in *Computer Vision and Pattern Recognition Workshops, 2008. CVPRW '08. IEEE Computer Society Conference on*, pp. 1 –6, June 2008.

[138] N. Ziraknejad, P. Lawrence, and D. Romilly, "The effect of time-of-flight camera integration time on vehicle driver head pose tracking accuracy," in *Vehicular Electronics and Safety (ICVES), 2012 IEEE International Conference on*, pp. 247 –254, July 2012.

[139] G. C. and K. A., "A comprehensive evaluation of indoor ranging using ultra-wideband technology," *Wireless Communications and Networking, EURASIP Journal on*, vol. 2007, pp. 1–12, May 2007.

[140] G. Alici and B. Shirinzadeh, "A systematic technique to estimate positioning errors for robot accuracy improvement using laser interferometry based sensing," *Mechanism and Machine Theory*, vol. 40, no. 8, pp. 879 – 906, 2005.

[141] A. Tobergte, F. Frohlich, M. Pomarlan, and G. Hirzinger, "Towards accurate motion compensation in surgical robotics," in *Robotics and Automation (ICRA), 2010 IEEE International Conference on*, pp. 4566 –4572, May 2010.

[142] N. Michael, D. Mellinger, Q. Lindsey, and V. Kumar, "The grasp multiple micro-uav testbed," *Robotics Automation Magazine, IEEE*, vol. 17, pp. 56 –65, September 2010.

[143] M. Windolf, N. Götzen, M. Morlock, *et al.*, "Systematic accuracy and precision analysis of video motion capturing systems–exemplified on the Vicon-460 system.," *Journal of biomechanics*, vol. 41, no. 12, p. 2776, 2008.

[144] T. Sievers and S. Fatikow, "Visual servoing of a mobile microrobot inside a scanning electron microscope," in *Intelligent Robots and Systems, 2005. (IROS*

2005). 2005 IEEE/RSJ International Conference on, pp. 1350 – 1354, August 2005.

[145] K. Nakao, K. Kondo, S. Kobashi, Y. Hata, T. Yagi, and T. Hayashi, "Object position/pose estimation using cad models for navigation of manipulator with a single CCD camera," in *Computational Intelligence in Robotics and Automation, 2003. Proceedings. 2003 IEEE International Symposium on*, vol. 3, pp. 1433 – 1438 vol.3, July 2003.

[146] J. Fischer and O. Pribula, "Precise sub-pixel position measurement with linear interpolation of CMOS sensor image data," in *Intelligent Data Acquisition and Advanced Computing Systems (IDAACS), 2011 IEEE 6th International Conference on*, vol. 1, pp. 500 –504, September 2011.

[147] D. Schindele, I. Menn, and H. Aschemann, "Nonlinear optimal control of an overhead travelling crane," in *Control Applications, (CCA) Intelligent Control, (ISIC), 2009 IEEE*, pp. 1045 –1050, July 2009.

[148] H. Higa, K. Tsuha, R. Onaga, and I. Nakamura, "Position tracking of the mouth using image processing," in *Engineering in Medicine and Biology Society, 2006. EMBS '06. 28th Annual International Conference of the IEEE*, pp. 3460 –3463, September 2006.

[149] M. Fukuzawa, H. Hama, N. Nakamori, and M. Yamada, "High-speed distance measurement between moving vehicles with NIR-LED markers," in *Computer and Information Technology, 2008. ICCIT 2008. 11th International Conference on*, pp. 516 –520, December 2008.

[150] J. Jason, H. Nilsson, B. Arvidsson, and A. Larsson, "Experimental study of an intensity modulated fiber-optic position sensor with a novel readout system," *Sensors Journal, IEEE*, vol. 8, pp. 1105 –1113, July 2008.

[151] N. Krouglicof, *Noncontact position and orientation measurement techniques for real-time systems*. PhD thesis, Concordia University, 1991.

[152] T. Inoue, A. Torii, K. Doki, and A. Ueda, "Position measurement system for a microsystem," in *Micro-NanoMechatronics and Human Science, 2005 IEEE International Symposium on*, pp. 175 –180, November 2005.

[153] W. Schottky, "About the origin of the photoelectron in Copper-Cuprous Oxide photocells (in German)," *Phys. Z. 31*, vol. 31, pp. 913–925, 1930.

[154] J. Wallmark, "A new semiconductor photocell using lateral photoeffect," *Proceedings of the IRE*, vol. 45, pp. 474 –483, April 1957.

[155] W. M., "Calibrating lateral-effect photodiodes for use as measuring devices in manufacturing," in *Modern Manufacturing 1990 conference. Proceedings of the*, pp. 1–9, September 1990.

[156] R. Myers, D. Montgomery, and C. Anderson-Cook, *Response Surface Methodology: Process and Product Optimization Using Designed Experiments*. New York, NY, USA: John Wiley & Sons, Inc., 3rd ed., 2011.

[157] L. Euler, "Formulae generales pro translatione quacunque corporum rigidorum," *Novi Commentari Acad Scientiarum Imperialis Petropolitanae*, vol. 20, pp. 189–207, 1775.

[158] K. Levenberg, "A method for the solution of certain non linear problems in least squares," *Quarterly of Applied Mathematics*, vol. 2, no. 2, pp. 164–168, 1944.

[159] J. U. Cho, Q. N. Le, and J. W. Jeon, "An fpga-based multiple-axis motion control chip," *Industrial Electronics, IEEE Transactions on*, vol. 56, pp. 856 –870, March 2009.

[160] E. Monmasson, L. Idkhajine, and M.-w. Naouar, "FPGA-based controllers," *Industrial Electronics Magazine, IEEE*, vol. 5, no. 1, pp. 14–26, 2011.

[161] H.-C. Huang and C.-C. Tsai, "FPGA implementation of an embedded robust adaptive controller for autonomous omnidirectional mobile platform," *Industrial Electronics, IEEE Transactions on*, vol. 56, pp. 1604 –1616, May 2009.

[162] N. Chakravarthy and J. Xiao, "FPGA-based control system for miniature robots," in *Intelligent Robots and Systems, 2006 IEEE/RSJ International Conference on*, pp. 3399 –3404, October 2006.

[163] Y. Sun, Y. Fang, Y. Zhang, and X. Dong, "Field programmable gate array (FPGA) based embedded system design for AFM real-time control," in *Control Applications (CCA), 2010 IEEE International Conference on*, pp. 245–250, 2010.

[164] C. Li, Y. lin Zhang, and Z. na Zheng, "Design of image acquisition and processing based on FPGA," in *Information Technology and Applications, 2009. IFITA '09. International Forum on*, vol. 3, pp. 113 –115, May 2009.

[165] S. Popescu, A. Gontean, and G. Budura, "Simulation and implementation of a BPSK modulator on FPGA," in *Applied Computational Intelligence and Informatics (SACI), 2011 6th IEEE International Symposium on*, pp. 459 –463, May 2011.

[166] A. Fernandes, R. Pereira, J. Sousa, A. Batista, A. Combo, B. Carvalho, C. Correia, and C. Varandas, "HDL based FPGA interface library for data acquisition

and multipurpose real time algorithm processing," in *Real Time Conference (RT), 2010 17th IEEE-NPSS*, pp. 1–5, May 2010.

[167] S. Jin, D. Kim, T. Song, Q. N. Le, and J. W. Jeon, "An FPGA-based motion-vision integrated system for real-time machine vision applications," in *Industrial Electronics, 2009. ISIE 2009. IEEE International Symposium on*, pp. 700 –705, July 2009.

[168] W. Qi, "FPGA-based digital signal processing algorithm research," in *Computer Science and Information Technology (ICCSIT), 2010 3rd IEEE International Conference on*, vol. 4, pp. 690 –692, July 2010.

[169] A. Bonatto, A. Soares, and A. Susin, "Multichannel SDRAM controller design for H.264/AVC video decoder," in *Programmable Logic (SPL), 2011 VII Southern Conference on*, pp. 137 –142, April 2011.

[170] L. Nianqiang, W. Yongbing, and Z. Guoyi, "A preferable method on digital filter in ECG signal's processing based on FPGA," in *Intelligent Information Technology and Security Informatics (IITSI), 2010 Third International Symposium on*, pp. 184 –187, April 2010.

[171] K. Nguyen, J. Zheng, Y. He, and B. Shah, "A high-throughput, adaptive FFT architecture for FPGA-based space-borne data processors," in *Adaptive Hardware and Systems (AHS), 2010 NASA/ESA Conference on*, pp. 121 –126, June 2010.

[172] W. El-Medany and M. Hussain, "FPGA-based advanced real traffic light controller system design," in *Intelligent Data Acquisition and Advanced Computing Systems: Technology and Applications, 2007. IDAACS 2007. 4th IEEE Workshop on*, pp. 100 –105, September 2007.

[173] W. Jiang and M. Gokhale, "Real-time classification of multimedia traffic using FPGA," in *Field Programmable Logic and Applications (FPL), 2010 International Conference on*, pp. 56 –63, September 2010.

[174] T. ming Shih and H. chung Chang, "FPGA based hardware in the loop test platform of small size uav," in *Computational Intelligence in Robotics and Automation (CIRA), 2009 IEEE International Symposium on*, pp. 551 –556, December 2009.

[175] G. Spampinato, J. Lidholm, C. Ahlberg, F. Ekstrand, M. Ekstrom, and L. Asplund, "An embedded stereo vision module for 6D pose estimation and mapping," in *Intelligent Robots and Systems (IROS), 2011 IEEE/RSJ International Conference on*, pp. 1626 –1631, September 2011.

[176] S. Falsig and A. Soerensen, "An FPGA based approach to increased flexibility, modularity and integration of low level control in robotics research," in *Intelligent Robots and Systems (IROS), 2010 IEEE/RSJ International Conference on*, pp. 6119 –6124, October 2010.

[177] Z. Yili, S. Hanxu, J. Qingxuan, and S. Guozhen, "Kinematics control for a 6-DOF space manipulator based on arm processor and FPGA co-processor," in *Industrial Informatics, 2008. INDIN 2008. 6th IEEE International Conference on*, pp. 129 –134, July 2008.

[178] Z. Zhou, T. Li, T. Takahashi, and E. Ho, "FPGA realization of a high-performance servo controller for PMSM," in *Applied Power Electronics Conference and Exposition, 2004. APEC '04. Nineteenth Annual IEEE*, vol. 3, pp. 1604–1609 Vol.3, 2004.

[179] K. Jezernik and M. Rodic, "High precision motion control of servo drives," *Industrial Electronics, IEEE Transactions on*, vol. 56, no. 10, pp. 3810–3816, 2009.

[180] Y.-Y. Tzou and T.-S. Kuo, "Design and implementation of all FPGA-based motor control IC for permanent magnet AC servo motors," in *Industrial Electronics, Control and Instrumentation, 1997. IECON 97. 23rd International Conference on*, vol. 2, pp. 943–947 vol.2, 1997.

[181] T. Li, S.-J. Chang, and Y.-X. Chen, "Implementation of human-like driving skills by autonomous fuzzy behavior control on an FPGA-based car-like mobile robot," *Industrial Electronics, IEEE Transactions on*, vol. 50, no. 5, pp. 867–880, 2003.

[182] H. Zhuang, K.-S. Low, and W.-Y. Yau, "A pulsed neural network with on-chip learning and its practical applications," *Industrial Electronics, IEEE Transactions on*, vol. 54, no. 1, pp. 34–42, 2007.

[183] Y. F. Chan, M. Moallem, and W. Wang, "Design and implementation of modular FPGA-based PID controllers," *Industrial Electronics, IEEE Transactions on*, vol. 54, pp. 1898 –1906, August 2007.

[184] N. Krouglicof, "Implementing CPLD-based interfaces for sensors and actuators in a mechatronic design course," in *American Society for Engineering Education 2004 American Society for Engineering Education Annual Conference and Exposition, Proceedings of the*, vol. Session 1520, June 2004.